UNIVERSIDADE FEDERAL DE SANTA CATARINA
PROGRAMA DE PÓS-GRADUAÇÃO EM CIÊNCIA E ENGENHARIA DE MATERIAIS
Departamento de Engenharia Mecânica

Mayka Schmitt

PORE STRUCTURE CHARACTERIZATION OF LOW PERMEABILITY ROCKS

Florianópolis
Março, 2014

UNIVERSIDADE FEDERAL DE SANTA CATARINA
PROGRAMA DE PÓS-GRADUAÇÃO EM CIÊNCIA E ENGENHARIA DE MATERIAIS
Departamento de Engenharia Mecânica

Mayka Schmitt

PORE STRUCTURE CHARACTERIZATION OF LOW PERMEABILITY ROCKS

Tese submetida ao Programa de Pós-Graduação Em Ciência e Engenharia de Materiais da Universidade Federal de Santa Catarina para a Obtenção do Grau de Doutor em Ciência e Engenharia de Materiais.

Orientador: Prof. Dr. Eng. Celso Peres Fernandes
Coorientador: Prof. Dr. Fabiano Gilberto Wolf

Florianópolis
2014

Ficha de identificação da obra elaborada pelo autor,
através do Programa de Geração Automática da Biblioteca Universitária da UFSC.

Schmitt, Mayka
PORE STRUCTURE CHARACTERIZATION OF LOW PERMEABILITY ROCKS / Mayka Schmitt ; orientador, Celso Peres Fernandes ; coorientador, Fabiano Gilberto Wolf. - Florianópolis, SC, 2014.
223 p.

Tese (doutorado) - Universidade Federal de Santa Catarina, Centro Tecnológico. Programa de Pós-Graduação em Ciência e Engenharia de Materiais.

Inclui referências

1. Ciência e Engenharia de Materiais. 2. Arenitos de baixa permeabilidade. 3. Rochas selantes. 4. Caracterização de rochas. I. Fernandes, Celso Peres. II. Wolf, Fabiano Gilberto. III. Universidade Federal de Santa Catarina. Programa de Pós-Graduação em Ciência e Engenharia de Materiais. IV. Título.

MAYKA SCHMITT

PORE STRUCTURE CHARACTERIZATION OF LOW PERMEABILITY ROCKS

Esta Tese foi julgada adequada para a obtenção do Título de Doutor, e aprovada em sua forma final pelo Programa de Pós-Graduação em Ciência e Engenharia de Materiais.

Florianópolis, 28 de Março de 2014.

Prof. Dr. Antônio Pedro Novaes de Oliveira – Coordenador do PGMAT

Prof. Dr. Eng. Celso Peres Fernandes – Orientador, UFSC
(Presidente)

Prof. Dr. Fabiano Gilberto Wolf – Coorientador, UFSC

Banca Examinadora:

Prof. Dr. José Agnelo Soares
Universidade Federal de Campina Grande
(Membro Externo)

Eng. Dr. Rodrigo Surmas
CENPES/Petrobras
(Membro Externo)

Prof. Dr. Roberto Sacks de Campos
Universidade Federal de Santa Catarina
(Membro Externo)

Prof. Dr. João Cardoso de Lima
Universidade Federal de Santa Catarina
(Membro)

Prof. Dr. José A. Bellini da Cunha Neto
Universidade Federal de Santa Catarina
(Membro)

AGRADECIMENTOS

Quatro anos e meio que se passam, período não tão fácil mas no qual muito aprendi e me fortaleci para a vida. Esses anos do doutorado eu considero prósperos, de grandes desafios, bons momentos e realizações. Hoje é um dia feliz e de olhar ansiosa para o futuro!

Pela realização deste doutoramento, não poderia deixar de agradecer:

À família LMPT

Prof. Celso, meu orientador desde o mestrado, muito obrigada pela confiança atribuída, ensinamentos e oportunidade oferecida para o conhecimento na área do petróleo; Prof. Fabiano, meu coorientador e demais professores e colegas que estão ou já passaram pelo LMPT, agradeço imensamente toda a ajuda com experimentos e simulações (Anderson, Denise, Emerich, Iara e Keijo), boa convivência e momentos extraclasse.

Aos membros da banca por sua disposição e contribuição ao trabalho.

Ao laboratório LSCM, Prof. João e Claudio Poffo

Pela ajuda e desenvolvimento dos trabalhos com a técnica PAS.

Ao PGMAT e CAPES

Pelo apoio e suporte nessários à realização do doutorado.

Ao centro de pesquisa CENPES/Petrobras

Vinícius e Viviane; e pessoal do Laboratório de Petrofísica, Nelita, Leandro, Leonardo, Gilson, Claudio, Lucas, Gerson, pelo auxílio aos experimentos e bons momentos no Rio de Janeiro.

Ao centro de pesquisa CSIRO/ARRC e ao CNPq pela oportunidade e fomento necessários para a realização do estágio sanduíche em Perth

Ben Clennell, Lionel, Claudio Piane, Michael Verrall e Marina Pervukhina, pelo apoio científico, técnico e experimental;

Por fim, a minha amada e estimada família

Minha mãe e amiga, Ivanilda, fiel até nas coisas mais simples da vida; Willian e Me, Gilliard e Tati, pelo apoio total e alegria proporcionada trazendo ao mundo a Yasmin e a Nicolly. Ao meu pai querido, Lori, que sempre foi zeloso e amoroso e com toda a sua força lutou, mas infelizmente partiu neste periodo, hoje é luz e paz no meu caminho. Ao Christoffer que me faz sorrir, é atencioso, me conhece e me faz tão bem!

Obrigada de coração!

"In Europe, during the latter half of the 17th century, Newton and Leibniz independently developed infinitesimal calculus, which grew, with the stimulus of applied work that continued through the 18th century, into analysis topics such as the calculus of variations, ordinary and partial differential equations, Fourier analysis, and generating functions. During this period, calculus techniques were applied to approximate discrete problems by continuous ones."
Mathematical analysis, WIKIPEDIA

"Engineers like to solve problems. If there are no problems handily available, they will create their own problems."
Scott Adams (1957 -)

"It always seems impossible until it's done."
Nelson Mandela (1918 - 2013)

ABSTRACT

Nowadays, significant research effort in low-permeability rocks (a wide tendency elsewhere and soon in the Brazilian petroleum industry) has been focused on pore-scale petrophysics, morphologies and distributions, as well as fluid flow circulation described by the values of permeability. The evaluation of these properties in turn is essential for the assessment and exploitation of hydrocarbon reserves; however, determining pore system parameters in such rocks as tight gas sandstones (TGS) and seal rocks (SR) remains challenging because of the extreme variability in depositional environments resulting in complex pore structures comprised by clays and length scales from sub-microns to Angstroms. In this work we applied a set of techniques to characterize submicron-pore structures in TGS and SR. Therefore it was divided into two main topics of interest: (i) Characterization of petrophysical properties and pore systems in very low permeability TGS using Pulse-Decay Permeability (PDP), Low Field Nuclear Magnetic Resonance (LFNMR), Nitrogen Gas Adsorption (N_2GA), Mercury Intrusion Capillary Pressure (MICP) and Multi-scale 3D X-ray Nano- and MicroCT (down to 0.7 μm resolution) techniques; (ii) Study of Photoacoustic Spectrometry (PAS) for determining thermal diffusivity (TD) and porosity in three seal rocks originating from dissimilar fields as a key issue for safe exploration, storage purposes (CO_2 sequestration) and developments in shale characterization. The values obtained for TD were between 0.01667 and 0.09298 (cm^2/s) while porosity ranged from 1.42 to 9%. For the analyzed TGS the 3D pore-structure characterization lead to pore tortuosity and shape factors ranges of 2.19-5.47 and 3.2-8.5, respectively, and pore size distributions tended to be bimodal for MICP, trimodal for 3D multi-scale and tetramodal for LFNMR measurements. The porosity values ranged from 1.94 to 11.96% obtained by the combination of N_2GA and MICP techniques and permeability from 0.036 to 0.00066 mD by PDP technique. The measured pore-structure parameters were also used to predict empirical permeability in TGS (using e.g. Carman-Kozeny (Dullien, 1992) and Coates (1999) models). The set of applied methods has shown to be a useful tool for the unconventional reservoir characterization since it allows obtaining pore morphological and quantitative parameters which account for the permeability values.

Key-words: Tight gas sandstones, Seal rocks, rocks characterization

RESUMO

Hoje as pesquisas em rochas de baixa permeabilidade (grande tendência no mundo e em breve na indústria petrolífera brasileira) se voltam à escala de poros seja para investigação petrofísica, morfológica, de distribuição de tamanhos de grãos ou poros ou escoamento de fluidos, prática descrita pelos valores de permeabilidade. A avaliação destas propriedades por sua vez, é essencial ao desenvolvimento e exploração de reservas de hidrocarbonetos. No entanto, a determinação de parâmetros do sistema poroso nessas rochas, arenitos de baixa permeabilidade (TGS) e rochas selantes (SR), continua a ser um grande desafio devido à extrema variabilidade de ambientes deposicionais e complexa microestrutura composta por argilas e tamanhos de poros de submícrons a ângströms. Nesta tese empregou-se um conjunto de técnicas experimentais para a caracterização da estrutura porosa de TGS e SR. De tal modo, o trabalho foi dividido em dois tópicos principais: (i) Caracterização do sistema poroso e propriedades petrofísicas em TGS utilizando-se as técnicas de permeabilidade por decaimento de pulso (PDP), NMR de baixo campo, adsorção gasosa N_2 (N_2GA), porosimetria por intrusão Hg (MICP), nano- e microtomografia de raios X (res. $<0,7$ µm); (ii) Estudo por espectrometria fotoacústica (PAS) em SR de distintos campos geológicos para a determinação de porosidade e difusividade térmica (TD), de forma a estimular a exploração segura de gás e óleo, o armazenamento de CO_2, bem como a caracterização de folhelhos. Para SR os valores de TD variaram entre 0,0167 e 0,0930 (cm^2/s) e a porosidade entre 1,42 e 9%; para TGS a caracterização 3D da estrutura porosa forneceu valores de tortuosidade e fator de forma entre 2,19-5,47 e 3,2-8,5. As distribuições de tamanho de poros mostraram-se bimodais nos ensaios MICP, trimodais na multiescala 3D e tetramodais na NMR, enquanto a porosidade pela combinação N_2GA e MICP variou entre 1,94 e 11,96% e a permeabilidade PDP de 0,036 a 0,00066 mD. Alguns dos parâmetros microestruturais obtidos em TGS foram correlacionados na estimativa de permeabilidade utilizando-se modelos como Carman-Kozeny (Dullien, 1992) e Coates (1999). O conjunto de técnicas e metodologias aplicado nesta tese mostrou ser ferramenta imprescindível na caracterização de rochas de baixa permeabilidade, uma vez que permitem integrar atributos da rede de poros que influenciam nas macro-propriedades das rochas analisadas.

Palavras-chave: Arenitos de baixa permeabilidade, rochas selantes, caracterização de rochas.

LIST OF FIGURES

LIST OF TABLES

LIST OF ACRONYMS AND ABBREVIATIONS

ARRC –	Australian Resources Research Centre
BET –	Analysis BET (Brunauer, Emmett and Teller) for the specific surface area calculation
BJH –	Model after Barret, Joyner and Halenda for the calculations of pore size distribution
CSIRO –	Commonwealth Scientific and Industrial Research Org.
CENPES –	Leopoldo Américo Miguez de Mello Research Centre
CPMG –	Carr, Purcell, Meiboom, and Gill, sequence from NMR
ER –	Equivalent resistor pore network
IUPAC –	International Union of Pure and Applied Chemistry
K-C –	Kozeny-Carman model
L-B –	Lattice-Boltzmann model
LMPT –	Laboratório de Meios Porosos e Propriedades Termofísicas, Departamento de Eng. Mecânica/UFSC
LSCM –	Laboratório de Síntese e Caracterização de Materiais, Departamento de Física/UFSC
MICP –	Mercury Intrusion Capillary Pressure
MicroCT –	X-ray Micro Computed Tomography
N_2GA –	Nitrogen Gas Adsorption
NanoCT –	X-ray Nano Computed Tomography
NMR –	Nuclear Magnetic Resonance
PAS –	Photoacoustic spectroscopy
PDP –	Pulse-Decay Permeability (PDP) techniques
PSD –	Pore size distribution
Res1 –	Resolution 1 (~ 0.7 µm)
Res2 –	Resolution 2 (~ 0.3 µm)
Res3 –	Resolution 3 (0.064 µm)
ROI –	Selected region of interest of a 3D image
SE/BSE –	Secondary electrons/backscattered electrons
SEM/FESEM –	Scanning Electron Microscopy/ Field Emission SEM
S-P –	Series-Parallel model
SR/TGS –	Seal rocks/Tight gas sandstones
XRD –	X-ray Diffraction

TABLE OF CONTENTS

1. INTRODUCTION

1.1. Materials characterization

In material science and engineering, characterization refers to the application of external techniques (experimental analyses) to probe into the internal structure and properties of a material (WIKIPEDIA). Fundamentally, material science is the investigation of the relationship among processing, structure, properties, and performance of materials – which comprises a systematic characterization (CALLISTER, 2002). In Figure 1.1 this relationship is summarized considering that in the characterization of natural materials such as reservoir rocks from the petroleum industry, the processing can be simply replaced by extraction process, once that the analyzed material (natural rock) had been already processed for ages.

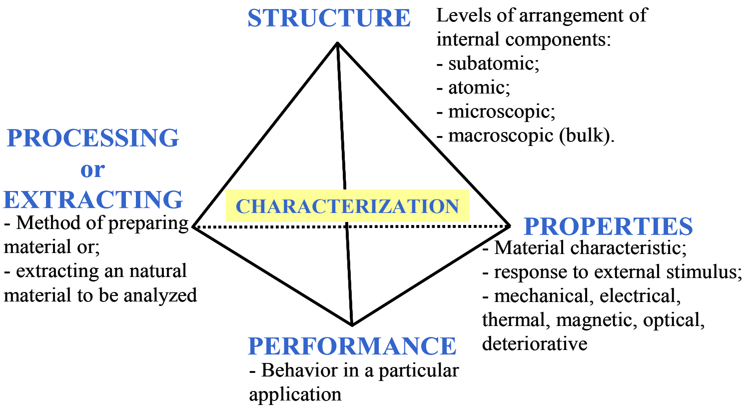

Figure 1.1: Scope of material science and engineering including the process of extraction for the case of rock's analysis (modified from NATIONAL RESEARCH COUNCIL, 1989).

Understanding the relationship among structure, properties, processing/origin, and performance of materials is fundamental for any technological development and benefit to the society. In the beginning of the material science, humans began to make tools from stone; started to hammer or cast bronze in a variety of shapes; use iron and steel as stronger and cheaper material changing drastically daily life of a common person; and finally many new types of materials have been introduced, such as ceramic, semiconductors, polymers, composites, etc. All these events are historically associated to Ages to be known as *Stone*

→ *Bronze* → *Iron* Age*;* and why not add the *Advanced Materials* Age. Material engineers and scientists are at the head of new technologies, process fabrication and characterization. Theu push forward the boundaries of science and engineering interacting with researchers and professionals of every discipline, including the petroleum engineering. Research and development on petroleum engineering areas can assure a safe and optimized hydrocarbon extraction leading to the increase and autonomy of the energy in all sectors of societies worldwide.

1.2. Motivation and context

1.2.1. World primary energy demand and hydrocarbons role

According to YUSGIANTORO (2004):

> "There is a sheer importance of energy for the evolution of mankind. Petroleum has long been the main source in the world energy and is expected to remain into the 21st century. However, there are challenges in the years ahead in an industry which is highly competitive and operates at the sharp end of technology. E.g., producers must meet the estimate rising oil and gas demand in a manner which is both timely and compatible with such objectives as sustainable development and social, economic and environmental harmony."

Additionally new energy resources must be developed to assure the development of societies. Figure 1.2 shows the world primary energy demand (in million tons of oil equivalents) by sector and type for 2008 and the perspective for 2035 (WEO-2011).

In Figure 1.2 it is possible to see that (referring to the sum of these resources) even for the years ahead, all the economy sectors will stay reliant on the gas, oil and coal natural resources. Facing the needs of the global energy scenario, the search for hydrocarbon resources is intensified pressuring to enhance the recovery in conventional reservoirs, and even further: to the exploration and development of resources once considered impracticable - the unconventional reservoirs. In this context and in view of the growing production from rocks with small pore sizes, closely analyzing the properties of rocks of unconventional reservoirs becomes increasingly important for geologists and petrophysicists, as recovery of gas and oil from fine-grained sandstones, siltstones, and shale blurs the distinction between reservoir and seal (NELSON, 2009).

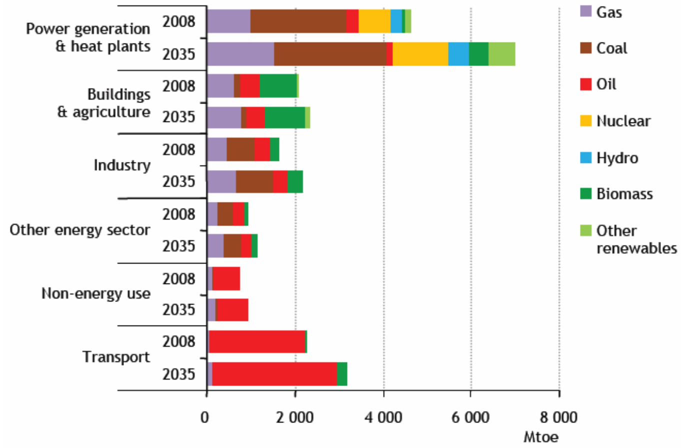

Figure 1.2: World primary energy demand by sector and type in the WEO[1] 2011 New Policies Scenario.

1.2.2. Insights about the petroleum system

The petroleum system is a unifying concept that encompasses all of the disparate elements and processes of petroleum geology. Practical application of petroleum systems can be used in exploration, resource evaluation, and research. The essential elements of a petroleum system include (MAGOON and BEAUMONT, 1999; HAO *et al.,* 2000):

- Source rock;
- Reservoir rock;
- Seal rock;
- Overburden rock.

Linking these elements to the processes of petroleum geology (trap formation and hydrocarbon generation–migration–accumulation) is an effective exploration approach. Mapping and studying a petroleum system helps explorationists predict which traps will contain petroleum and which will not. It also helps them focus on that part of a region that will most likely contain accumulations (MAGOON and BEAUMONT, 1999). Figure 1.3(a) exemplifies a cross section showing a structural anticline trap where the oil and gas accumulation is performed by the seal (cap) rock capacity. One can also see the primary and secondary

---

[1] WEO – World Energy Outlook.

migration processes. Primary migration is the process by which hydrocarbons are expelled from the source rock into an adjacent permeable carrier bed (reservoir rock). Secondary migration is the movement of hydrocarbons along the reservoir rock from the source area to the trap. Migration mostly takes place as one or more separate hydrocarbons phases (gas or liquid depending on pressure and temperature conditions). The ideal situation for the petroleum industry recovery would be to have reservoir rocks comprised by enough amount of connected pores (effective porosity) attributing considerable values of permeability to the explored oil/gas field.

1.2.3. From conventional to unconventional reservoirs

For more than 100 years conventional resources have been the focus of the oil and gas industry. Although conventional and unconventional oil and gas come from the same original geologic formations (sediments accumulated in multiple layers in sediment basins all over the world) they have distinct characteristics. Conventional reservoirs are resources from which no special exploration process needs to be applied in the recovery since rock and fluid characteristics typically permit oil or natural gas to flow readily into wellbores. Usually they show high to medium permeability values (> 0.6 mD) and are drilled vertically just by the natural pressure of the wells and pumping or compression operations. On the other hand, unconventional reservoirs require special recovery operations in order to make it monetarily viable; they do not produce economic volumes of oil and gas without assistance from massive stimulation treatments or special processes and technologies, such as hydraulic fracturing or steam injection (NAIK, 2004). Unconventional reservoirs have low permeability (<0.1 mD going even to the nD order) and are usually drilled horizontally or by multistage hydraulic fracturing (NAIK, 2004; PERRY and LEE, 2007). The optimum drilling, completion and stimulation methods for each well are a function of the reservoir characteristics and the economic situation. Like conventional hydrocarbon systems, unconventional gas reservoirs are characterized by complex geological and petrophysical systems as well as heterogeneities — at all scales (RUSHING *et al.*, 2008).

The unconventional gas resources (tight gas, coalbed methane, and shale) will play a significant role in world energy supply because of their potential to offset declines in conventional oil and gas production (DARABI *et al.*, 2012; PHILIPPE & PARTNES, 2011). In conventional reservoirs hydrocarbons are stored in the interconnected pore spaces of sands and carbonates and often sourced from proximal organic-rich shales; in shale gas or tight gas reservoirs, they are stored in interconnected pore space (mineral matrix) or adsorbed onto organic matter (kerogen or bitumen) and often sourced from the same reservoir rock. Figure 1.3(b) depicts, e.g., a schematic geology of natural gas from where one can see the main differences within reservoir characteristics and recovery processes; Figure 1.4 illustrates the principle of the natural resource triangle available in the world and studied by different authors.

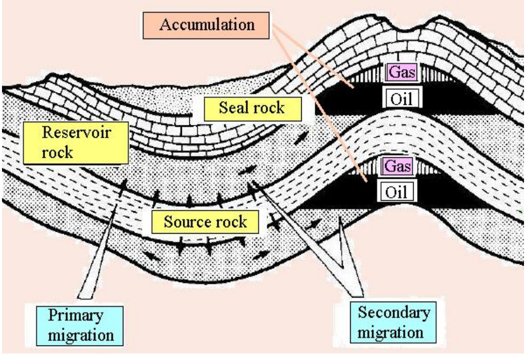

(a)

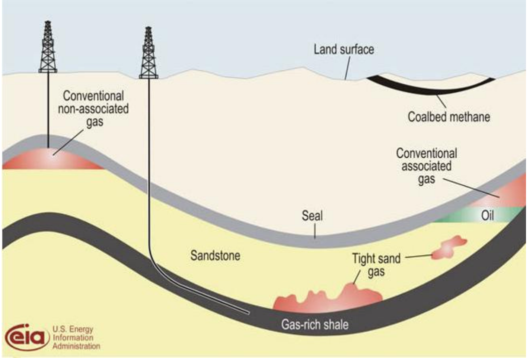

(b)

Figure 1.3: (a) Definitions of primary and secondary migration (TISSOT and WELTE, 1984); (b) Schematic geology of natural gas resources, EIA[2].

The concept of the resource triangle to find a large gas field was for the first time used by Masters in 1979 were all natural resources are

---

[2] EIA – US Energy Information Administration.

distributed log-normally in nature (MASTERS, 1979). As it can be seen in the scale on the right side of Figure 1.4 the hard part is finding high permeability gas and oil fields. Once you find a high-grade deposit, recovery producing in the resource is rather easy and straightforward. The common theme is that low quality deposits of gas/oil require improved technology and adequate gas prices before they can be developed and produced economically; however, in deposit volumes they are much larger if compared to high quality ones (WIKIPETRO – Tight Gas Reservoirs).

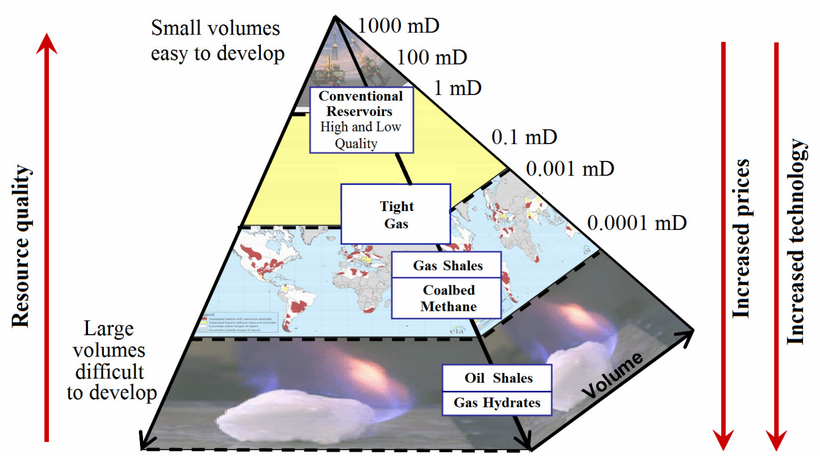

Figure 1.4: Gas/oil resource triangle (modified from NAIK, 2004; CAPP).

Since the 1950s, the oil and gas industry has been completing and fracture treating low permeability wells in the United States. Nowadays the unprecedented interest worldwide, the high resource volume, long-term potential and attractive prices bring the unconventional gas and oil reserves into the forefront of our energy future. Figure 1.5 shows the United States conventional and unconventional gas/oil reserves transformation from 1980 to 2035 (a) according to WEO-2012 data; and (b) illustrated the gas evolution for China, Canada and US in 2008 and 2035 (source: EIA). As one can see for US in 2008, more than half of gas production was already ensued from unconventional fields. Also for Canada and China in 2035 the prevision reaches 50 and 70%, respectively. In this context it is significant that Brazil advances developments and studies in unconventional resources to assure the prospects of the Brazilian energy matrix.

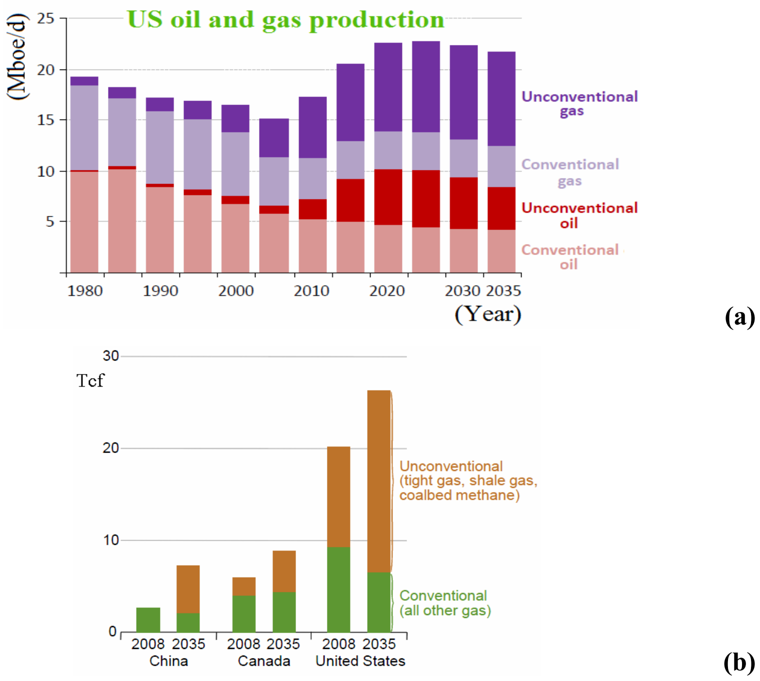

Figure 1.5: (a) The surge in unconventional oil and gas production has implications well beyond United States, WEO-2012. (b) Natural gas production in China, Canada and US (2008 and 2035), IEO-2011, EIA.

The awareness into the characteristics of pore-structure continuum provides a useful insight for considering the emplacement and exploration of petroleum in consolidated siliciclastics and fluid flow through fine-grained source rocks now being exploited as reservoirs (NELSON, 2009). For example, if we consider the size order of hydrocarbon molecules (ranging from 0.01 µm for asphaltenes to 0.00038 µm for methane) and compare it to the pore-throat sizes found in different reservoir rocks:

- conventional reservoir rocks: generally greater than 2 µm;
- tight gas sandstones: from about 2 to 0.03 µm;
- shale: from 0.1 to 0.005 µm (NELSON, 2009);
- seal (cap) rocks: from 0.1 to 0.002 µm (SCHMITT *et al.*, 2013).

One can see that even being comprised of a fine-grained pore-structure, both tight gas sandstones (TGS) and shale might have stored considerably amount of hydrocarbon (mainly gases) in their structure; the recovery process, though, particularly for shale needs to be stimulated by the usage of specific methods such as hydraulic fracturing. On the other hand in seal rocks the pore geometries and sizes need to be formerly settled to impede the escape of hydrocarbons from the reservoir rock, assuring a successful recovery in conventional reservoirs. Only by understanding the structure of pore networks can engineers and geologists make more accurate predictions of producible gas/oil and optimize its extraction (BUTCHER and LEMMENS, 2011).

Currently, significant research effort in oil and gas field reservoirs are focused on pore-scale petrophysics, grain distribution, pore geometry and distribution besides the fluid flow circulation. Textural and structural facies analysis also provided an important potential database for the assessment of parameters controlling the reservoir quality (BENZAGOUTA, 2012). In the present work a textural and morphological pore structure evaluation is done for the low permeability reservoir rocks: tight gas sandstones and seal rocks.

The seal rocks' investigation will help in judging the sealing efficiency of these rocks once that for the conventional reservoirs exploration higher pressures have been applied every day. Additionally it will give incites to the shale rocks characterization considering the similarity between the microstructure of both rocks. Therefore three seal rocks originated from distinct geological oil/gas fields were investigated by Photoacoustic Spectroscopy (PAS) procedure to determine the thermal diffusivity and porosity. The results were compared with textural and mineralogical information obtained by Field Emission Scanning Electron Microscopy (FESEM) and X-Ray Diffraction (XRD) techniques. Tight gas sandstones from dissimilar gas fields had petrophysical properties and pore structure parameters characterized by usage of Nitrogen Gas Adsorption (N_2GA), Mercury Intrusion Capillary Pressure (MICP), Low Field Nuclear Magnetic Resonance (LFNMR), X-ray Nano and Micro Computed Tomography (NanoCT and MicroCT), Pulse-Decay Permeability (PDP), FESEM and XRD techniques. After performing and optimizing a single-phase gas flow permeability characterization using the pulse-decay permeability (based in the transient method), we could compare the predicted permeability values to the obtained PDP experimental data. For the prediction of permeability distinct models were applied having as input data the pore structure parameters measured in this work by the set of techniques.

1.3. Objectives

The main objective is to develop and apply a compendium[3] of techniques for the pore structure characterization in low permeability reservoir rocks since the desire to acquire understanding of these rocks has become a wide tendency in the petroleum industry in Brazil and elsewhere. Thereby we divided this thesis in two main topics of interested to accurately evaluate the analyzed rocks:

- Characterization of petrophysical properties and pore structure morphology on very low permeability tight gas sandstones using distinct methodologies and techniques;
- Usage of the Photoacoustic Spectroscopy technique to determine the thermal diffusivity and porosity in seal rocks (overlaying conventional reservoirs) as a key issue for safe exploration, storage purposes (CO_2 sequestration) and developments in shale characterization (also a very fine layered porous media and comprised by distinct clays).

1.3.1. Specific objectives

TGS and seal rocks originated from distinct depths and oil/gas fields were provided by CENPES/Petrobras and were available for the study. As the location of sample is confidential, letters from A to G were attributed to the analyzed fields (see Table 4.1). Following the specific objectives are described.

Petrophysical and pore structure characterization of tight gas sandstones from distinct fields:

(i) Applying low permeability PDP technique to:

- Study the influence of effective pore pressure (net stress) in the permeability of analyzed TGS/
- Obtain the Klinkenberg permeability and equation correction;
- Compare and evaluate the accuracy of pulse-decay method using steady-state measurements considering all mistakes associated to this last one;
- Measure PDP permeability on TGS to evaluate their efficiency as reservoir and validate the obtained results to the

---

[3] The word compendium was also used by CRISP *et al.* (1987) when reporting and studying geological and chemical data of Australian oil shale.

predicted permeabilities using various microstructural parameters obtained for TGS in this work.

(ii) From the N_2GA and MICP experiments:

- Evaluate the pore geometry by comparing the obtained shape of the N_2GA isotherms;
- Measure and compare pore size distributions (PSDs) in the micro- and mesopore ranges obtained by BJH, Dollimore-Heal and DFT models from the adsorption data;
- Combine MICP and N_2GA techniques to obtain total porosity and PSD of TGS;
- Measure and compare specific surface area from the N_2GA experiment calculated by BET and Langmuir theories.

Petrophysical and pore structure characterization only for tight gas sandstones of field A:

(iii) Applying Low-Field NMR technique by usage of a 23 MHz spectrometer having very low encoding/decoding intervals to:

- Investigate the contribution of very small pore classes present in the analyzed rocks, by collecting the transverse relaxation T_2 distributions measured using CPMG (Carr, Purcell, Meiboom, and Gill) sequences;
- Identify from the locations signal contribution, the amount of porosity and specific pore types present in analyzed rocks;
- Measure the volumes of pore sizes as Irreductible Bulk Volume (BVI) and Free Fluid Index (FFI), important parameters used to predict permeability from the NMR data;
- Compare the obtained PSD curves and total porosity with results of N_2GA + MICP combination.

(iv) Using output 3D image analysis acquired in distinct resolutions by X-ray Nano- and Microtomography to:

- Evaluate microstructure changes (in multi-scale) for two distinct regions of field A;
- Evaluate the filtering effect on pore segmentation for acquired TGS' images;
- Extract pore network using mathematical morphology, equivalent resistor (skeleton) and whateshed segmentation;
- Calculate the correlation of measured and quantified 3D sub-volumes to evaluate how representative they are;

- Obtain 3D multi-scale pore size distributions using a combination of pore size frequencies in distinct resolutions, and using (for both mathematical morphology and equivalent resistor methods) the “Multiscale Model” (MANTOVANI, 2013) validated for carbonates rocks;
- Calculate for the distinct resolutions pore geometry properties such as: connectivity, shape and tortuosity factors, specific surface area, aspect ratio and preferential orientation.

(v) Predicting intrinsic permeability for TGS:

- Use distinct models proposed in the literature and correlate the pore structure parameters measured by the compendium of techniques described above;
- Compare and validate the obtained results using Klinkenberg permeability measured by PDP technique.

(vi) Investigation of textural and structural composition in TGS of field A (as well as in analyzed seal rocks) using: XRD, SEM and FESEM techniques.

Photoacoustic spectroscopy study on seal rocks originated from distinct fields on powder compressed and as collected clean samples to:

(vii) Characterize thermal diffusivity from the observed PAS mechanisms found in the three seal rocks analyzed;

(viii) Propose an empirical relation between samples of seal rock taken in the vertical direction of field bedding and powder compressed samples to estimate porosity values.

2. LITERATURE REVIEW

2.1. Hydrocarbon generation and migration

Hydrocarbon generation is the natural result of the maturation of buried organic matter. This organic matter (organic carbon) very often consists of microalgae and microorganisms which are deposited in aquatic environments, especially on the sea bed. Lagoons and restricted seas are favorable for high preservation of organic matter. During deposition and at the onset of burial of these sediments, most of the materials are dissolved, particularly by oxidation. The remaining part contains kerogen which, due to the gradual burial of the sediments causing high compression and a sharp rise in temperatures (for very long time intervals), is transformed into hydrocarbons by thermal cracking (COSSÉ, 1993).

Kerogen consists of very large molecules and is a kind of polymer. When it has been exposed to sufficient time and temperature these large molecules will crack into smaller molecules, mostly petroleum. When the temperature is about 100◦C a long period of geological time is required. In rapidly subsiding basins the exposure time is shorter and oil generation may only start at about 140–150◦C (BJØRLYKKE, 2010). Usually around 120–150^{o}C, the oil is cracked yielding first wet and then dry gas (TISSOT and WELTE, 1984; BJØRLYKKE, 2010). The “oil window” lies between two temperatures levels. It usually corresponds to burial depths among 1 and 3.5 km. The depth (temperature) range where oil is generated is called the “oil window”. At higher temperatures oil will be altered into gas by cracking (BJØRLYKKE, 2010). The general scheme of evolution of the organic fraction and the hydrocarbons produced is depicted in Figure 2.1 (TISSOT and WELTE, 1984) where it is possible to see that organic matter undergoes changes in composition with increasing burial depth and temperature. The three steps in the transformation of organic matter to hydrocarbons are termed diagenesis, catagenesis, and metagenesis. Petroleum hydrocarbons exist as gaseous, liquid, and solid phases, depending on temperature, pressure, burial time, and composition of the system.

Petroleum migrates from low permeability source rocks into high permeability reservoir rocks from which the petroleum can be produced. The main driving force for petroleum migration is buoyancy because it is less dense than water. The forces acting against migration are the capillary forces and the resistance to flow though rocks with low permeabilities. It is necessary to assume that oil is mostly transported as a separate phase. In order to pass through the narrow passage between pores (pore throat), the oil droplets must overcome the capillary forces. When the pores are sufficiently small in a fine-grained sediment, these forces will act as a barrier to further migration of oil. The small gas molecules, however, can diffuse through extremely small pores and thus escape from shales which form tight seals for oil (BJØRLYKKE, 2010)

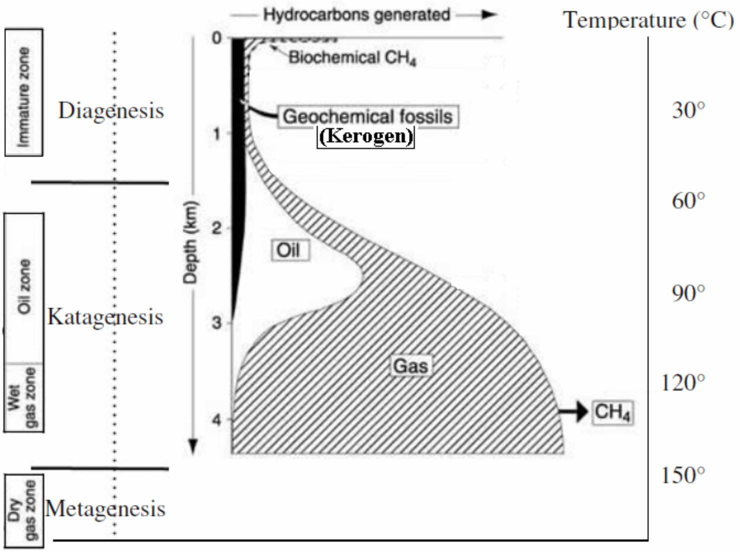

Figure 2.1: Scheme of the evolution of the organic fraction and the hydrocarbon produced (maturation of organic matter and generation of oil and gas) as a function of temperature and depth (TISSOT and WELTE, 1984; BJØRLYKKE, 2010).

2.2. Related studies and characteristics of analyzed rocks

2.2.1. Tight gas sandstones

A tight gas sandstone (TGS) reservoir is generally characterized as a formation with effective permeability less than 0.1 mD (LAW and CURTIS, 2002). Unique characteristics make this reservoir poor conductor of fluids (BLASINGAME, 2008):

- Low permeability – which yields poor utilization of reservoir pressure, caused in part by depositional (very small grains, mixed with detrital clays) and diagenetic (clay precipitation, massive cementation, pressure compaction, etc) issues.

- Reservoir heterogeneity – which is dictated by deposition and post-deposition (diagenetic) events including vertical heterogeneity (layering, laminate, etc), lateral heterogeneity (medium to large scale geologic features, e.g., turbidite deposition, faults, etc) and differential diagenesis (hydrocarbon generation and migration).

As a result of storage and flow characteristics that are intimately tied to depositional and diagenetic processes in TGS, exploitation of this resource requires a comprehensive reservoir description and characterization program to identify properties which control production. In particular, TGS reservoirs have significant primary and secondary porosity[4] and pore connectivities dominated by clays and slot-like pores. This makes these reservoirs particularly susceptible to the effects of overburden stress and variable water saturation (GOLAB *et al.*, 2010). Figure 2.2 illustrates the main differences in conventional sandstone, near tight and tight gas sandstone reservoirs, according to Rezaee *et al.* (2012). As one can see important morphological and textural attributes in the reservoirs (grain size, sorting, packing, shape, pore heterogeneities and connected pore orientation) are distinguished. For TGS reservoir the grains in the matrix are much more compacted and also relative high amount of clay is found in the pore walls.

Since the 1970´s when tight gas sandstones reservoirs were defined as being the one in which the expected value of permeability to gas flow would be less than 0.1 mD, various studies have being focus in the optimization of developments in these resources (HOLDITH, 2006; NELSON, 2009). Rushing *et al.* (2008) presented a work-flow to describe and characterize tight gas sands making reference to distinct methods applied in works at the literature. Clarkson *et al.* (2011) measured small-angle and ultra-small-angle neutron scattering (SANS

---

[4] Primary porosity is the porosity preserved from deposition through lithification; secondary porosity is the porosity created through alteration of rock, commonly by processes such as dolomitization, dissolution and fracturing. This type of reservoirs are also called dual-porosity reservoir, a rock characterized in which all flow to the well effectively occurs in one porosity system, and most of the fluid is stored in the other. These reservoirs are layered with extreme contrasts between high-permeability and low-permeability layers (OILFIELD GLOSSARY).

and USANS) on tight gas reservoir samples from Western Canada in order to determine the applicability of these techniques for characterizing the full pore size spectrum and to gain insight into the nature of the pore structure and its control on permeability. They used N_2 and CO_2 adsorption to interpret the total porosity distribution obtained. Desbois *et al.* (2011) shown in that the imaging of pore space at scales below 1 μm in tight gas sands remains difficult due to limits in resolution and sample preparation, so they explored the use of high resolution SEM in combination with argon ion beam cross sectioning (BIB, Broad Ion Beam) to prepare smooth, and damage-free, true-2D surfaces of TGS, to image porosity down to 10 nm. They evaluated textures and porosity though no other properties quantifications were performed.

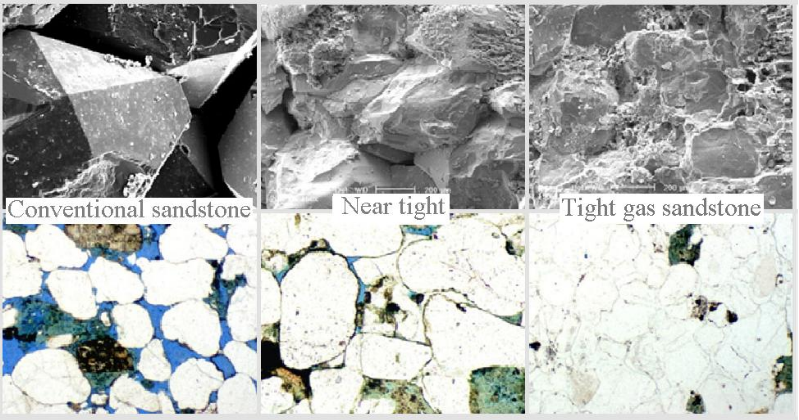

Figure 2.2: Conventional, near tight and tight gas sandstone micrographs showing the differences between pore connection (REZAEE *et al.*, 2012).Images on fractured (above) and polished (below) samples acquired respectively by SEM and Optical Microscopy.

However, using distinct methods and techniques to obtain and compare pore structure parameters in tight gas sandstones is kind new proceeding. Also the obtained parameters were used in empirical permeability models and compared with experimental pulse-decay measurements. The low-permeabilities (and porosities) associated with tight gas sands can be attributed directly to a large distribution of small to very small pores and/or a very tortuous system of pore throats connecting those pores (RUSHING *et al.*, 2008). These are some of the pore system parameters that can be used to predict empirical permeability. An understanding of the rock’s pore structure, mineralogical composition and petrophysical properties using a compendium of techniques will help to judge the exploration potential as hydrocarbons reservoirs in the analyzed TGS and also permit the estimation of permeability values using distinct methods.

2.2.2. Seal rocks

Seal rocks are geological formations with extremely low porosity and permeability overlying oil or gas reservoirs, which constitute a barrier against the volumetric flow of hydrocarbons into the upper layers. Although a seal rock can be considered as a seal to hydrocarbons, it is erroneous to regard it as a completely impermeable layer (LI *et al.*, 2005). Seal rock, also called cap rock, is a crucial and sometimes overlooked factor in the evaluation of a potential hydrocarbon accumulation. Together with source rocks, reservoir rocks and overburden rocks, they represent one of the four essential elements of petroleum systems (HAO *et al.*, 2000).

The retention of hydrocarbons by overlying seals is controlled by the capillary entry pressure, the permeability and the extent of diffusive losses (molecular transport) through the fluid-saturated pore space (SCHLÖMER and KROOSS, 1997). Today, data on the porosity and thermal diffusion of seal rock can find wide usage in the context of petroleum and gas exploration and also in the storage of anthropogenic CO_2 in the subsurface region, e.g. saline aquifers or exploited gas reservoirs, e.g. cap rocks are formed in the process of sedimentary rock accumulation and so the physical and chemical parameters of these rocks change under the influence of lithogenic processes. In general, the microstructure of cap rocks is highly complex and anisotropic and contains very small-diameter pores (in the order of Angstroms) and considerable presence of clays. Therefore, similarly to the microstructure of shale from the unconventional reservoirs, seal rock morphology is difficult to characterize, making it necessary to use and development of distinct methods. Figure 2.3 compares the microstructure of a seal rock (a) and a shale (b), where one can observe its complexity and presence of small pore sizes for both rocks.

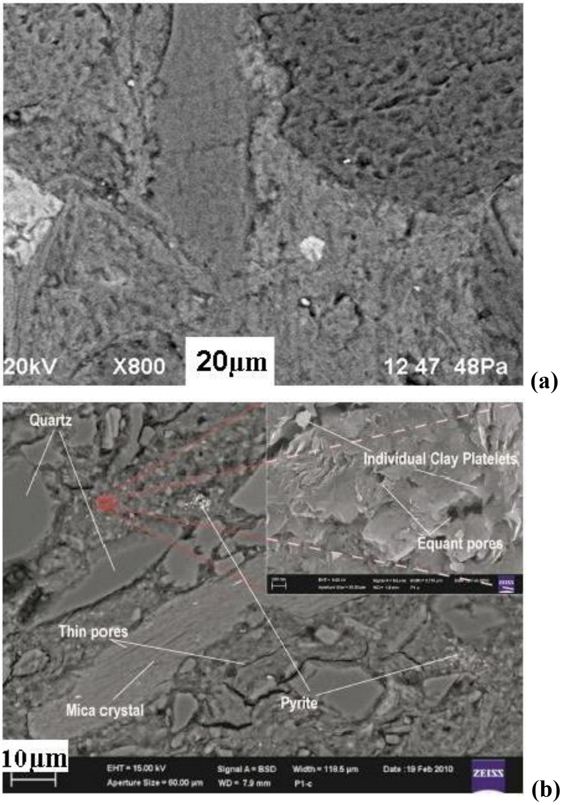

Figure 2.3: (a) Seal rock originating from a Brazilian field (SCHMITT *et al.*, 2013); (b) Shale showed in (CSIRO) with a complex microstructure.

The precise and accurate knowledge of transport properties of rocks and soils are extremely important for investigating the heat flow processes in geothermal phenomena and for petrophysical studies of geological materials. The determination of such properties has become important with the widespread interest in the formation and evolution of hydrocarbon resources, with the subsequent extraction of oil and gas. The thermal diffusivity and thermal conductivity depend upon many factors such as the thermal parameters of constituent phases, their corresponding volume fraction, the contact areas, the shape of particles and the type of packing. The porosity of the materials plays also an important role among the many factors that influence thermal parameters (GUIMARÁES *et al*, 2013). The most relevant thermal parameters of rocks are thermal conductivity, specific heat and thermal diffusivity (FENG *et al.*, 2013; RUBIO, 2013), and these parameters are related to the pore structure. The evaluation of seal rocks using the open photoacoustic cell (OPC) technique is an accurate and reliable method to investigate the thermal diffusivity and in our knowledge not yet done in the literature for these rocks, especially when it goes into the topic of correlating obtained values of thermal diffusivity to predict porosity. It requires a simple experimental setup, few analytical equations to be adjusted to the results besides very small quantities of the material to be analyzed. Herein we show to be possible from a same experiment to obtain the thermal diffusivity and calculate the porosity in very low-permeability rocks such as seal rocks from conventional reservoir.

2.3. Insights about reservoir rocks characterization

Two basic sources of data for reservoir characterization are from specific reservoir data and information from analogous reservoirs (JACKSON *et al.*, 1993). Reservoir data (on a range of scales from basin to field-scale information, km, to pore size information, Angstrons) can be broadly divided into three categories: (i) rock properties (the container), (ii) fluid properties (the contents), and (iii) rock/fluid interactions. Imbibition is fundamental to oil and gas recovery from reservoirs under most secondary and improved recovery processes of practical interest. It is also dependent of porous medium wettability. The rate and the extent of imbibition depend critically on the viscosity of the wetting and nonwetting phases (KOVSCEK *et al.*, 2001).

Microscopic (pore-scale) information that affects fluid flow in reservoir rocks includes mainly the surface roughness, grain size, sorting mineralogy, clay content, pore and throat dimensions, geometry, size, distribution and connectivity. The major controls on these features are the sediment source (provenance) and the subsequent diagenetic processes of compaction, cementation, and dissolution (JACKSON *et al.*, 1993). An attempt to correlate pore structure information to petrophysical rock properties such as effective porosity and absolute permeability is desired in the reservoir characterization. Petrophysics is the study of the physical properties of rocks. For a rock to form a reservoir (COSSÉ, 1993):

(a) It must have a certain storage capacity: this property is characterized by the porosity;

(b) The fluids must be able to flow in the rock: this property is characterized by the permeability;

(c) It must contain a sufficient quantity and concentration of hydrocarbons: the impregnated volume and saturations are factors here.

Measurements of petrophysical properties in core samples can be obtained by various techniques such as injection/extraction flow fluids or image analysis. In this sub-chapter we describe briefly notions about porous media properties and fluid behaviors used in the thesis.

2.3.1. Porosity and pore size distribution

Porosity, which is a measure of the rock's storage capacity, is affected not only by the primary depositional processes but also by all subsequent diagenetic processes (RUSHING *et al.*, 2008). In a rock sample its apparent volume, or total volume *(V_T)*, consists of a solid volume V_S and a pore volume V_P, where the porosity (in %) is defined (COSSÉ, 1993):

$$\phi = \frac{V_P}{V_T} = \frac{V_P}{(V_S + V_P)} = \frac{(V_T - V_S)}{V_T}. \tag{2.1}$$

The porosity of interest to the petroleum engineering, that which allows the fluids in the pores to circulate, is the effective porosity ϕ_E, which corresponds to the pores connected to each other and to other formations (COSSÉ, 1993). Therefore the total porosity ϕ_T, corresponding to all the pores in an analyzed sample, is defined, whether interconnected or not:

$$\phi_T = \phi_E + \phi_R, \tag{2.2}$$

where ϕ_R is the residual porosity which only takes account of isolated pores. Effective porosity is often slightly less than total porosity. However, effective porosity in tight gas sandstones is typically much lower than the total porosity because of diagenesis. The type and magnitude of diagenesis governs the connectivity of the primary porosity. Unlike conventional sandstone reservoirs that are characterized mostly by a primary intergranular porous system, TGS may exhibit several other types of porosity - including both primary and secondary inter-granular porosity, detrital matrix porosity, micro-porosity, and grain fracture porosity (RUSHING *et al.,* 2008).

The effective porosity of rocks varies between less than 1% and over 40%. It is often stated that the porosity is (COSSÉ, 1993):

- Low if $\phi < 5\%$;

- Mediocre if 5 < ϕ < 10%;
- Average if 10% < ϕ < 20%;
- Good if 20% < ϕ < 30%;
- Excellent if ϕ > 30%.

2.3.1.1. Classification of microporosity

Distinct spectrums of pore size distributions (PSD) can be observed in the various reservoirs rocks. These spectrums of pore types also capture some important petrophysical properties of the pores, so in petroleum engineering a pore classification based on the PSD spectrum is useful, though varying definitions exist in the literature (CANTRELL and HAGERTY, 1999; HILDENBRAND *et al*., 2005). This is exacerbated by the fact that geologists, petrophysicists and engineers often have their own definitions. Furthermore, the precise definition often depends on the method of observation (BARNETT *et al.,* 2010). As presented by LOUCKS *et al.* (2012) in a study on pore types and networks applied to mudrocks (also fine-grained as TGS and seal rocks), the pore-size terminology of the International Union of Pure and Applied Chemistry (IUPAC) moreover defined by Rouquerol *et al.* (1994), might be more appropriate. In this terminology:

- micropores have widths less than 2 nm;
- mesopores have widths between 2 and 50 nm, and
- macropores have widths greater than 50 nm.

LOUCKS *et al*. (2012) considered that in this classification, nearly all mudrock pores would be grouped with larger pores in carbonates and sandstones as macropores (see Figure 2.4, B). Although the pore-size classification of ROUQUEROL *et al.* (1994) may be appropriate for chemical membranes, other controlled syntactic materials or even in seal rocks (SCHMITT *et al.*, 2013) it is insufficient for most of the reservoir systems comprised by a wide pore spectrum and main average pore sizes in the micrometer order. Another useful pore classification for carbonate rocks was proposed by CHOQUETTE and PRAY (1970), within which they provided size modifiers (LOUCKS *et al.*, 2012). They defined micropores as being less than 62.5 µm, mesopores as being between 62.5 µm and 4 mm, and megapores as being between 4 and 256 mm. These authors included no subdivisions of pores smaller than 62.5 µm, see “A” in Figure 2.4.

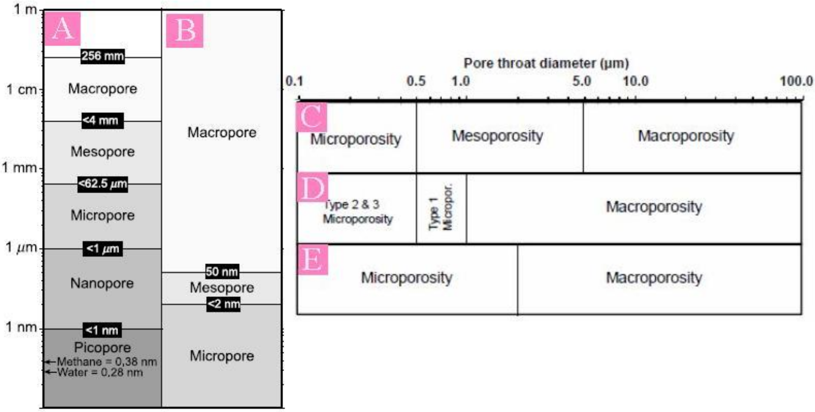

Figure 2.4: Pore sizes classification according distinct authors: (A) COQUETTE and PRAY (1970), (B) IUPAC, (C) AHR *et al.*, (2005), (D) CLERKE *et al.* (2008) and (E) published geological descriptions.

According to Barnett *et al.* (2010), see "C", "D" and "E" in Figure 2.4, distinct authors also have recently defined microposocity based on their method of observation. For example, AHR *et al.*, 2005 (C) defines micropores as those pores with pore throat diameters ≤ 0.5 µm and usually containing mostly irreducible water and little hydrocarbon; CLERKE *et al.* (D) propose an alternative scheme recognizing three types of microporosity based on pore throat size. This classification is useful recognizing that a spectrum of microporosity exists based on pore throat diameter from that which is effectively tight (Types II and III) to that which can store and flow hydrocarbons (type I); these three types are also in agreement with the SOEDER and CHOWDIAH (1990) classification for tight gas sandstones. Lastly, (E) is a proposed scheme based on published geological descriptions of microporosity (BARNETT *et al.*, 2010). In our work only when the nitrogen gas adsorption experiments were performed the IUPAC classification was assumed; for all other discussions we referred to microporosity as described in "D" Figure 2.4.

Understanding the abundance, distribution, and spatial interrelationships of each pore type is important because each type may contribute differently to permeability (LOUCKS *et al.*, 2012). To address the questions of pore size distribution in TGS we performed and compared distinct techniques and methodologies: N_2GA and MICP combination, Low Field NMR and Multi-scale 3D X-Ray Tomography.

The pore connectivity, tortuosity and shape factors (also important parameters in the permeability prediction), pore aspect ratio, pore preferential orientations were measured by usage of X-ray nano- and microCT techniques.

2.3.2. Specific surface area

Specific surface area is another significant petrophysical parameter for understanding the physics of rocks' porous media and for permeability prediction (HOSSAIN *et al.,* 2011). It is well known in the literature that the BET method allows the estimation of specific surface areas from nitrogen adsorption isotherms on the basis of the multilayer adsorption model. The surface area *(S)* of a solid material is the contribution of internal pore boundary area and external sample surface. When a material has considerable pore boundary (high porosity or for low porosity reservoir clay bearing the pore walls) the fraction of external surface area is irrelevant. Therefore, *S* is closely related to the size and volume of pores present in a material being larger as the pores get bigger in volume and smaller in size.

The specific surface area *(S_o)* of a material can be defined as the total pore surface area divided by the total volume of solid material *(V_S)* comprised in one analyzed sample (in m^{-1}) or, divided by the sample mass (in m^2/g), respectively:

$$S_o = \frac{S}{V_s}, \tag{2.3}$$

$$S_o = \frac{S}{w_S}. \tag{2.4}$$

Some rocks having extremely small pore sizes show high values of S_o. In shale gas systems (as well seal rocks), nanopores play an important role where for the same pore volume, the exposed surface area in nanopores is larger than in micropores. This is because surface area is proportional to 4/d, where d is the pore diameter (JAVADPOUR *et al.*, 2007).

In this context the S_o results of different methods reflect the different properties of pores at different scales. By using a high resolution BET (which will be explained later) or a highly smoothed surface derived from image analysis, from which usually a much smaller value of S_o is derived (HOSSAIN *et al.*, 2011) and the value is related to the used resolution, the values of S_o can varying in several orders of magnitude. In image analysis the most widely method used to calculate surface area from image analysis is to have an equivalent diameter (usually spherical or cylindrical) calculated from the 3D pixel volume objects (segmented pores). So considering the object shape as a sphere, the volume-equivalent diameter (D_{volume} = diameter of a sphere with the same volume as the 3D object) is:

$$D_{volume} = \left(\frac{6}{\pi} V_{object} \right)^{1/3}. \tag{2.5}$$

In the same way the surface-equivalent sphere diameter ($D_{surface}$ = diameter of a sphere with the same surface as the object S_{object}) is:

$$D_{surface} = \left(\frac{6}{\pi} S_{object} \right)^{1/2}. \tag{2.6}$$

Having the sample volume from analyzed 3D images it is possible to calculate the values of specific surface area.

In the present work S_o determination is done by N_2GA and X-ray Nano- and MicroCT techniques. For N_2GA BET method is applied while for Nano- and MicroCT each obtained resolution is investigated using *Avizo Fire 7.1* Software on the segmented pore phase and C3DE program in the generated equivalent resistor pore network.

2.3.3. Pore morphological parameter: tortuosity

The ability of a rock to store and flow fluids is dependent upon the pore volume, pore geometry and its connectivity (KNACKSTEDT *et al*, 2006). Tortuosity is one of the most widely studied petrophysical parameters yet it is not very well understood (CLENNELL, 1997; ZIARANI and AGUILERA, 2012). Introduced by CARMAN (1937), tortuosity accounts for the sinusoidal flow path through a porous medium. It is defined as the ratio of effective flow (l_e) path to the macroscopic length of sample (l) having any shape (most are core or plug):

$$\tau = \frac{l_e}{l}. \tag{2.7}$$

In his work CARMAN (1937) points out that tortuosity affects both permeability and the leakage velocity by a factor of (l_e/l). Therefore, further work proposed that the overall factor by which the flow is retarded in a tortuous path is proportional to the square of tortuosity, which is referred to as the hydraulic “tortuosity factor” (DULLIEN, 1992; CLENNELL, 1997):

$$T = \left(\frac{l_e}{l} \right)^2 = \tau^2. \tag{2.8}$$

The tortuosity factor *(T)* is not a true pore structure parameter, but rather a parameter associated with one-dimensional models of pore structure. Notwithstanding this, the tortuosity of a porous medium is a fundamental property of the streamlines, or lines of flux, in the conducting capillaries. It measures the deviation from the macroscopic flow direction of the fluid at every point (DULLIEN, 1992). Already BEAR and BACHMAT (1966) suggested in their porous medium model that the permeability of a porous medium is shown to depend on three elementary porous medium properties: porosity *(ϕ)*, average medium conductance ($\overline{B}$) and the medium´s tortuosity *(τ)* (BEAR, 1972). $\overline{B}$ is related to the cross-sections of the elementary channels through which the flow takes place. One should recall that the discussion at this point is restricted to the case of laminar flow of a Newtonian fluid in a porous medium, visualized as a network of narrow channels through which flow takes place. Figure 2.5 shows a bundle of parallel channels with the same diameter (a), with non-uniform diameters (b) and channels with a ratio of the length of the flow to the length of the porous medium bigger than one, i.e. the tortuosity. Figure 2.6 illustrates a sedimentary rock and the increasing of tortuosity as the porosity between the sand grains more compacted becomes smaller. Figure 2.7(a) compares the values of tortuosity for two distinct geometrical forms.

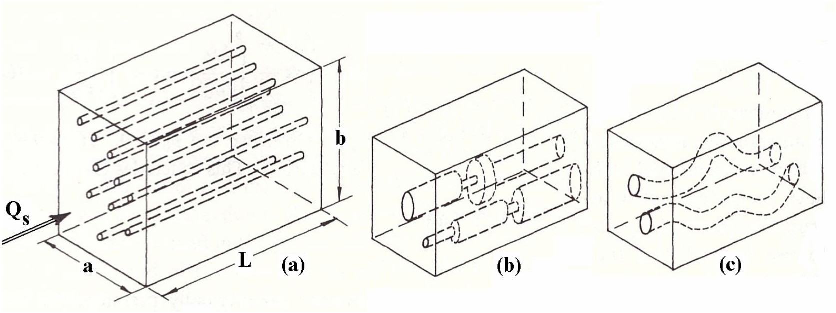

Figure 2.5: Capillary tube models (BEAR, 1972).

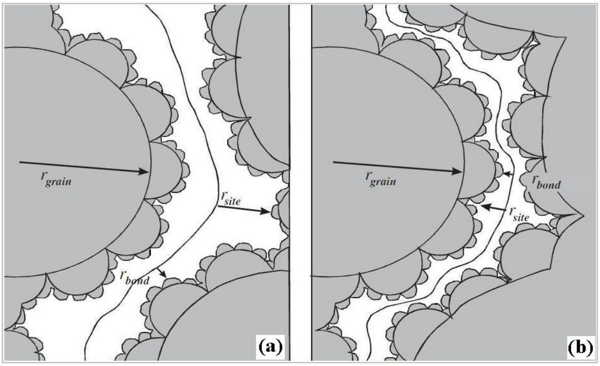

Figure 2.6: Sedimentary rock according to (PAPE *et al.*, 2006) showing pore expansions with radii r_{site} and pore constrictions with radii $r_{bond} \approx r_{eff}$. As an analogy (a) and (b) can exemplify a sandstone and a TGS showing stages of compaction and increase of tortuosity.

To calculate pore morphological parameters such as tortuosity, shape factor, aspect ratio and characteristic orientation, geometrical procedures in the 3D images were calculated using *Avizo Fire* 7.1 software. To exemplify, the definition taken by the program to calculate tortuosity consists of computing a path formed by centroids of each planes of a binary 3D image along the Z-axis (Figure 2.7(b)). Tortuosity is the ratio of the length of a curve to the distance between its ends along Z-axis. In our case the distance between the ends of a curve is given by the number of 2D acquired plans along the Z-axis.

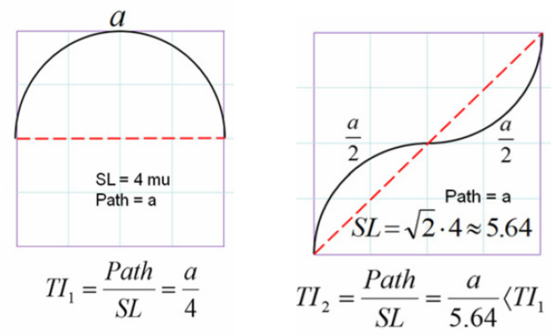

Figure 2.7: A vessel that bends gradually yields higher tortuosity comparing to one that bends more frequently when the arc over chord length. SL: straight line (chord) length, path: path (arc) length, TI: tortuosity index, mu: measuring units tortuosity.

2.3.4. Wettability and capillarity in porous media

Oil recovery from low permeability reservoirs is strategically important because of the large resources locked in such formations. Imbibition is fundamental to oil recovery from such reservoirs under most secondary and improved recovery processes of practical interest. It is also characteristic of porous medium wettability. The rate and the extent of imbibition depend critically on the viscosity of the wetting and nonwetting phases (KOVSCEK *et al.*, 2001).

Wettability is the term used to describe the relative adhesion of two fluids to a solid surface. In a porous medium containing two or more immiscible fluids, wettability is a measure of the preferential tendency of one of the fluids to wet (spread or adhere to) the surface (TIAB and DONALDSON, 2004). The parameter that quantifies wettability is the contact angle created by the liquid and solid phases. A lower contact angle formed by the intersection of the solid-liquid interface, σ_{SL}, implies in a better wettability of the surface. Figure 2.8 shows distinct configurtions for a liquid in contact to a flat and horizontal solid surface.

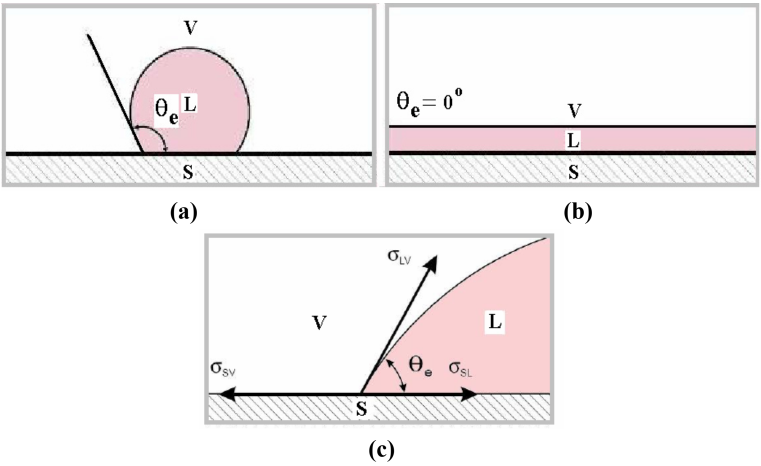

Figure 2.8: Contact angles: (a) θe > 90o showing the unfavorable surface wetting; (b) θe = 0 showing the favorable surface wetting since the droplet covers the completely surface; (c) general three-phase equilibrium configuration showing the interfacial tensions.

In Figure 2.8 the situation (a) the contact angle is greater than 90° indicating that the wetting of the surface is unfavorable so the fluid will minimize its contact with the surface and form a compact liquid drop.

On the other hand, situation (b) shows the fluid totally spreaded over the solid surface area with the contact angle around zero (smaller than 90°) and so the wetting of the surface is favorable. Situation (c) illustrates the "threephase contact line" where the solid, liquid and vapor phases co-exist. The static contact angle resulted through a force balance (therefore stationary) with respect to an solid surface at the contact line was fisrt established by Thomas Young in 1805. In this relationship the generated interfacial surface tensions, σ, and the static contact angle θ_e of a liquid drop on an ideal solid surface was described as (YOUNG, 1805):

$$\cos\theta = \frac{\sigma_{SV} - \sigma_{SL}}{\sigma_{LV}}, \tag{2.9}$$

where the subscripts SV, SL and LV denote the solid-vapor, solid-liquid and liquid-vapor phases, respectively.

The tendency for the drop to assume a curved interfacial shape to reach its equilibrium is due to its surface tension. As a consequence there will be a pressure difference, capillary pressure, across the interface with the highest pressure residing on the concave side. The capillary pressure in descrived by the Laplace-Young equation, for a spherical drop or bubble, $r_{p1} = r_{p2} = r_p$ and hence (YEO, 2006):

$$\Delta P = P_{nw} - P_w = \frac{2\gamma_{nw}\cos\theta}{r_p}, \tag{2.10}$$

where P_{nw} and P_w are the pressures of nonwetting and wetting fluids in the interface, e. i. inside and outside the drop or buble. A simple model explaining what happens in the void space in a rock, is the capillary tube (simulating the narrow opening between grains) shown in Figure 2.9. In the left side note the capillary rise for the liquid being the wetting phase while in the right side the pressure of wetting fluid *(P_w)* (in this case gas) just below the meniscus. In the figure h_{me} is the mechanical equilibrium achieved by the liquid column of length h'_{me} and written as (BERG, 1975):

$$h'_{me} = \frac{1}{\rho_w g}\frac{2\gamma_{nw}\cos\theta}{r_p} = \frac{P'_c}{\rho_w g}. \tag{2.11}$$

The capillary pressure affects the two-phase flow in a rock, especially for low permeability rocks such as tight gas sandstones and seal rocks. That capillary pressure could results in a significant contribution to the fluid flow through the imbibition of the wetting fluid (COSSÉ, 1993).

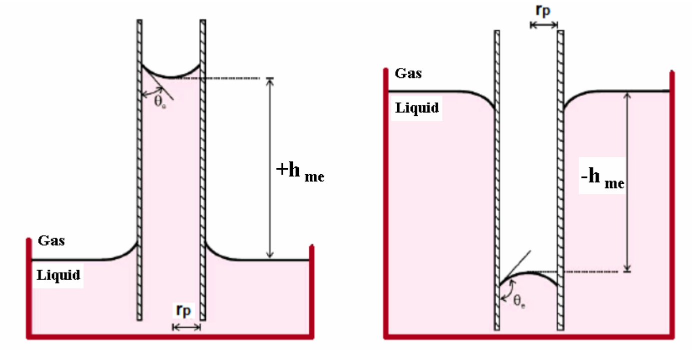

Figure 2.9: Capillary tube model showing wetting liquid (left side) and wetting gas (right side), (WOLF, 2006).

The vast majority of porous media are capillary systems. In a “capillary system” the interfaces separating the various bulk phases play a significant part in determining the physical-chemical state of the system. In these systems, mechanical equilibrium is determined not only by the hydrostatic pressure and gravitational attraction but also by forces associated with surface tension (DULLIEN, 1992).

In this chapter, the discussion is related to the capillary pressure and how this important parameter is applied to the characterization of porous media, such as tight gas sandstones and seal rocks, containing two or more fluids. The capillary pressure curves can be modeled intending to describe the pore structure as discussed next.

2.3.4.1. Capillary mechanisms in heterogeneous reservoirs

Capillary imbibition is the spontaneous displacement of a non-wetting fluid by a wetting fluid (e. g. oil by water) and it is a favorable mechanism for hydrocarbons recovery. If we consider a reservoir which two different porous media coexist (Figure 2.10, COSSÉ (1993)):

(i) A fractured reservoir (a);
(ii) A stratified reservoir (b);
(iii) A reservoir with average compact nodules (c), as shown below.

If we denote a permeable medium by “P” and one much less permeably by “I” we assume zone P has more large pores than zone I. Consequently we expect to have for the same saturation S_I a capillary pressure $P_{CI} > P_{CP}$. When a fluid 1 is injected, it occupies the pores of higher permeable medium rapidly, accordingly $S_{WP} > S_{WI}$ at a given time, see Figure 2.10(d).

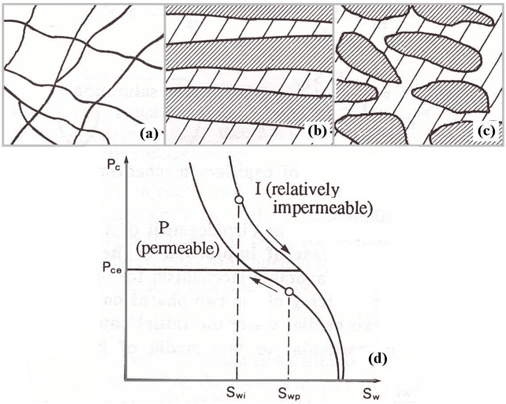

Figure 2.10: Different porous media, a, b and c with the matrix in white. Capillary pressure curves for a more (P) and less (I) permeable media (d), (COSSÉ, 1993).

In higher permeability zones in a reservoir, the saturation with displacing fluid S_W thus reaches a value S_{WP}, whereas in less permeable zones, it only has the value S_{WI}. Yet an equilibrium of the capillary pressures must be established between the two media present, at the contact of the two zones; this occurs only if the fluid saturation in zone I rises, while it decreases in zone P until it corresponds to identical pressures P_{CE}, as displayed by the arrows in Figure 2.10(d).

"Thus the low permeability medium tends to be imbibed with wetting fluid 1 (water), at the expense of the high permeability medium, and tends to flush the non-wetting fluid 2 (oil) into the high permeability medium. This mechanism tends to increase the overall oil (fluid 2) recovery rate". Compare (COSSÉ, 1993). In practice:

- If the displacement is very rapid, the less permeable zones can produce oil only through permeable zones already swept by a wetting fluid, where the relative permeability to oil is very low;
- If the displacement is slow, the less permeable zones will have the time to produce more oil as the displacement front moves forward.

Thereby identifying such permeable zones (also called "sweet spots") in unconventional reservoirs exploration is of extreme importance. One of the methods applied to obtain the porosity and pore size distributions of TGS rocks originated from three distinct reservoirs (Field A, B and C), was the combination of N_2GA and MICP techniques. From the obtained PSD curves we could evaluate the changes of porosity and main pore sizes within reservoir depth.

2.4. Single-phase transport through porous media

2.4.1. Permeability and reservoir engineering

Permeability is a measure of the ability of fluid to flow within the interconnected pore network of a porous medium. Reservoir flow rates, including oil production rates, are proportional to the permeability values of reservoir rock. On the other hand, rock permeability determines the pressure drop required to produce or inject fluid from an existing reservoir at a desired rate (JACKSON *et al.*, 1993).

Permeability is a term used to express the conductivity of a porous medium with respect to permeation by a Newtonian fluid. The parameter that measures the contribution of the porous medium to the conductivity and is independent of both flow mechanisms and fluid properties is denominated “specific permeability”, *k,* onward in the present work called “permeability”. Its value depends uniquely by the pore structure of the analyzed material. Usually darcy is the most used unit of permeability (DULLIEN, 1992). In the petroleum engineering however de unit milidardy = 0.001 darcy is used with 1mD equal to $0.987 \times 10^{-15} m^2$. In this work, the studied unconventional reservoir rocks such as tight gas sandstones and shale, leads to the measurements of permeability even low, into the microdarcy (μD) range.

Mathematical models of petroleum reservoirs have been utilized since the late 1800s. In the simulation of flow in the reservoir, the momentum equation is usually given in the form of Darcy’s law (Darcy, 1856). Derived empirically, this law indicates a linear relationship between the fluid velocity relative to the solid and the pressure head gradient. Darcy’s empirical flow law was the first extension of the principles of classical fluid dynamics to the flow of fluids through porous media (DAKE, 1978). For the reservoirs petroleum engineering the significance of Darcy’s law is that it introduces flow rates into this area and, since the total surface oil production rate from a reservoir is:

$$q_{res} = \frac{dN_p}{dt} \tag{2.12}$$

with N_p being the cumulative oil production, it implicitly introduces a time scale in oil and gas recovery calculations.

2.4.2. Darcy’s law definition

In 1856, by flowing water through a pack of sand, the French engineer Henry Darcy established that, for any flow rate, the velocity of flow was directly proportional to the difference in manometric heights, the relationship being:

$$u = K\frac{h_1 - h_2}{l} = K\frac{\Delta h}{l}, \tag{2.13}$$

where *u* is the flow velocity, which is the total measured flow rate *(q)*, divided by the cross-sectional area of the sand pack; *Δh* is the difference in manometric leves, (water equivalent); *l* is the total length of the sand pack, and, *K* is a constant. Subsequently Darcy’s experimental law was repeated by others and proved to be independent of the direction of flow in the Earth’s gravitational field (DAKE, 1978).

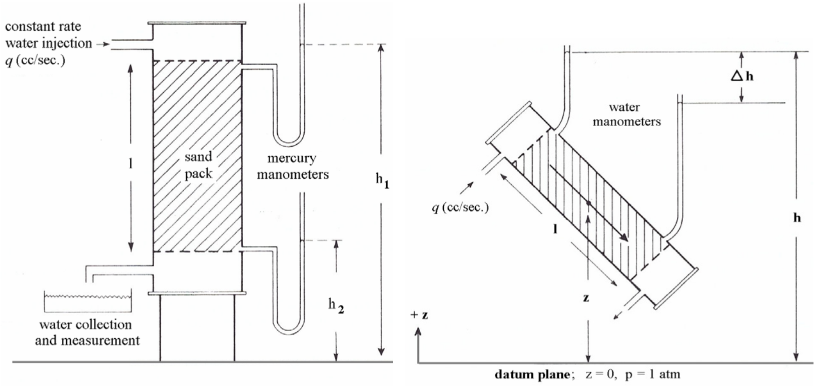

(a) **(b)**

Figure 2.11: (a) Schematic of Darcy´s experimental apparatus; (b) Orientation of Darcy’s apparatus with respect to the Earth´s gravitational field (DAKE, 1978).

As shown in Figure 2.11 the pressure at any point in the flow path, which has an elevation, *z*, relative to the datum plane with respect to the prevailing atmospheric pressure, can be expressed in absolute units as:

$$p = \rho g(h - z), \tag{2.14}$$

alternatively

$$hg = \left(\frac{p}{\rho} + gz \right).$$

In this equation ρ is the liquid (water in Darcy's experiment) density. Now, if equation (2.13) is written in differential form as:

$$u = K \frac{dh}{dl}, \tag{2.15}$$

then differentiating equation (2.14) and substituting equation (2.15) gives:

$$u = \frac{K}{g} \frac{d}{dl} \left(\frac{p}{\rho} + gz \right) = \frac{K}{g} \frac{d(hg)}{dl}. \tag{2.16}$$

The constant *(K/g)* is only applicable for the flow of water, which was the liquid used exclusively in Darcy's experiments. The experiments performed with a variety of different liquids revealed that the law can be generalized as:

$$u = \frac{k\rho}{\mu} \frac{dP}{dl}. \tag{2.17}$$

In which the dependence of flow velocity on fluid density ρ and viscosity μ is observed. The constant *k* is described as the permeability. It is denominated the absolute permeability of analyzed material, completely saturated with a fluid and, because of the manner of derivation, will have the same value irrespective of the nature of the fluid (DAKE, 1978).

The specific or absolute permeability *(k)* of a rock is the ability of the rock to allow a fluid with which it is saturated to flow through its pores. In the petroleum engineering, the derivation of Darcy's law as exposed in equation (2.18) is used to determine the flow through permeable media for a one-dimensional, homogeneous rock with a fluid of constant viscosity. Such situation is illustrated by Figure 2.12, where a sample of length *dl* and cross-section *A*, saturated with a fluid of dynamic viscosity μ, and crossed horizontally by flow rate *Q* (measured in the condition of section *dl*) is considered. In steady-state conditions, the upstream pressure is *P1,* and the downstream pressure is *P2 = (P1-dP)*. The lateral sides are impervious to fluids. If the fluid does not react with the rock, which is the general case, permeability is expressed like an area:

$$Q = A\frac{k}{\mu}\frac{dP}{dl} \tag{2.18}$$

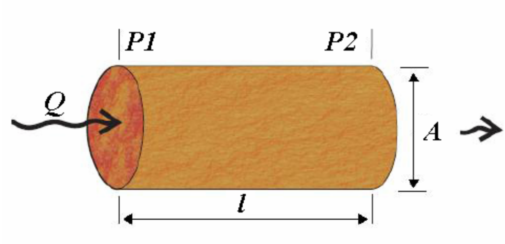

Figure 2.12: Sample of length *dl* and cross-section *A*, Darcy's law scheme.

Darcy's law applies only to the cases where the interstitial flow (i.e., the flow through pores of a porous medium) may be modeled as Stokes flow, ignoring the inertial term restricts the analysis to creeping (laminar) flow where viscous forces dominate in the flow regime. According to SCHEIDEGGER (1974), deviations of Darcy's law (non-linearity between flow velocity and gradient) are: (1) non-Newtonian behavior of the fluid itself; (2) particle migrations that cause blocking and unblocking of pores; (3) local consolidation and swelling of the soil; (4) molecular or ionic effects and (5) turbulent effects associated with high flow rates.

2.4.3. Deviations from Darcy's law in low-permeability rocks

In conventional gas reservoirs, Darcy flow is the dominant flow transport mechanism; however, in some tight sands and particularly in shale sediments, where pore-throat radii as small as a few nanometers are common, diffusion plays an important role and it must be taken into account (ZIARANI and AGUILERA, 2012). To describe how gas fluids are driven respectively by pressure gradient, concentration and surface tension, through a porous media, permeability, diffusion and adsorption are the main mechanisms used (HOU, 2012). Permeability is one of the most fundamental properties of any reservoir rock required for modeling hydrocarbon production (SAKHAEE-POUR and BRYANT, 2012).

2.4.3.1. Knudsen number and flow regimes

Knudsen number, a dimensionless parameter, is commonly used to classify flow regimes in small pores where deviation from continuum flow is important (ZIARANI and AGUILERA, 2012). It is defined as the ratio of molecular mean free path, λ (nm), and a characteristic length, such as pore radius, r (nm), and is given by:

$$Kn = \frac{\lambda}{r} \tag{2.19}$$

According to ZIARANI and AGUILERA (2012) an accurate description of gas flow through porous media must include both diffusion and viscous flow. The authors say that bulk diffusion, Knudsen's diffusion, and surface diffusion are the various forms of diffusion flow. As illustrated in Figure 2.13, in large pores, with diameter much larger than mean free path of gas molecules $(r >> \lambda)$, interaction between gas molecules is more frequent than collision of gas molecules with pore surface (walls). This is simply called bulk diffusion. Therefore, in large pores, viscous flow and bulk diffusion are the dominant transport mechanisms (situation a); as the pore diameter decreases or molecular mean free path increases (at lower pressures), the gas molecules tend to collide more with pore surface than other gas molecules. This means that a point is reached in which the gas molecules move almost independently from one another. This is called Knudsen's diffusion (situation b). In pores with much smaller diameters (situation c) or stronger surface forces, molecules are adsorbed on the surface of the pore; as a result surface diffusion occurs.

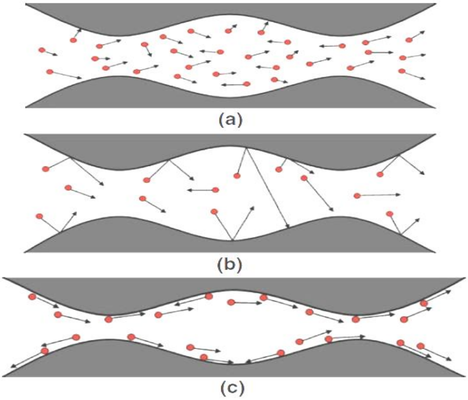

Figure 2.13: Schematic of a cross-section of a pore and gas molecules illustrating types of diffusion flow: (a) Bulk diffusion, (b) Knudsen's diffusion, and (c) surface diffusion. In a real pore situation all three types of diffusion can co-exist (ZIARANI and AGUILERA, 2012).

With the advent of tight and shale gas reservoirs playing significant importance in today's energy market, the slippage gas flow regime in fine-grained rocks have been discussed by various researches (JAVADPOUR, 2009; CIVAN, 2010; DARABI, *et al*., 2012; ZIARANI and AGUILERA, 2012). In this context gas flow that considers slippage phenomenon date started to be developed more than a century ago with the works of MAXWELL (1867), KNUDSEN (1909) and KLINKENBERG (1941). Table 2.1 summarizes the flow regime classification proposed and discussed nowadays, related to the respective Knudsen number and models to be applied. In the present work we investigate the gas flow in TGS rocks (also having pores in the nanometers order) using the Pulse-Decay Permeability (PDP) technique and assuming Darcy permeability. Sensitivity analyses to describe the effect of pore size, pressure and temperature on gas flow, performed during the testes, are presented. Thereby the contribution of Knudsen diffusion and Klinkenberg slip flow on total flow are also discussed.

Table 2.1: Models and flow regimes classification for porous media (ZIARANI and AGUILERA, 2012).

Flow regime	Knudsen number[a]	Law to be used[b]	Comments[b]
Continuum (Darcy/Viscous) flow	$Kn < 0.001$	Darcy's equation for laminar flow and Forchheimer's equation for turbulent flow	Assumes immobile fluid at the pore wall. Hence, no permeability correction is generally required
Slip flow	$0.001 < Kn < 0.1$	Darcy's equation with Klinkenberg or Knudsen's correction	Knudsen's correction is more accurate, but Klinkenberg's correction is easier and, as a result, is generally implemented
Transition flow	$0.1 < Kn < 10$	Darcy's law with Knudsen's correction can be applied	Knudsen's diffusion equation is a more reliable approach, especially when Kn is closer to 10
Knudsen's (free-molecule) flow	$Kn > 10$	Knudsen's diffusion equation. Lattice Boltzmann alternative method[c]	Usually occurs in shale formations where the pore-throat radius is very small

[a] Knudsen number classification taken from DARABI *et al.* , 2012

[b] Taken from ZIARANI and AGUILERA, 2012

[c] AGARWAL *et al.* , 2001

2.4.3.2. Klinkenberg corrections

The empirical Klinkenberg model (KLINKENBERG, 1941) accounts for gas slip flow in tight porous media. As previously discussed in this work, Darcy's law is based on the assumption that the flow is governed by the viscosity (condition of Poiseuille flow). In this flow only collisions between molecules occurs which are represented by the notion of viscosity. However, when the pore size present in the porous medium is so small compared to the mean free path of the fluid molecules, this is the case of low pressure gradient or very small pores. For this type of flow, called Knudsen flow, there are no collisions between molecules but only between solid walls and molecules (KNUDSEN, 1950) and so, there is still proportionality between flow rate and pressure drop, but the coefficient is not related to viscosity anymore. However, gas slippage in porous media and its effect on permeability was first addressed by (KLINKENBERG, 1941). In his pioneering study, Klinkenberg showed how the slip of gas molecules at the surface of rock can influence permeability and proposed an equation in which permeability is related to the inverse of pressure (ZIARANI and AGUILERA, 2012). In this matter a correction can be applied to Darcy's law to account for the deviation from the Poiseuille's law according to (KLINKENBERG, 1941):

$$k_a = k_\infty \left(1 + \frac{b_k}{P} \right), \qquad \textbf{(2.20)}$$

where k_∞ is the absolute permeability at a very high gas-phase pressure at which condition the Klinkenberg's slippage effect can be negligible (WU, *et al.*, 1998). k_a is the apparent (measured) gas permeability, P is the average pore pressure and b_k is the Klinkenberg's slippage factor which depends on the gas and the properties of the analyzed material: gas molecular mean free path *(λ)*, material pore-throat radius *(r)*, and gas pressure *(P)* as depicted on (KLINKENBERG, 1941):

$$\frac{b_k}{P} = \frac{4c\lambda}{r}, \qquad \textbf{(2.21)}$$

where b_k and P are in psi, λ and r, are in nm, and $c \approx 1$.

Also other authors have been proposed correlations for factor b in experimental permeability measurements as shown in Table 2.2.

Table 2.2: Corrections for factor b in permeability measurements.

Model	Correlation	Units and comments
Klinkenberg (1941)	$b_k = 4c\lambda P / r$	*c* is a constant close to unity
Florence *et al.,* (2007)	$b_k = \beta(k_\infty / \phi)^{-0.5}$	β-value Nitrogen = 43.345 Air = 44.106
Civan (2010)	$b_k 0.0094(k_\infty / \phi)^{-0.5}$	Correlation for nitrogen. Units: b_k (Pa), k_∞ (m^2)

Units: b_k,P and β (psi), k_∞ (mD), r and λ (nm), ϕ (fraction).

According to KLINKENBERG (1941), the apparent permeability of a porous medium to gas changes with gas pressure, becoming lower as the mean pressure increases. As the mean pressure becomes increasingly high, the apparent permeability approaches a value, (k_∞), which has been shown to be equal to the permeability of the porous medium to a nonreactive liquid. In an unsteady-state permeability determination, pressure in a core changes both with position (high at the inlet face to atmospheric pressure at the outlet face) and with time. Since apparent permeability is a function of pressure, it too must change with both position and time. The time required for any given pressure interval measured is roughly inversely proportional to the permeability of the analyzed core (JONES, 1972).

2.4.3.3. Apparent permeability and correction factor definition

Figure 2.14 shows the Klinkenberg's and Knudsen (CIVAN, 2010) correction factors for distinct flow regimes. As one can see, compared to the Knudsen's correction, Klinkenberg underestimates the correction factor particularly as it becomes larger than 1, besides no significant differences are observed. For slip flow regime, where $0.0001 < Kn < 0.1$, the correction factor is very small (DARABI *et al.*, 2012). When the Knudsen number increases (in the direction of transition and free-molecule flows) the magnitude of the correction factor gets substantially large. However, such a high Knudsen's flow is not commonly found at reservoir condition unless the formation is extremely tight as in the case of shale (JAVADPOUR, 2009; ZIARANI and AGUILERA, 2012). As both the correction factor and Knudsen number are dimensionless, the graphic in Figure 2.14 can be used to generalize the permeability correction between the apparent and absolute (here called Darcy) permeability.

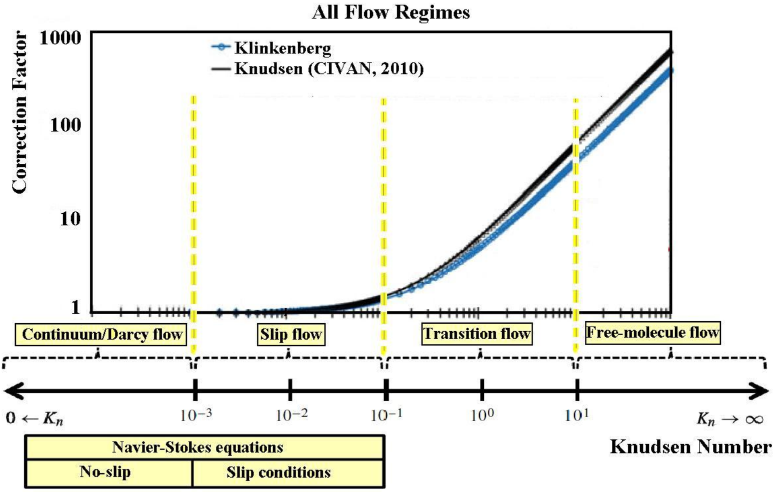

Figure 2.14: Knudsen's and Klinkenberg's correction factor versus Knudsen number for all transition flow regimes (modified from: ZIARANI and AGUILERA, 2012; DARABI, et al., 2012).

2.4.3.4. Parameters of influence

Pore-throat radius, pressure and temperature are the main parameters playing a role in the magnitude of Knudsen's correction factor. The contribution of Klinkenberg effects and Knudsen diffusion to total gas flow is larger at lower pressures (JAVADPOUR, 2009). Pressure and temperature affect the molecular mean free path and consequently Knudsen number and Klinkenberg's correction factor. It happens because molecular mean free path, defined as an average distance traveled by molecules between collisions, is a function of pressure, temperature and collision diameter of the molecules which can be obtained from the following equation (CUSSLER, 1997):

$$\lambda(P,T) = \frac{K_B T}{\sqrt{2}\eta^2 P}, \qquad \textbf{(2.22)}$$

where T is the temperature (K), P is the pressure (Pa), K_B is the Boltzmann constant (1.3805 x 10^{-23} J/K), and η is the gas collision diameter (m) equal to 0.44 for nitrogen and 0.42 for methane. In the present work, the permeability experiments (PDP) were performed using gas nitrogen, at temperature of 22 ^{o}C and mainly at mean pressure of gas equal 6.89 MPa. In these condition the value of λ is equal 2.15 nm.

2.5. Review of utilized permeability models

Knowledge of pore space properties of sedimentary rocks is a prerequisite for the exploitation of hydrocarbon reservoirs (PAPE *et al.*, 2006). The rock permeability is one of most important properties concerning the reservoir since it allows calculation of the fluid flow. Predicting permeability becomes much more difficult in formations with small grain size and an abundance of clay minerals such as tight gas sandstones rocks - a sub-millidarcy reservoir. The empirical relations used in this work to estimate permeability from measured pore structure parameters on TGS of field A are briefly discussed as follows.

2.5.1. Permeability correlation from capillary pressure curve

The existing correlations from Winland-Pittman (KOLODZIE, 1980), Aguilera (AGUILERA, 2002) and Katz-Thompson (KATZ and THOMPSON, 1986) are permeability models based on the concept of capillary pressure where a characteristic throat size governs the flow at the percolation threshold of the porous medium. Thereby, each model uses a different method to estimate that characteristic throat size. Winland developed a power law model that relates permeability with porosity and pore throat radius (later published by KOLODZIE, 1980) using data from more than 10 formations:

$$k = 17.6\phi^{1.470} r_{35}^{1.701}, \tag{2.23}$$

where r_{35} is the pore radius corresponding to 35% mercury saturation.

Aguilera (2002) also proposed a correlation for pore throat radius assuming 35% mercury saturation. To develop his correlation, Aguilera used over 2500 sandstone and carbonate samples from 28 formations:

$$k = r_{35}^{2.222} 11.324\phi, \tag{2.24}$$

with values of r_{35} given in µm, k in mD, and ϕ is the fractional porosity. Starting from percolation concept, Katz and Thompson have related the permeability of a porous medium to a length scale l_c:

$$k = \frac{1}{226}\frac{l_c^2}{F}, \tag{2.25}$$

where l_c is the size of the smallest throat invaded by a non-wetting phase at the percolation threshold. l_c can be estimated from the inflection point of the mercury injection curve. F is the formation factor of a homogeneus porous media related to the tortuosity (τ) and already demostrated by WYLLIE and SPANGLER in 1952 as being:

$$F = \frac{1}{\phi^m} = \frac{\tau}{\phi}. \tag{2.26}$$

In the equation above m is the Archie's cementation factor which is a unique property of a given porous media. Ranges of $1.2 < m < 3$ have been presented by CLENNELL (1997).

In this study, we apply all correlations discussed above to estimate the permeability using the parameters r_{35}, l_c and ϕ measured by the combination of N_2GA and MICP techniques. The tortuosity parameter obtained by X-ray CT technique allowed us to estimate the formation factor of analyzed samples and it is one important pore structural parameter in the Kozeny-Carman model, also used to predict permeability. Measured pore structure parameters obtained by the applied techniques in the present work were correlated to empirical models to estimate or simulate permeability.

2.5.2. Models used for fine-grained rocks

The fluid transport in fine-grained porous rocks such as tight gas sandstones rocks can be described as Darcy flow/advection (HILDENBRAND *et al.*, 2005; SCHLÖMER and KROOSS, 1997). However, as noted by Civan *et al.* (2010) for shale gas, by Javadpour (2009) for nanopores mudrocks, by Rushing *et al.* (2008) for tight sandstones and previously in this work, gas flow is often affected by several phenomena, e.g. possible transition from volume flow to molecular transport, which may cause deviations from Darcy's law. Nevertheless, it remains the common base for several mathematical models to measure permeability in sandstones and most TGS. In general, these models are correlated to physical parameters such as density, porosity, grain and pore diameter or specific surface area (YANG and APLIN, 2007). In the sub-chapter reported here after, the Kozeny-Carman equation, Pape *et al.* (1999) pore fractal model and the Series-Parallel model were used to estimate permeability coefficients from the measured physical parameters of the TGS rocks samples using N_2GA and MICP in combination and X-ray CT, as described below.

2.5.2.1. Kozeny-Carman model

One of the most widely used expressions, the Kozeny-Carman law that relate permeability to the structural characteristics of the medium have been derived analytically for capillary tube models (LATIEF and FAUZI, 2012). The Kozeny-Carman law expresses the permeability of the medium assumed to be equivalent to a conduit, the cross section of which has an extremely complicated shape but, on the average a constant area (Dullien, 1992) it is therefore a function of pore geometry.

The general form for the Kozeny-Carman (KC) model can be simplified as (DULLIEN, 1992):

$$k_{KC} = \frac{\phi^3}{F_o S_o^2 (1-\phi)^2 \left(\frac{l_e}{l}\right)^2}, \tag{2.27}$$

where ϕ is the porosity of the sample, F_o is a shape factor, l_e is the average path length of flow and S_o is the specific surface area based on the volume of the solid. The parameter (l_e/l) is the tourtuosity and $(l_e/l)^2$ is the hydraulic "tortuosity factor". The intrinsic permeability is given in m^2, the porosity has no unit and the specific surface area multiplied by grain density is given in m^{-1}.

2.5.2.2. Fractal permeability-porosity relationship (PAPE et al., 1999)

The permeability-porosity relationship presented by PAPE *et al.* (1999) was demonstrated using several data sets of permeability and porosity measured on samples from different types of sandstones and shale. In this work they observed that different diagenetic processes may superpose each other as mechanical compaction, mineral solution, and cementation changing permeability-porosity relationships. They also affirmed that as long as the fractal dimension of the pore space equals the standard value D=2.36, the diagenetic path is characterized by a power-law curve with an exponent of 10 in the porosity-permeability plot. However, conditions may be different in the low-permeability range. Usually the decrease of the effective pore radius and the increase of the tortuosity *(τ)* is less pronounced for low permeabilities, i.e., at later stages of diagenesis. This is reflected by the smaller increase in permeability with porosity in the low-porosity range (for more details see PAPE *et al.*, 1999). Therefore to characterize samples with low permeability they proposed the following equation:

$$k_{PAPE-SHALE} = 0.1\phi + 26\phi^2 + (10\phi)^{10}, \qquad \textbf{(2.28)}$$

where porosity *(ϕ)* is given in fraction volume.

2.5.2.3. Series-Parallel model

The Series-Parallel (S-P) equations emerged originally from the work of Childs and Collis-George (1950) and Reznik (1971). Later Fernandes *et al.* (2003) studying reservoirs rocks, applied this model considering the probability of pores being connected based on the amount of pores. Also, the pore size distribution was obtained by 2D image analysis. The authors concluded that the probability of pores being connected can be evaluated considering the amount of pores by calculating the quotient between the number of pores in a certain class and the total number of pores present in the medium. Therefore, generalizing for *n* classes of pore size, the intrinsic permeability obtained applying the S-P procedure *(k_{SP})* is defined as:

$$k_{SP} = \sum_{i=1}^{n} \phi_i \frac{r_i^2}{8} P_i \left(P_i + 2\sum_{j=i+1}^{n} P_j \right), \qquad \textbf{(2.29)}$$

where r_i and ϕ_i are the pore radius and porosity in the i class, respectively.

Also, the probability of pores connecting *(P_i)*, considering cylindrical pores of class *i* is given by

$$P_i = \frac{\left(\dfrac{\phi_i}{r_i^2}\right)}{\sum_{k=1}^{n}\left(\dfrac{\phi_k}{r_k^2}\right)}. \qquad \textbf{(2.30)}$$

The complete pore size distribution and porosity data obtained by N_2GA and MICP combination were used as the input values for the S-P model, while BET specific surface area values were used in the K-C model.

2.5.3. Estimating permeability from NMR measurements

The porosity and pore-size information from NMR measurements can be used to estimate both the permeability and the potentially producible porosity (that is, the movable fluids). The NMR estimate of producible porosity is called the free-fluid index (FFI). The estimate of

FFI is based on the assumption that the producible fluids reside in large pores, whereas the bound fluids reside in small pores. The spin–spin relaxation time obtained performing a NMR test is denominated *(T_2)*. T_2 is one of the pore structural parameters determined in this thesis and it will be explained in a later section. Because T_2 values can be related to pore sizes a T_2 value can be selected below which the corresponding fluids are expected to reside in small pores and above which the corresponding fluids are expected to reside in larger pores. Then this T_2 value is called the $T_{2\ \mathrm{cutoff}}$ (MARSHALL *et al.,* 1995; COATES *et al.*, 1999).

Through the partitioning of the T_2 distribution, $T_{2\ cutoff}$ divides effective porosity of tight sandstones into FFI and bound-fluid porosity, or bulk volume irreducible (BVI). The $T_{2\ cutoff}$ can be determined with NMR measurements on water-saturated core samples. Specifically, a comparison is made between the T_2 distribution of a sample in a fully water-saturated state, and the same sample in a partially saturated state, the latter typically being attained by centrifuging the core at a specified air-brine capillary pressure. Although capillary pressure, lithology, and pore characteristics all affect $T_{2\ cutoff}$ values, common practice establishes local field values. E.g. in the Gulf of Mexico $T_{2\ cutoff}$ values of 33 and 92 ms are generally appropriate for sandstones and carbonates (COATES, *et al.,* 1999). In the TGS rocks analyzed in the present work only measurements of 100% saturated on mini plugs were performed, suggesting therefore the usage of theoretical values of 33 ms as $T_{2\ cutoff}$. However, Ashkar *et al.* (2010) studying sandstone ranging from tight gas to poorly lithified obtained $T_{2cutoff}$ values between 1.45 ms and 242 ms where clay content played a key factor in reducing cutoff time.

NMR relaxation properties of rock samples are dependent on porosity, pore size, pore-fluid properties and mineralogy (COATES, *et al.*, 1999). The NMR estimate of permeability is based on theoretical models that show that permeability increases with both increasing porosity and increasing pore size. Traditionally, two related kinds of permeability models have been developed: the free-fluid or Coates model (applicable in formations containing water and/or hydrocarbons); the Mean-T_2 model or SDR (applicable to the pore systems containing only water) (MORRISS *et al.,* 1997). The use of these particular size parameters in their respective expressions is based on empirical considerations. The Mean-T_2 model, however, fails when the pore contains hydrocarbons because then T_{2gm} (with gm refering to the geometric mean of the T_2 distribution) is not controlled exclusively by pore size.

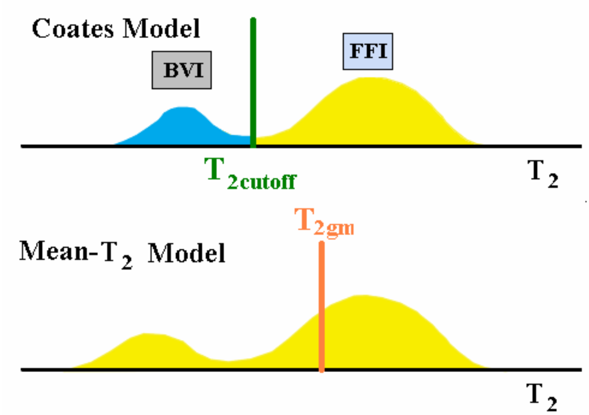

Figure 2.15: The Coates permeability model (top) uses the FFI/BVI ratio to describe changes in the surface-to-volume ratio. The Mean-T_2 permeability model (bottom) uses an average T_2 value to describe changes in surface-to-volume ratio (COATES *et al.*, 1999).

From the Coates model, permeability is estimated by:

$$k_{Coates} = \left[\left(\frac{\phi}{C} \right)^2 \left(\frac{FFI}{BVI} \right) \right]^2 \qquad \textbf{(2.31)}$$

where porosity, ϕ, is given in percentage, C is a constant which is a term that reflects the correlation between the rock's pore throat and pore size and in fact it is a function of pore geometry dependent on the processes that created the formation. In sandstones C is usually around 10. *FFI* is the free fluid index, and *BVI* is the bound volume of irreducible water. Core porosity and permeability should be used to estimate C for the Coates model. In this work we found a mean C value for the well A formation based on the obtained $T_{2cutoff}$ values.

The Mean-T_2 model, also called SDR (Schlumberger Doll Research) is a similar expression to $k = T_1^2 \phi^4$ which has been used to estimate matrix permeability in sandstones (LATORRACA *et al.*, 1993) and given by (MORRISS *et al.*, 1997):

$$k_{Mean-T2} = bT_{2gm}^2 \phi^4 \qquad \textbf{(2.32)}$$

Applying this equation with porosity as a decimal fraction and T_{2gm} in ms gives permeability estimates in mD. T_{2gm} is the geometric mean of the T_2 distribution and b is a coefficient that depends on the formation type and can be determined through calibration with core porosity and permeability. Rezaee *et al.* (2012) used b equal to 4 for sandstones; Morriss *et al.* (1997) found b equal 4.6 as a good agreement for 110 sandstones from three reservoirs.

All the models described above were used to predict permeability of tight gas sandstones originatted from the field named A in this work. For all five TGS samples analyzed, the values of permeability measured by PDP technique were used to compare and validate the empirical and simulated results. In the next chapter the set of methods and techniques applied in the present study is summarized.

3. ANALYTICAL METHODS: THEORETICAL ASPECTS

3.1. Pulse-decay permeability

Difficulties in measuring permeability in reservoirs rocks below 1 (mD) is mainly due to very low flow rate, difficult to establish in such rocks. Experiments require therefore an adaptation of the experimental devices initially used for more permeable rocks. In recent years, both pulse-decay technique and steady-state technique have been used to make gas permeability measurements in tight rocks. One of the purposes of this study is to apply the pulse-decay technique as proposed by JONES (1997) to obtain the experimental permeability values of low (and ultra-low) permeability tight gas sandstones from distinct wells. For obtained values up to 0.001 mD we also compare the transient method from PDP with the traditional steady-state method. Another objective of this work was to determine the correlations of Klinkenberg correction in a sense of build up a database through tight gas sandstones. Additionally, the measured Klinkenberg permeability on TGS was used to validate empirical permeability obtained by the correlation of measured pore-structure parameters. Accurate determination of petrophysical properties (such the ones used in the empirical permeability models) of geological formations are necessary, among them precise permeability values.

Transient (or pulse-decay) permeability techniques have been discussed and unsteady-state permeameters have been built and reported in the literature (JONES, 1972). This differential technique permits accurate measurements of permeability in the micro-Darcy range in a reasonable length of time. According to Jones (1997) laboratory pulse-decay measurements using a gas or liquid are effective for determining the permeability of rocks in the range from 0.1 mD to 0.01 μD. With the currently advent in the petroleum industry in characterizing the properties of unconventional reservoirs, the usage of pulse-decay technique has made feasible to measure the permeability of very tight rocks and shale. The scheme of a conventional pulse-decay apparatus, shown in Figure 3.1, consists of an upstream reservoir for gas or liquid of Vu, sample holder capable of applying high confining pressures, which contains a cylindrical rock sample (plug) of pore volume V_p, and a downstream reservoir of volume Vd. A differential pressure transducer measures the pressure difference between the reservoirs Vu and Vd through the analyzed sample, and a second transducer measures the absolute pressure, P_m, in the downstream reservoir.

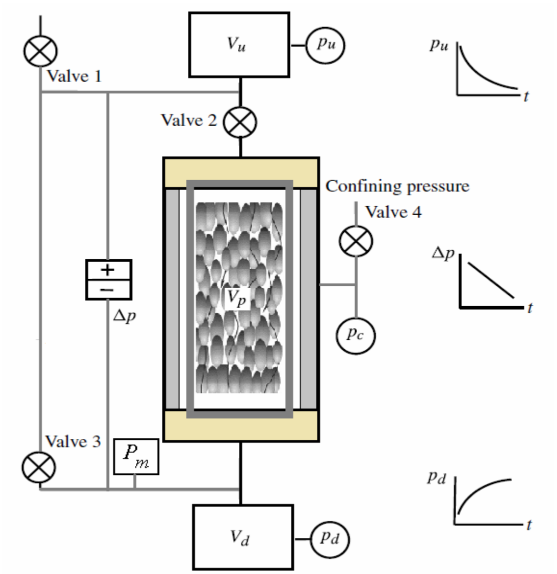

Figure 3.1: Scheme of a pulse-decay apparatus showing upstream and downstream: reservoirs volumes *(Vu, Vd)*, instantaneous pressures (*Pu, Pd)*. The core holder contains a pore volume *(V_p)* sample under confining pressure *(p_c)*. During the test, the pressure difference across the sample *($\Delta P=P_u-P_d$)* is measured (JONES, 1997; DARABI *et al.*, 2012).

In this scheme the pressure in the upstream reservoir is increased by *ΔPu*, which is 1 to 3% higher them *Pd*, and is allowed to stabilize while achieving thermal equilibrium. When Valve 2 is open "pressure pulse" is created to flow through the sample. The initial pressure difference across the sample, *ΔP*[0], is slightly less than *ΔPu* because of the "dead volume" in the flow line between Valve 2 and the face of the sample.

Data are analyzed from the solution of the diffusivity equation, which is derived by combining the differential form of Darcy's law with the continuity equation (JONES, 1997). The sample is pressured to be initially at a uniform pore pressure, *Pd*[0], throughout. The time required for this step when analyzing tight gas sandstones is about 2 hours. At a time *t=0,* a pulse of slightly higher pressure, *ΔP*[0], is applied to its upstream reservoir. As gas flows from *Vu* into the sample, the pressure in *Vu* declines, while the pressure in *Vd* remains constant for a short period of time until the pressure pulse has transversed the length of the sample. Then the pressure in *Vd* rises. Because *Pu*[t] declines and *Pd*[t] rises, *ΔP*[t] continues to diminish and gradually approaches zero. The rate of pressure decay depends on permeability. The lower the permeability is the slower the decay. Figure 3.2 exemplifies the decay for rocks belonging to a same field as well as shale. Observe the time differences between TGS and shale, also fractured shale “A”.

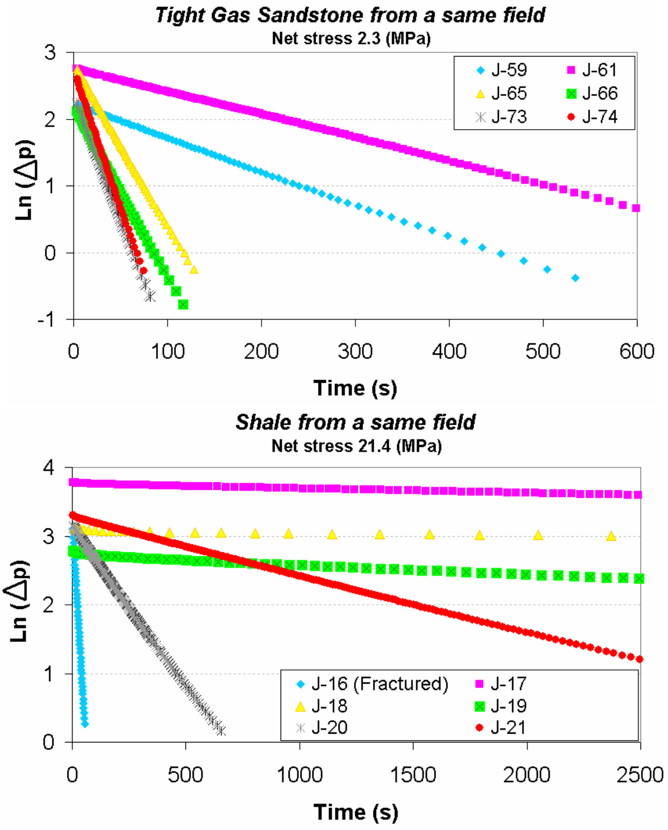

Figure 3.2: Semi-log pulse-decay *ΔP x t*: TGS (top) and shale (bottom).

The general solution for the pressure difference as a function of time was presented by DICKER and SMITS (1988) and described as follows (JONES, 1997).

Having adequate bounding conditions it is possible to show that dimensionless pressure difference, ΔP_D, between *Vu* and *Vd* decays exponentially with elapse time, t_D as:

$$\Delta P_D = 2\sum_{m=1}^{\infty} \frac{a(b^2+\theta_m^2)-(-1)^m b\sqrt{(a^2+\theta_m^2)(b^2+\theta_m^2)}}{\theta_m^2(\theta_m^2+a+a^2+b+b^2)+ab(a+b+ab)} \exp(-\theta_m^2 t_D), \quad \textbf{(3.1)}$$

wherein θ_m are roots of the equation:

$$\tan\theta = \frac{(a+b)\theta}{\theta^2-ab}, \quad \textbf{(3.2)}$$

a is the ratio of the compressive storage of the sample's pore volume to that of the upstream reservoir,

$$a = \frac{V_p(c_g+c_{pv})}{V_1(c_g+c_{V_1})}, \quad \textbf{(3.3)}$$

b is the ratio of the compressive storage of the sample's pore volume to that of the downstream reservoir,

$$b = \frac{V_p(c_g+c_{pv})}{V_2(c_g+c_{V_2})}. \quad \textbf{(3.4)}$$

In Eq. (3.1) t_D is the dimensionless time equal to:

$$t_D = \frac{[6,8046x10^{-5}]k_g t}{\mu_g\phi(c_g+c_{pv})L^2}, \quad \textbf{(3.5)}$$

where μ_g, ϕ, L and k_g are respectively gas viscosity, sample porosity, length and permeability.

For the late-time solution, where a single exponential applies, the first factor on the right-hand side of Eq. (3.1) becomes:

$$f_o = \frac{2\left[a(b^2+\theta_1^2)+b\sqrt{(a^2+\theta_1^2)(b^2+\theta_1^2)}\right]}{\theta_1^2(\theta_1^2+a+a^2+b+b^2)+ab(a+b+ab)} \quad \textbf{(3.6)}$$

Therefore, under typical pulse-decay (i.e. high P_m and small pressure difference across the core sample) the analytical solution may be used to estimate apparent permeability for extremely low-permeability samples. However, when the pressure difference across the core is large or the initial core pressure is low, the test in low-permeability samples will take some time and the analytical solution may lead to a significant error in pressure-decay prediction (DARABI *et al.*, 2012). It happens because of the deviations on the assumptions that the gas density (ρ_g), viscosity (μ_g) and volumetric gas compressibility (defined by $c_g = 1/\rho_g \times \partial\rho_g / \partial P$) are constant. DARABI et al. (2012) performing a sensitive analysis to determinate the effects of pressure-dependence of these constants and observed that the variation of (ρ_g) with pressure has a large impact and is not a negligible effect on the pressure solutions at late transient times.

3.1.1. Apparatus

Figure 3.3(a and b) shows the PDP-200 from CoreLab apparatus, including the upper and lower nitrogen lines, a Hassler holder, associated calibration thermocouple and manometer, and the panel containing the needle valve and all the electronic devices and transducers necessary to the measurements.

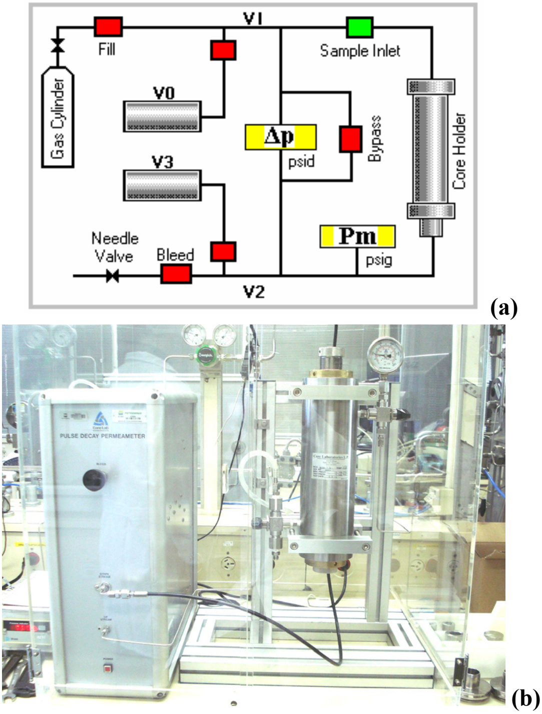

Figure 3.3: Pulse decay permeameter apparatus used for the studies, cells (a) and equipment (b) views.

For both confining pressure in the Hassler holder and obtaining the data during the operation of the equipment, the nitrogen gas was used. The calibration of internal parts of the equipment such as the tank volumes and the transducers have been realized by the equipment supplier and, the volume of external upper and lower nitrogen lines were measured and added to the equations of the PDP equipment. One of the most critical difficulties while performing a PDP experiment is maintenance of constant temperature as the equations developed using this technique assume isothermal nitrogen expansion (JONES, 1972). To ensure a constant temperature we isolated the experimental setup in a plastic casing as shown in Figure 3.3(b).

3.2. Nitrogen gas adsorption

3.2.1. Principles and properties

Physical gas adsorption is a technique that accurately determines the amount of gas adsorbed on a solid material, which is a direct measure of the porous properties and structure. The isotherm obtained from N_2 adsorption, when applied over a wide range of relative pressures (P/P_o), can provide information on the surface area, pore volume and PSD from 0.5 to 200 nm (GROEN *et al.*, 2003). The classical pore size model developed by Barret *et al.* (1951), BJH after Barret, Joyner and Halenda, which is based on the Kelvin equation and corrected for multilayer adsorption, is most widely used for calculations of the PSD over the mesopore range. On the other hand, the BET (Brunauer, Emmett and Teller) method of Brunauer *et al.* (1938) is the most widely used to assess the specific surface areas of porous materials from adsorption data.

Low temperature nitrogen adsorption measurements are largely used for characterization of porous solids where adsorbed amounts and capillary condensation/evaporation pressures are related to the geometrical properties of the porous matrix (GREGG and SING, 1982). For instance, the specific surface area of porous materials is usually assessed from the adsorption experiments prior to the capillary condensation of the fluid on a region which the fluid is assumed to cover uniformly the pore walls. The thickness of the film adsorbed on the pore surface (t) is also an essential parameter to describe the phenomenon of capillary condensation (COASNE *et al.,* 2004).

In Figure 3.4 snapshots of gas atoms adsorbed in the pore walls (considering a medium with pore bodied and throats) at different pressures are shown. As one can see at low pressures, the pore surface is covered by a quasi-homogeneous layer of gas atoms (a). As the relative pressure is increased the filling of the pore with constriction (pore throats) starts with followed condensation of gas atoms in the part of the constricted pore. As expected, this condensation pressure is smaller than that obtained for the pore bodies (cavities). The condensation in the constricted part leads to the presence of hemispherical menisci in the interfacial region between the largest cavity and the constriction. These curved interfaces together with the film adsorbed on the wall of the pore body define a gas bubble inside the pore (see Figure 3.4 (b) and (c)). Finally, all remained open pore cavity on the sample get completely filled once that the condensation of gas bubble occurs at a pressure $P/P_o \sim 1$.

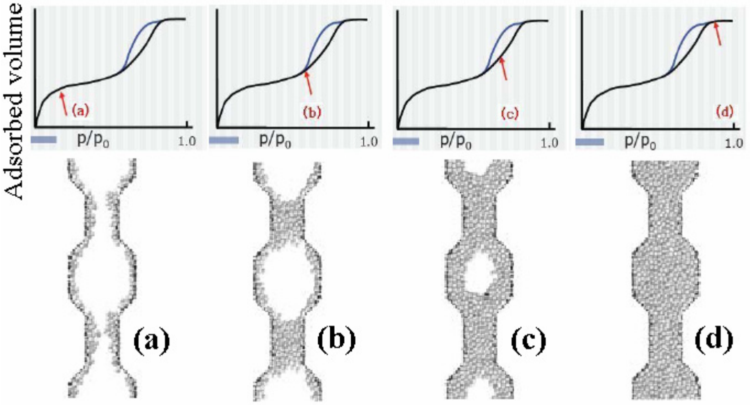

Figure 3.4: Configurations of N_2 atoms at 77 K in a pore with constrictions, from the beginning of the N_2GA experiment (a) $P/P_o \sim 0.01$ to the end of it (d) $P/P_o \sim 1$ (modified from COASNE *et al.*, 2004).

3.2.2. Isotherms acquisition and classification

When a specific gas is put in contact with a solid surface, molecules of this gas will be adsorbed to the surface in amounts that are a function of their partial pressure in the bulk pressure. An adsorption isotherm is simply the measurement of the quantity of a gas adsorbed over a range of relative pressures at a single temperature (77 K for the nitrogen gas adsorption). Depending on the type of the adsorbent (solid) or the adsorbate (gas) and on the intermolecular interactions between the gas and the surface, different shapes can be displayed by the isotherms. The first systematic attempt to interpret the adsorption isotherms shapes into a classification was introduced by Braunauer, Deming, Deming and

Teller (BDDT) in 1940 (BRUNAUER *et al.*, 1940) who described five types. Much later SING *et al.* (1985) introduced an additional isotherm, which completes the International Union of Pure and Applied Chemistry (IUPAC) classification as illustrated in Figure 3.5.

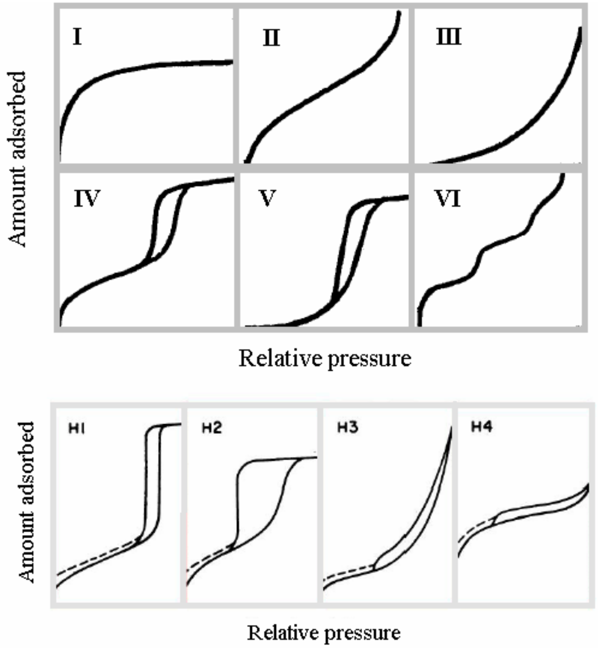

Figure 3.5: IUPAC classification for gas adsorption isotherms (above) and types of hysteresis loops (below) (SING *et al.,* 1985).

Type I isotherms characterize microporous adsorbents. Types II and III describe adsorption on macroporous adsorbents with strong and weak adsorbate-adsorbent interactions, respectively. Types IV and V represent adsorption isotherms with hysteresis. Finally, Type VI has distinct adsorption steps (step-like) characteristics of multi-surface on non-porous adsorbents. The hysteresis loop (Type IV and V isotherms) is the change where a lower branch of which represents measurements obtained by progressive addition of gas to the system, and the upper branch by progressive withdrawal; hysteresis effects are liable to appear in isotherms of other types too (GREGG and SING, 1982).

Figure 3.5 (bellow) illustrates the types of hysteresis loops according to SING *et al.* (1985). Hysteresis appearing in the multilayer range of physisorption isotherms is usually associated with capillary condensation in mesopore structures. Two extreme types are shown as H1 and H4. In the former the two branches are almost vertical and nearly parallel over an appreciable range of gas uptake, whereas in the latter they remain nearly horizontal and parallel over a wide range of P/P_o. A feature common to many hysteresis loops is that the steep region of the desorption branch leading to the lower closure point occurs (for a given adsorptive at a given temperature) at a relative pressure which is almost independent of the nature of the porous adsorbent but depends mainly on the nature of the adsorptive (e.g. for nitrogen at its boiling point at P/P_o~ 0.42 (SING *et al*, 1985; GROEN *et al*., 2003).

Type H1 is often associated with porous materials compacts of approximately uniform spheres in fairly regular array, and hence to have narrow distributions of pore size. For Type H2 loops the pore systems of size and shape is not well-defined yet., indeed, in the past it was attributed to a difference in mechanism between condensation and evaporation processes occurring in pores with narrow necks and wide bodies (ink-bottle pores). The Type H3 (which does not exhibit any limiting adsorption at high P/P_o) is observed with aggregates of plate-like particles giving rise to slit-shaped pores. Similarly, the Type H4 loop is often associated with narrow slit-like pores, but in this case the Type I isotherm character is indicative of microporosity (SING *et al.*, 1985). Besides giving an indicative of the complexity of pore morphologies, the isotherms in the present work were also used to obtain pore size distribution (micro- and mesopore regions) and the specific surface area for the analyzed TGS.

3.2.3. Adsorption theory for PSD calculation

Nowadays the types of models available for the pore size calculation using gas adsorption measurements are the density functional theory (DFT) or classical theory. Classical models are based on the Kelvin equation and thickness for determining the pore size distribution. Although the pore size distributions were calculated in the present work by usage of the BJH and Dollimore-Heal (DH) (DOLLIMORE and HEAL, 1964; DOLLIMORE and HEAL, 1970) methods based on the adsorption isotherms data and DFT method (DO and DO, 2003), only the traditional BJH method was applied for the combination of N_2GA and MICP. Therefore, a brief revision to this model is exposed.

The Barret, Joyner and Hallenda (BJH) theory (BARRET *et al.*, 1951) was applied to find the size distribution of the micro- and mesopores. The BJH analysis describes the capillary condensation phenomenon in a cylindrical pore as described by Figure 3.6.

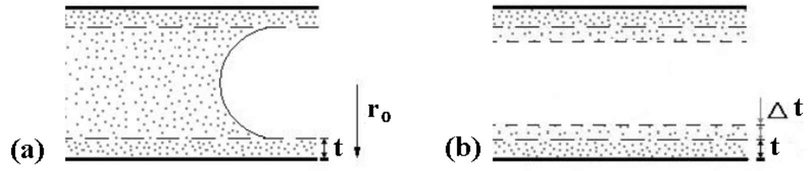

Figure 3.6: (a) Pore filled by gas at P/Po ~1; (b) increasing on the adsorbed gas layer as P/Po increases (FERNANDES, 1990).

It is assumed that the condensation of a fluid in a pore of radius r_o takes place in the 'core' region, i.e., the inner part of the pore that has a radius r_o - $t(P/P_o)$, where $t(P/P_o)$ is the thickness of the film adsorbed on the pore wall as a function of the relative pressure (P/P_o) of the gas. Using this model, it is predicted that the condensation of nitrogen in a pore of radius r_o occurs at a pressure given by the following modified Kelvin equation:

$$\ln\left(\frac{P}{P_o}\right) = -\frac{\alpha\gamma_N V_1}{RT\left[r_o - t\left(\frac{P}{P_o}\right)\right]}, \tag{3.7}$$

where P is the system pressure, P_o is the saturation vapor pressure of nitrogen, γ_N and V_1 are the surface tension and molar volume, respectively, of liquid nitrogen, R is the gas constant, T is the temperature at which the isotherm is measured (77 K) and α is a factor that accounts for the shape of the gas/liquid interface. The latter is assumed to be cylindrical during the adsorption process (α = 1) and hemispherical during the desorption process (α = 2) (COASNE *et al.*, 2004). In this study, t (in both models BJH and DH) was determined using the empirical Halsey equation for nitrogen (HALSEY, 1948):

$$t = 3.54\left[-\frac{5}{\ln\left(\frac{P}{P_o}\right)}\right]^{1/3}. \tag{3.8}$$

3.2.4. Adsorption theory for surface area measurements

In the present thesis two methods were applied to measure specific surface area of analyzed tight gas sandstones: Langmuir and BET theories. The Langmuir equation describes better microporous material exhibiting Type I isotherms; it assumes adsorption limited to monolayer. On the other hand BET method allows the estimation of specific surface areas from adsorption isotherms on the basis of the multilayer adsorption model (compare Figure 3.7).

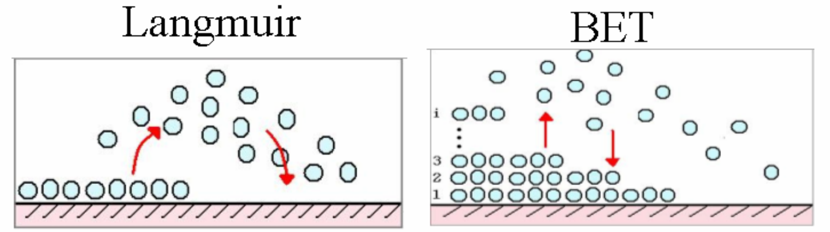

Figure 3.7: Gas-surface interactions in the adsorption process in Langmuir and BET theories modified from FERNANDES (1990).

The hypothesis of the BET model is that (i) adsorption occurs on energetically homogeneous sites having energy ε_1 (also, the surface density of the sites is constant) and (ii) molecules can adsorb onto each other. In this case, the adsorption energy ε_o for all molecules adsorbed above the first layer is constant and equal to the cohesion energy in the bulk liquid. With these assumptions, it can be shown that adsorption data (the adsorbed amount N versus the relative pressure P/P_o) must obey the following equation:

$$\frac{\left(\frac{P}{P_o}\right)}{N\left[1-\left(\frac{P}{P_o}\right)\right]}=\frac{1}{N_oC}+\frac{C-1}{N_oC}\left(\frac{P}{P_o}\right), \tag{3.9}$$

where N_o is the monolayer capacity, i.e., the number of atoms needed to uniformly cover the substrate with one complete monolayer. The factor C is related to the energy of the system, $C=\exp\left[\left(\varepsilon_1-\varepsilon_o\right)KT\right]$, where K is the Boltzmann constant. The parameters C and N_o are estimated from the slope and the intercept of the BET plot given by equation above. The monolayer capacity is converted into a surface area

(S) using the known values for molecular weight of the adsorbate *(M),* Avogadro's number ($N_A = 6.023\text{x}10^{23}$) and the absorbate cross sectional area, for N_2 molecule *(A_{N2})* adsorbed at 77 K equal 0.162 nm^2, according to equation for specific area as described by REED (1995):

$$S = \frac{N_o N_A A_{N2}}{M}. \tag{3.10}$$

Finally the specific surface area *(S_o)* is then determined by total surface area divided by sample weight or volume, as already exposed by equations (2.3) and (2.4).

3.3. Mercury intrusion capillary pressure

The mercury intrusion capillary pressure (MICP) method has been a viable tool for characterizing reservoir rocks for over 60 years (COMISKY *et al.,* 2011) and is based on the fact that mercury behaves as a non-wetting liquid when in contact with most solids. Consequently, it does not penetrate into the openings and cracks of these substances without the application of pressure. Figure 3.8 illustrates the cumulative pore structure acquired by Hg intrusion and respective stages of Hg invasion of the sample in the penetrometer. The pressure *(P_w)* required is a function of the contact angle *(θ_{Hg})* of mercury with the porous material to be intruded, its gas/liquid surface tension *(γ_{Hg})* and equivalent pore radius *(r_p).* This relationship is given by the Young-Laplace law for the particular case of cylindrical pores as the Washburn equation (KATE and GOKHALE, 2006):

$$r_p = -\frac{2\gamma_{Hg}\cos\theta_{Hg}}{P_W}. \tag{3.11}$$

This equation dictates that with increasing pressure, the mercury will intrude into progressively narrower pores for constant values of θ_{Hg} and γ_{Hg}. The volume of mercury invading the pores is measured directly as a function of applied pressure where the *P-V* data provides a unique characterization of the pore structure (ROOTARE and PRENZLOW, 1967). The elevated pressures reached by the MICP equipments nowadays make the evaluation of very small pores possible, although the integrity of the pore structure of analyzed medium is sometimes doubted and discussed in the literature. Nevertheless, the maximum pressure used in the present work was $P_w = 413$ MPa ($r_p \approx 20$ Å).

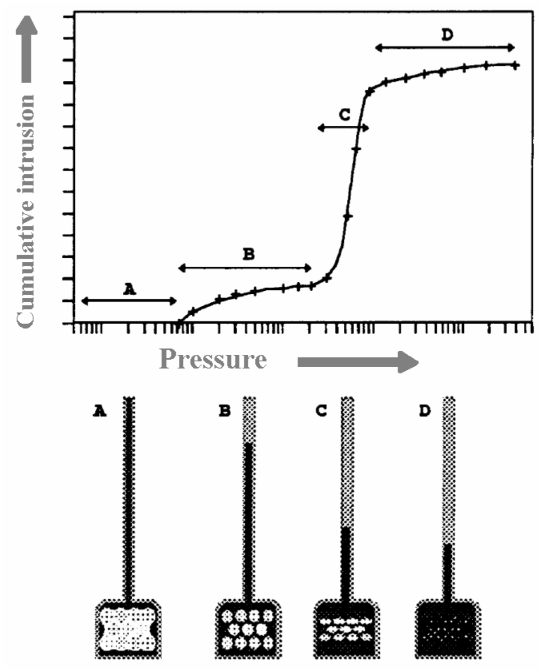

Figure 3.8: Hg volume versus pressure plot indicating structural strength (above) and respective states of Hg intrusion (in black) inside of pore sample in a penetrometer (below) (WEBB, 1993).

During the MICP experiments some issues can be encountered which create errors in the results. The two most likely sources of errors in MICP measurements are caused by mercury conformance at low pressures (COMISKY *et al.*, 2011) and system compressibility at high pressures (WEBB, 2001). Besides that another limitation on the results is related to the pore system geometry of natural materials such as reservoir rocks, being comprised by the so-called ink-bottle configuration. Therefore the pore system may be described as a system of large chambers (ink-bottle type pores) interconnected by smaller throats. In such a system pore network effects hence are assumed to be the most important reason for the large hysteresis between intrusion and extrusion in MICP experiments (KAUFMANN *et al.*, 2009); also a super estimation of the smaller pores (throat) in detriment of the bigger ones (FERNANDES, 1994) might be observed shifting the pore size distribution in the direction of the smaller pores. In Figure 3.9 a simplified model of pore system with ink-bottle type pores is assumed, allowing the visualization of pore filling aspects. As one can see, in (a) the pores connected to the surface are still empty; filling starts with the largest external surface connected pores as mercury is non-wetting and only with increasing pressure smaller pores are filled (a→b→c). Dark gray represents the pores already filled in a pressure step backward and light gray are the pores filled in a ahead pressure step. Ink-bottle type pores will not be filled at the pressure corresponding to their radius but at a higher pressure level which corresponds to the largest connecting radius. Relatively large voids or even small pores which are connected just through even smaller pores to the external surface may be filled at higher pressure as it would correspond to their actual size.

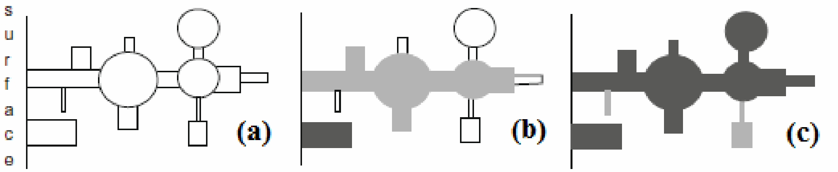

Figure 3.9: Scheme of an array of chambers which are connected by smaller throats (ink-bottle type pores) limitation the entrance of mercury in the bigger pores (KAUFMANN, 2009).

3.4. X-ray diffraction (XRD)

As known TGS and seal rocks are comprised by considerable amount of very fine grained structures that X-ray methods, rather than hand specimen or optical methods, are used to identify them. X-Ray diffraction is considered to be one of the best methods in defining clay minerals (ELGMATI, 2011).

In 1912 the German physicist Max Von Laue discovered the diffraction of X-rays on crystals as he related the passage of waves of light through a periodic, crystalline arrangement of particles. The principle of X-ray diffraction measurements originated afterwards from Bragg´s law formulated by Willian Henry Bragg and Willian Lawrence Bragg. Bragg´s law (1912) explains the relationship between an incident and its detected beams with respect to the examined sample as (BUHRKE *et al*., 1998):

$$n\lambda = 2d_{hkl}\sin\theta, \tag{3.12}$$

where n is an integer (i.e. 1, 2, 3…), λ is the wavelength of the incident X-ray beam, d_{hkl} is the distance between atomic layers in a crystal with the Müller index (hkl) and θ is the angle between the incident ray and the scattering planes. When X-ray radiation passes through matter, the radiation interacts with the electrons in the atoms, resulting in scattering of the radiation constructive and destructive interference will occur (FORMOSO, 1984). If the atoms are organized in planes (i.e., the matter is crystalline) and the distances between the atoms are of the same magnitude as the wavelength of the X-rays undergo constructive interference in accordance to Bragg's law. This result where X-rays are emitted at characteristic angles based on the spaces between the atoms organized in crystalline structures called plane is shown in Figure 3.10.

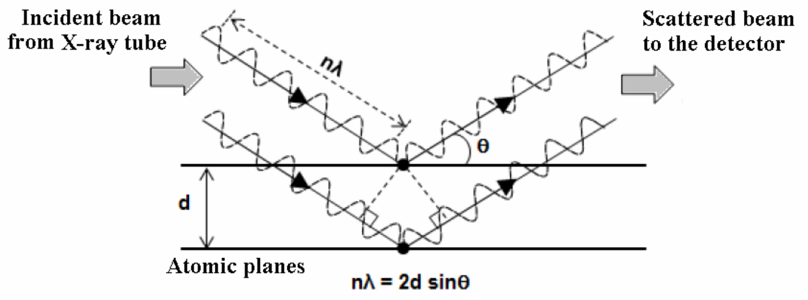

Figure 3.10: X-ray incident and scattered beam base on Bragg´s law (ELGMATI, 2011).

We used X-ray diffraction (XRD) to semi-quantify clay and non-clay minerals in the TGS from field A and in the three studied seal rocks.

3.5. Field emission scanning electron microscopy

Characterizing TGS formations remains daunting, because its microstructure presents unique challenges in measurement and description since the resources are typically located in heterogeneous and complex geologic systems (BUCTHER and LEMMENS, 2011). In TGS formations usually the hydrocarbons are trapped in rocks marked by poorly connected networks of pores with dimensions as small as a few nanometers; clays are commonly associated with this small grain size being highly variable and often associated to other minerals such as quartz, feldspar and calcite. In this context, the geometry and nature of the mineralogical components are easier to be described optically.

Table 3.1: Comparison of different electron optical modes of analysis commonly used for studies of clay mineral textures and compositions (modified from HUGGETT and SHAW, 1997).

Instrument	**Nature of sample**	**Primary function in clay studies**	**Spacial precision**
Field emission SEM (SE) (FESEM)	coated or un-coated fracture surface	morphology, diagenesis	0.5 nm
Conventional SEM (SE) (CSEM)	coated or un-coated fracture surface	morphology, diagenesis	2.5 nm
Backscattered SEM (BSEM)	polished, C-coated surface	petrography, diagenesis, chemistry	0.5 - 3 µm
Microprobe	polished, C-coated surface	chemistry	0.5 - 3 µm
Analytical electron microscopy (AEM)	ion-milled, dispersion mount	morphology, sedimentary microstructures, chemistry	>2.5 nm
High-resolution TEM	ion-milled, microtomed	lattice imaging, micro-diffraction, chemistry	0.3 nm

The scanning electron microscopy (SEM) permits the observations and characterization of heterogeneous organic and inorganic materials on a nanometer (nm) to micrometer (µm) scale (GOLDSTEIN *et al.* 2003). Table 3.1 compares the limitations of different optical modes for analyzing clay mineral fabrics and compositions. High-resolution field emission scanning electron microscopy (FESEM) is achieved through use of a field emission gun (FEG) in place of the more conventional tungsten hairpin or LaB6 filaments (HUGGETT and SHAW, 1997) where a resolution of 0.5 nm can be accomplished. For backscattered scanning electron microscopy (BSEM) the optimal resolution is 0.5 µm and 2.5 nm for conventional secondary electron microscopy (CSEM). In the SEM techniques, the microvolume to be analyzed is irradiated with a finely focused electron beam, which may be swept in a raster across the surface of the specimen to form images or may be static to obtain an analysis at one position. The types of signals produced from the interaction of the electron beam with the sample include secondary electrons, backscattered electrons, characteristic X-rays, and other protons of various energies. These signals are obtained from specific emission volumes within the sample and can be used to examine many characteristics of the sample (surface topology, crystallography, composition, etc) (GOLDSTEIN *et al.,* 2003). Figure 3.11 shows a schematic illustration of the interaction volume of incident electron beam within the analyzed material. It is possible to see the origin of distinct sources of generated electrons in the sample.

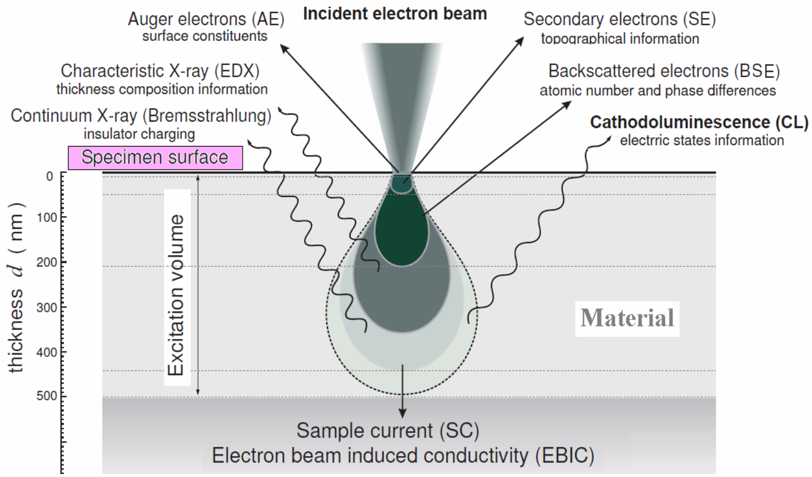

Figure 3.11: Schematic representation of processes resulting from electron bombardment showing the emissions coming from different depths, e.g. CL and X-rays are emitted from deeper section levels than the secondary electrons (SALH, 2011).

The number of backscattered electrons (BSE) produced from a given atom is proportional to the atomic number, thereby materials composed of heavy atoms will backscatter more electrons, resulting in brighter gray tones in the image relative to less dense materials. Hence, BSE produce an image that is related to material composition, providing both spatial and chemical information. With the use of backscattered scanning electron microscopy, e.g., it is possible to identify individual mineral constituents of the TGS and seal rocks by virtue of their atomic number (Z) contrast and differential hardness (relief). Valuable information can be obtained relating to particle form, orientation, texture, internal structure and mineralogical composition of the analyzed rock. On the other hand secondary electron images are acquired for documenting topographic variation within the rock.

In the present thesis we analyzed polished and fractured samples by SEM and FESEM techniques. Mechanically polishing TGS were selected to investigate mainly the microstructure (including pore morphology and porosity), composition, and mineral phases; while fractured samples provided new insight about the clays content and showing topographic variations. For this task, samples were examined using two equipments: a Philips (FEI) XL40 and a Zeiss Ultra Plus for respectively SEM and FESEM analysis. Both systems are located at the Australian Resources Research Centre: Perth, Western Australia. Use of FESEM equipped with in-lens secondary electron (SE) detectors provided greatly increased detail of nanometer-scale in analyzed TGS and seal rocks. Lower accelerating voltages (1–10 kV) were used to prevent beam damage of the sample which was also coated with carbon. Working distances were 3 to 10 mm.

3.6. X-ray computed tomography (CT)

The development of modern imaging methods relies on the acquisition of three-dimensional reconstructions from a series of two-dimensional projections taken at different angles: the sample is rotated and the absorption of X-rays in different directions is recorded and used to produce a three-dimensional representation of the rock and fluids (BLUNT *et al.,* 2013). X-ray computed tomography (CT) is an established and rapidly evolving technology of proven value for geological investigations. Because of its origin outside of the earth sciences, the potential for application of CT imagery to geological problems is only beginning to be explored (KETCHMAN and CARLSON, 2001). Typical X-ray energies are in the range 30–160 keV for microCT machines (with corresponding wavelengths 0.04-0.01 nm). Resolution is determined by the sample size, beam quality and the detector specifications; for cone-beam set-ups (in laboratory-based instruments) resolution is also controlled by the proximity of the sample to the beam, while detecting absorption at a sufficiently fine resolution. Current microCT and nanoCT scanners will produce images of around 1000^3-2000^3 voxels. To generate a representative image, the cores are normally a few mm across, constraining resolution to a few microns; sub-micron resolution is possible using specially designed instruments and smaller samples (BLUNT *et al.*, 2013).

3.6.1. Principles of image acquisition

Any image, seen in the microscope or taken by any type of camera or other device, has to be transferred into computer memory. This process is called image acquisition and can be performed in several ways (WOJNAR, 1998). There are numerous methods for digital image acquisition intending the characterization of materials where

Complementary Metal Oxide Semiconductors (CMOS) and Charge Coupled Device (CCD) are the most commonly used devices.

Computed Tomography (CT) technology involves taking a number of X-ray radiographs (projection images) at distinct angles by projecting an X-ray beam through a sample to be analyzed (object) (KUMAR *et al.*, 2011). When photons interact with solids and complex biological materials they are absorbed, scattered (elastic or inelastic), diffracted, refracted, or transmitted through the material. During absorption of photons, emission of electrons, visible light, and X-rays also takes place. At its most basic level, absorption of X-rays occur when an incoming X-ray photon is absorbed, and this results in the ejection of electrons from the inner shell of the atom, and the atom is ionized. The ionized atom will eventually return to its neutral state (filling the vacated spot in the inner shell) often with the emission of an X-ray characteristic of the atom (WILDENSCHILD and SHEPPARD, 2013). As the X-rays beams traverse through the object being scanned its energy is attenuated and the projection images are formatted on a detector. The attenuation of X-ray beam energy depends primarily on the density and thickness of the object in the beams path. The basic equation for attenuation of a mono-chromatic beam, i.e. one in which all photons have the same energy and wavelength, through a solid object is described by the Lambert-Beer's Law (KAK and SLANEY, 1999):

$$I = I_o \exp[-\mu x], \qquad \textbf{(3.13)}$$

where I is the X-ray beam intensity after passing through an object, I_0 is the initial X-ray intensity, μ is the linear attenuation coefficient for the material being scanned (units: 1/length), and x is the length of the X-ray path through the material, i.e. the thickness of the object in the direction of the X-ray beam. From Eq. (3.13) we see that I is a decreasing function of distance, x, (the exponential argument is negative), indicating that the incident X-rays, I_0, are attenuated as they pass through the object. Materials with a high attenuation coefficient will therefore allow X-rays to penetrate only a relatively short distance, whereas materials with a low attenuation coefficient are more easily penetrated (KETCHAM and CARLSON, 2001; WILDENSCHILD and SHEPPARD, 2013).

3.6.2. The basics of X-ray micro- and nanotomography

If both I_o and $I(x)$ can be measured from Eq. (3.13), it is possible to calculate the average linear attenuation coefficient of a material having *n* phases (a composite material such as rocks). To accurately identify and classify objects of different composition and density, sufficient variation in attenuation coefficients are needed. The gray level value of each pixel in each projection image is a representation of the net intensity *I* of the X-ray beam emerging out of the object in the direction along a line connecting the X-ray source to the image pixel. In other words, it represents the sum of attenuation coefficients of a number of tiny volume elements of the object lying along that direction of the beam. As shown in Figure 3.12, during acquisition of an X-ray micro- or nanoCT scan the sample is mounted on a high-resolution rotary stage and illuminated with X-rays.

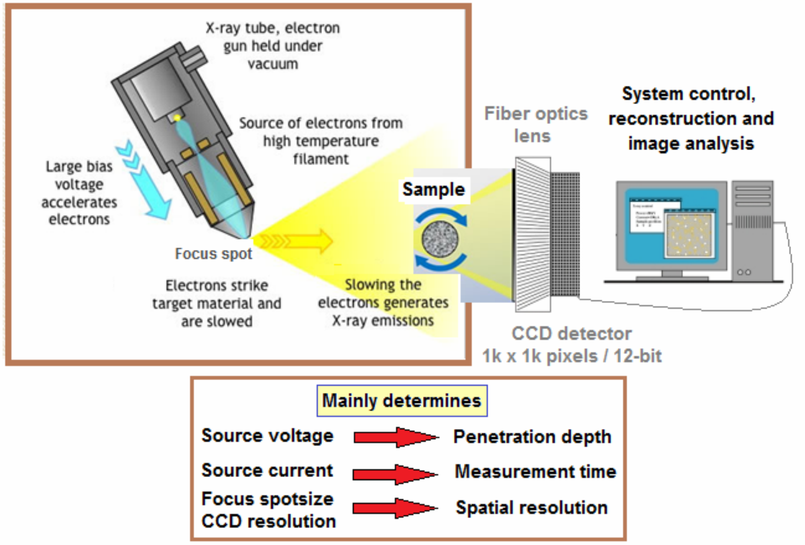

Figure 3.12: Scheme of a X-ray CT station.

Projections (radiographs) are typically collected at fixed and angular increments while the sample is either rotated continuously or step scanned. The total rotational angle depends upon the geometry of the sample and the beam, but typically is either 180° when a nearly parallel beam is used (typically at a synchrotron) or 360° for a cone-beam geometry (typically in a laboratory apparatus) (BAKER *et al.,* 2012). After passing through the sample the X-rays are then imaged with a 2D detector. The X-rays are normally converted into visible light by a scintillator screen. The visible light image is magnified with a lens and then detected by either a cooled CCD (charge-coupled device) camera or a CMOS-based detector. Each of these 2D radiographic projection, carrying the information of X-ray attenuation through different volume elements (voxels) are collected at different angles of the object and then combined together to reconstruct (back-calculate) the 3D volume of the analyzed specimen (KUMAR et al., 2011). The most used algorithm for reconstructing the 3D volume from a cone-beam microCT is based in Feldkamp, DAVIS and KRESS (1984) work.

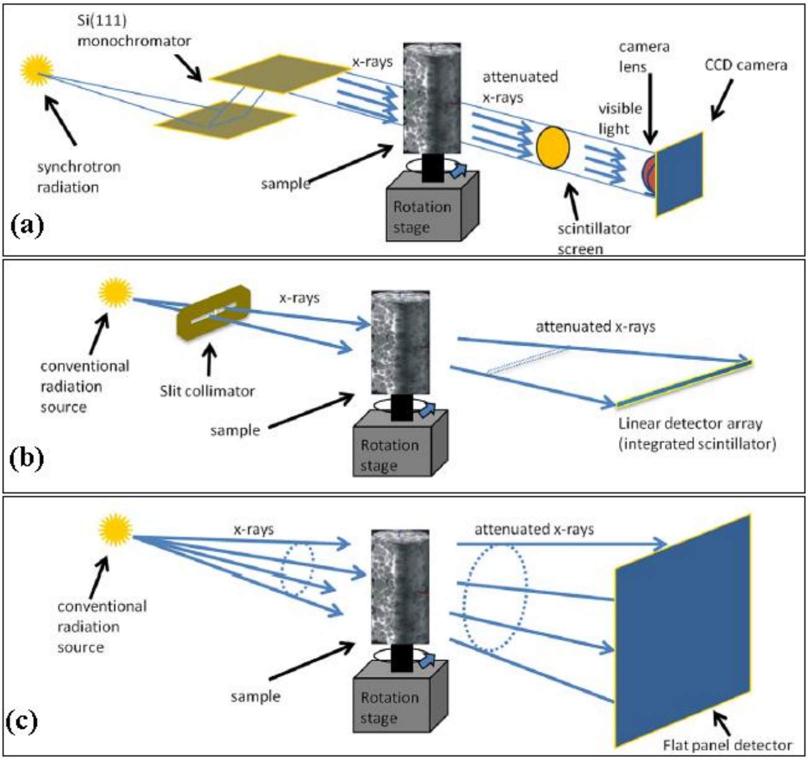

Figure 3.13: Typical tomography setup at a synchrotron beam-line(a) and for a microCT system with fan- (b) and cone- (c) beam configurations (WILDENSCHILD and SHEPPARD, 2013).

In 2001 Ketcham and Carlson point out the divergence in the calculation from Lambert-Beer law for industrials CT, as the precise form of the X-ray spectrum and its variation at off-center angles in a fan- or cone-beam, is usually only estimated theoretically rather than measured. However, the scintillation and detection devices used nowadays are very similar for the three types of systems (synchrotron, fan-beam and cone-beam) with any differences being due to the need to keep electronic components out of the beam-line at synchrotrons. Besides, the fact that geometric magnification from cone shaped beam (as the one used in the present work) allows efficient large area detectors to be used in lab-scale systems (WILDENSCHILD and SHEPPARD, 2013). The setup comparing synchrotron, fan-beam and cone-beam tomography imaging configuration according WILDENSCHILD and SHEPPARD (2013) is illustrated in Figure 3.13.

3.6.3. Evolution of microCT in material science

In the last few years micro computed tomography (microCT) a non-destructive imaging procedure has become an important technique for research of material properties (TORQUATO, 2000; YOUSSEF *et al.*, 2005; LIU and REGENAUER-LIEB, 2011). CT imaging was introduced in 1970s and was principally used for clinical and bio-medical purposes (BERA *et al.,* 2011). MicroCT, i.e., tomography imaging with a resolution in the order of µm came into existence in the early 1980s and was quickly extended to other fields like geology, electronics and composite materials (RITMAN, 2004; BERA *et al.*, 2011). Recent technology developments allow the 3D characterization of samples, up to few millimeters in diameter, at a detail resolution down to nanometer scale. This technology is what we call in the present work as nanoCT.

Despite being rather slow and expensive, the methodology has proved its worth, particularly in very important applications such as understanding the pore structure and transport properties of reservoir rocks for oil, gas and CO_2 geo-sequestration (YANG *et al.*, 2013). For reservoir engineering related applications, in this work we exposed tight gas sandstones (TGS) samples to X-ray microCT and nanoCT to determine information about its pore network morphology, down to the sub-microns order. One of the key steps for realistic pore space determination with the help of microCT and nanoCT techniques is the preparation of the samples for a given image resolution. For micron and/or nano scale resolution, one needs a very small sample size in the order of a few to sub-millimeters as shown in Figure 3.14 where a relation between sample size and image resolution is plotted for different 3D imaging techniques. As the resolution is very high, the field of view decreases proportionally (BERA *et al.*, 2011) so the sample diameter is selected as the maximum size which permits sufficient X-ray transmission for imaging (YANG *et al.*, 2013). In the present study all analyzed samples were manufactured as mini core samples to minimize losses. The diameters of mini cores were respectively 7 mm, 2 mm and 0.1 mm for resolutions of 0.7, 0.3 and 0.064 µm.

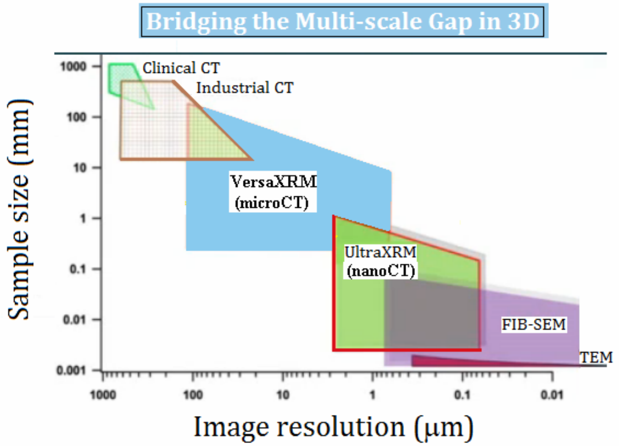

Figure 3.14: Relation between sample size and image resolution obtained by different 3D image techniques (courtesy from Carl Zeiss X-ray Microscopy, Inc).

3.6.4. Post-processing and 3D images analysis

Beyond visualization of the reconstructed sample volume via 3D rendering procedures, the main purpose of image processing is the quantitative characterization of data volumes (BAKER *et al.,* 2012). A number of parameters related to the microstructure can be extracted from an X-ray CT data set when the coherence of the X-ray beam and the spatial resolution are adequate to resolve the features of interest in the analyzed material. In geosciences, the geometry and organization of rock components, such as pores or fractures, and zones with chemical alteration or with different compositions, are the main interest by performing X-ray micro- and nanoCT analysis. In our particular case of low-permeability TGS, micro- and nanoCT were used to image and quantify the textural and morphological characteristics of the rock constituents, such as porosity, pore size distribution, geometry and orientation of pores and specific surface. The tortuosity which describes the topology of the overall pore and pore-throat networks (BAKER *et al.,* 2012) was also measured.

Prior to the quantification and morphological analysis of the 3D reconstructed images is the selection of a region of interest (ROI) of the sample. The ROI should be large enough to be representative of the sample complexity and heterogeneity (i.e., a representative elementary volume), but small enough to not overwhelm the available computing resources (BAKER *et al.*, 2012). After extracting a ROI, processing step involving the application of one or more grayscale-to-grayscale filters can also be performed. These filters are applied to reduce noise and eliminate artifacts, enhance object edges, and increase the visibility of different phases based upon their X-ray attenuation (BAKER *et al.,* 2012). Next step is to procedure the segmentation. One of the most straightforward techniques to segment a gray-scale CT image into a binary (or two-level) image is to define a threshold value. Traditionally, accomplishing a segmentation based in thresholding is to define a range of brightness values in the original image, select the pixel within this range as belonging to the foreground, and reject all of the other pixels to the background. Voxels with a gray value lower than that threshold value are considered to be the material phase to be analyzed (most cases pores). Following segmentation, a cleaning procedure using morphological operations can be applied to remove e.g. small numbers of pixels supposed not to be of interest, which are caused by artifacts. Once the segmented volume has been extracted microstructural information of individual or connected objects of interest can be quantified. From this data, conclusions may be drawn as to the effect of pore network on the transport properties (BLUNT *et al.*, 2002; AL-KHARUSI and BLUNT, 2007) as permeability of tight sandstones as unconventional resource.

3.6.5. Permeability modeling based upon CT reconstructions

In addition to quantifying and evaluating pore structure information, X-ray CT datasets can be used as a basis for permeability simulations, still in its infancy in geosciences (BAKER *et al.*, 2012). Permeabilities can be calculated by combining lattice-Boltzmann simulations with microCT reconstructions that have been segmented into fluid-containing vesicles (pores) and solid matrix. The lattice-Boltzmann (LB) method simulates continuum fluid flow by modeling gas-molecule collisions on a lattice (DOS SANTOS *et al.*, 2005) and it yields approximate solutions of the unsteady, incompressible Navier-Stokes equations furnishing the fluid velocity and stress on the lattice at discrete time points (BAKER *et al.*, 2012). Nonetheless, there is still a lack in the studies of permeability modeling based upon CT reconstructions for unconventional reservoirs, especially for TGS in µDarcy order as the ones analyzed in this thesis. To point out, e.g., TIWARI *et al.* (2013) recently published a work in which they characterize oil shale pore structure before and after pyrolysis by using X-ray microCT. The 3D pore network structure had pores as large as 500 µm generated after pyrolysis and the results of permeability found by LB simulation were from 173 to 2919 Darcy due to the considerable amount of fractures generated.

Figure 3.15 illustrates, according to BAKER *et al.* (2012), a transformation from a microCT image to a permeability simulation.

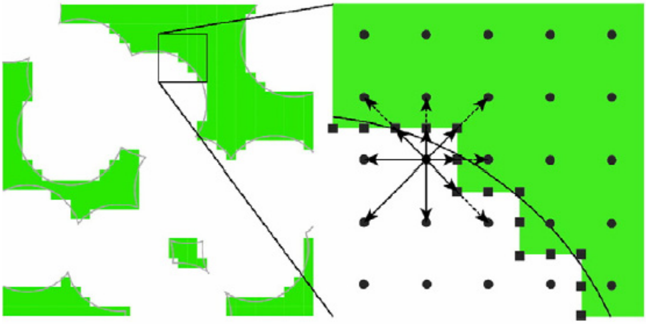

Figure 3.15: LB simulations from CT image. On the left side, a segmented image is shown with the true shape of the vesicles superimposed on white (pores) and green (solid) voxels. Enlarged on the right side are representative lattice nodes and the discrete fluid particle velocities; the mean fluid velocity and stresses are obtained from moments of this discrete velocity distribution. Note that particles are "bounced back" when they intercept a boundary node (squares), thereby enforcing a no-slip condition at the fluid-solid interface (BAKER *et al.*, 2012).

In this figure one can see a thresholded image ROI is converted to a binary image comprised by distinct voxels either a pore (white) or solid (green), with its center at a lattice node (circles in the figure). Fluid "particles" at every lattice node can move in distinct directions to the nearest and next-nearest nodes on a 3D cubic lattice. At each time step, collision and streaming steps relax the discrete fluid-particle velocity distribution toward equilibrium, while conserving mass and momentum. Moments of the particle velocity distribution furnish the velocity and stress; and nodes that are separated by a fluid-solid interface are "bounced back", thereby achieving a no-slip boundary condition at the boundary nodes (squares in Figure 3.15). Note that fluid within every domain that is enclosed by boundary nodes (i.e., the solid) develops a hydrostatic pressure when a steady uniform body force is applied to all lattice nodes. After reaching steady state, which typically occurs in $O(10^4)$ lattice-Boltzmann time steps (depending on the porosity and fluid viscosity), the permeability is calculated as the product of the fluid viscosity and the ratio of the steady superficial fluid velocity to the mean pressure gradient. One challenge for these simulations is to obtain sample volumes that are large enough and have adequate spatial resolution but small enough to not overwhelm the available computing resources. The size of X-ray tomograms with micron-scale spatial resolution is limited by X-ray beam dimensions and detector size. Furthermore, simulation time becomes prohibitive on a single processor with more than $O(100^3)$ lattice nodes (BAKER *et al.*, 2012).

3.7. Low-field nuclear magnetic resonance

For the past decades the nuclear magnetic resonance (NMR) technology has gained acceptance as a petrophysical tool for evaluating reservoir properties (CAI *et al.*, 2013). NMR has been widely used, e. g., in petrophysical characterization of sandstones and carbonates (MARSCHALL *et al.*, 1995; YAO *et al.*, 2010), although little attention has been paid in the use of this technique concerning to the study of petrophysical properties of tight gas sandstones.

Low-field nuclear magnetic resonance spectrometers were developed currently with logging tools so that wellbore measurements could be duplicated on core samples in the laboratory (GRIFFIN *et al.*, 1993). The low frequency NMR spin–spin relaxation time (T_2) distributions have been routinely applied in the petroleum industry to characterize rock matrix and measure downhole fluid properties (HIRASAKI *et al.*, 2003). NMR analysis can be performed in both the saturated and partially saturated states samples. In the laboratory NMR studies are routinely conducted for the following purposes (WIKIPETRO – NMR Petrophysics):

- Verifying formation porosity;
- Evaluating textural effects, such as microporosity, on NMR-log response;
- Determining formation-specific models that enhance the accuracy of determining bulk-volume-irreducible (BVI) water, free-fluid index (FFI), and, ultimately, permeability;

- Developing models to identify and quantify hydrocarbons, including residual oil;
- Developing models to predict changes in pore size (facies).

The connection between NMR measurements and petrophysical parameters stems from the strong effect that the rock surface has in promoting magnetic decay of saturating fluids. Therefore, a brief survey on the principles and the applicability of low-field NMR in structural studies of reservoir rocks is presented following.

3.7.1. Principles of NMR

The NMR phenomenon is based on the fact that nuclei of atoms have magnetic properties that can be utilized to yield chemical information. Quantum mechanically subatomic particles (protons, neutrons and electrons) have spin. In some atoms (e. g. ^{12}C, ^{16}O, ^{32}S) the spins are paired and cancel each other out so that the nucleus of the atom has no overall spin. However, in many atoms such as ^{1}H, ^{13}C, ^{31}P, ^{15}N, ^{19}F the nucleus does possess an overall spin (EDWARDS, 2010). In this matter, NMR measurements can be made on any nucleus that has an odd number of protons or neutrons or both. Hydrogen, which has only one proton and no neutrons, is abundant in both water and hydrocarbons, has a relatively large magnetic moment, and produces a strong signal (COATES *et al.*, 1999). Following the monograph “NMR Logging: principles & applications.” by COATES *et al.* (1999), the concepts in fundamentals of NMR physics can be found to be: nuclear magnetism, polarization, T_1 and T_2 relaxation times, pulse tipping, free induction decay and spin echoes and CMPG pulse sequences.

3.7.1.1. Polarization

The first step in a NMR measurement consists in aligning magnetic nuclei with a static magnetic field, B_0. When B_0 is applied to a magnetic nucleus, B_0 exerts a torque on the nucleus that acts to align the nuclear spin axis with B_0. When a torque is applied to a spinning object, the axis of the object moves perpendicular to the torque in a motion called precession (Figure 3.16, left). Thus, when B_0 is applied to a magnetic nucleus, the nucleus will precess around B_0. The precessional frequency (f) is called the Larmor frequency and given by:

$$f = \frac{\gamma B_o}{2\pi}, \tag{3.14}$$

where γ is the gyromagnetic ratio, a measure of the strength of the nuclear magnetism. For hydrogen, $\gamma/2\pi$ = 42.58 MHz/tesla. For a given magnetic field, different nuclear species have different Larmor frequencies; therefore, the various species can be differentiated on the basis of these frequencies. Alternatively, for a given nuclear species, such as hydrogen, γ has a fixed value being the Larmor frequency is a function of the strength of the static magnetic field.

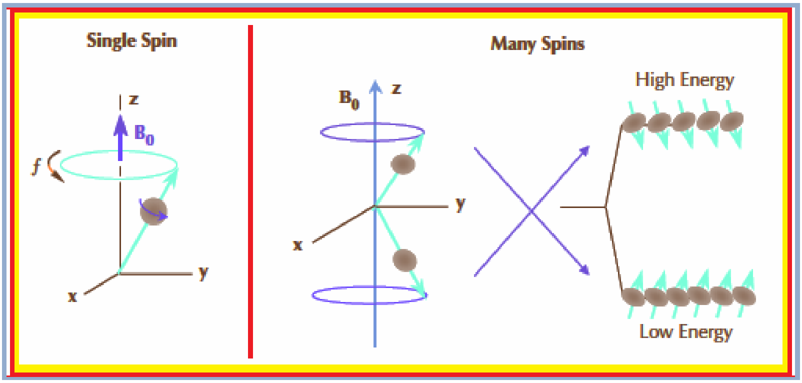

Figure 3.16: Under external magnetic field application (left), the precessional frequency of a nucleus will depend on its gyromagnetic ratio and the strength of this field. The alignment of the precessional axis of the nucleus with respect to the direction of the external field (right) will determine the energy state of the nucleus (COATES *et al*., 1999).

According to quantum mechanics, when a proton is subjected to an external magnetic field it is forced into one of two energy states as shown in Figure 3.16 (right). This energy state of a particular proton depends on the orientation of the precessional axis of the proton with respect to the direction of the external field. When the precessional axis is parallel to B_0, the proton is in the low-energy state, which is the preferred state. When the precessional axis is anti-parallel to B_0, the proton is in the high-energy state. The direction of B_0 is designated as the longitudinal direction.

When a large number of spinning protons are precessing about B_0, more spins are precessing parallel to B_0 than anti-parallel (COATES, *et al*., 1999). The difference between the number of protons aligned parallel and anti-parallel to the B_0 field forms the bulk magnetization M_0 that provides the signal measured by a NMR device. Therefore, the macroscopic magnetization M_0 is defined as the net magnetic moment per unit volume, given by the Curie's Law for the case of N nuclei per unit volume:

$$M_o = N\frac{\gamma^2 h^2 I(I+1)}{3(4\pi^2)kT}B_o, \qquad \textbf{(3.15)}$$

with k being the Boltzman's constant, T the absolute temperature in Kelvin; h the Planck's constant and I the spin quantum number of the nucleus.

3.7.1.2. Pulse tipping and free induction decay

The second step performed in a NMR measurement is to tip the magnetization from the longitudinal direction to a transverse plane. This tipping is accomplished by applying an oscillating magnetic field (B_1) perpendicular to B_0. For effective tipping, the frequency of B_1 must be equal the Larmor frequency of the protons relative to B_0. From the quantum mechanics view, if a proton is at the low-energy state, it may absorb energy provided by B_1 and jump to the high-energy state. The application of B_1 also causes the protons to precess in phase with one another. This change in energy state and in-phase precession caused by B_1 is called nuclear magnetic resonance.

The B_1 field used in NMR logging is a pulsed oscillating magnetic field. Macroscopically, magnetization is tipped 90° B_1 pulse and precesses in the transverse plane. When the B_1 field is turned off, the proton population begins to lose phase coherency (diphase), i.e., the precessions of the protons will no longer be in phase with one another. Therefore, a receiver coil that measures magnetization in the transverse direction will detect a decaying signal, usually exponential and called free induction decay (FID). The FID time constant (T_2^*) is very short (in the microseconds order) and caused by magnetic-field inhomogeneity, (ΔH), that are due to the magnetic field gradient and to certain molecular processes that occur in the measured material (COATES, *et al.*, 1999). In rocks, the internal gradients that degrade the measurements (G) resulting from field inhomogeneity are a complicated function of microgeometry but are on the order of ΔH divided by the grain size (STRALEY *et al.,* 1997).

3.7.1.3. Spin echo detection and CPMG sequence

The dephasing discussed about is reversible once the proton magnetization vectors in the transverse planes can be re-phased when a 180° B_1 pulse is applied. Considering that if a transverse magnetization vector has phase angle α, then application of a 180° B_1 pulse will change the phase angle to $-\alpha$. In effect, the phase order of the transverse magnetization vectors is reversed, so that the slower vectors are ahead of the faster vectors. When the faster vectors overtake the slower vectors the rephrasing occurs and a signal is generated, see analogy in Figure 3.17. This signal is called a "spin echo" or "Hahn echo" and its intensity depends only of the intrinsic T_2 sample. The same time τ transpired between the application of the 90° B_1 pulse and the 180° B_1 pulse will transpire between the application of the 180° B_1 pulse and the peak of the spin-echo, so the spin echo peak occurs at 2τ. This process of rephrasing (encoding) time equals dephasing (decoding) time defines the inter-eco spacing (TE) and it is illustrated in Figure 3.18(a) which also shows that although a single spin echo decays very quickly, 180° pulses can be applied repeatedly to rephase the magnetization components and generate a series of spin echoes. The number of pulses in a pulse train is called NE. The entire pulse sequence of a 90° B_1 pulse followed by a long series of 180° B_1 pulses is called a CPMG sequence after, Carr, Purcell, Meiboom, and Gill (COATES *et al.*, 1999; CHEN *et al.*, 2002).

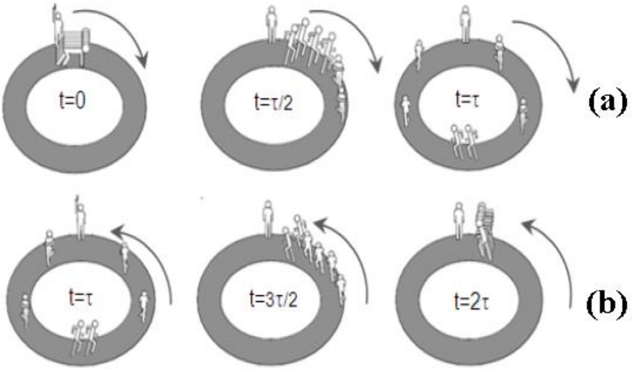

Figure 3.17: Analogy of dephasing process: (a) After departure the runners are dispersed (rephase); (b) Reversing the direction (180° B_1 pulse), they can arrive together (dephasing) (DA SILVA JÚNIOR, 2013).

During a CPMG sequence, the 90° B_1 pulse reorients the polarization so that there is no longer any longitudinal polarization of the protons, and the 180° B_1 pulses suppress the buildup of new longitudinal polarization. Hence, the protons are completely randomized at the end of a CPMG sequence. To start the next CPMG sequence, the protons must be polarized again, so a waiting time (TW) during which repolarization occurs is necessary. In Figure 3.18(b) a typical NMR measurement timing diagram is illustrated. In the upper section of this figure two CPMG sequences are shown with each consisting of a 90° B_1 pulse, followed by a series of 180° B_1 pulses. In the bottom polarization events (T_1 relaxation curves) and the spin-echo trains (T_2 relaxation curves) associated with two CPMG sequences are occurring, where T_2 is obtained from the fitting of the generated curve by the maximal amplitude of the spin echoes. In this thesis one-dimensional CPMG experiments were performed to obtain transverse relaxation decays, which were subsequently inverted by one-dimensional inverse Laplace transformation (GODEFROY and CALLAGHAN, 2003; HOLMES, 2012) to obtain a transverse relaxation time distribution of T_2.

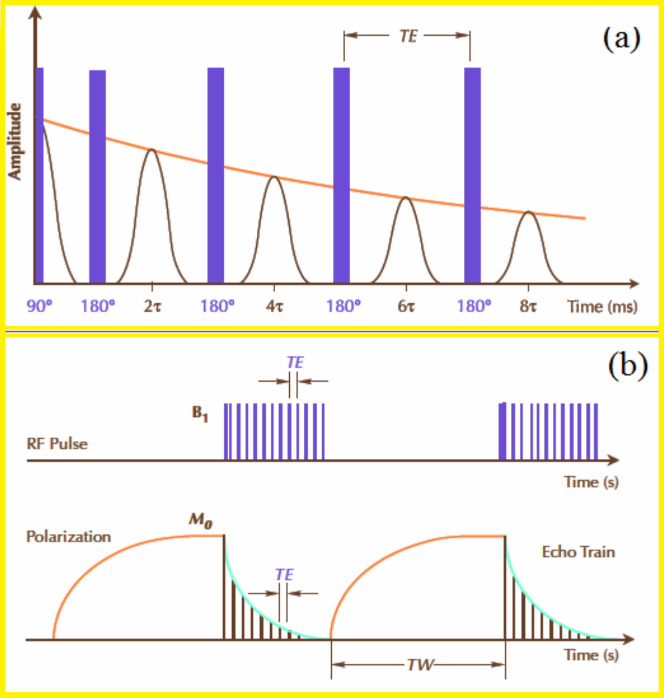

Figure 3.18: CPMG pulse sequence used for generating a spin-echo train where spin-echoes of decreasing amplitude follow the 180° B1 pulses (a). (b) NMR measurement timing diagram showing (top) CPMG pulse sequences and (bottom) polarization *(T_1)* curves and spin-echo train acquisition (COATES et al., 1999).

Simply put, the low-field NMR procedure measures three properties: the equilibrium nuclear magnetization, M_{eq} and the two principal NMR relaxation times, T_1 (longitudinal relaxation time) and T_2 (transverse relaxation time). M_n is proportional to the fluid-filled porosity, and T_1 and T_2 have been correlated with petrophysical properties such as pore size, producible fluid, and permeability. Although T_1 measurements are more common in the literature, they are more time consuming to measure than T_2 measurements (STRALEY *et al.,* 1997). Hence, the parameter T_2 is widely obtained in CPMG sequences and also the measured parameter in this work.

3.7.2. Multi-exponential decay and properties in reservoir rocks

Reservoir rocks commonly exhibit a distribution of pore sizes and frequently contain more than one fluid type. Therefore, the spin echo train (transverse magnetization measurements) recorded with a CPMG sequence does not decay with a single T_2 value but instead with a distribution of T_2 values that can be described by:

$$M(t) = \sum M_i(0) e^{-\frac{t}{T_{2i}}}, \tag{3.16}$$

where $M(t)$ is the measured magnetization at time t, $M_i(0)$ is the initial magnetization from the i^{th} component of relaxation; T_{2i} is the decay constant of the i^{th} component of transverse relaxation and the summation is over the whole sample; i.e., all pores and all different types of fluid. Figure 3.19 illustrates the multi-exponential decay character of a porous medium containing pores of different sizes and a single wetting phase. Surface to volume ratio (*S/V)* becomes dominant when a short inter echo spacing is used and the formation is only brine-saturated. Under this condition, T_2 is directly proportional to the pore size. When all pores are assumed to have the similar geometric shape, the largest pores (in the left column) have the lowest *S/V* and thus the longest T_2 value, while the smallest pores have the highest *S/V* and the shortest T_2 values. For a single pore, the magnetization decays exponentially, and the signal amplitude is given by:

$$M(t) = M_0 e^{-\rho_2 \left(\frac{S}{V}\right) t}, \tag{3.17}$$

where ρ_2 is the surface relaxivity and M_0 is proportional to the volume of fluid in the pore. When the complete distribution (bottom of Figure 3.19) of the 100% water-saturated pores is considered, these pores exhibit a distribution of T_2 values.

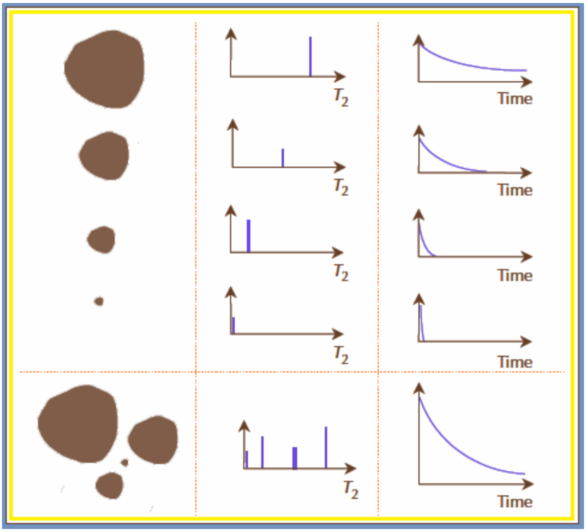

Figure 3.19: A 100% water-saturated pore (upper left) has a single T_2 value that depends on pore size, and thus its spin-echo train exhibits a single-exponential decay (upper right) that also depends on pore size. Multiple pores at 100% water saturation (bottom left) have multiple T_2 values that depend on the pore sizes, and thus their composite spin-echo train exhibits multi-exponential decay (bottom right) (COATES *et al.*, 1999).

The associated signal amplitude is the sum of the signal amplitudes arising from the fluid in individual pores, and the signal amplitude is given by:

$$M(t) = \sum M_{0i} e^{-\rho_2 \left(\frac{S}{V}\right)_i t}, \tag{3.18}$$

where $(S/V)_i$ is the surface-to-volume ratio of the i^{th} pore. Obviously,

$$M(0) = \sum M_{0i}. \tag{3.19}$$

If the measured magnetization for 100% bulk water with the same sensitive volume, $M_{100\%}(0)$, is known, then $M(0)$ and M_{0i} can be calibrated to porosity:

$$\phi = \frac{M(0)}{M_{100\%}(0)} = \frac{\sum M_{0i}}{M_{100\%}(0)} = \sum \frac{M_{0i}}{M_{100\%}(0)} = \sum \phi_i, \tag{3.20}$$

where: ϕ is the calibrated porosity of the formation, ϕ_i is the calibrated porosity associated with all pores of the i^{th} pore size (the incremental porosity). Therefore, the T_2 distribution (in the form of the amplitudes M_{0i} associated with the time constants T_{2i}) can be calibrated to the porosity distribution considering the individual pores ϕ_i with the associated time constants T_{2i}.

The fact that NMR porosity depends only on the fluid contents of the sample makes its measurements very capable to furnish connected and unconnected porosities. The strength of the NMR signal is proportional to the number of hydrogen atoms in a NMR tool-dependent rock volume (HAMADA *et al.*, 2001). For water, oil and gas, NMR results can be expressed as the percentage of fluid volume in the rock volume (MENGER and PRAMMER, 1998). Figure 3.20 shows, in a qualitative way, the NMR properties of different fluids that can be found in the pore space (COATES *et al*, 1999). Hence, to allow reliable fluid typing, linear gradient field NMR tools have to be capable of measuring relaxation times from less than 1 ms to several seconds (HAMADA *et al.*, 2001). As one can see in Figure 3.20, clay-bound water, capillary-bound water, and movable water occupy different pore sizes and locations. Hydrocarbon fluids differ from brine in their locations in the pore space, usually occupying the larger pores. In general, bound fluids have very short T_1 and T_2 times, along with slow diffusion *(D)* that is due to the restriction of molecular movement in small pores, behavior that we expect to find in unconventional reservoir rocks such as the tight gas sandstones analyzed in this work. Free water commonly exhibits medium T_1, T_2, and D values. Natural gas exhibits very long T_1 times but short T_2 times and a single-exponential type of relaxation decay. NMR characteristics of oils dependent manly on oil viscosities, lighter oils are highly diffusive, have long T_1 and T_2 times, and often exhibit a single-exponential decay. Based on the unique NMR characteristics of the signals from the pore fluids, applications have been developed to identify and, in some cases, quantify the type of hydrocarbon present (COATES *et al.*, 1999). However, in this work NMR is used only to analyze the pore structure of cleaned tight gas sandstones samples 100% saturated under NaCl brines of 10 g/l salinity.

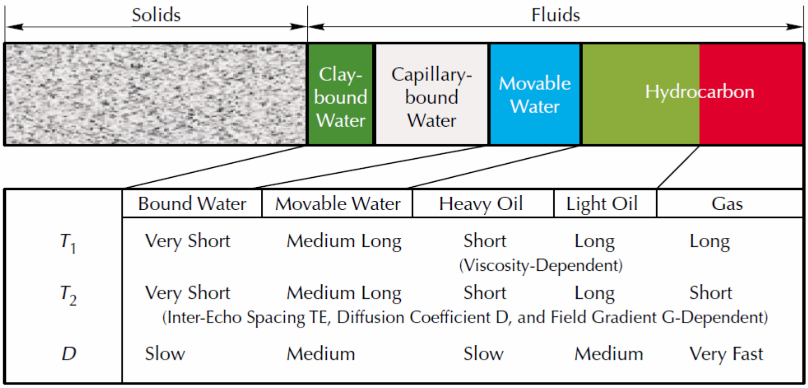

Figure 3.20: T_1, T_2 and diffusion (NMR parameters) according to Coates *et al.,* (1999), for different fluid types and pore sizes demonstrating the variability and complexity of the T_1 and T_2 relaxation measurements.

3.7.3. Transforming a T_2 distribution to a pore size distribution

The essential information on rock or sedimentary samples, which can be provided by low-field NMR, is the size distribution of fluid-filled pores (CHEN *et al.*, 2002). As already stated above, theoretically, pulsed NMR applied in the present work measures the magnetization *(M)* and the transverse relaxation time *(T_2)* of hydrogen nuclei contained in the pore fluids. The measurement of T_2 relaxation is preferred as it is fast and usually provides similar distribution to T_1 (KLEINBERG *et al.*, 1993; YAO *et al.*, 2010). For fluids confined in pores, the T_2 value can be shorter than that of the bulk fluid if the fluid interacts with the rock surface, which promotes NMR relaxation (KENYON *et al.*, 1992). Three different mechanisms, which operate in parallel, contribute to the overall apparent relaxation rate *($1/T_{2A}$)* of fluid in porous media (CHEN *et al.*, 2002):

$$\frac{1}{T_{2A}} = \frac{1}{T_{2B}} + \frac{1}{T_{2S}} + \frac{1}{T_{2D}}. \qquad \textbf{(3.21)}$$

The subscripts A, B, S and D indicate respectively: apparent, bulk, surface-induced, and diffusion-induced mechanisms. The bulk relaxation time is a property of the fluid only. Because the relaxation time of liquid in rocks is much shorter than the relaxation time of bulk liquid, the bulk term above can be neglected. The surface-induced relaxation (due to interaction between fluid and the solid surface) and diffusion-induced relaxation rates are given by (COATES *et al.,* 1999; CHEN *et al.,* 2002):

$$\frac{1}{T_{2S}} = \rho_2 \frac{S}{V}, \tag{3.22}$$

$$\frac{1}{T_{2D}} = \frac{(\gamma G \tau)^2 D_o}{12}, \tag{3.23}$$

where γ is the gyromagnetic ratio, G is an internal magnetic field gradient, τ is the echo time and D_o is the self-diffusion coefficient of the liquid. For low frequency and short pulse spacing, T_2 carries the same pore information as T_1, and diffusion relaxation can be reduced when a low and uniform magnetic field and a short pulse spacing is used (YAO *et al.*, 2010). In the present work we used low-field NMR technique, thus, the NMR T_2 relaxation examined is mainly attributed to surface relaxation, which occurs at the interface between water and rock grains. Under this condition the enhancement in T_2 decay coming from diffusion in the inhomogeneous local magnetic fields is negligible compared with the surface relaxation mechanism. Therefore, according to KENYON (1992) and KLEINBERG (1996) the measured T_2 values are a function of the surface to volume ratio of pores given by:

$$\frac{1}{T_2} = \rho_2 \left(\frac{S}{V}\right), \tag{3.24}$$

where T_2 is the transverse relaxation time resulting from surface interactions and ρ_2 is a constant representing the transverse relaxation strength. As T_2 is proportional to V/S, which in turn is proportional to pore size in rock samples, this means that in small pores relaxation is faster than in large pores as shown in Equation (3.24).

A rock generally consists of a large number of pores of different sizes. When two or three fluid phases are present, however, the non-wetting phases occupy the larger pores while the wetting phase occupies the smaller pores because of the capillary effect. In addition, the relaxation rate of non-wetting fluids is smaller than that of wetting fluids because the T_2 of non-wetting fluid does not include the surface term. Both the capillary and surface effect result in shorter T_2 for wetting-phase fluids compared to the T_2 for the same fluid types in bulk. Much less change is expected for the non-wetting fluid T_2. Thus, different fluid phases can be identified by carefully analyzing the T_2 distribution for multiphase saturation cases, not the case of present thesis where cleaned samples saturated with water were analyzed.

In conventional reservoir, NMR has the capacity to sense fluids in the pore space pretty much independent of lithology. The strength of the NMR signal is directly proportional to the number of hydrogen atoms present which provides a direct porosity measurement in brine saturated rocks. The relaxation time in the fast diffusion limit can be directly related to the pore body containing the fluid. On the other hand, because in unconventional reservoir (like shale and TGS), the porosities are typically much smaller than in other reservoir rocks, the signal strength is very weak. E.g., in a situation where there is a significant fraction of components with T_2 of 1 ms or shorter, the CPMG with τ of 1 ms will underestimate the contribution from this part (smaller pores) in an ordinary T_2 distribution. Therefore, as one can see from Eq. (3.23) a way to include signal and information that is initially lost or weighted differently with a bigger τ value is simply to use smaller τ values. According to SONDERGELD *et al.* (2010), for a fully saturated Berea sandstone plug only 24 scans are required for accurate porosity measurement while an equivalent shale measurement 10,000 scans need to be taken. Small pore size equates to fast T_2 relaxation time (SONDERGELD, *et al.,* 2010). A typical T_2 relaxation spectrum for AR gas shale is shown in Figure 3.21(a) (SONDERGELD, *et al.,* 2010) where most of the signal occurs below the 3 ms cutoff (red vertical line) for “clay bound” water. The authors used a surface relaxivity conversion of 0.05 µm/ms and found consistent results of body pore sizes distribution with SEM observations. Figure 3.21(b) illustrates the contributions of T_2 components using distinct motional encoding/ decoding intervals, τ, from a CPMG sequence in a brine saturated rock core sample (SORLAND *et al.*, 2007). As one can see the usage of high τ values might not represent the complete T_2 distribution of the system.

To assure the investigation of the smaller pores associated with the clay content for the analyzed TGS, a total of 250 scans were performed in small rock plugs (7 mm x 7 mm) using distinct intervals of τ data points, ranging from 0.01 to 5000 ms. A Maran Ultra 23 MHz (0.5 Tesla) instrument was used to acquire data. In general, spectrometer frequencies are specified using two parameters, a fixed number that depends on the magnetic field strength of the instrument and the observed nuclei, and a user adjustable offset that is added to the fixed number to give the frequency of the transmitted pulse. The spectral width is adjusted to be just large enough to span all of the resonance lines in the spectrum. The used 23 MHz NMR Spectrometer had a 10 mm NMR tube where the cylindrical samples were added.

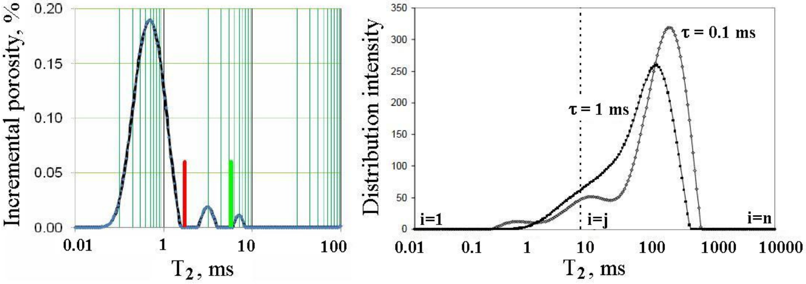

(a) **(b)**

Figure 3.21: (a) A typical T_2 relaxation spectrum for a gas shale, 10,000 scans, $\phi = 7.1\%$ (SONDERGELD *et al*., 2010); (b) T_2 distributions of a brine saturated rock core sample at two t values (SORLAND *et al*., 2007).

3.8. Photoacoustic spectroscopy and thermal diffusivity

The thermal diffusivity, *(α)*, of a material is defined as:

$$\alpha = \frac{K}{C_p \rho} \tag{3.25}$$

where K is the thermal conductivity, C_p is the specific heat and ρ is the mass density.

Thermal diffusivity is a dynamic thermal property which characterizes heat conduction inside a material under non-stationary conditions; this characteristic makes the thermal property essential for the study and modeling of thermal processes (ANDREW, 1986; BALDERAS-LÓPEZ, 2006). Thermal diffusivities of rocks are generally strong functions of temperature, values decreasing with increasing temperature (SOMERTON, 1992). VOSTEEN and SCHELLSCHMIDT (2003) studing magmatic, metamorphic and sedimentary rocks, observed that in the interval of temperature range of 1-300 ^{o}C, the thermal conductivity decreases between 25% and 44% and the thermal diffusivity however by 42–54%. The rate of the heat flow, and hence how deep the changes in the temperature at the surface penetrate, depends on α (SMITH, 2001). So in the context of the petroleum reservoir engineering, for a same geologic formation, the increase of temperature with depth would be favorable to the efficiency of seal rocks but decrease the flow rate for the petroleum exploration. The thermal diffusivity is directly related to the thermal conductivity and rock thermal conductivity within any geothermal reservoir is a key parameter to the conductive heat flow, to the distribution of temperatures and to the definition of a barrier to hold the accumulated energy (ARRIAGA, 1993). The thermal conductivity of volcanic rocks depends mainly on the characteristics of its mineral elements, on the conductivity of the fluids filling the pores and on the size and geometry of the pore space (ZIMMERMAN, 1988). In the present thesis we apply the photoacoustic spectroscopy technology (PAS) in an open photoacoustic cell (OPC) to investigate the thermal diffusivity of seal rocks originating from three different geologic fields. The obtained results were correlated within mineralogy and pore structures of analyzed rocks.

3.8.1. PAS signal and mechanisms

When a modulated light beam impinges on the material inside a photoacoustic gas cell, the absorbed light is converted into periodic heat and a PAS signal is created. The dependence of the PAS signal on the optical absorption coefficient and the light-to-heat conversion efficiency may be used to calculate the nonradiative de-excitation efficiency and to study the photoinduced energy conversion process. The PAS signal is directly proportional to the light-to-heat conversion efficiency due to nonradiative processes in the material (ZIEGLER and HASSELMAN, 1981). After the work of Rosencwaig and Gersho (1976), the PAS effect has been used for measuring the thermal properties of solid samples in different material science areas such as semiconductors (DE LIMA *et al.,* 2007; POFFO *et al.*, 2011); metals (LIMA *et al.,* 2005; ROUSSET *et al.*, 1983); polymers (LACHAINE and POULET, 1984); sedimentary rocks (GUIMARÃES *et al.*, 2013) and coals (BISWAS *et al.*, 1983). As well as coal, being an opaque material which highly absorbs the incident light, seal rocks are extremely heterogeneous materials and constituted of a very fine porous structure. It is well known that the elastic and thermal properties of microscopically inhomogeneous materials are substantially different from homogeneous materials (IVANOV *et al.*, 1992). In the modern view of materials, a solid may be comprised of free electrons and atoms bound in a periodic arrangement called the lattice. Accordingly, transport of thermal energy may be due to two effects: the migration of free electrons and lattice vibrational waves. When viewed as a particle-like phenomenon, the lattice vibration quanta are termed phonons. In pure metals, the electron contribution to conduction heat transfer dominates, while in nonconductors such as seal rocks and semiconductors, the phonon contribution is dominant (INCROPERA *et al.*, 2006). For a thermally thick sedimentary seal rock sample, we expect the following two processes contributing to the PAS signal amplitude:

(i) Thermal diffusion or intraband nonradiative thermalization:

When the absorbed photon energy is greater than the band gap an electron is created in the conduction band and a hole is left in the valence band. The excess energies of the electron (the energy difference between the conduction band and the initial energy of the photogenerated electron) and the hole (the energy difference between the valence band and the initial energy of the photogenerated hole) appear in the respective carriers as kinetic energy. The initial electron and hole distributions are not Boltzmann-like, and the first step toward establishing equilibrium is for the electrons and holes to interact separately through their respective carrier-carrier collisions and inter-valley scattering to form separate Boltzmann distributions of electrons and holes. The two Boltzmann distributions of electrons and holes can then be separately assigned an electron and hole temperature that reflects the distributions of kinetic energy in the respective charge carrier populations. The Boltzmann distribution applies only to particles at a high enough temperature and low enough density that quantum effects can be ignored. If photon absorption produces electrons and holes, each with initial excessive kinetic energies at least kT (k = Boltzmann's constant, and T = the temperature in Kelvin) above the conduction and valence bands, then both initial carrier temperatures are always above the lattice temperature; these carriers are called hot carriers (i.e. hot electrons and hot holes). This first stage of relaxation occurs very rapidly (<100 fs where 1 femtosecond = 10^{-15} s). It is often referred to as carrier thermalization and results in a thermal distribution described by Boltzmann statistics. The next step is for the hot electrons and hot holes to achieve thermal equilibrium with the semiconductor lattice. The lattice temperature is determined by thermal equilibrium of the phonons with the surroundings, and is the ambient temperature, which is lower than the initial hot-electron and hot-hole temperatures. Equilibrium of the hot carriers with the lattice is achieved through carrier-phonon interactions (phonon emission through electron- and hole-scattering), in which the excess kinetic energy of the carriers is transferred to the phonons. The phonon emission results in cooling of the carriers and heating of the lattice until the carrier and lattice temperatures become equal. This process is called carrier cooling (NOZIK, 2001; SUN *et al.*, 2005). IVANOV *et al*. (1992) performed a theoretical and experimental investigation of the transport of vibrational excitations in ceramic materials and ROSENCWAIG and GERSHO (1976) carried out a deeper analysis of the theory of the photoacoustic effect with solids. The contribution of the thermal diffusion (TD) process in a thermally thick sample to the PAS signal decreases exponentially with the modulation frequency as:

$$S = \frac{1}{f}\exp(-a\sqrt{f}), \tag{3.26}$$

where $a = l_s\sqrt{\pi / \alpha_s}$, f is the modulation frequency, l_s is the thickness and α_s the thermal diffusivity of analyzed sample. The PAS signal phase shows a modulation frequency dependence of:

$$\Phi_{ph} = \frac{\pi}{2} - a\sqrt{f}. \tag{3.27}$$

Also considering the thermal diffusion process contribution in the PAS signal, Balderas-López et al. (BALDERAS-LÓPEZ *et al.*, 1999) reported a new photoacoustic methodology to measure thermal diffusivity of materials. It is based only on the identification of the first discontinuity in the photoacoustic phase lag predicted by using the Roscencwaig model without the need to fit a set of experimental data. According to these authors, the complete photoacoustic signal for an optically opaque sample is given by the following expression:

$$\begin{aligned} S = W & \frac{1}{\sqrt{[\cos(x)\sinh(x)]^2 + [\sin(x)+\cosh(x)]^2}} \\ & \times \exp\left[i\left(-\frac{\pi}{2} - \arctan\left(\frac{\tan(x)}{\tanh(x)} \right) \right) \right], \end{aligned} \tag{3.28}$$

where

$$W = \frac{Y\sqrt{\alpha_g \alpha_s}}{2\pi f}, x = \sqrt{f/f_c} \text{ and}$$

$$f_c = \frac{\alpha_s}{\pi l_s^2}. \quad \textbf{(3.29)}$$

Here, α_s and f_c are, respectively, the thermal diffusivity of the gas inside the photoacoustic chamber and the characteristic frequency which characterizes the modulation frequency where there is a transition from the thermally thin regime *($f < f_c$)* to the thermally thick regime *($f > f_c$)*. The photoacoustic phase lag mentioned above has discontinuity points due to the *tan(x)* dependence, which occur at frequencies given by:

$$f = \left(2n+1\right)^2 \frac{\pi^2}{4} f_c, \quad \textbf{(3.30)}$$

where *n* is a numeral. The first discontinuity in the photoacoustic phase lag corresponds to *n=0*. When TD process is present in an analyzed sample, it is observed in the low frequency range.

(ii) Thermoelastic bending:

When a temperature gradient is generated within the sample, across its thickness, the thermoelastic bending process contributes to the PAS signal. This contribution shows a modulation frequency dependence of the type $f^{-1.0}$. The thermal diffusivity can be determined by fitting the phase of the PAS signal to the expression:

$$\Phi_{ph} = \Phi_o + \tan^{-1}\left[\frac{1}{a\sqrt{f-1}}\right]. \quad \textbf{(3.31)}$$

With constant *a* being the same as showed in process (i). When the process (ii) is present, it occurs in the higher frequency range after the thermal diffusion process. Thus, analysis of the phase of the PAS signal can be used to identify this process and determine the thermal diffusivity.

In a practical manner, the contribution of each process to the pressure variation in the photoacoustic cell can easily be found through the following procedure (POFFO *et al.*, 2011): (a) by plotting *ln S* versus $\sqrt{f}$ and Φ_{ph} (in radians) versus $\sqrt{f}$, the "a" value is the slope of the straight line fitting the data in the low modulation frequency range and, the values calculated from both plots must be equal, when the thermal diffusion process in present; (b) by plotting *log S* versus *log f*, the slope of the straight line fitting the data in the high modulation frequency range highlights the contribution of the thermoelastic bending (TB) process showing a modulation frequency dependence of the type $f^{-1.0}$. In this case, α_s can be determined by fitting the plot Φ_{ph} (in radians) versus *f*, in the appropriate modulation frequency range, to the expression of phase in Eq. (3.31). In this work we executed this procedure using the software OriginPro v.7.

4. EXPERIMENTAL PROCEDURE

4.1. Materials and methods

All rock samples analyzed were parts of slab or broken core and free of any hydrocarbon. The cores were carefully cleaned intending to keep the organic contents of rock samples in a state as preserved as possible however free of hydrocarbons. Therefore, in the petrophysical laboratory an ultrasonic cleaning method using mixtures of toluene and/or methanol was applied to remove hydrocarbons from the samples. By this process we intended to retain the clay material present on the surface of the porous medium of fine grained rocks such as the seal rocks and the tight gas sandstones (TGS) analyzed in the present work.

Table 4.1 shows an overview over the analyzed TGS and seal rocks and the performed experiments.

Table 4.1: Experimental setup and analyzed samples.

Experimental analyses for the present work

Materials				Techniques						
Rock	**Field**	**Sample**	**Depth (m)**	**PDP**	**MICP**	**N_2GA**	**LFNMR**	**nano- and microCT**	**XRX, SEM and FESEM**	**PAS**
Tight Gas Sandstone	A	A-11V	4944.20	x	x	x	x	x	x	
		A-12H	4993.20	x	x	x	x		x	
		A-12V	4993.25	x	x	x	x		x	
		A-17V	5036.05	x	x	x	x	x	x	
		A-18H	5039.20	x						
		A-19V	5040.65	x	x	x	x		x	
	B	B-36	3348.00		x	x				
		B-43	3230.30		x	x				
		B-48	3428.00		x	x				
	C (outcrop)	C-51	245.00		x	x				
		C-63	878.00		x	x				
		C-69	1080.5		x	x				
	D	D-32	-	x						
		D-50	-	x						
Seal Rock	E	SR-42	4413.35		x	x			x	x
	F	SR-47	4892.05		x	x			x	x
	G	SR-57	270.90		x	x			x	x

In Table 4.1 the field of origin is denominated with an initial letter which was included in the sample number; also “V” and “H” refers to vertically and horizontally to the bedding plane. The samples (from oil or gas fields) were provided by the Brazilian center for research on petroleum, CENPES/Petrobras. In the subsequent chapters we expose a short explanation bearing the experimental procedure and techniques applied in the present work.

4.1.1. Pulse-decay permeability

Measuring the permeability of tight gas sandstones is a challenging task because standard measuring techniques are generally impractical and difficult to apply. Customary methods of measuring permeability in the laboratory are based on steady-state flow. However, if the permeability is low, long periods of time are required to establish steady-state flow and thus these procedures are impractical. The transient flow method applied in the present work used nitrogen gas as fluid flow from the upstream reservoir through the sample to the downstream reservoir. Thereby the sample permeability could be calculated from the observed pressure decay in the upstream reservoir.

Pulse decay measurements were carried out using a CoreLab PDP-200 pulse decay permeameter, which is ideal for low-permeability porous media with intrinsic permeabilities below 0.1 mD. It was built according to the design described by JONES (1997), which is shown in Figure 3.3(a) with the two small reservoirs being equal in volume (around 5 cm^3 each). In this method, the pore volume must be determined independently so we used the values obtained from the N_2GA and MICP combination. The PDP-200 software calculates the permeability of the sample based on the pressure decay curves. Rock samples of 1.5 inches in diameter and about 1 inch in length were dried to a constant weight in an oven at 80 ^{o}C before all measurements. The gas permeability was measured at net confining stresses representative of in-situ conditions, i.e., for each sample originating from distinct wells, a distinct confining pressure was applied. A consequence of using gas to measure permeability is the gas slip on the solid surface, which creates a deviation from the Poiseuilles flow, known as the Klinkenberg correction (TIAB and DONALDSON, 2004). The Klinkenberg permeability was calculated from multiple measurements at different mean pore pressures. The high mean pore pressure reduces the effect of gas slippage and reduces the gas compressibility and the magnitude of its change with small pressure variations (JONES, 1997). Therefore, it should be as high as practicable. In the experiments reported herein the maximum mean pore pressures allowed by the PDP transducer used was 6.89 MPa, only sample A-17V was also tested at 13.10 MPa.

4.1.2. Mercury intrusion capillary pressure

The mercury intrusion capillary pressure experiments were carried out with an Autopore IV 9500 by Micromeritics with a pressure range up to 413.69 MPa. The eleven samples analyzed (crushed into pieces of about 1.4 mesh size) had masses between 3.190 and 8.810 g. The equivalent pore radius was computed according to the capillary pressure using the Washburn equation with P_w ranging from 0.003 to 413 MPa, interfacial tension γ_{Hg} = 485 mN/m and wetting angle θ_{Hg} = 140^o. It is of interest to mention that the wetting angle is not a function of the material pore size but is an intrinsic property of a solid-fluid system (ADAMSON, 1990). Values between 130 and 140^o are conventionally assumed since the cohesive forces between the mercury atoms are greater than the adhesive forces between mercury and other solids, leading to no relevant changes in the contact angle. Several authors have assumed a mercury contact angle of around 140^o (ECHEVERRÍA *et al.*, 1999; FAVVAS *et al.*, 2009; SCHLÖMER and KROOSS, 1997), and 130^o (KAUFMANN *et al.*, 2009). In this study we chose the value 140^o.

4.1.3. Nitrogen gas adsorption

Nitrogen adsorption isotherms were obtained at 77 K on an accelerated surface area and porosimetry system (ASAP 2020, Micromeritics Instruments). The samples were previously crushed into pieces of about 3 mesh size (mass between 0.89 and 1.72 g), dried in an oven at 80 ^oC overnight and outgassed under high vacuum (<10 mmHg) for 10 h at 110 ^oC on the apparatus. The free space (dead volume of the tube) was determined volumetrically using helium before the measurements were taken for the adsorption isotherm. The saturation vapor pressure P_o of N_2 at 77 K was determined every 120 min. during the experiment using a nitrogen vapor pressure thermometer. An equilibration time of 10 s was applied in the analysis. Both adsorption and desorption isotherms were measured, although only the adsorption data was used to determine the pore structure information. In addition, the nitrogen statistical film thickness for the BET surface area was assessed for relative pressures between 0.021 and 0.203.

4.1.4. X-ray diffraction analysis

Sample preparation for XRD analysis was performed by crushing a fine powder from rock pieces. For finer and controlled particle size grinding we used a swing/disc mill (Spex Shatter Box) commercial machine operating for 3 min. for each sample. According to Buhrke *et al.*, (1998) three conditions are necessary to achieve high degrees of accuracy in quantitative XRD: total randomness of the crystallite orientations, sufficient number of crystallites in the experimental specimen to meet statistical requirements, and sufficient diffraction intensity measured to satisfy counting statistics. Since we had enough amount of sample, the reduction of the sample particle size and an ideally random specimen (in which the probability of orientation for any and all Bragg planes is equally likely for any direction in space) were obtained. Thus, the samples within particle size smaller than 400-mesh (38 µm) were prepared in a specific XRD sample holder to minimize preferred orientation and surface roughness.

The XRD measurements were performed in a D4 ENDEAVOR equipment from Bruker company coupled by graphite secondary monochromator and Co K-alpha radiation. After being acquired the XRD patterns were analyzed using Diffract.Suite EVA Software, for semi-quantitative identification of mineralogical phases. The qualitative identification procedure was to search initially for a mineral that had the strongest peaks, and follows with confirming the choice by finding the positions of weaker peaks for the same mineral.

4.1.5. Low-field NMR analysis

In this work, one set of low-field NMR experiments was designed to study the pore structures, pore types and sizes, porosity and parameters for permeability prediction on five tight sandstones from the Brazilian gas field named A. The NMR analysis was conducted on five mini plugs (~ 7mm x 7mm) of the TGS samples (A-11V, A-12V, A-12H, A-17V and A-19V) fully saturated with 10,000 KCl brine in a MARAN 23 MHz Ultra Magnetic Resonance Core Analyzer. The samples were kept immersed in the solution under vacuum for more than 48 h and then taken out for pressure-saturation at 3 MPa for another 96 h. Following that, they were placed in jars full of brine and transferred into the water bath with a temperature of 40 °C for a minimum of 1 or 2 h to be prepared for NMR tests. Each mini plug was placed in a NMR tube coupled in the equipment operating at 23 MHz for the hydrogen nucleus, to obtain the data of spin-spin relaxation time determined by CPMG (Carr-Purcell-Meiboom-Gill) technique. The 90° pulse of 10 µs was calibrated automatically by the software of the instrument. The amplitude of the FID was sampled for 255 data points, ranging from 0.01 to 5000 ms; the intervals of spin-spin relaxation time determined by CPMG technique started from 0.5 to 250793 µs. The relaxation values and relative intensities were obtained by fitting the exponential data with the aid of the program. The schematic of the experimental setup of NMR is shown in Figure 4.1.

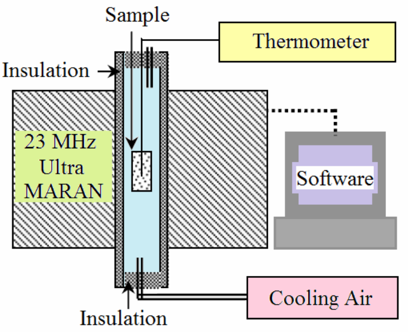

Figure 4.1: NMR experimental schematic (GAO *et al.*, 2009).

4.1.6. X-ray nano- and microCT

In order to investigate 3D images of tight gas sandstones' pore microstructure ranging to sub-micrometers in size, a computer tomography (CT) characterization at high resolutions is applied. In the present work this was performed in two microCT (XRadia Versa XRM-500) and one nanoCT (XRadia UltraXRM-L200) equipments with resolution from 0.7 µm to 64 nm. Table 4.2 shows the parameters used for the micro- and nanoCT acquisitions in the analyzed tight gas sandstones. As one can see, we exposed two TGS samples of field A (A-11V and A-17V) to the X-ray CT technique in distinct resolutions. For the experiments we had the criteria of preparing the samples as cylinders (to decrease image artifacts) and we chose the diameters to be as big as possible (to have enough representative volume) but still permitting sufficient X-ray transmission for imaging acquisition (YANG *et al.*, 2013). The diameter of the mini cores prepared for the three distinct acquired resolutions (Res1, Res2 and Res3) were respectively 7 mm, 2 mm and 0.1 mm.

Table 4.2: Micro- and nano-CT scan settings.

Sample		**Equipment**	**Pixel size (µm)**	**Source voltage (keV)**	**Number of Projection**	**Exposure time (s)**	**Camera binning**	**Sample size (mm^3)**	**Scan time**
A-11V	**Res1**	XRadia VersaXRM-500 (CSIRO)	0.755	80	2000	14	1	243	10h 20min
	Res2	XRadia VersaXRM-500 (LMPT)	0.35	50	1600	11	2	8	6h 40min
	Res3	XRadia UltraXRM-L200 (LMPT)	0.064	8	1600	120	1	0.001	54h 30min
A-17V	**Res1**	XRadia VersaXRM-500(CSIRO)	0.746	80	2000	14	1	243	10h 20min
	Res2	XRadia VersaXRM-500(LMPT)	0.31	50	1600	18	2	8	10h 50min
	Res3	XRadia UltraXRM-L200 (LMPT)	0.064	8	1600	120	1	0.001	54h 30min

Besides of sample size the image resolution also depends on: the X-ray detector itself, the focal spot size, the geometric magnification, the stability of the rotation mechanism and the filtering algorithm used to reconstruct the images. For the acquisition taken in the microCT measurements (XRadia VersaXRM-500) we optimized the resolution by locating the source and detector as close as possible to the sample. For each of the two tight gas sandstones analyzed, a total of 1600 to 2000 projections were taken at equal angular intervals within distinct exposure times and source voltage as shown in Table 4.2. It is usual, that, during the microCT image acquisition, noise filters including those used to counter various artifacts or image anomalies which can occur due to the reconstruction algorithms and the imaging processing itself (NGUYEN, 2011), are applied. However, aiming to obtain a bigger pore contrast no filter was used for the acquisition using the XRadia Versa XRM-500 microCT. The samples were glued on a metal extension and mounted between the source and the detector including the lenses for optical magnification using the clamp for the XRadia Versa XRM-500 equipment. An optical magnification of 4 times was achieved, and, as the sample rotates 360° during the acquisition, the mounting position of the analyzed cylinders was well centered allowing a complete rotation stage. For the XRadia UltraXRM-L200 equipment the sample preparation is much more difficult considering the sample size has to be very small and without fractures, therefore, prepared by laser ablation.

After experimental conditions were applied allowing the acquisition of radiographic projections, the X-ray shadow projections of the measured 3D object are defined as digitalized *n x p* pixel images. These images are then processed to obtain reconstructed cross-section images of linear attenuation coefficient values using a mathematical algorithm based on the filtered back-projection procedure implemented in the used equipment. Thus, a complete stacking of 2D cross-sections of the object with a single pixel distance between the slices is obtained, resulting in a 3D stack of isotropic voxels with a gray-scale of 16 bits, from which the 3D internal structure can finally be analyzed.

4.1.7. The open photoacoustic cell

Three seal rocks originating from distinct fields and depths were analyzed by photoacoustic spectrometry. The basic requirements of the photoacoustic detection technique can be summarized as (ALMOND and PATEL, 1996):

(iii) A light source and focusing instruments;
(iv) Means of modulation light;
(v) An appropriate photoacoustic cell itself and;
(vi) A microphone and processing electronics.

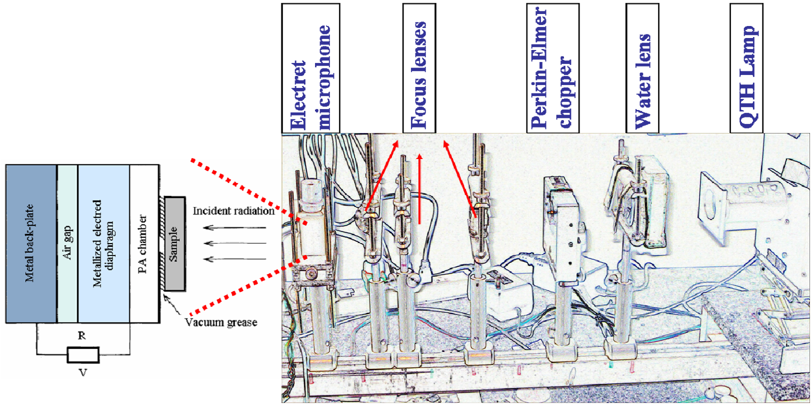

Figure 4.2: Conceptual sketch from a picture of the OPC located at the LSCM laboratory and used in the analysis.

The PAS measurements were performed on a simple Open Photoacoustic Cell (OPC) configuration, as shown in Figure 4.2 with an accuracy of thermal diffusivity property of 5%. This configuration consisted of a 250 W quartz-tungsten-halogen (QTH) lamp and a Bentham 605 current power supply. After being heat filtered by a water lens, the light is mechanically chopped by a Perkin-Elmer chopper, model 197, and focused onto the sample. As one can see the sample is mounted directly onto the front sound inlet of an electret microphone (DE LIMA *et al.,* 1992) and sealed by vacuum grease. The output voltage from the microphone was connected to a computer through a lock-in amplifier in order to record the amplitude and phase of the PAS signal as functions of the modulation frequency. The experimental setup used for the present investigation is calibrated by evaluating the thermal diffusivity of Al powder (Aldrich 99.999 %); the obtained value of $0.968 \pm 0.001\ cm^2.s^{-1}$ agrees well with earlier reported values (PERONI and MIRANDA, 1987).

In order to compare the thermal diffusivity values and to measure porosity in the three analyzed seal rocks, pieces of the rocks sliced vertically to the bedding well direction and power compacted discs were prepared for the PAS measurements. The vertical sliced samples were obtained by dry hand-sanding process, while the compacted discs were initially mechanical powdered (particle size of ~10 µm) followed by compression using 6 tf/in^2 (~90MPa). The powders had controlled particle size grinding using swing/disc mills (Spex Shatter Box) commercial machine operating during 3 min. for each sample. The obtained pellets (both sliced and compressed discs) were small with an average diameter of 10 mm. The thicknesses obtained for the vertical and powder compressed samples were respectively: 510 µm and 500 µm for sample SR-42; 470 µm and 510 µm for sample SR-47 and; 390 µm and 475 µm for sample SR-57. The PAS measurements were taken in the modulation frequency range of 10 to 250 Hz in order to achieve the thermally thick regime. Figure 4.3 shows the FESEM micrographs images of analyzed seal rocks (a) and the compacted powder (b) analyzed by PAS technique.

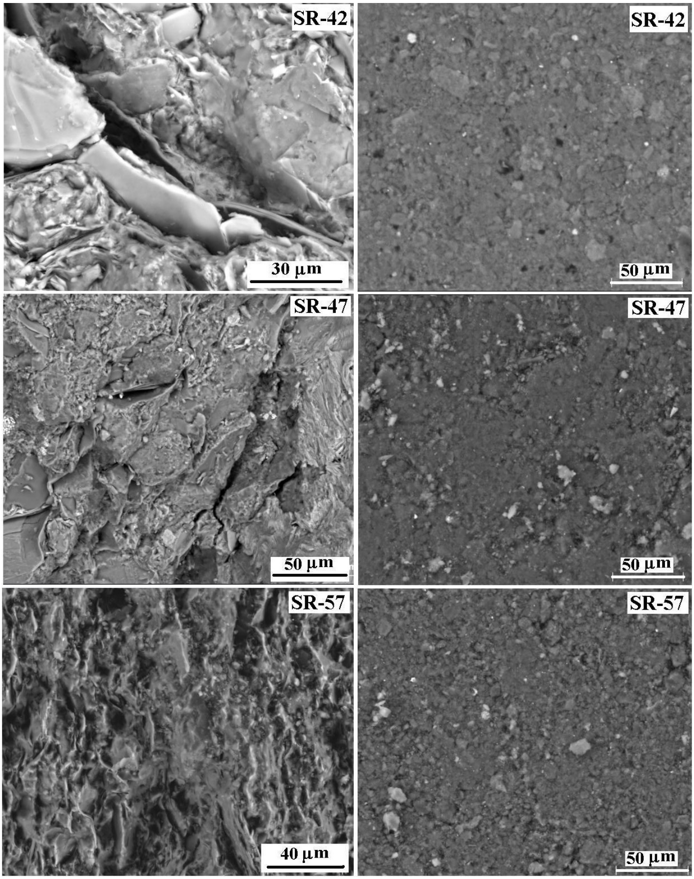

(a) **(b)**

Figure 4.3: BSE images from FESEM analysis acquired to study seal rocks: (a) shows fractured surface of seal rocks and (b) the powder compressed pellets analyzed by PAS.

5. PERMEABILITY MEASUREMENTS AND PORE STRUCTURE CHARACTERIZATION IN TGS

In this and the following chapters the results obtained by a set of techniques for the pore structure characterization and the analysis of the permeability on tight gas sandstones are exposed. By the usage of distinct techniques it was possible to evaluate the benefits and limitations of each method and consequently obtain specific properties in these rocks which allow estimate permeability. The main properties measured in the present chapter for tight gas sandstones originating from dissimilar gas fields were: porosity, pore size distribution, specific surface area and experimental permeability. Nitrogen Gas Adsorption (N_2GA), Mercury Intrusion Capillary Pressure (MICP) and Pulse-Decay Permeability (PDP) were the techniques applied. On the other hand, only TGS of field A (next Chapter) were evaluated by the usage of Low Field Nuclear Magnetic Resonance (LFNMR), X-ray Nano and Micro Computed Tomography, SEM, FESEM and XRD techniques. Also the prediction and simulation of permeability were performed and discussed for samples of field A.

5.1. PDP analysis

In the two actual reservoirs (A and D) investigated in this sub-section the local depositional and tectonic stresses add components of stress in distinct directions. Only samples A-12H and A-18H were plugs extracted from the horizontal direction to bedding field. Although we knew fairly the nature of in situ stresses (net stress) to the vertical bedding direction studies here have been performed under distinct hydrostatic conditions. The in situ net stress (overburden pressure) value for Field A was equal 27.58 MPa while for Field D it was 25.79 MPa. The time required before the PDP test to reach a uniform pore pressure on the sample confined in the core holder was about 1 to 2 hour for the analyzed TGS.

5.1.1. Effect of TGS rock stress on permeability to gas

Nitrogen gas permeability results for different net pressures at constant high pore pressure (6.89 MPa inlet for all samples and 13.10 MPa inlet only for A-17V) are shown in Figure 5.1 for the rocks of well A and D. Note that the denominated inlet pressure is the mean pore pressure performed during PDP tests. In a PDP test the measurement speed is roughly proportional to the mean pore test pressure, and it should be as high as practicable (JONES, 1997), while the net stress is the difference between the hydrostatic confining pressure and the inlet pressure applied on the sample located in the core holder.

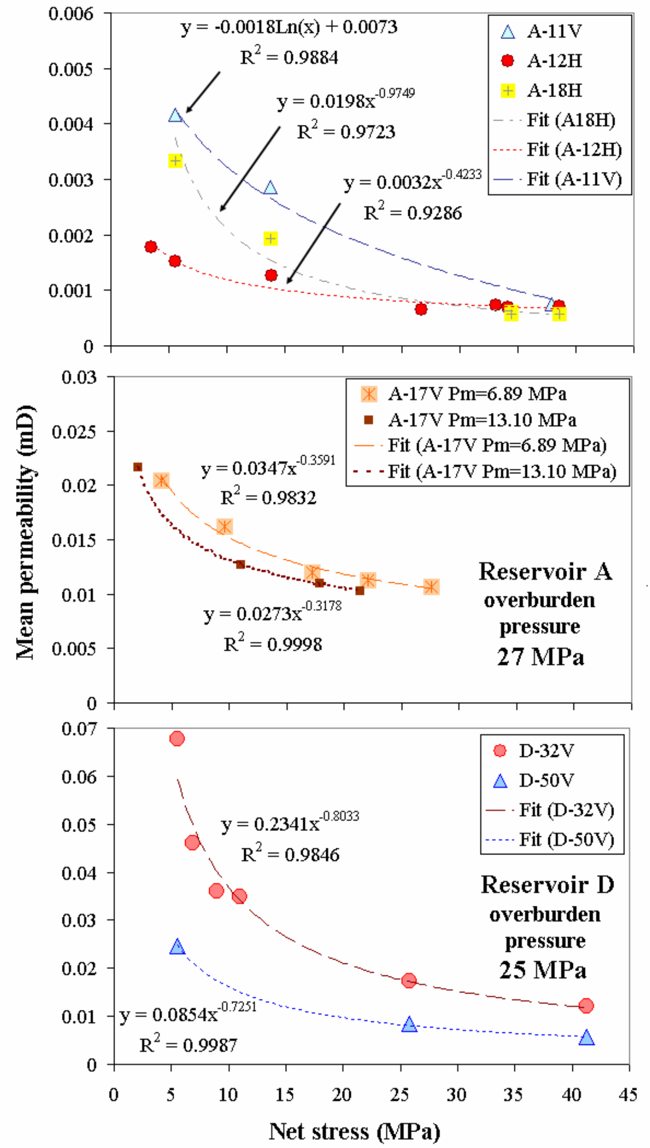

Figure 5.1: Effect of net stress versus measured *k* in TGS. All samples were measured at P_m = 6.89 MPa, A-17V was also analyzed at P_m= 13.10 MPa.

As one can see in Figure 5.1 for all analyzed samples under increasing net stress values permeability is reduced. Permeability ranges from about 0.02 mD to less than 0.001 mD at net stress equal 27.58 MPa. For sample A-17V the permeability value is reduced as an average by 13.4% at 13.10 MPa inlet (mean pore pressure) in comparison to 6.89 MPa inlet. All these trends agree that the analyzed TGS have a significant variation in the permeability values within the applied net stress. E.g., considering the calculated fittings of samples A-11V and A-17V, the value for permeability at atmospheric pressure (1 atm $\approx$ 0.103 MPa, and so without the net stress pressure effect) would be respectively in the order of 0.0113 and 0.078 mD. One of the main controlling parameters for permeability is the pore throat size (REZAEE *et al.,* 2012). In many cases, the pore/pore throat radius has a greater effect than the porosity on the permeability (JAYA *et al*., 2005; RUSHING *et al*., 2008). Fatt and Davis (1952) observed that tight sandstones exhibit a stronger dependence on net stress pressure than higher permeability rocks do. Further, fractures and shale streaks have a strong effect on permeability reductions in tight sands (VAIRIGS *et al.*, 1971).

5.1.2. Klinkenberg' correction

The TGS samples were tested with 3 to 5 step mean pore pressures to obtain the Klinkenberg slippage factor and corrections to gas permeability. The results are shown in Table 5.1 and Figure 5.2. From the graphics plotted in Figure 5.2 one can see the agreement to equation (2.20) where the apparent gas permeability at low mean pore pressures is bigger than the Klinkenberg permeability extrapolated to an infinite high mean pore pressure. As one can see we investigated the gas slippage effects using the conventional Klinkenberg plot, i.e., the inverse mean pore pressure plotted against the apparent gas permeability. By fitting the data it was also possible to calculate the Klinkenberg slippage factor. Only for samples A-19V and A-12H non-Darcy effects may be identified as deviations from the fit line trend at high mean pressures. However, if we consider the characteristic radius found in A-12H and A-19V being equal 20 and 100 nm (as it will be shown later in the PSD results), the nitrogen molecular mean free path equal 2.15 nm and apply Eq. (2.19) the values $0.0215 < K_n < 0.1075$ are found. This range of Knudsen numbers is located in the slip flow regime where Klinkenberg' corrections are still valid.

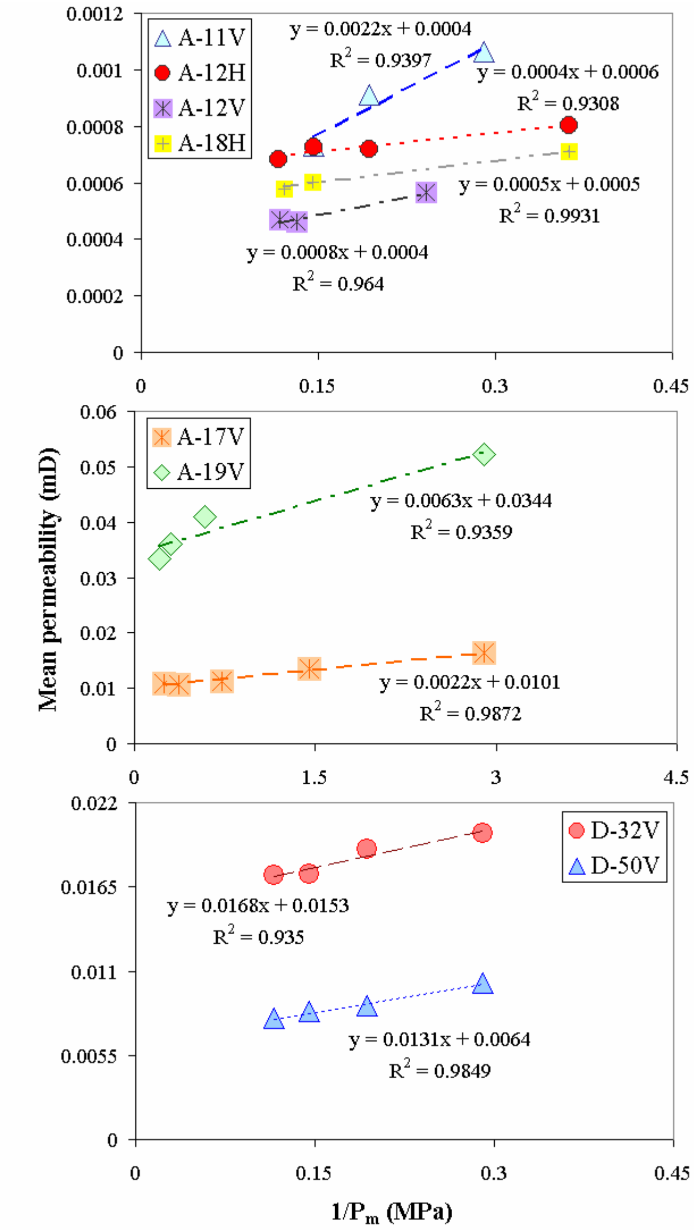

Figure 5.2: Plot of correction for obtaining Klinkenberg permeability where *(1/P_m)* tends to zero.

Comparing the values of the Klinkenberg' correction factors found one can observe that in general the values were bigger for field D than for field A. This tendency supported by the Equation (2.21) can lead us to the conclusion that samples of field D were probably comprised by significant amount of very small pores, even smaller than the ones found on samples of field A. However we could not confirm this assumption since samples of field D were not available for further experiments realized in this thesis.

Table 5.1: Values of Klinkenberg permeability (k_a) and slippage factor

Samples		Field A						Field D	
		A-11V	A-12H	A-12V	A-17V	A-18V	A-19V	D-32V	D-50V
Klinkenberg	Permeability, k_K (mD)	0.0004	0.00066	0.00046	0.0101	0.0005	0.0344	0.0153	0.0064
	Slippage factor b_K	0.0022	0.0004	0.0008	0.0063	0.0005	0.0022	0.0168	0.0131

5.1.3. Steady-state versus PDP measurements

In order to evaluate the accuracy of pulse-decay technique measurements applied in the present work, results of the steady-state (permanent method) technique were compared with the unsteady-state (pulse-decay or transient method) measurements. Aiming to validate the comparison, each sample was tested with both techniques under the same net stress and using the same gas (nitrogen). For the steady-state and unsteady-state measurements, a *Core Lab UP-400* (applicable for k>0.001 mD) and a *Core Lab PDP-200* (for 0.1 mD>k>0.01 μD) were respectively used. The analyses were performed in four tight gas sandstones samples originating from gas fields A or D and in a calibrated pattern made of metal (pattern A). These samples were chosen considering their permeability range which does not surpass the higher and lower limit of the transient and permanent technique, respectively. The obtained results are shown in a log-log graphic plotted in Figure 5.3 (a) and (b), where all the values represent the absolute permeability, i.e. corrected from the Klinkenberg effect.

Figure 5.3 (a) shows the results for the analyzed samples under specific net stress pressures as described in the graphic. As it can be seen in this figure for the investigated samples there is a good agreement between the two methods within the defined permeability range as emphasized by the correlation line (1:1) in the graphic; the higher deviations shown are of samples A-19V and D-32. For sample A-19V the unsteady-state technique gives a value 27.64 % smaller than the steady-state technique while for sample D-32 the value is 38.94 % higher. Still, this deviation found in our rocks lies within reasonable margins, unlike the results presented in the literature. So have RUSHING *et al*. (2004) reported a ratio of about 8 for the two methods (higher for steady-state method) in the permeability range less than 0.01 Md, while CARLES *et al*. (2007) presented that the permeabilities from unsteady-state are roughly twice the permeability from steady-state.

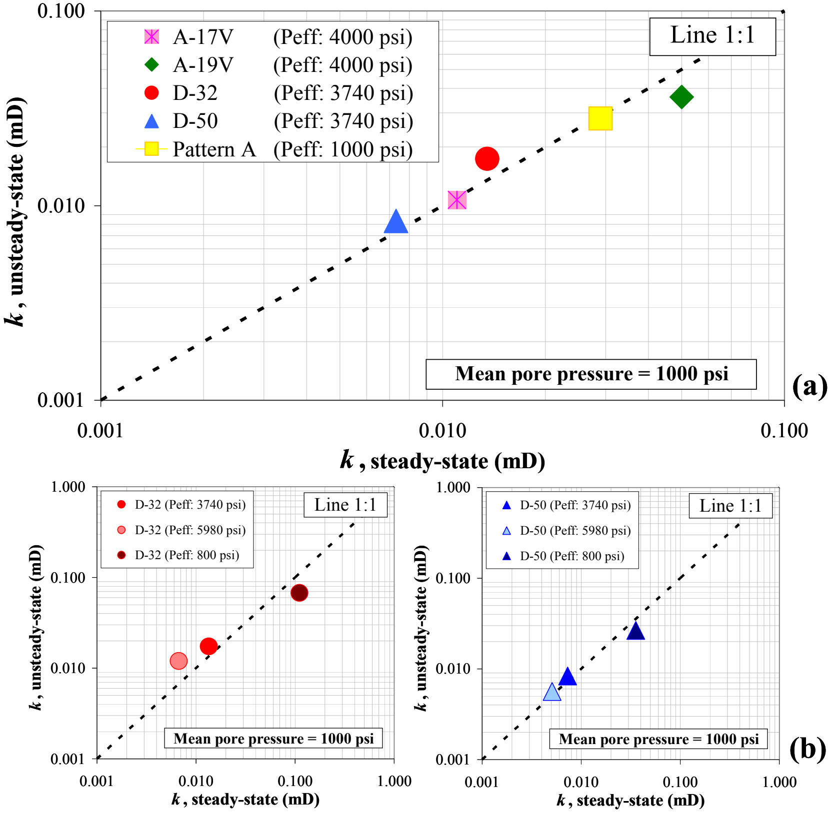

Figure 5.3: Comparison of absolute permeability agreement for the five analyzed plugs (a) and, the influence of net stress *(P_{eff})* pressure on gas permeability (b), using both the pulse-decay and the steady-state techniques.

We also investigated the relation of permeability results using both techniques in a sample under distinct mean effective pressures, as shown in Figure 5.3 (b) for samples D-32 and D-50. In this situation we observed in both samples that in the range of higher permeabilities (around 0.1 mD) the unsteady-state PDP method tends to underestimate the values. The same happens in the lower ranges of permeabilities (around 0.05 mD) where in turn the conventional steady-state method underestimates the values. This is in complete agreement between limitations of each technique within the permeability ranges. As one can see for the middle permeability ranges (P_{eff} =25.79 MPa) the values are very close. Overall we believe that the agreements found between the techniques corroborate that either method provides reasonable results for the permeability range found in the analyzed rocks.

5.2. Results for N_2GA and MICP techniques

5.2.1. N_2 isotherms

Nitrogen isotherms for selected TGS samples of field A, B and C are shown in Figure 5.4. It can be noted that the adsorption-desorption process is not reversible, as observed by the presence of hysteresis loops. Desorption hysteresis is mainly due to the presence of ink-bottle type pores (RUTHVEN, 1984) and is usually explained by pore blocking effects (GROEN *et al.*, 2003; RAVIKOVITCH and NEIMARK, 2002; SING *et al.*, 1985). Although the eleven rock samples differed in terms of the amount adsorbed and shape of hysteresis loops, the N_2 isotherms obtained at 77 K were similar and fall within Type II from the IUPAC classification group (SING *et al.*, 1985). At high relative pressures, the isotherms exhibit high adsorption, an indication that the rocks contain macropores not reached by N_2GA experiments. At average relative pressures (P/P_o > 0.45) the curve exhibits a hysteresis loop indicating the multilayer range associated with capillary condensation in mesopores (SING *et al.*, 1985). A feature common to the hysteresis loops obtained from nitrogen gas adsorption measurements is this closure point at similar pressures. This lower closure point is attributed to the surface tension of the liquid adsorbate reaching an unstable state at a specific pressure, influenced by the nature of the adsorbate at a given temperature (ECHEVERRÍA *et al.*, 1999; GROEN *et al.*, 2003; SING *et al.*, 1985). For rocks, i.e. a realistic case of heterogeneous pore size distribution and interconnected pore system, with this forced closure of the hysteresis loop, the PSD derived from the desorption branch is often much more affected by pore network effects. Thus, for PSD calculations only the adsorption branch was considered.

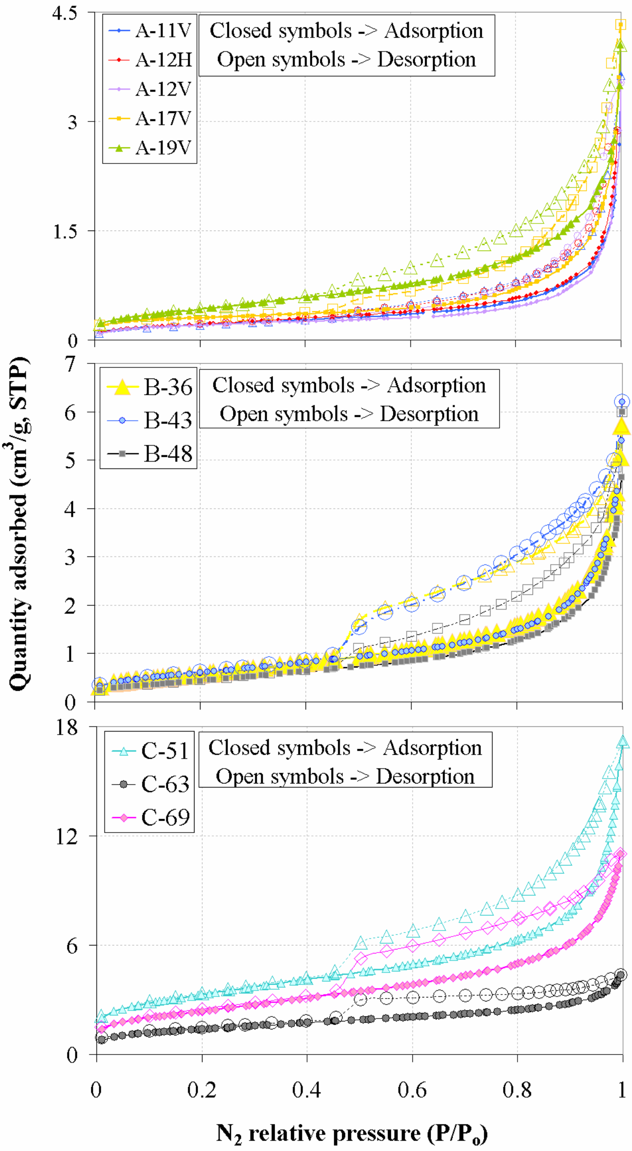

Figure 5.4: N_2 adsorption-desorption isotherms for the TGS rocks of Field A, B and C obtained at 77 K.

As it can be seen in Figure 5.4 the rocks analyzed (a natural material) have a porous microstructure in which small and large pores are present. Thus, for TGS rocks the horizontal plateau at relative pressures close to 1 does not occur, as it happens for microporous or synthetic materials with a defined pore range. Additionally, a considerable increase in the gas condensed in the capillary for a small variation in the relative pressure is observed. TGS rocks from field A present an amount of adsorbed N_2 between 3 and 5 cm^3/g (in STP conditions) while for field B these values are around 6 cm^3/g. For field C (outcrop TGS rocks) the amount of adsorbed N_2 is very dissimilar between the samples, varying from 4 to 18 cm^3/g. Shapes of hysteresis loop are similar for samples belonging to the same field and fall within the type H3, H2 and H4 for fields A, B and C, respectively (BRUNAUER *et al.,* 1940; SING *et al.*, 1985). In the type H2 samples, pores with narrow necks and wider bodies (ink-bottles) can be observed; type H3 is associated with aggregates of plate-like particles giving rise to slit-shaped pores (JANSSEN *et al.*, 2011; SING *et al.*, 1985; WANG *et al.*, 2010; YU *et al.*, 2003) while type H4 loop is often associated with narrow slit-like pores, but in this case the type I isotherm character is indicative of microporosity (SING et al., 1985). Nevertheless, for natural materials, such as TGS rocks, this interpretation has to be considered with caution since it is subject to error. The same caution was recommended by CLARKSON *et al.* (2011) who studied also TGS though using USANS/SANS and gas adsorption analysis.

5.2.2. PSDs from N_2GA models

The pore size distributions are calculated using the BJH and Dollimore-Heal (DH) (DOLLIMORE and HEAL, 1964; DOLLIMORE and HEAL, 1970) methods based on the adsorption isotherms data and the more recent DFT method (DO and DO, 2003; LANDERS *et al.,* 2013) assuming a slit-like pore geometry of carbon as a substrate and N_2 at 77 K. The calculations were performed using ASAP 2020 Software (ASAP 2020, 2007). The PSDs curves of cumulative pore volume measured using the three models are shown in Figure 5.5, with left column showing results for samples of field A and right column results from fields B and C.

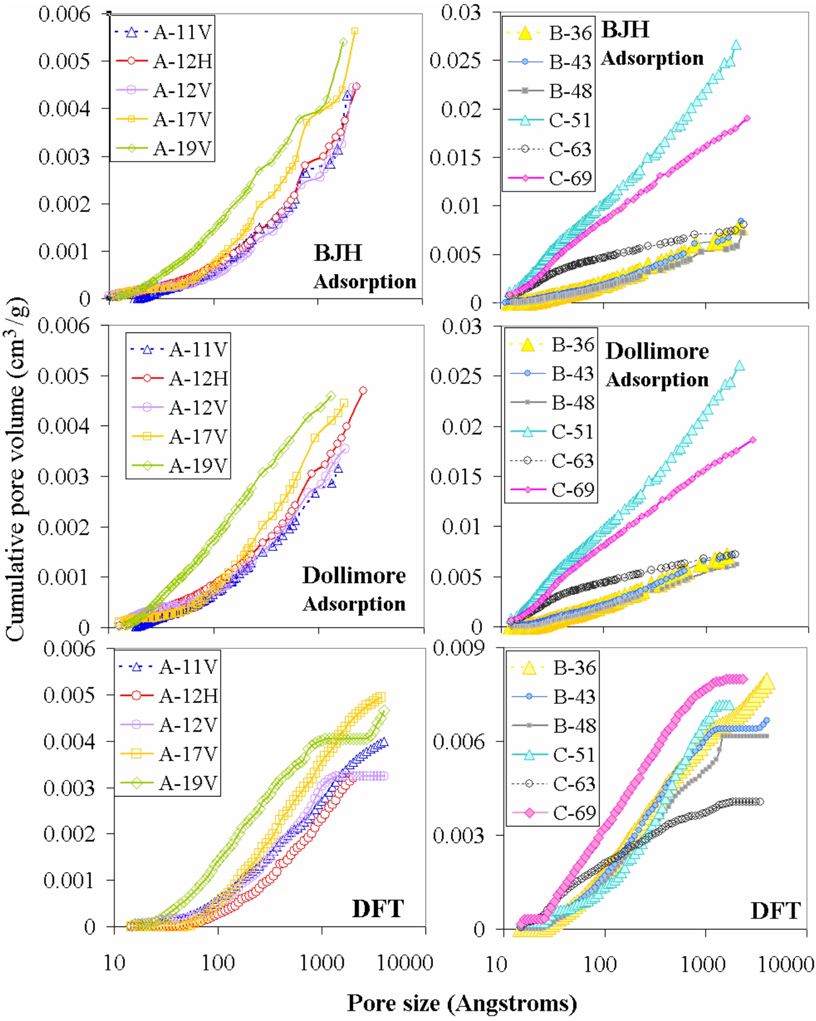

Figure 5.5: Cumulative pore volumes measured from N_2GA isotherms using BJH, Dollimore-Heal and DFT models.

From the results shown in Figure 5.5, in all analyzed samples it is possible to observe more differences in the PSDs curves obtained by the DFT model, while BJH and Dollimore-Head are very similar. Recently, LANDERS *et al.* (2013) published an extensive review on the adsorption characterization of mesoporous and microporous materials by using the density functional theory (DFT) methods. As they stated in their work, the DFT methods have found numerous applications for calculating pore size distributions in traditional and newly discovered nanoporous solids. All materials discussed in that work were either H1 or H2 hysteresis type, within a defined pore range size in the micro- or mesoporous region. In summary, for the TGS analyzed rocks analyzed in our work we observed that the pore volumes tend to be underestimated when performing the DFT model, especially for the fields B and C. On the other hand the fact that BJH and Dollimere-Heal models are based on the Kelvin equation leads to the similarity of calculated cumulative volumes curves between these models. Nevertheless we only choose the BJH results to perform the PSD using the N_2GA and MICP combination, as it will be discussed in sub-chapter 5.2.4.

5.2.3. PSDs from MICP

Figure 5.6 and Figure 5.7 depict the PSD curves for the cumulative and incremental pore volumes obtained by the Washburn equation (3.11). The porosity conversion is displayed in Table 5.2. As one can see, in the three analyzed fields, the samples showed a significant variation in the cumulative porosity while incremental PSD curves are mainly bimodal with peaks differing by at least one decimal order. For lower porosity samples the mean PSD tends to be around 100 Angstroms while for the others it is around 1000–10000 Å (fields A and B) unlike the outcrop samples (field C). E.g., sample C-51 practically has all pores concentrated in the region of about 100 Å. An interesting behavior to be observed for the MICP incremental curve is in sample C-63: even for the lower pore sizes it was not possible to measure a considerable amount of porosity. In this case the usage of N_2GA is of more use, as it will be observed in the combination of N_2GA and MICP techniques for PSD results.

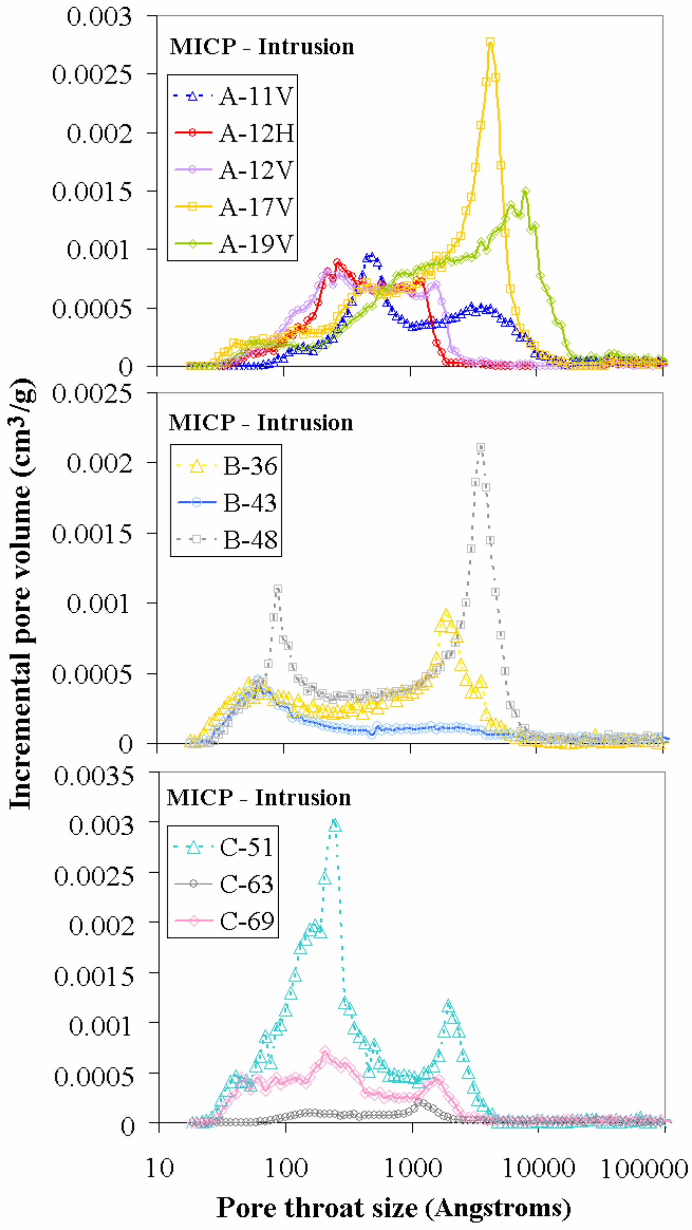

Figure 5.6: Incremental pore volumes versus pore throat size obtained by MICP technique.

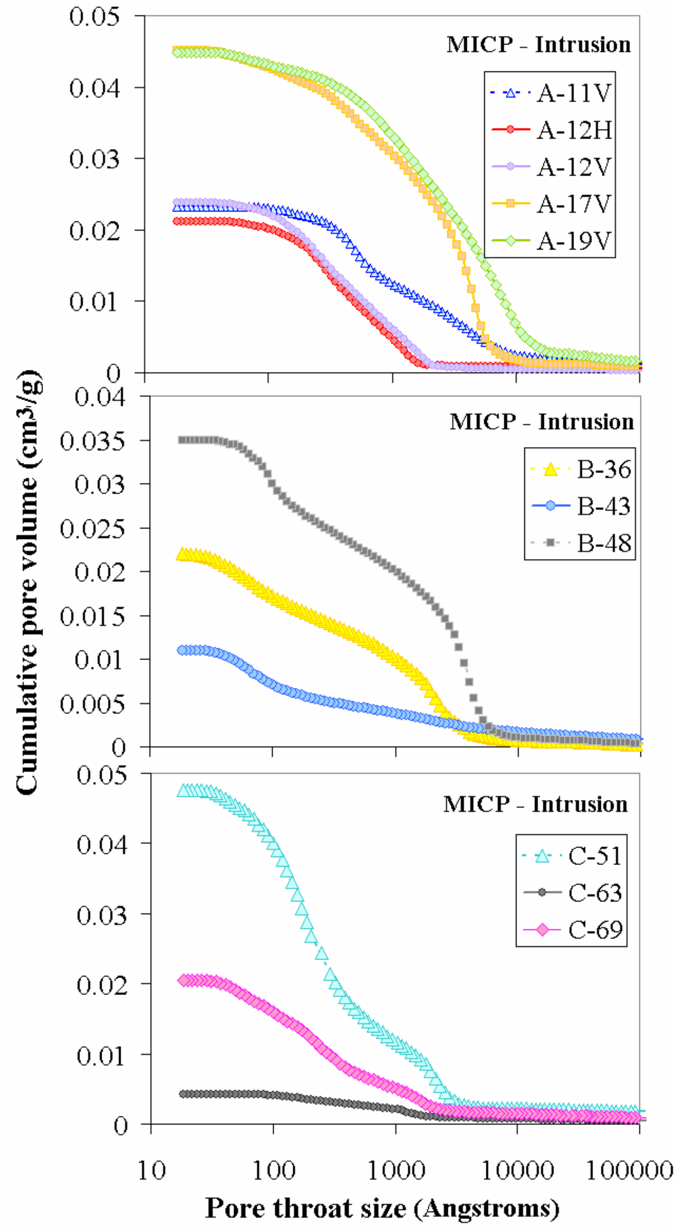

Figure 5.7: Cumulative pore volumes versus pore throat size obtained by MICP technique.

5.2.4. PSDs from N_2GA and MICP combination

Figure 5.8 shows in detail the applied methodology for one sample of each analyzed TGS reservoirs.

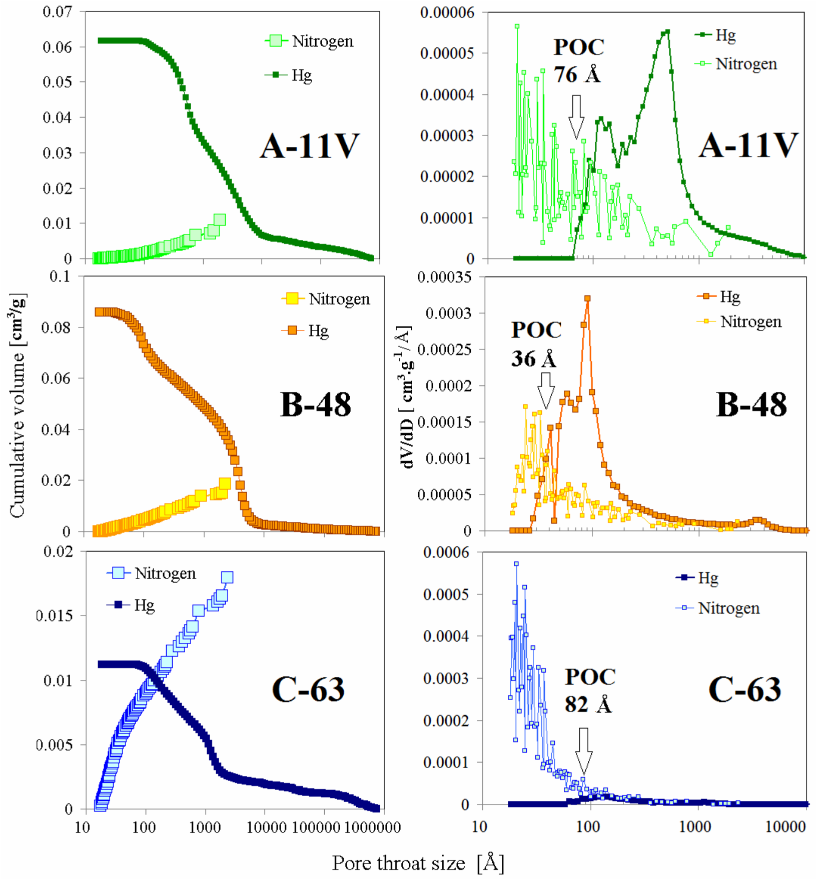

(a) **(b)**

Figure 5.8: Cumulative pore volume (a) and intersection of dV/dD (b) versus PSD curves, calculated from the BJH model (Nitrogen) and the Washburn equation (Hg).

The main difficulty in determining the complete pore size distribution in low-permeability rocks is that this material can be comprised of a wide range of pores making the use of a single technique inappropriate. For this reason we combined N_2GA, ideal for micro- and mesoporous materials (GROEN *et al.*, 2003), and MICP, one of the most used technique in measuring PSD in the range of meso- and macropores, to investigate the total pore spectrum in the studied TGS. The approach chosen follows the ideas exposed by a differential combination of the N_2GA and MICP cumulative curves to find at which pore size the techniques should be connected (point of connection – POC) as described in detail elsewhere (SCHMITT *et al.*, 2013) when studing seal rocks. Such approach is for the first time used in tight gas sandstones reservoirs.

Having for each rock sample the cumulative pore volume distribution for N_2GA obtained by BJH model (Figure 5.5) and MICP obtained by Washburn equation (Figure 5.7), the intersection between the curves of the first derivative (POC) are obtained where the fluid variation (volume) is the same for both techniques. After calculating a defined POC value for each sample, thus, the sum of total pore volumes starting from the incremental volumes measured in the smaller pores, i.e., the volumes measured by the N_2GA technique are continued above the POC by those calculated using the MICP technique. Figure 5.9, Figure 5.10 and Figure 5.11 show the results for samples of field A, B and C with total incremental pore volumes, *f(x),* and cumulative porosity plotted against the pore size diameter. Note that both the incremental and cumulative pore volumes have been multiplied by the apparent density values determined by MICP. From these figures it is possible to see that field C (an outcrop) is comprised by considerable amount of micro- and mesopores detected by N_2GA technique, though porosity values and the peaks of incremental PSD curves between the three samples do not necessarily match; the same was also observed for samples B-36 and B-43 of field B. On the other hand for samples of field A very little porosity in the micro- and mesopore range was identified, practically all pore spectrum was already detected by MICP analysis. In summary, for all samples the total cumulative curves (white fill) have nonlinear curvatures of the convex type, with less augmentation at the upper extremes, showing that TGS rocks analyzed have predominantly small pore sizes and also that there are no larger pores outside the pore size range studied by N_2GA and MICP. The results for the complete pore size distributions and also the ones obtained separately applying the two techniques are given in Table 5.2. The specific surface area results are discussed in the next chapter.

Table 5.2: Structural pore parameters obtained for TGS rocks.

Method	MICP				N_2GA				Combination (N_2GA + MICP)		
Sample	**Mass (g)**	**Real density (g/cm^3)**	**V_{pore} (cm^3/g)**	**Porosity (%)**	**Mass (g)**	**V_{pore} (cm^3/g)**	**Porosity (%)**	**BET S_o (m^2/g)**	**POC (Å)**	**Total V_{pore} (cm^3/g)**	**Total Porosity (%)**
A-11V	4.09	2.66	0.0232	6.17	1.36	0.0043	1.14	0.76	76	0.0236	6.28
A-12H	5.67	2.61	0.0212	5.54	1.75	0.0044	1.16	0.84	40	0.0209	5.45
A-12V	5.79	2.60	0.0238	6.18	1.15	0.0044	1.14	0.75	29	0.0235	6.12
A-17V	3.98	2.65	0.0451	11.96	1.39	0.0056	1.49	1.00	30	0.0451	11.96
A-19V	3.19	2.41	0.0448	10.80	1.00	0.0054	1.30	1.57	40	0.0453	10.91
B-36	5.95	2.56	0.0220	5.63	1.47	0.0079	2.01	2.12	50	0.0251	6.41
B-43	3.80	2.65	0.0110	2.90	0.89	0.0084	2.22	2.20	36	0.0114	3.03
B-48	5.59	2.45	0.0350	8.57	1.22	0.0072	1.76	1.60	36	0.0355	8.69
C-51	6.96	2.34	0.0476	11.13	1.04	0.0267	6.25	11.65	51	0.0505	11.81
C-63	8.81	2.66	0.0042	1.12	1.72	0.0080	2.13	4.93	82	0.0073	1.94
C-69	6.59	2.48	0.0205	5.07	1.17	0.0191	4.72	8.51	60	0.0232	5.76

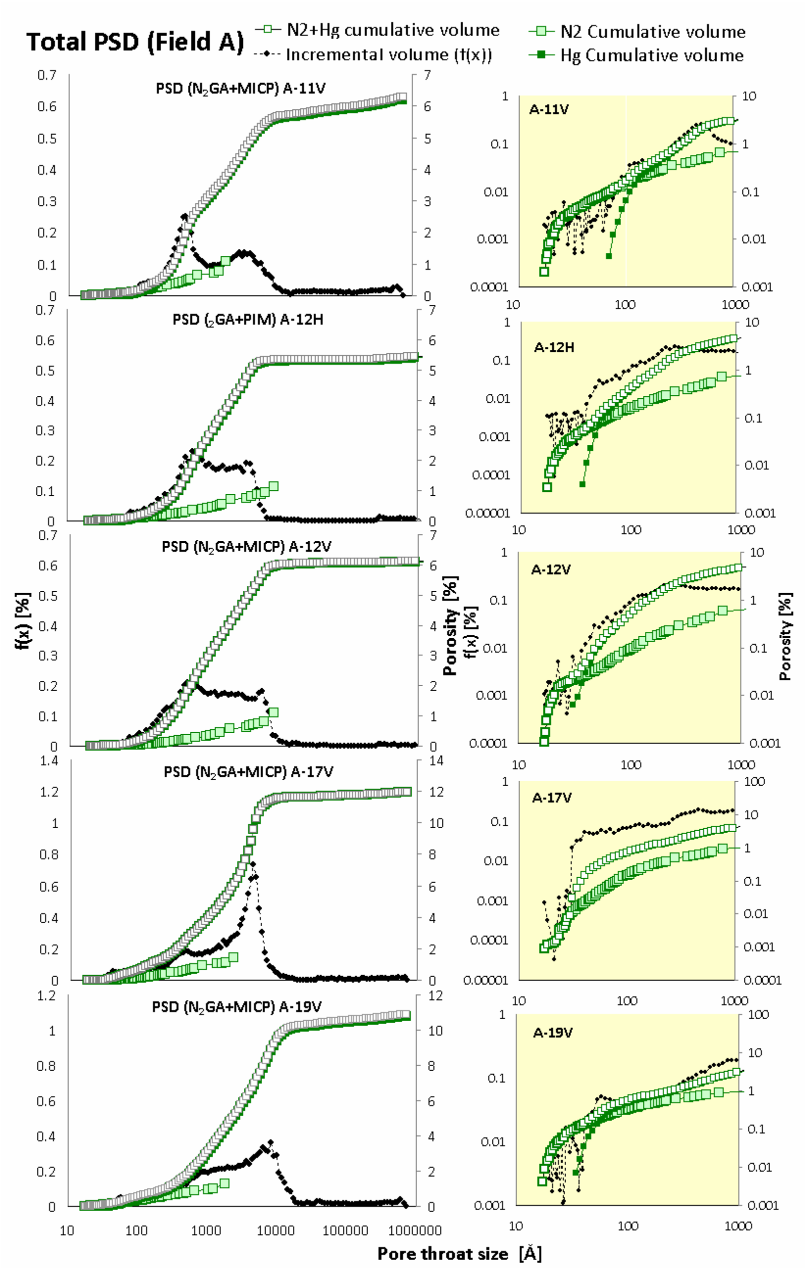

Figure 5.9: Curves of total PSD for field A: N$_2$GA+MICP combination.

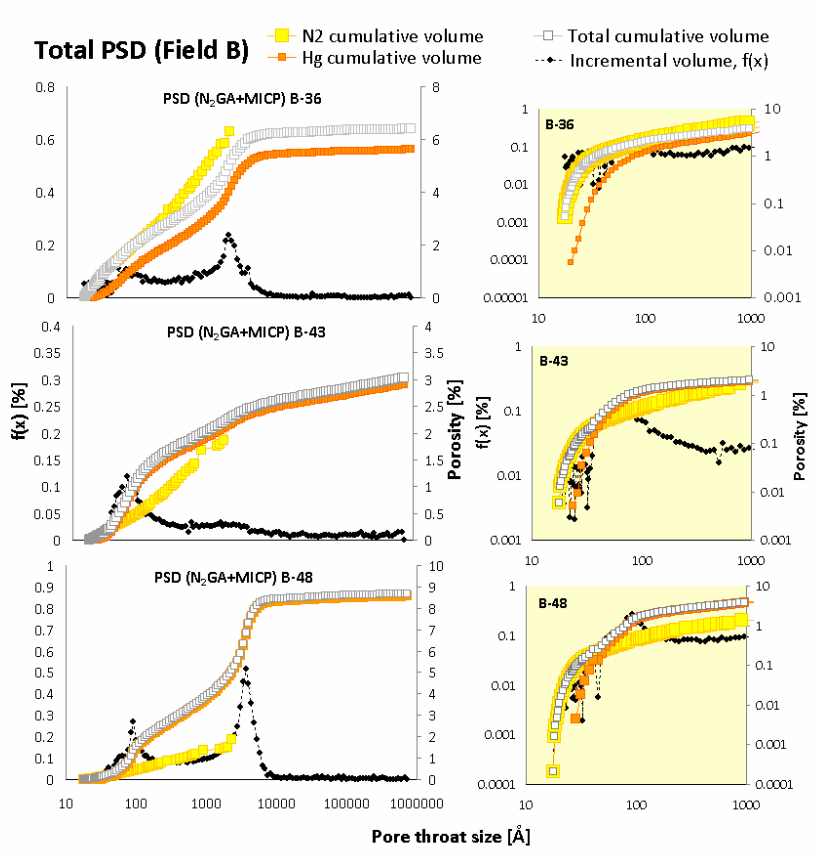

Figure 5.10: Curves of total PSD for field B: N_2GA+MICP combination.

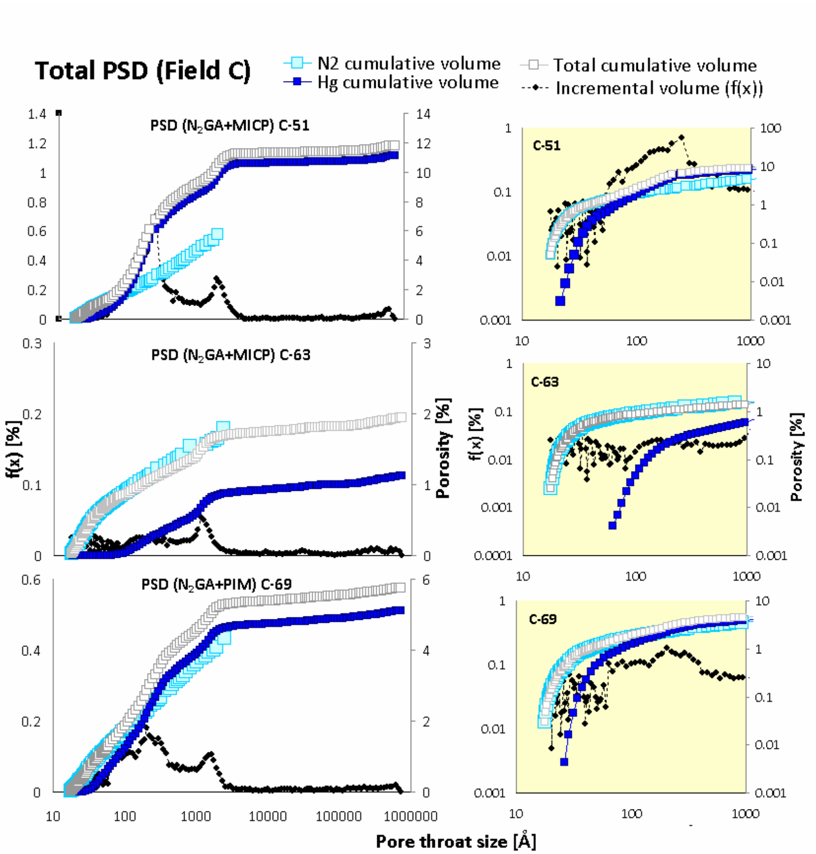

Figure 5.11: Curves of total PSD for field C: N_2GA+MICP combination.

5.2.5. Specific surface area results

Poiseuilles's and Carman-Kozeny's equations showed that permeability is a function of porosity, pore/pore-throat radius, surface area, and tortuosity (JAYA *et al.*, 2005; ZHANG, 2011). In many cases, the pore/pore throat radius has a greater effect than the porosity on the permeability (JAYA *et al.*, 2005; RUSHING *et al.*, 2008). Also the specific surface area is a property that characterizes the connectivity of the pore space and is therefore considered as one of the main factors affecting the permeability of soils and sedimentary rocks (ESEME *et al.*, 2012). Furthermore, the presence of pore-lining and/or pore-bridging clays in the rocks may reduce the permeability significantly by affecting the pore/pore throat radius and surface area (JAYA *et al.*, 2005). The results for the specific surface area (m^2/g) measured for TGS rocks of field A, B and C are illustrated in Figure 5.12. This figure depicts the measurements from the N_2GA data for the specific surface area calculated using the two models BET and Langmuir in ASAP 2020 Software. The Langmuir model leads to higher surface areas in all analyzed samples. This fact is expected because the Langmuir theory is better at describing microporous materials exhibiting Type I isotherms (SING *et al.*, 1985 classification) and so assumes adsorption limited to one monolayer. However as shown in Figure 5.4, most of the analyzed TGS samples are Type II (though with hysteresis loop) isotherms.

The adsorption analysis was carried out applying the BET and Langmuir equations for low relative pressures ($0.051 < P/P_o < 0.22$). This range was defined considering the linearity restricted to a limited part of the isotherm, usually not outside the P/P_o range of 0.05-0.30 (BRUNAUER *et al.*, 1938; GREGG and SING, 1982) required for solving the mathematical approach on BET and Langmuir equations.

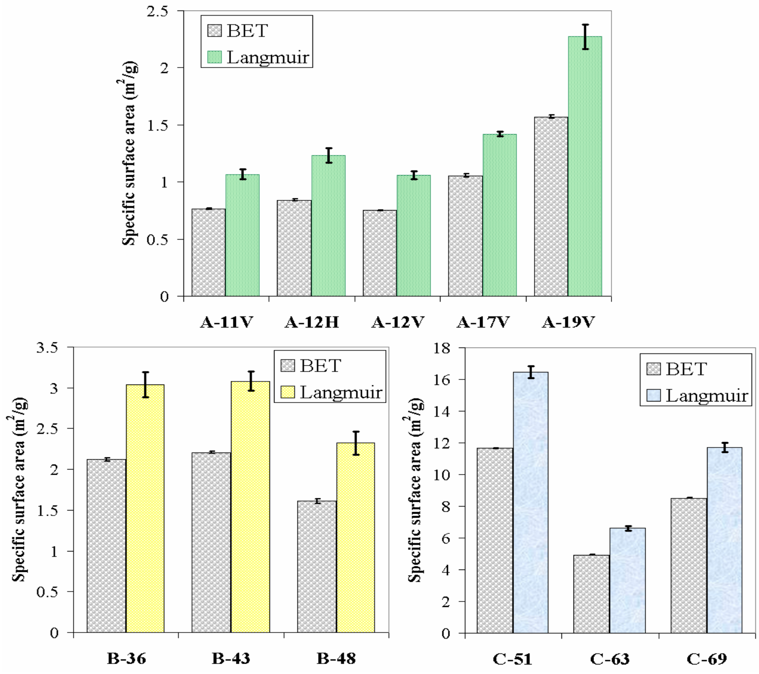

Figure 5.12: Surface area results using BET and Langmuir models.

6. PORE STRUCTURE CHARACTERIZATION, MULTI-SCALE 3D X-RAY TOMOGRAPHY AND PERMEABILITY PREDICTIONS

In this chapter we performed a study to obtain pore structure parameters using low-field NMR and 3D X-ray tomography where the PSD results were compared with those from the N_2GA and MICP combination. Also, the measured pore structure parameters obtained by the applied techniques were correlated to empirical models to estimate or simulate permeability. Only the samples of field A were analyzed in this chapter. The TGS samples of field B, C and D were not available to the further analyses.

6.1. Low Field Nuclear Magnetic Resonance analysis

The NMR measurements can provide information about the pore structure, the amount of fluid in-situ and interactions between the pore fluids and surface of pores, as numerous authors have explored the link between NMR measurements and petrophysical properties. In this sub-chapter the results of laboratory low-field NMR measurements performed in mini core samples of TGS rocks will be displayed and evaluated. Within these results it was possible to obtain the total porosity and correlated the relaxation time distribution to the pore size distribution. Besides, the identication of the specific pore types on each sample and the measurement of irreductible bulk volume (BVI) and free fluid index (FFI) regions to find $T_{2cutoff}$ and T_{2gm} values were performed to estimate the absolute permeability.

6.1.1. Acquired transverse relaxation curves

Each low-field NMR measurement yields a T_2 spectrum at saturated samples and these T_2 spectra are shown in Figure 6.1. Typically T_2 spectra for sandstones present unimodal (COATES *et al.*, 1999) or bimodal (HODGKINS and HOWARD, 1999; LIANG *et al.*, 2013) distributions; also REZAEE *et al.,* (2012) working with tight gas sandstones found a bimodal distribution with main T_2 times appearing as major dominant peak at T_2 about 1.0 ms and a minor tail distribution of T_2 in larger times around 10 to 40 ms, corresponding to the larger pores. YAO *et al.,* (2010) studding coals observed commonly three peaks for the analyzed samples. HABER *et al.* (2010) obtained for fine sand soil a bimodal distribution and for two silt loams soils multimodal distributions. They attibute this differences to the textural composition of each sample observing that with increasing silt and clay content, the T_2 relaxation times desreased significantly.

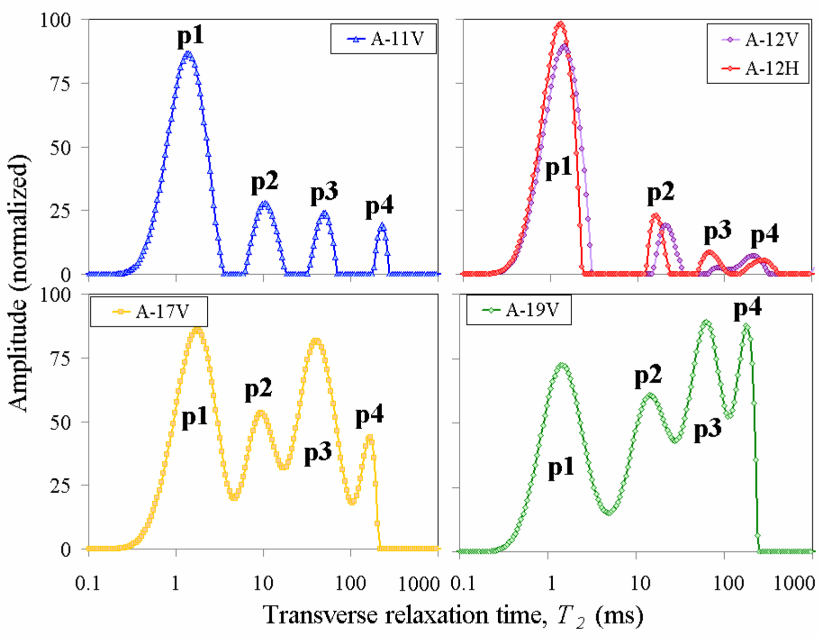

Figure 6.1: Amplitude normalized for transverse relaxation time (T_2) obtained with the NMR measurements in the five TGS of well A.

In the present work, as it can be seen in Figure 6.1 the analyzed TGS shown four peaks for the transverse relaxation T_2 distribution, strongly related to the pore structure and microestructure of analyzed TGS. From the PSD curves obtained by the N_2GA+MICP combination it was already possible to know that the samples to be analyzed by low-field NMR were comprised by relatively small pore sizes (~ 100 – 5000 Å) and low porosities (~ 6 – 12%), while textural aspects related to the mineralogy will be discussed in section 6.3. Mini cylinders of about 7mm x 7mm diameter and length were manufactured and considered representative enough to the low-field NMR analysis. The tests were performed in a 23 MHz Spectrometer having a 10 mm NMR tube and very low intervals of spin-spin relaxation time (starting from 0.5 to 250793 μs), also high number of scans (255), just large enough to span all of the resonance lines in the spectrum. For more details see section

3.7.3. The low-field NMR results gladdened that for the five TGS analyzed we observed four T_2 spectrum peaks identified by the relaxation time at 0.71–1.5 ms, 3.86–13.91 ms, 11.90–27.10 ms and 232.47–590.07. These peaks correspond to pores <0.1 µm, <0.5 µm, <2 µm and >2 µm, as it will be discussed in the next sub-chapter considering the results obtained from the N_2GA+MICP combination, and later also compared with the multi-scale tomography.

Figure 6.2 illustrates the difference of pore structures among the samples of Field A. In (a) one can see that the locations of each specific pore types (component) are very similar in all samples, while judging by the contribution in percentage of the components it is very distinct between the samples located in the upper regions (A-11V, A-12H and A-12V) from the ones located in the lower regions (A-17V and A-19V) of field A.

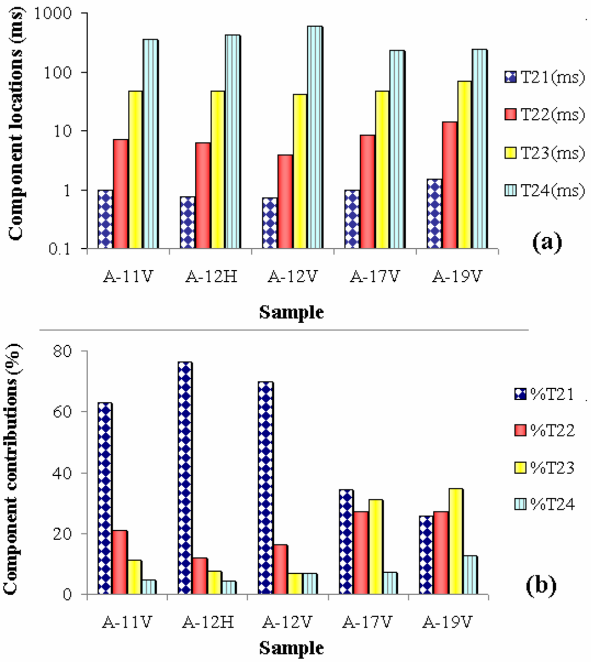

Figure 6.2: Pore component location (a) and contribution (b) identified from low-field NMR measurements in TGS of well A.

Low-field NMR analysis confirms the major pore size in samples A-11V, A-12H and A-12V occurring at about 1.0 ms. This amount of porosity for these samples is about 60-80% as shown in Figure 6.2(b), and it is considered to be the clay bound water content, which is much higher than for samples A-17V and A-19V (30-40%). Clay volume in homogeneous reservoir rocks can be estimated by conventional methods; however, a mixture of clay minerals, quartz, and calcite occurring in TGS notably complicates the interpretation making the usage of advanced techniques such as low-field NMR necessary. Comparing T_2 distribution of analyzed TGS, it can be seen that larger T_2 times are present only in A-17V and A-19V due to the lack of the macropores in the other three samples where only minor peaks or a tail distribution of T_2 around 10 to 200 ms were found. From T_2 spectrum of samples A-17V and A-19V one can assume that the proportion of macropore components is dominating. Based on these experimental results we can conclude that samples from upper regions in the analyzed field contain less volumes of pores responsible to the flow fluid in the reservoir (bound-fluid porosity), consequently lower permeability values are also expected, as it will be verified and discussed later. As a rule, the T_2 transverse relaxation time from rocks of field A reaches from 0.71 to 590 ms characterizing a spectrum which proved to be tetramodal. The measured NMR signals correlation to the pore size distributions are exposed as follows.

6.1.2. Surface relaxivity for PSD results

As exposed in Eq. (3.24) the measured T_2 values are a function of the surface to volume ratio *(S/V)* and the surface relaxivity *(ρ_2)* of the analyzed material. The value of ρ_2 can be estimated by comparing the NMR signal to the MICP curves (HOSSAIN *et al.*, 2011; REZAEE *et al.*, 2012). While studying petrophysical properties of greensand, HOSSAIN *et al.* (2011) found a conversion value for T_2 time signal of 20.4 µm/s and 28.4 µm/s for two distinct formations to generate P_c curves from NMR measurements; MARSCHALL *et al.* (1995), investigating carbonate rocks, arrived at a value between 4-20 µm/s while for sandstones it was between 7.92-25.1 µm/s. SONDERGELD *et al.* (2010), analyzing shale rocks, came across a surface relaxivity conversion of 50 µm/s and found consistent results of body pore sizes distribution with SEM observations. In our study, we used the pore size distribution curves obtained by the N_2GA+MICP combination to fit the low-field NMR T_2 distributions. The best fitting was reached using a value of surface relaxivity equaling 30 µm/s applied for the five analyzed TGS rocks. One can compare the PSD results for low-field NMR (Figure 6.3) and the N_2GA+MICP combination (Figure 6.4).

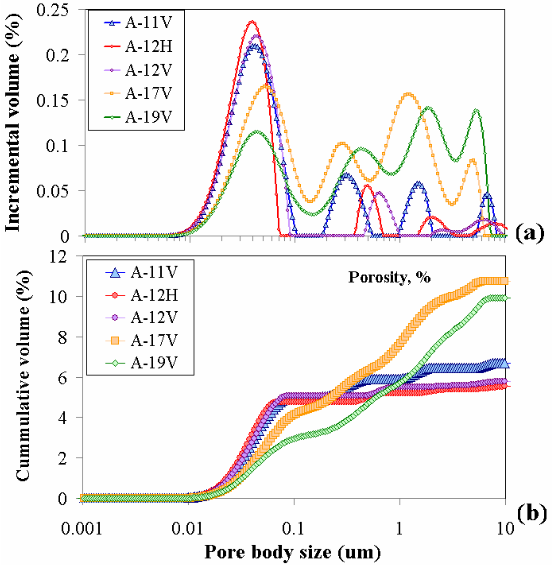

Figure 6.3: PSD of TGS field A measured by Low-field NMR T_2 signal: (a) incremental curves and (cumulative) curves.

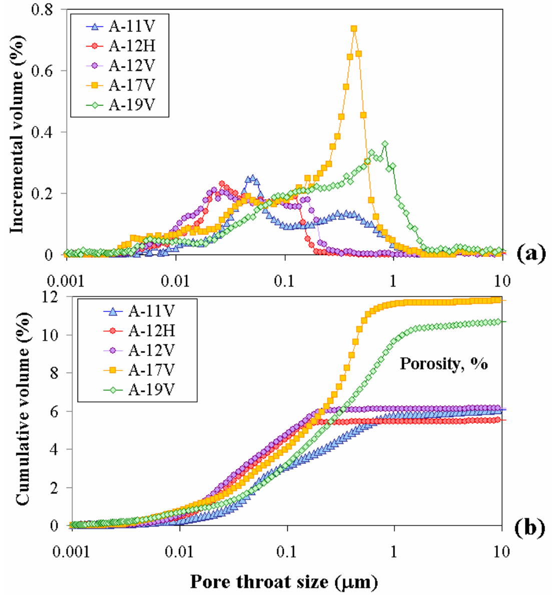

Figure 6.4: PSD of TGS field A measured by N_2GA+MICP combination: (a) incremental curves and (cumulative) curves.

In Figure 6.3 and Figure 6.4 (a) refers to the incremental pore volumes while (b) is the cumulative porosity where a good match was found between the NMR and N_2GA+MICP curves and porosity values. Naturally, when comparing the incremental PSD curves one can see that even though the spectrum's range of pore sizes is very analogous (e.g. from 0.004 to 4 μm in samples A-11V, A-17V and A-19V), the peaks tend to be distinct between both techniques: mainly tetramodal for low-field NMR measurements and bimodal for N_2GA+MICP results. This behavior can be explained pondering the principles of each technique as discussed in the next paragraph.

According to the Washburn and BJH equations utilized for the MICP and N_2GA data calculation, at each recorded pressure a volume of fluid is determined and converted into a cylindrical pore volume with a radius n. On the other hand, the connection between NMR measurements and petrophysical parameters stems from the strong effect that the rock surface has in promoting magnetic decay of saturating fluids. Therefore, T_2 is directly proportional to the pore size with the associated signal amplitude being the sum of the signal amplitudes arising from the fluid (hydrogen atoms in our case) in individual pores. Thus, the measured NMR porosity depends only on the fluid saturating the analyzed sample and it is the sum of connected and unconnected porosities. The PSD curves obtained from the N_2GA+MICP combination (Figure 6.4) are mainly comprised by pore ranges measured by MICP techniques, see sub-chapter 5.2.4, Figure 5.9 and Table 5.2. In a MICP experiment, the effective pore throat radius is calculated from the Hg injection pressure, and the injected Hg volume gives the corresponding volume of pores that can be accessed by that level of capillary pressure (or less). In this manner, Hg injection is really giving a pore throat size distribution, but at each limiting pore throat size, the actual volume of Hg that enters the sample is the volume of all associated larger pore bodies and pore throats (ink-bottle effect). It is generally thought that, from the original deposition environment and the diagenesis processes influencing the development of the rocks which will establish a reservoir, there will be a strong relationship between the existence of pore bodies and pore throats. A textural and structural evaluation in the five TGS rocks of field A will be done further in sub-chapter 6.3, as well as the quantification of pore bodies and pore throats using nano- and microCT (Figure 6.20 and Figure 6.21 "b" left side). As a consequence, MICP experiments performed in rocks having such a high amount of ink-bottle pore types will bring this influence in the results, whereas NMR measurements do not bring this effect turning to be an effective reliable method for obtaining PSD curves having both opened (connected) and closed porosity.

6.1.3. Measuring $T_{2cutoff}$ and T_{2gm} for permeability predictions

In section 2.5.3 it was stated that to predict the permeability from NMR results using Coates model, Eq. (2.31), and Mean-T_2 model, Eq. (2.32), the values of $T_{2cutoff}$ and T_{2gm} need to be calculated. To obtain the T_{2gm} in the present work we consider merely the mean value under the T_2 signal distributions. As a result, the free fluid index (FFI) and irreductible bulk volume (BVI) have roughly the same values. Progressing, to obtain the $T_{2cutoff}$ value, various works have been reported in the literature. E.g., SONDERGELD *et al.* (2010), studying shale rocks, found most of the signal in the T_2 distribution occurring below the 3 ms cutoff for “clay bound” water (or simple FFI). MARSHALL *et al.* (1995) reported that a typical value for $T_{2cutoff}$ in sandstones is 33 ms and that the cutoff T_2 correlates with rock type as defined by lithology and, especially, by the well of origin. HOSSAIN *et al.* (2011) defined $T_{2cutoff}$ as the relaxation time at the point where the cumulative porosity of the fully saturated sample equals the irreducible water saturation. So the cumulative porosity over the range $T_2>T_{2cutoff}$ was the macro-porosity and below the range $T_2<T_{2cutoff}$ was the micro-porosity with $T_{2cutoff}$ equal 3.68 ms and 5.21 ms for two distinct greensand formations. Since we performed low-field NMR only for cleaned samples 100% saturated with 10% KCl brine, our task was to define the region representing the clay bond water, which defines de FFI and BVI regions in our samples. As already discussed in section 6.1.1 we considered the first peak in the lower relaxation times as being the BVI volume whereas the values to the higher relaxation times were considered to be the FFI volumes. Succeeding, the FFI and BVI values were parameters employed to predict permeability using the COATES *et al.* (1999) model. Table 6.1 shows the obtained T_{2gm} and $T_{2cutoff}$ and respective FFI and BVI values for the five TGS of well A. All these parameters were used to predict permeability which will be also compared with the experimental PDP permeability, as will discussed in sub-chapter 6.4.1. The proceeding on choosing the T_{2gm} and $T_{2cutoff}$ values for samples A-12V, A-12H and A-17V is shown in Figure 6.5.

Table 6.1: Parameters obtained after defining T_{2gm} and $T_{2cutoff}$.

Samples	T_{2gm} Geometric mean values for TGS field A			$T_{2cutoff}$ From literature in sandstones			$T_{2cutoff}$ Measured for TGS field A		
	T_2 (ms)	**FFI**	**BVI**	**T_2 (ms)**	**FFI**	**BVI**	**T_2 (ms)**	**FFI**	**BVI**
A-11V	1.63	9.33E+04	9.56E+04	33.90	2.51E+04	1.59E+05	3.53	4.88E+04	1.35E+05
A-12H	1.26	8.19E+04	7.85E+04	33.90	1.34E+04	1.41E+05	2.59	2.50E+04	1.29E+05
A-12V	1.47	8.51E+04	8.38E+04	33.90	1.78E+04	1.45E+05	3.02	2.98E+04	1.33E+05
A-17V	9.87	9.25E+04	9.19E+04	33.90	5.69E+04	1.28E+05	4.80	1.09E+05	7.43E+04
A-19V	20.31	1.13E+05	1.11E+05	33.90	9.68E+04	1.27E+05	5.06	1.52E+05	7.02E+04

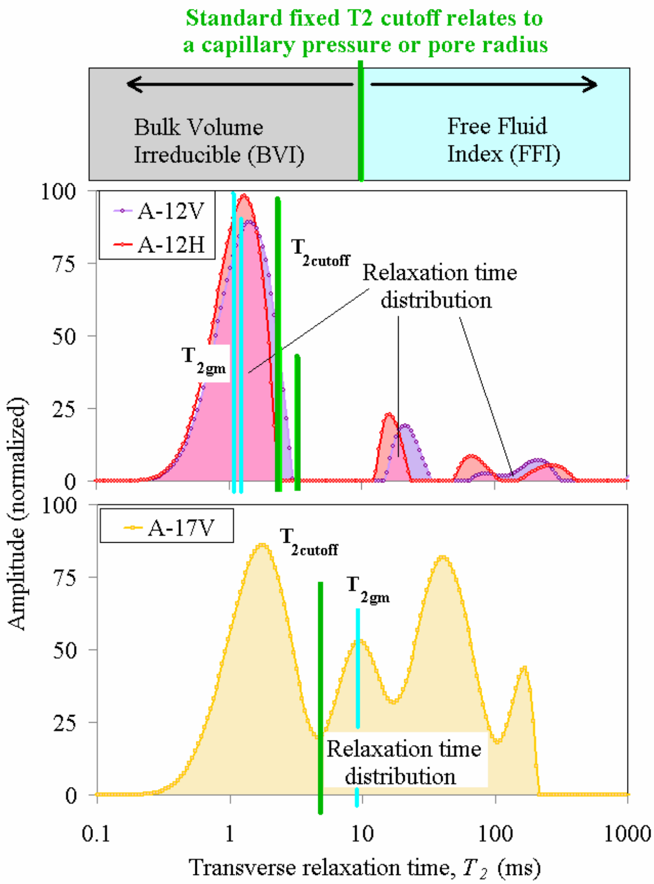

Figure 6.5: Defined T_{2gm} and $T_{2cutoff}$ values for samples A-12V, A-12H and A-17V. From $T_{2cutoff}$ values FFI and BVI volumes were obtained.

6.2. Results for the 3D X-ray nano- and microCT

The 3D high definition analyses were performed for two TGS samples of field A using nano- and microCT techniques. Figure 6.6 shows the analyzed samples and one projection of all acquired images. The criteria to choose samples A-11V and A-17V were based on the porosity and pore size range: as we want to evaluate (in three dimensions) the differences on the pore structures of low permeability TGS of field A, we decided to take samples showing as much as possible distinct PSD and porosity values, though having pore size ranges comprised in the resolution of the used X-ray CT equipment.

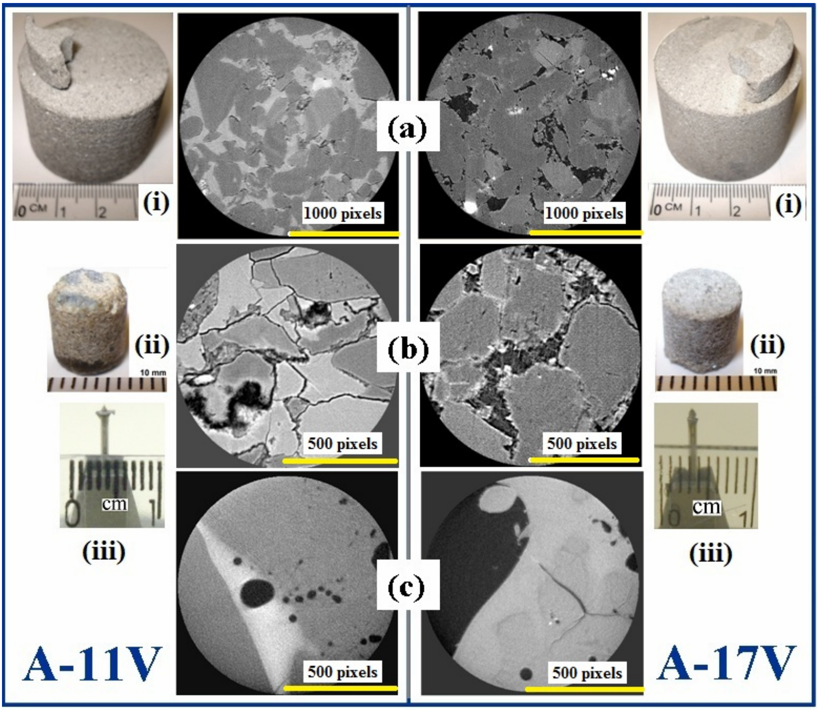

Figure 6.6: Macro and CT images of TGS A-11V and A-17V. Cores of 3.5 cm x 3.5 cm were used for extraction of the smaller specimens: 7 mm x 7 mm for microCT analysis of 2000 projections and 0.7 µm res. (a); 2 mm x 2mm for microCT analysis of 1600 projections and 0.3 µm res. (b) and 0.1 mm x 0.1 mm for nanoCT analysis of 1600 projections and 0.064 µm res. (c). The reconstructed CT slices (a, b and c) show the distribution of the solid and void structures present in the TGS with black being the pores.

The main 3D pore structure information aimed at was: porosity, pore size distribution, pore shape and tortuosity, connectivity, orientation and specific surface area. Having the porosity and PSD curves obtained from the combination of N_2GA and MICP techniques, as exposed in Figure 5.9, we selected then samples A-11V and A-17V for the nano- and microCT analyses. Figure 6.6 shows the macro and micro images of samples A-11V (left column) and A-17V (right column). In this figure it is possible to see (i) the original core samples from were pulse-decay permeability analyses were performed and slices for extraction of sub-samples were cut; (ii) mini core samples used for microCT acquisition and (iii) ultra mini core samples used for nanoCT analysis. (a), (b) and (c) are X-ray CT reconstructed slices for Res1, Res2 and Res3, with pixel sizes exposed in Table 4.2. From the image (c) acquired with the nanotomography, it is possible to see for both rocks the presence of spheric and unconnected pores located inside of the matrix grains.

6.2.1. 3D image processing and segmentation

The key for capturing image features that are relevant for simulations is good image segmentation. Because we are interested mainly in the pore structure analysis, the filters to remove impulse noise were applied based on pore phase segmentation. A filter transforms an image to emphasize or stress a specific feature of its structure (AVIZO*,* 2012). Filtering techniques are often useful to extract desired information from input data or simply to improve the appearance of the input data. Considering that our interest is related mainly with the study of pore morphology and pore sizes ranging below the micrometer resolution, we need the application of an ideal filter to remove the noise from the acquired 3D images and to enhance contrast between solid and voids. A common problem in filtering theory is to estimate a signal mixed with noise. Usually a solution is the moving average, where the value of each pixel is replaced by the average of its neighbors. This is based on the assumption that short ranged variations result from noise so the filtered output can then be viewed as the main trend of the function (ZHANG, *et al.,* 2013; AVIZO, 2012).

For all acquired resolutions using X-ray nano- and microCT, the Non-Local Means (NLM) filter was the best choice for the 3D image pre-processing. The NLM filter replaces a considered pixel by the weighted mean of all the pixels in the whole image or the surrounding neighborhoods (ZHANG, *et al.*, 2013). Only for Res1 (in both samples

A-11V and A-17V) two additional filters were performed in the following order: non-local means (NLM) → Despeckle → Median. For a better understanding on the theory and applications concerning to the NLM, Despeckle and Median filtering algorithms, see the related literature (LOIZOU and PATTCHIS, 2008; DANDEKAR, 2008; IQBAL *et al.,* 2013; ZHANG *et al.*, 2013). Figure 6.7 shows the usage of additional filters in 3D images of sample A-17V Res1.

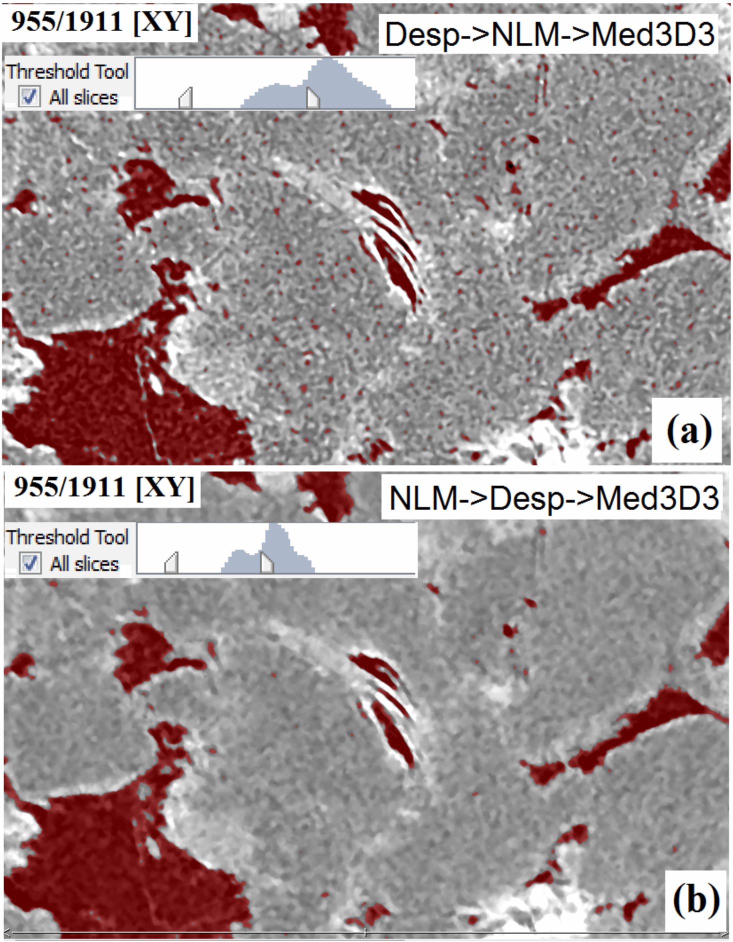

Figure 6.7: Distinct filters used in the pre-processing of the 3D image acquired for sample A-17V in the Res 1. The value of histogram-based thresholding for the pore segmentation was 130 for both (a) and (b).

Considerable efforts were taken on finding the best sequence of filters in the pre-processing analysis of Res1, since the acquired images were comprised of very small artifacts corrupting an accurate segmentation even after applying the NLM filter. As one can see in Figure 6.7 (a) the black spots on the segmentation process are identified as mismatch pores, which are in truth image noise. Both (a) and (b) pore segmentations were done using the same value of histogram-based thresholding at the 16 bits image. In (a) the data set shows results of super-estimated pore segmentation inside of grains while in (b) the data set shows less noise. We believe that the main reasons for the occurrence of very small artifacts on 3D images of Res1 are related to the usage of such a high voltage energy (80 keV) and to the sample size (7 mm^2) which might have been still too big for resolution of 0.7 µm.

After choosing an adequate filter, among a wide range of techniques we used histogram-based iterative thresholding to reach a best-fit segmentation. Thresholding becomes a simple but effective tool to separate objects from the gray levels of the pixels belonging to the background where the gray-level samples are clustered in two parts as background and foreground (object), or alternately are modeled as a mixture of two Gaussians (SEZGIN and SANKUR, 2004). The foreground is represented by gray-level 0, that is, black and the background by the highest luminance is 255 in 8-bit images. The output of the thresholding operation is a binary image from which the rock pore structure can be extracted, quantified and simulated. All filtering and thresholding steps were executed using *Avizo 7.1* Software. The quality control taken during the segmentation process was based on the histogram-based thresholding, 2D and 3D pore segmentation views as shown in Figure 6.8.

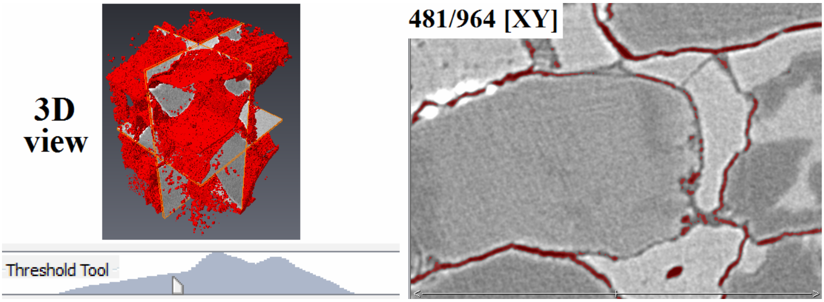

Figure 6.8: Thresholding histogram, 3D and 2D views displayed during the pore segmentation for sample A-11V, using *Avizo* Software.

6.2.2. Extraction of segmented 3D pore media

Figure 6.9 and Figure 6.10 show the 3D results of X-ray Nano- and MicroCT images and segmented pore media for A-11V and A-17V.

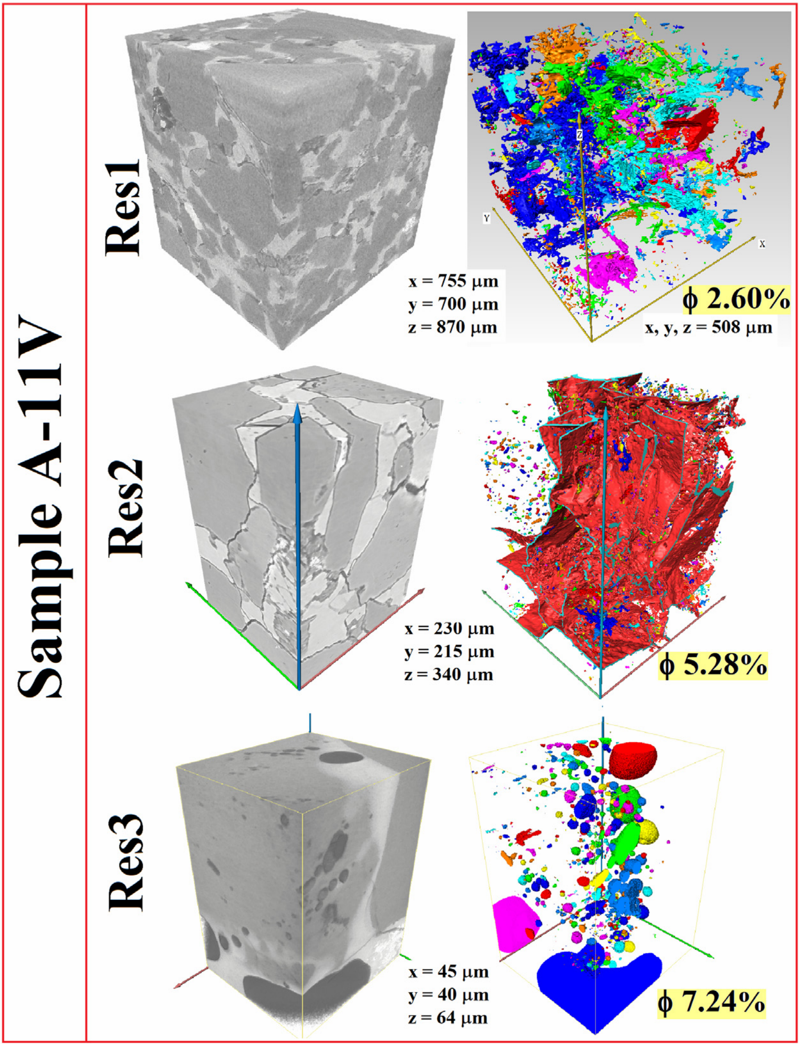

(a) **(b)**

Figure 6.9: 3D results for sample A-11V and A-17V: Reconstructed images from the X-ray Nano- and MicroCT (a); segmented pore media with isolated pores being represented by distinct colors (b).

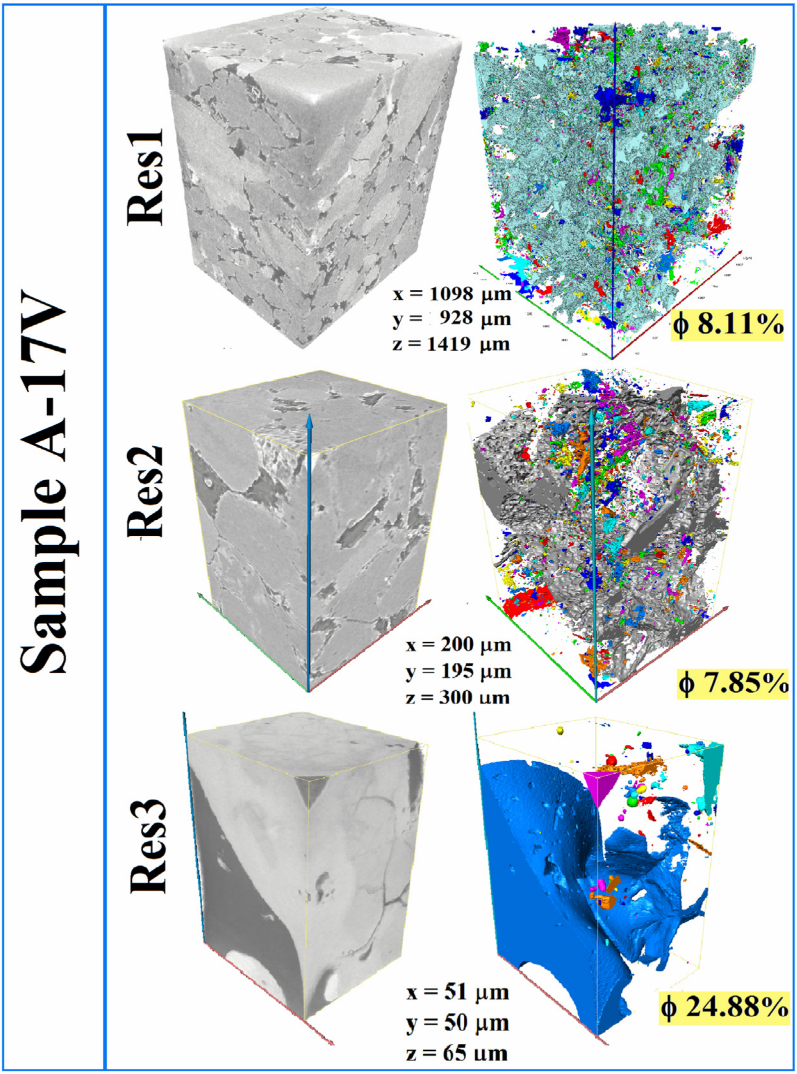

(a) **(b)**

Figure 6.10: 3D results for sample A-17V and A-17V: Reconstructed images from the X-ray Nano- and MicroCT (a); segmented pore media with isolated pores being represented by distinct colors (b).

A three-dimensional pore-network can be used to scan topology and pore space factors (tortuosity, shape, orientation, etc), in which the effective pore radius are distributed according to a given pore size distribution (PSD). Also, the connectivity of the pores, thickness of the network, and the effect of pore blockage can be observed from the pore-network extraction. There are innumerous theories and methods concerning the pore-network extraction to understand porous materials behaviors, based on adsorption concepts (CAI *et al.,* 2007) or on micro-computerized-tomography images (DONG and BLUNT, 2009). In the present work topological and equivalent resistor network (skeleton) methods were performed for the segmented pore-network, extracted using *Avizo* Software. For the three acquired resolutions both figures (Figure 6.9 and Figure 6.10) show the 3D microstructure images (a) and the 3D topological pore structure (b). As already explained above for all investigated resolutions the reconstructed 3D images were optimized by removing impulse noise through the application of filtering procedures, followed by thresholding, segmentation, pore morphology extraction and finally quantification analyses.

From the extraction of the segmented 3D pore structure based in a gray level histogram (Figure 6.9(b) and Figure 6.10(b)), as one can see, depending on the pixel resolution taken for the X-ray Nano- and MicroCT acquisition and also on the nature of the sample's pore system, the pore structure can be comprised of a connected or unconnected pore network. In these figures connected pores share a unique color while unconnected pores have distinct colors. For sample A-11V, e. g., only in Res2 it was possible to observe a connected pore network which represents 97.53% of the pore phase. On the other hand for sample A-17V the connected pore network could be observed in all resolutions and it represents for Res1, Res2 and Res3, respectively, 96.78%, 96.24% and 98.80% of the porosity measured in each resolution. The connected network observed for A-17V in Res1 and Res2 can be explained considering that this sample is constituted by a higher amount of pores bigger in body and throat sizes therefore a smaller resolution (Res1) was already able to detect the entire network while not detecting the connections in sample A-11V. Whereas for Res3, since the size of the samples to be analyzed ranges in the order of 100 μm in length and even smaller in diameter, it makes it hard to draw any conclusion about the pore network; a single pore can already make up a good portion of the sample, as it happened in sample A-17V, compare Figure 6.10(b).

6.2.2.1. Generating 3D sub-samples

Intending to extract the statistical information from the pore network, i. e. pore size distribution (frequency and volume) and coordination number, it is necessary to separate the pore bodies from their throats. There are different methods that have been presented in the literature to fulfill this task. In this work we initially tried to apply the watershed algorithm, a tool belonging to the *Avizo Fire* Software. As it will be discussed in the next section, we did not obtain good results for the analyzed samples, leading us to choose other methods:

(vii) Mathematical morphology using *Imago 2.3.40* Software (IMAGO), see related theory (MARQUES FILHO and VIEIRA NETO, 1999; HAI *et al.*, 2001; MOREIRA; 2013);

(viii) Generation of an equivalent resistor network (skeleton) using *C3DE* Software (CUNHA, 2012).

For this task we choose for each resolution one region of interest (ROI) to be analyzed considering the criteria that (i) for the pore size distribution analysis we intended to investigate the same amount of pixels in all resolutions measured in each sample (and as big as possible), and (ii) the softwares used to generate the 3D images for the mathematical morphology and skeleton only accepts cubic shapes with identical x, y and z axis.

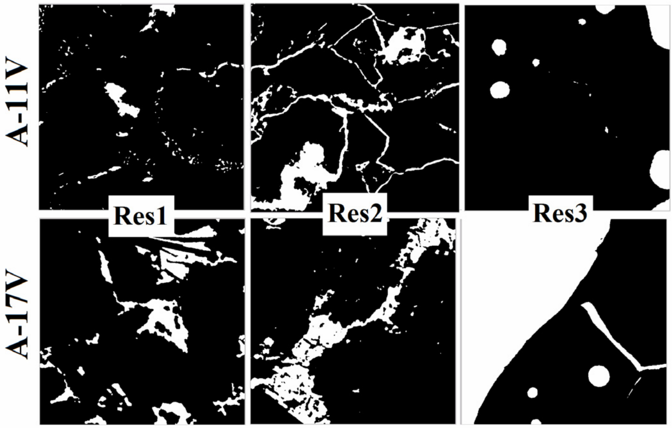

Figure 6.11: Representative cross-section through reconstructed A-11V and A-17V porous media with white representing the pore phase and x=y (μm) alike respectively: 453.3 and 448 (Res1); 210 and 186 (Res2); 38.4 (Res3).

In this matter, the three resolutions of samples A-11V and A-17V analyzed by X-ray Nano- and MicroCT are constituted by a fixed amount of pixels (600 x 600 x 600) therefore varying in size with a dissimilar investigated portion of the sample volume. Figure 6.11 shows the 2D cross-sections for each generated sub-sample for the three resolutions chosen and named as Res1, Res2 and Res3. As laid out before in Table 4.2 the three resolutions are just slightly different for Sample A-11V and A-17V. For sample A-11V, e. g., Res1 shows a pixel size of 0.75 μm investigating a volume of 9.11E+07 μm^3; Res2 displays a pixel size of 0.35 μm and a volume of 9.26E+06 μm^3 and Res3 has a pixel size of 0.064 μm leading to a volume of 5.66E+04 μm^3. Just to emphasize the differences between the investigated 3D volumes, Res2 would fit 10 times in to Res1, and it would take about 1600 distinct measurements with Res3 to cover the same volume as one shot with Res1. Therefore depending on the pore size more defined resolutions (such as Res3) might not present representative results of pore sizes distribution.

6.2.2.2. Autocorrelation function of 3D sub-samples

Intending to verify how representative the three resolutions of analyzed samples are from the original rock medium, we applied the autocorrelation function to the porosity. The autocorrelation function properties are defined as statistical averages of a binary phase function *Z(x)* that is equal to unity if a point *x* in space is occupied by void and zero otherwise (ADLER *et al.,* 1990):

$$Z(\overline{x}) = \begin{cases} 1, & \text{when } \overline{\text{x}} \text{ belongs to the pore space} \\ 0, & \text{otherwise.} \end{cases} \qquad \textbf{(6.1)}$$

The porosity ϕ and autocorrelation function $C(\bar{u})$ can be easily measured on 2D or 3D binary micrographs of segmented pore space as the first two moments of the binary phase function $Z(\overline{x})$ (CUNHA, 2012):

$$\phi = \langle Z(\overline{x}) \rangle ,$$

$$C(\overline{u}) = \langle Z(\overline{x}) Z(\overline{x} + \overline{u}) \rangle . \qquad \textbf{(6.2)}$$

The autocorrelation function gives the probability of two points separated by a distance *u* belong to the same image phase, in this case, ϕ. The vector $\bar{u}$ is called the displacement factor of image phase or simply Lag. From Eq. **(6.2)** it is possible to assume that:

1. If $\overline{u} = \vec{0}$,

$$C(\vec{0}) = \left\langle Z(\overline{x})^2 \right\rangle = \left\langle Z(\overline{x}) \right\rangle = \phi \qquad \textbf{(6.3)}$$

Taken that from the definition of $Z(\overline{x})$, Eq.(6.1), $Z(\overline{x})^2 = Z(\overline{x})$. This is also the maximal value that *C* (Eq. **(6.2**) can assume because with the increasing of $\left|\overline{u}\right|$, the product of the functions $Z(\overline{x})$ and $Z(\overline{x}+\overline{u})$ (which can only be 0 and 1) do not reach the value ϕ.

2. When $\left|\overline{u}\right| \to \infty$,

$$C(\overline{u}) = \left\langle Z(\overline{x}) Z(\overline{x}+\overline{u}) \right\rangle = \phi.\phi = \phi^2 \qquad \textbf{(6.4)}$$

In this case there is no correlation between the points in the same image phase; therefore the functions are statistically independent. This is then the minimum value of autocorrelation function *C(x)*.

For a “statistically homogeneous” porous medium, ϕ is a constant and *C(u)* is only a function of the lag vector *u*, i.e., they are independent of the location vector *x* (LIANG *et. al*., 2000).

Having the 3D sub-samples images (ROI = cubic 600 pixels) of Res1, Res2 and Res3 from samples A-11V and A-17V as shown in Figure 6.11, where the white phase represents pore, we extracted the autocorrelation functions using *Imago 2.3.40* Software. The volumes of image resolutions (Res1, Res2 and Res3) have a porosity of 3.22%, 5.77% and 5.40% for sample A-11V and, 9.62%, 9.38% and 43.17% for sample A-17V. The results comparing the target autocorrelation functions are shown in Figure 6.12 where the minimum of the curves represent ϕ^2. From this figure it is possible to see that for both samples Res1 and Res2 exhibit a long spatial correlation and revel close agreement suggesting that the low-order statistical properties (porosity and autocorrelation function) contain sufficient information to reproduce the real rock porous media. The representative elementary volume (REV), defined as the smallest volume of a material that captures the global characteristics (in our case porosity), is even smaller than the analyzed ROI for Res1 and Res2. On the other hand the spatial correlation of Res3, for both samples is very short. One can note that for A-17V Res3 the low level of correlation curve has a much higher value due to the high porosity comprised by this analyzed ROI. Considering that some loss of geometric and topological information may be expected to result at higher resolutions (such as Res3), even though the statistical information remains intact (IONNIDIS and CHATZIS, 2000) we judge that Res3 of sample A-17V does not represent the referred rock porous medium leading us to abandon this result. Although the importance of having structural information of the smaller pores in such accurate scale as Res3 is crucial in the study of unconventional reservoirs, attributing reproducibility to this resolution might be dangerous since it does not contain sufficient statistical information.

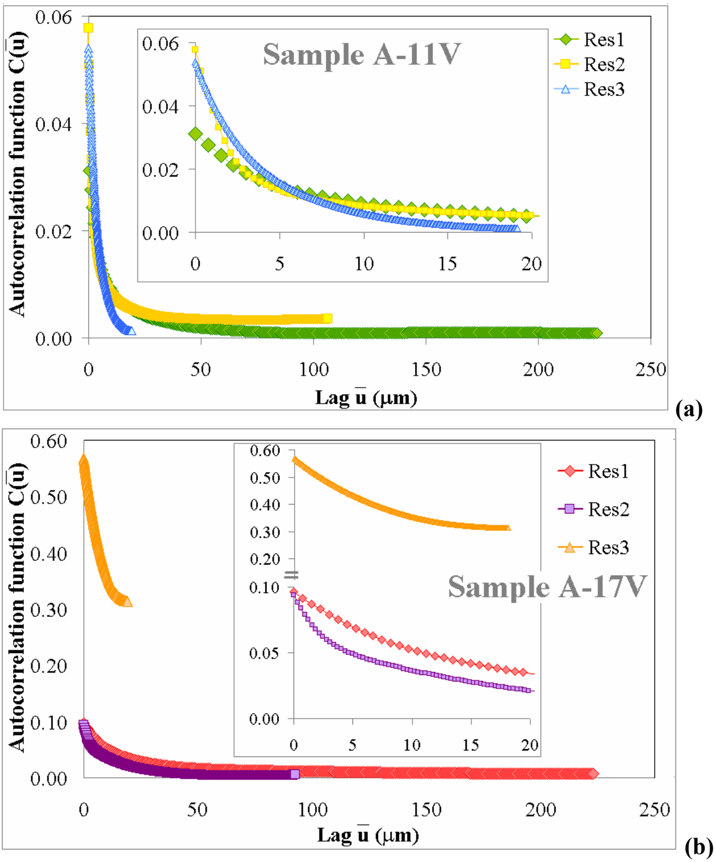

Figure 6.12: Effect of the pore space resolution: average autocorrelation of the 3D segmented images in all three resolutions obtained for samples A-11V (a) and A-17V (b).

6.2.2.3. Applying watershed algorithm

The watershed algorithm from *Avizo Fire* Software, was performed in the resolution Res2 for sample A-11V and Res1 for sample A-17 to characterize pore shape, tortuosity and orientations; only for sample A-17V (Res1) it was used to obtain pore size distribution separating in particles the main connected pore network. The principle of watershed algorithm is to compute watershed lines on the gray-level image for black objects or on the inverted image for white objects (pores in our investigation). It is a combination of the fast watershed, distance and numerical reconstruction algorithms. It detects surfaces that separate agglomerated particles and these surfaces are subtracted from the initial image. When performing watershed algorithm analysis the meaningful parameter to be chosen is the "depth of valley" or contrast factor.

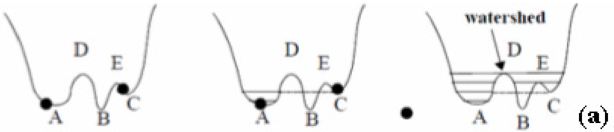

The curve represents three minima (A, B and C) and two maxima (D and E). A is flooded at levels 1 and 2, but not B, then it reaches point C. From the next level, A and C are flooded until reaching point D. D belongs to watershed but not E.

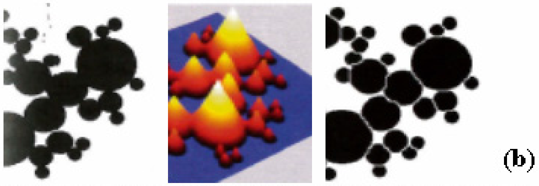

Watershed segmentation on an image of touching circles of different sizes: original, "surface" representation of the Euclidean distance map (EDM) and watershed result.

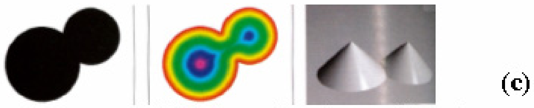

Euclidean distance map (EDM) for touching features: binary image, EDM with pixels colour-coded to show distance from boundary and rendered display showing pixel heights.

Figure 6.13: Principles of watershed and distance maps algorithms (AVIZO® 7, 2012; RUSS, 2007).

In Figure 6.13(a) a short explanation about this principle is exposed and so smaller the contrast factor is chosen to be (lower levels of flooding) more separated the pore-network will be and smaller pores will be identified. Simply put, the contrast factor is the parameter deciding how distinct the separation of two or more pores has to be in order to be counted individually. Thus, without the watershed command the 3D segmented image is comprised by one or several connected networks considered as singular big pores only and a high amount of smaller unconnected pores (see the results of “NoBin” for A-17V in Figure 6.14 and Figure 6.15). By applying the command the connected network structures will be broken into a certain amount of separated pore networks or simple pores, depending on the chosen contrast factor. Smaller the contrast factor (here also named “Bin”) is more connected pores will be considered individually and higher the amount of separated pore structures will be. Figure 6.15 compares the results obtained for incremental and cumulative pore volumes (a) and frequency (b) for sample A-17V (Res1) using contrast factors equal 1 and 10 and original (NoBin) pore structure. In Figure 6.14 one can visualize in 3D and 2D the results of pore separation after applying Bin1 and Bin2 (as well as NoBin) for the analyzed ROI = 1000^3 pixels.

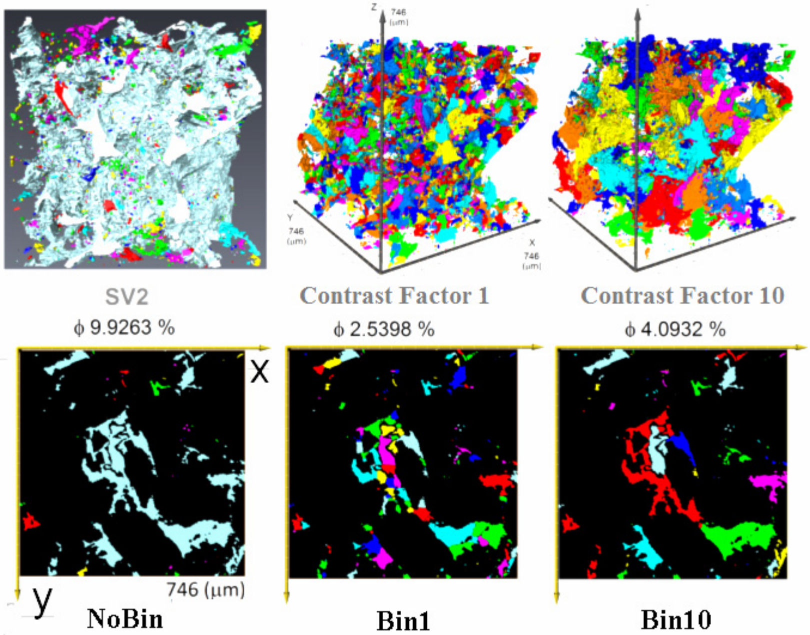

Figure 6.14: 3D and 2D visualizations for chosen ROI of sample A-17V (Res1) analyzed by watershed algorithm.

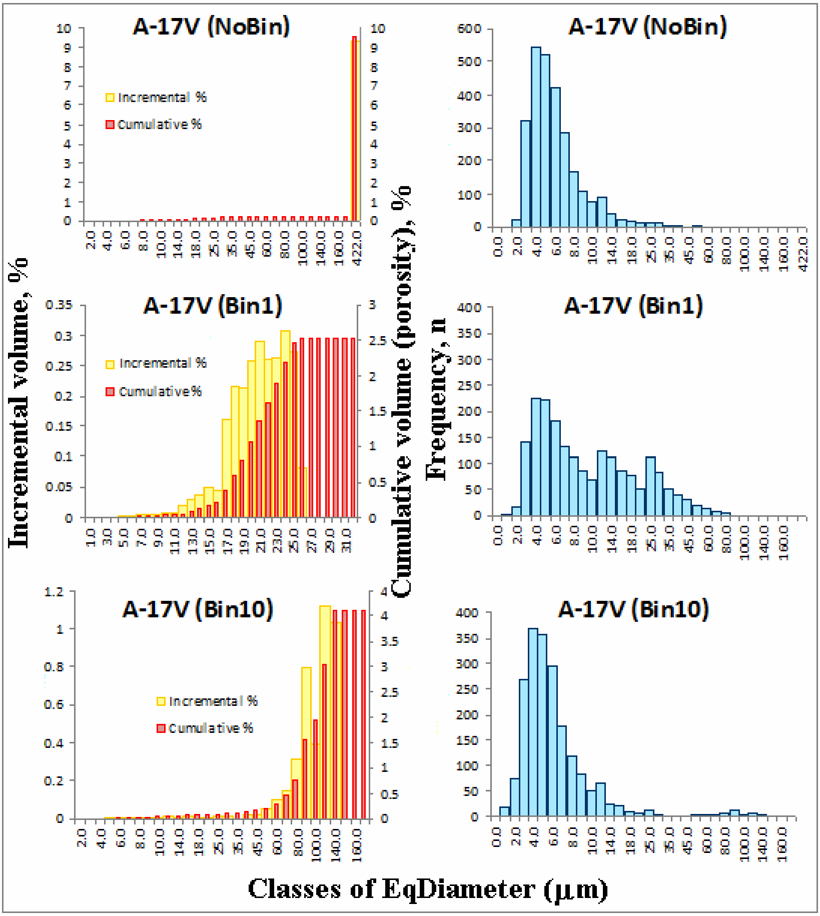

(a) (b)

Figure 6.15: Effect of contrast factor using watershed algorithm for the (a) pore size distribution in volume and (b) in frequency applied in a 3D segmented image (1000^3 pixels) of sample A-17V (Res1).

In Figure 6.15 the (a) column shows the incremental (yellow) and cumulative (red) volumes and the (b) column the frequency of pore sizes. After measuring the pore volumes in the 3D image, the program transforms every isolated porous object into a regular sphere displaying the equivalent diameter in the graph for pore size evaluation purposes. The calculation performed for the equivalent diameter shown in Figure 6.15 is:

$$d_{equivalent} = \left(\frac{6 \times V_{3D}}{\pi} \right)^{\frac{1}{3}} \tag{6.5}$$

An interesting observation can be made when comparing the frequencies of pore sizes against the pore volumes for each contrast factor. Without applying the watershed algorithm, though the pore sizes have a Gaussian distribution, the cumulative pore volume is almost entirely made up by a single connected network which is transformed into one big sphere with the diameter of 422 µm. After the application of the watershed algorithm with the contrast factor 10 (Bin10) the pore volumes show a Gaussian distribution fitting the corresponding frequencies, but the overall porosity is considerably reduced. With the contrast factor 1 the porosity is further reduced while the frequency of pore sizes is not anymore distributed in a Gaussian shape.

Besides being a simple and straightforward tool for pore separation, the watershed algorithm in particular with non-convex shapes may miss or separate too much (AVIZO® 7). We observed that for obtaining pore size distributions on the analyzed tight gas sandstones (comprised of constricted and heterogeneous pore's structure shapes), one negative point was found: the amount of porosity decreases considerably from 9.92% in "NoBin" to 2.54% in "Bin1" and 4.10% in "Bin10", thought the shape of incremental curve in Bin1 (bimodal) looks acceptable. However for obtaining the pore size distributions in all resolutions for the analyzed samples we decided to use only the mathematical morphology (Imago) and the equivalent resistor network (C3DE program) algorithms. The results are discussed following.

6.2.2.4. Mathematical morphology and equivalent resistor networks

Both mathematical morphology (MM) and equivalent resistor network (Skeleton) models were used to calculate pore size distributions for two analyzed samples in all resolutions as shown in Figure 6.11. Only Res3 for sample A-17V was not analyzed which besides not being possible to generate the skeleton due to the limitations of the computer in process extremely high porosity in the ROI, was considerate not representative enough for the PSD analysis.

The approach for the mathematical morphology analysis by *Imago 2.3.40* Software consists in the basic idea of taking binary pore morphology to probe an image with a simple, pre-defined shape, drawing conclusions on how this shape fits or misses the shapes in the

3D image. This simple "probe" is called structuring element, and is itself a subset of the chosen space or grid. The structuring element of tridimensional dominium used in Imago was the D345 for a 3D image (MOREIRA, 2013). The upper part of Figure 6.16 illustrates the obtained results for pore size distributions of individual scales of samples A-11V and A-17V, using mathematical morphology (Imago).

The other approach used is based on the equivalent resistor network (skeleton) model and was calculated using C3DE program (DONG and BLUNT, 2009; CUNHA, 2012). The principle is the implementation of a fully parallel thinning algorithm for 3D that extracts the smaller axis converted in equivalent cylinders volume (throats) which are connected to bigger spaces then converted in equivalent inscribed spheres volumes (pore space). Thereby this model has the advantage of calculating independently the pore and throat volumes. Figure 6.17 exposes the results for the generated skeletons using C3DE program in the 600^3 volumes pixels, while the lower part of Figure 6.16 illustrates the results for pore size distributions of each individual scales of samples A-11V and A-17V.

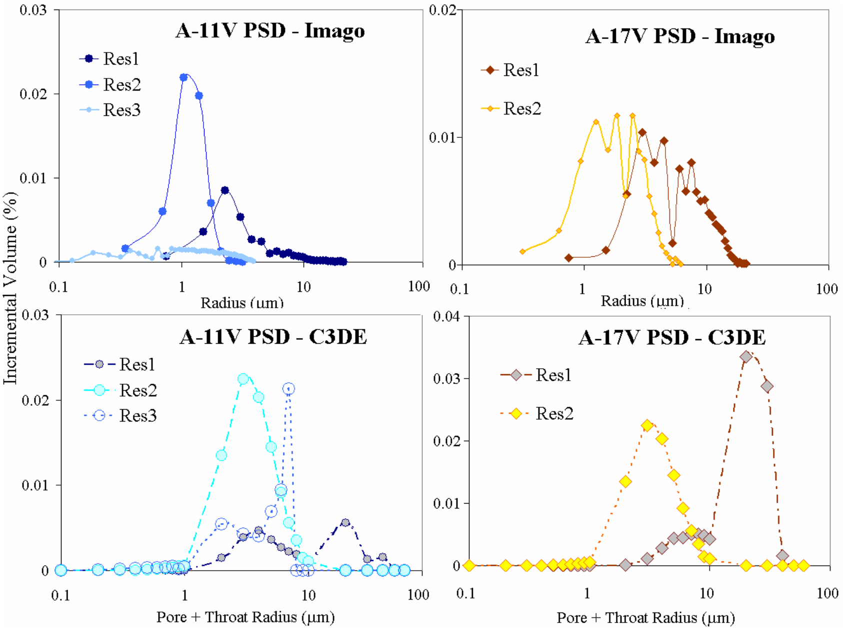

Figure 6.16: PSD of each scale obtained by mathematical morphology (Imago) and equivalent resistor network (C3DE) models.

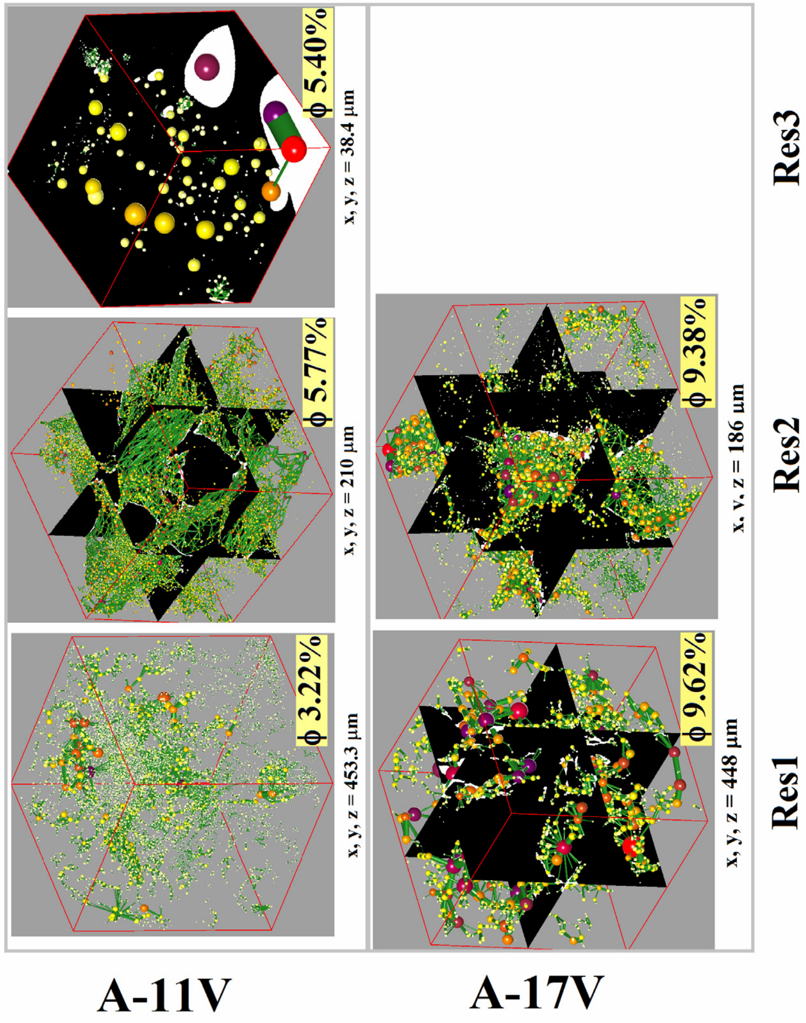

Figure 6.17: Generated skeletons for each acquired resulotion in samples A-11V and A-17V, using C3DE Software.

Comparing the results between PSD curves from the mathematical morphology and generated skeleton (Figure 6.16) one can see that (with the exception of Res3 in sample A-11V) for all acquired resolutions the shapes of the curves tend to be similar for both methods, though MM identifies a bigger amount of pore volume in the smaller pore ranges. This fact is predictable remembering the principles related to each of the two used methods. Also the experimental results, as shown in Figure 6.4(a), for PSD measured by the N_2GA+MICP combination (see samples A-11V and A-17V) indicate a much lower range of pore sizes, bellow to 1 µm. Nevertheless we decided to investigate the results given by both methods. One advantage of the generated skeleton method is that besides calculating the fraction of pore sizes it also gives the frequency in number (n) of each pore and throat size genereted (see Figure 6.18 and Figure 6.19). As a result it allows the operateor identify which pore and throat sizes are more representative in each analyzed scale resolution. So we propose the integration of 3D multi-scale PSD X-ray tomography by usage of the frequency curves. Also, the PSD results given by the MM method (which considers only pore fraction volumes) were used to integrate the multi-scale approach developed by MANTOVANI (2013), which in turn was compared to the obtained results, as will be presented as follows.

6.2.3. PSD from multi-scale 3D X-ray tomography

6.2.3.1. Combination of pore size frequencies

Figure 6.18 and Figure 6.19 show the results of PSD for A-11V and A-17V samples, obtained from the pore-network extraction using C3DE program. As one can see both pore's body and throat volumes are displayed with (a), (b) and (c) rows showing the incremental, the cumulative and the frequency volumes, all against pore radius. From these graphics one can see (for each resolution) that the ranges of pore sizes for the higher peaks in the curves of incremental pore volumes and pore frequencies do not necessary match. This is one indication that when analyzing PSD from image analysis the curve of pore size frequencies besides showing information about pore fractions, gives an idea of which pore classes are more representative in the analyzed sample volume. Therefore we suggest that for evaluating PSD from acquired 3D images data of pore size frequencies and volume fractions (incremental volume) needs to be displayed and evaluated together.

Having all the incremental pore volumes in the distinct resolutions, the question arises how to determine which scale (and range in this specific scale) should be included in the final combined 3D multi-scale PSD having distinct incremental pore volumes from each resolution (scale). As a general approach, the frequency (n) of pore sizes was taken into consideration to evaluate which pore class was best represented in which resolution. Since the size of the analyzed volume differs from resolution to resolution, a comparison of the absolute frequency (n) would not lead to the desired parameter. Therefore, the frequency (n) was transformed for each resolution into a percentage of the total amount of pores identified (see Appendix A, the column frequency (%)). The highest percentage of frequency for each pore class identifies the resolution that represents that pore class best and therefore its value of the incremental pore volume was taken into the calculation of the overall result. Naturally, the combination of frequencies are made up from the most accurate resolutions measured in the analyzed sample (in our work Res3 for A-11V and Res2 for A-17V) considering that this scale has the smallest pore sizes measured in more details. As an additional safeguard, it was defined to control the results by cross-comparing the incremental values directly against each other; e.g., in Res1 analyzing the throats of sample A-11V the pore class with the highest percentage of frequency (2 μm) an incremental porosity of (63.01%), while Res2 had an incremental porosity of 38.86%. In this case the pore size class (2 μm) was taken from Res2 since it was the highest frequency percentage in that scale although lower then the 63.01% in scale Res1. In such an occasion, if the 3D images do not present something unusual, the general rule is overridden. All calculation using the frequencial pore size combination obtained by the skeleton algorithm in C3DE software for samples A-11V and A-17V, the sub-volumes were the ones showed in Figure 6.17.

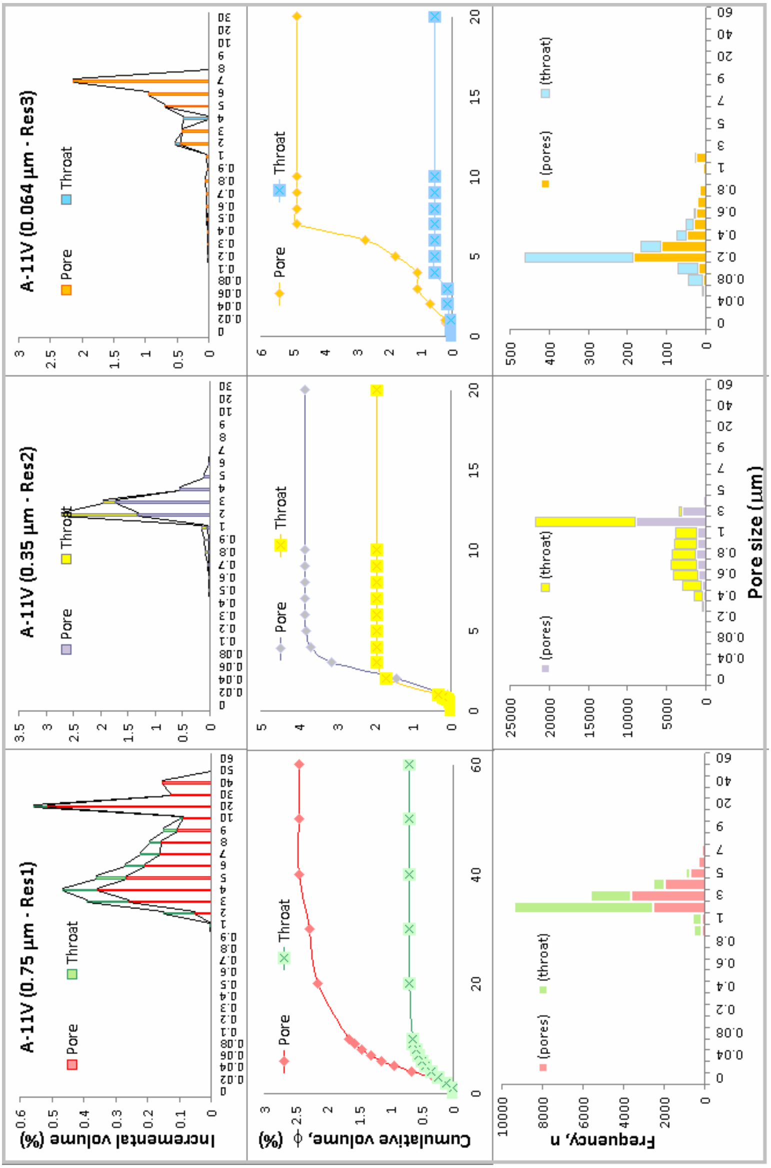

(a) (b) (c)

Figure 6.18: Sample A-11V: classes of incremental volume (a) cumulative volume (b) and frequency (c) against pore radius obtained using the C3DE program for Res1, Res2 and Res3.

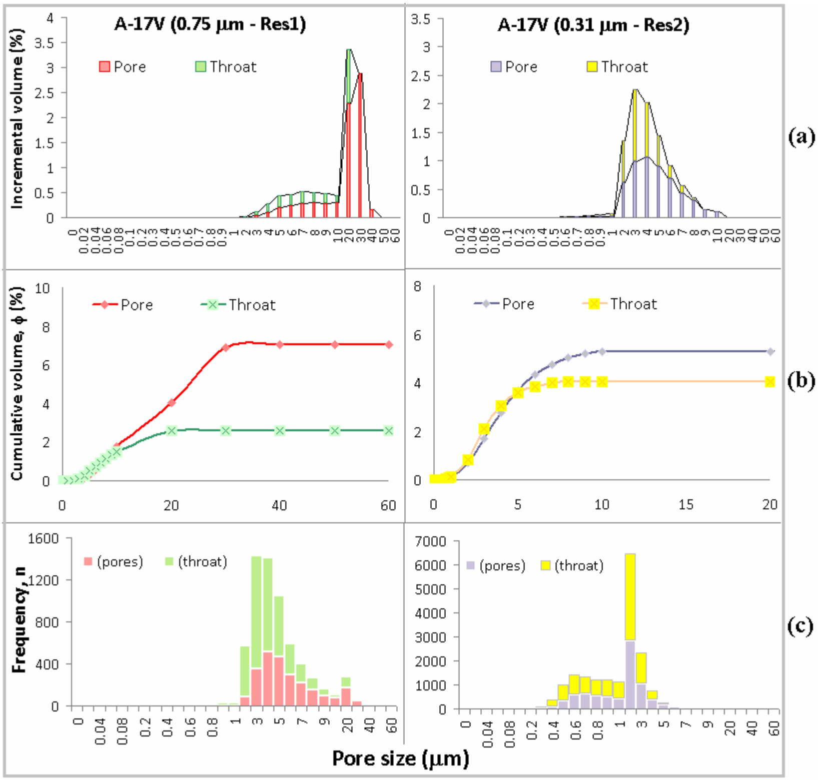

Figure 6.19: Sample A-17V: classes of incremental volume (a) cumulative volume (b) and frequency (c) against pore radius obtained using the C3DE program for Res1 and Res2.

The results obtained for 3D multi-scale PSD using the combination of frequencies are shown in Figure 6.20(b) for sample A-11V and Figure 6.21(b) for sample A-17V, where one can also see separated the incremental and cumulative distributions for throat and pore bodies. In Figure 6.20 and Figure 6.21 we also displayed the PSD results: (a) when a simple addition of all resolutions would be applied without considering the overlapping of pore classes (note as a consequence a higher value of porosity); (c) of multi-scale model proposed by (MANTOVANI, 2013) and validated in carbonate reservoir rocks, for both PSD's pore network obtained by mathematical morphology (Imago) and equivalent resistor (C3DE); (d) of N_2GA+MICP combination and low-field NMR.

Comparing all results of incremental PSD curves obtained by X-ray 3D multi-scale with N_2GA+MICP combination and low-field NMR results, one can see that the spectrum of pores size distribution obtained by X-ray is shifted right toward bigger pores. When the pore network extraction is performed using mathematical morphology model that effect is a bit lessened but still present. On the other hand the results of porosity (shown by the cumulative pore volumes) were closer to the experimental N_2GA+MICP and low-field NMR values when the combination of frequencies was performed, still overestimated even with the lack of small pores range which were not acquired in the measured 3D X-ray resolutions. PSD from the X-ray CT images is supposed to reflect the ‘‘real’’ pore geometry as X-ray CT images include both connected and isolated pores. However, because of the resolution limitation, the PSD from this method must be limited too.

One advantage on obtaining the curves of frequential number of pores sizes accounts to help the operator on choosing the range of pores in each scale to be more representative in the combined multi-scale 3D X-ray PSD. Finally, the results of integrating PSD from multi-scale 3D X-ray tomography indicate the quality of the imaging method allowing one to probe the spatial distribution of the macro and part of the micro porosity contributions across distinct scale resolution. As already stated in the literature review, the effective porosity in tight gas sandstones is typically much lower than the total porosity because of diagenesis. The type and magnitude of diagenesis governs the connectivity of the primary porosity. Unlike conventional sandstone reservoirs that are characterized mostly by a primary intergranular porosity system, TGS may exhibit several other types of porosity - including both primary and secondary inter-granular porosity, detrital matrix porosity, micro-porosity, and grain fracture porosity (RUSHING *et al.*, 2008). The identification of such smaller pores is still a challenge in the 3D X-ray tomography technology.

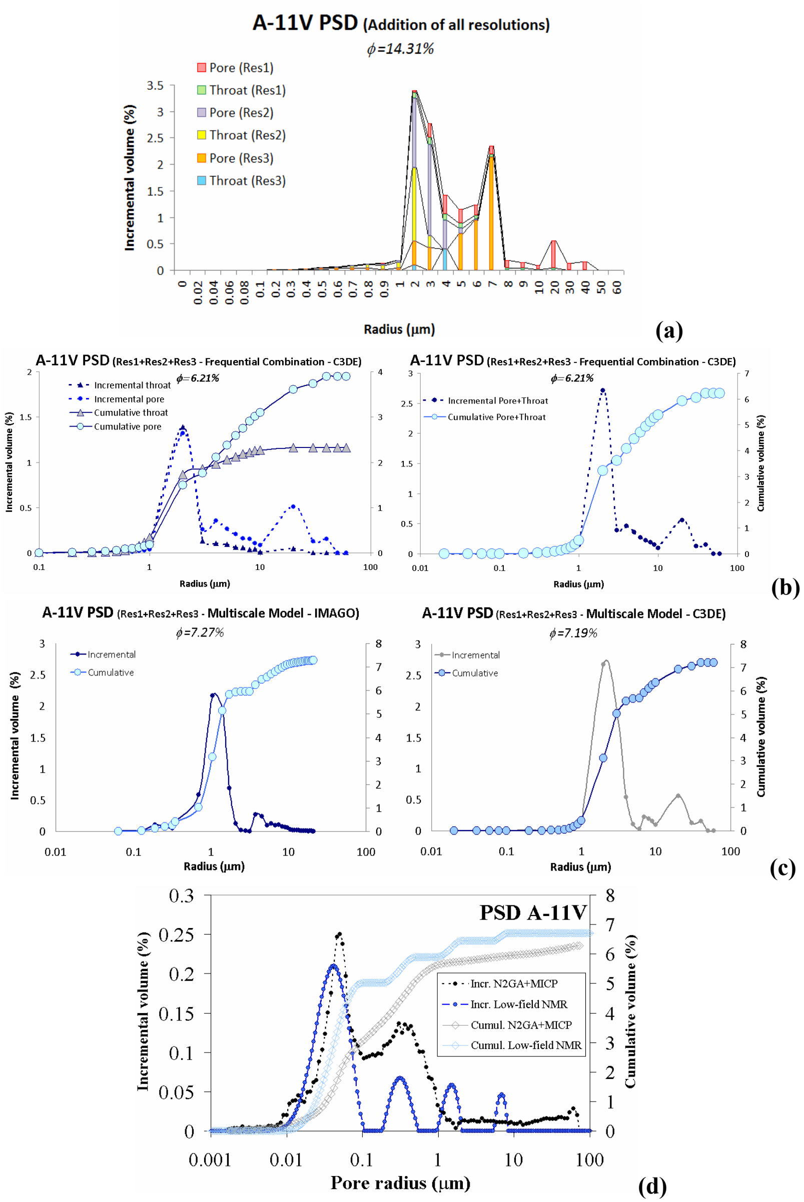

Figure 6.20: Comparison of PSD results for A-11V: (a) simple addition of all scales; (b) frequency combination; (c) Multi-scale model (MANTOVANI, 2013); (d) N_2GA+MICP combination and low-field NMR.

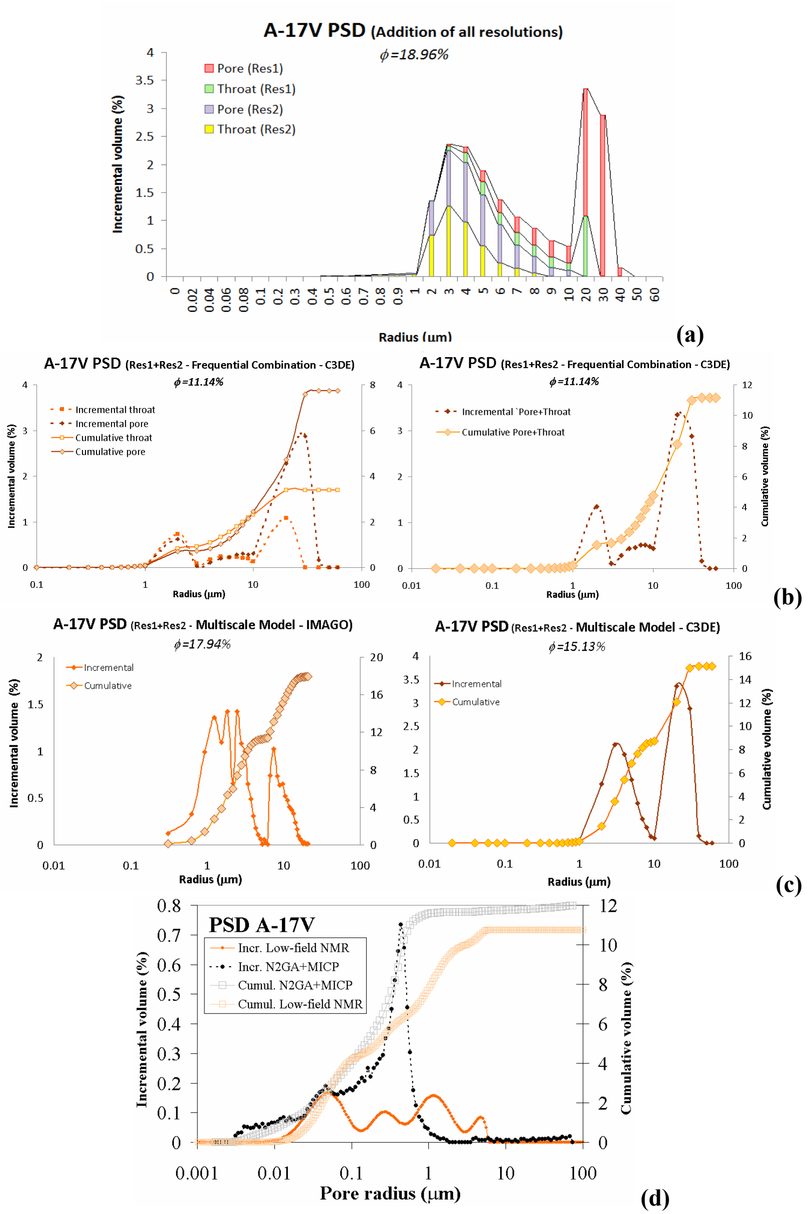

Figure 6.21: Comparison of PSD results for A-17V: (a) simple addition of all scales; (b) frequency combination; (c) Multi-scale model (MANTOVANI, 2013); (d) N_2GA+MICP combination and low-field NMR.

6.2.4. Quantifying pore's geometry properties

Key issues concerning tight gas reservoirs are related to their heterogeneities, tortuosity and hydraulic connectivity. Knowledge of a pore's reservoir geometry, axis orientations, and body connectedness is vital for meaningful reservoir modeling. The complex interconnection of multilateral and heterogeneous sand bodies is a result of lateral migration in conjunction with vertical stacking of fluid-based channels disposed in the depositional environment of the reservoir. The oil and gas industry has long recognized the importance of pore structures (i.e., pore and pore throat dimensions, geometry, size, distribution, etc.) on fluid flow and storage properties in all types of porous media. Understanding the pore structure and its properties is probably even more critical in tight gas sandstones since diagenesis often modifies the original pore structure and reduces the average pore throat diameter, typically causing an increase in both tortuosity and the number of isolated and/or disconnected pores (RUSHING *et al.*, 2008). Figure 6.22 illustrates the shapes and sizes of some isolated pore and the connected pore network observed in the TGS sample A-17V Res1. Following important pore characteristics related to the 3D pore medium of tight gas sandstones were measured and discussed.

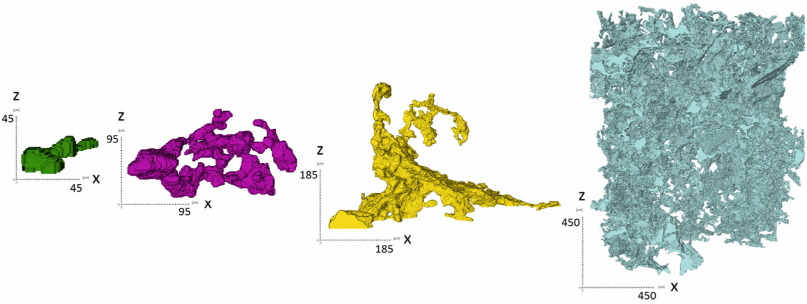

Figure 6.22: Distinct pore shapes and sizes found in rock A-17V Res1. Axes are given in µm.

6.2.4.1. Determination of pore connectivity

Pore connectivity is another critical property of the pore structure which defines how well the pores are connected and therefore will affect the local fluid flow (PENG *et al.,* 2012). The connectivity is a measure of the number of independent paths between two points in the pore space phase and, hence, of the degree of interconnectedness of the pores.

The permeability of sandstones is a direct function of the size and number of the interconnected pores (DULLIEN, 1992). In the last century innumerous researches (e. g., BARRETT and YUST, 1970; LIN and COHEN, 1982) performed metallographic serial sectioning of samples on porous media and have formed the basis of a number of pore structures studies. Most of the studies dealt with the problem of edge effects in the construction of the branch-node chart (treatment of the 2D stacking data). Nowadays with the use of X-ray CT techniques, the evaluation of the 3D connectivity of pore structures leads to more accurate results. The average values (Table 6.2) and distribution of pore connectivity (Figure 6.23) were calculated using the equivalent resistor network generated by C3DE program. As one can see for the higher resolutions on each sample the connectivity distribution is increased to the lower values indicating that the analyzed volume is comprised by a considerable amount of either isolated or low connected pores, while A-11V Res2 and A-17V Res1 show a Gaussian type curve. On Table 6.2 besides the average connectivity (coordination) number the volume-weighted average is also displayed. From this value we can determine the relative importance of neighboring pores related to the pore volume. As one can see, for both samples A-11V and A-17V, in Res1 and Res2 the averages as volume-weighted get bigger, indicating that the bigger pores are more connected. On the other hand for Res3 (sample A-11V) the bigger pores are the ones more isolated.

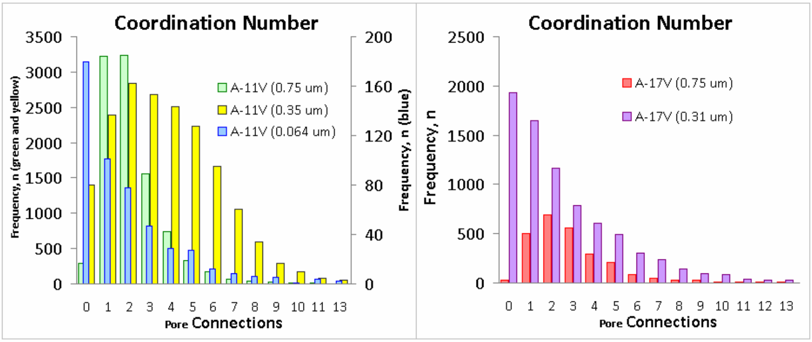

Figure 6.23: Distribution of coordination number (connectivity) for samples A-11V and A-17V.

Table 6.2: Average and volume-weighted average coordination number of samples A-11V and A-17V for the acquired resolutions.

Sample		**A-11V**		**A-17V**	
Resolution (μm)	Name	Average	Volume-weighted average	Average	Volume-weighted average
0.7	Res1	2.24	7.74	3.11	8.85
0.3	Res2	3.69	6.06	2.63	9.41
0.064	Res3	1.96	1.27		

6.2.4.2. Tortuosity and shape factor measurements

Tortuosity *(τ)* is one of the most widely studied petrophysical parameters yet it is not very well understood (ZIARANI and AGUILERA, 2012). As already previously discussed in this work, the tortuosity and shape factor (F_o) of a porous medium are fundamental properties that account for the sinusoidal flow path through its structure and can be empirical related to permeability estimation (CARMAN, 1937). The tortuosity and shape factors were measured on samples A-11V and A-17V in terms of path length and geometrical definitions from the 3D images measured by X-ray nano- and microCT. The calculations for the tortuosity were already described in section 2.3.3, while the obtained shape factor is equal to (AWCOCK and AWCOCK, 1995):

$$\frac{P_{Crofton}}{4 \times \pi \times A}, \qquad \textbf{(6.6)}$$

where A is the area of segmented object and $P_{Crofton}$ is its Crofton perimeter as defined by DO CARMO (1976). The analyses were performed using *Avizo Fire* Software on the 3D segmented pore structure of Res1, Res2 and Res3 (Figure 6.9(b) and Figure 6.10(b)) and the results are shown in Figure 6.24. For both tortuosity and shape factor properties, the values found in the sample A-11V were bigger than in A-17V. From the N_2GA, MICP, low-field NMR and 3D X-ray CT analyses we can judge that sample A-11V is comprised by grain textures and sizes much finer than A-17V (this conclusion is also supported in the subsequent chapter) which are mainly responsible for the heterogeneities in the pore network and decreasing of the analyzed parameters. Furthermore, studying mudrocks, YANG and APLIN (2007) fitted experimentally a value for $F_o(\tau)^2$ equal to 1000, confirming that smaller pores usually tend to be more tortuous. The measured tortuosity and shape factors were used in the Kozeny-Carman equation to estimate permeability in the analyzed TGS field A

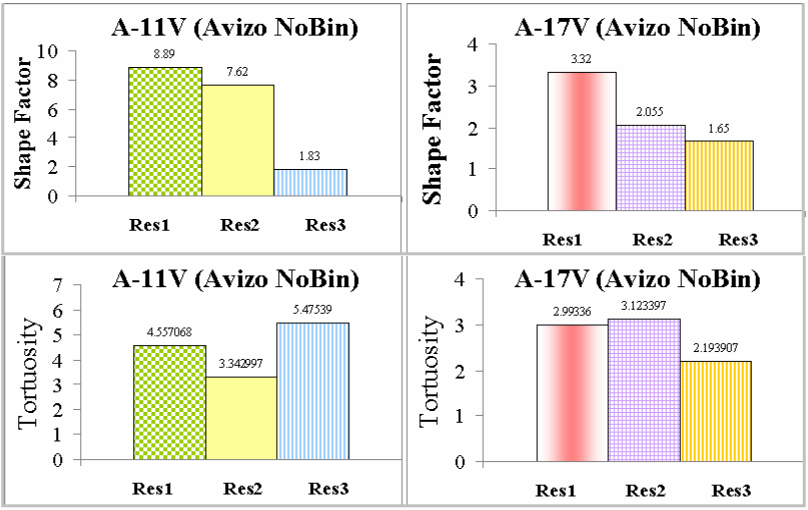

Figure 6.24: Obtained results of tortuosity and shape factors measurements from distinct resolution of samples A-11V and A-17V.

6.2.4.3. Surface area measurements

Because of the complexities in the microstructure of natural rocks the surface area obtained depends very strongly on the method used to make the measurement. Surface areas estimated by the BET gas adsorption method frequently differ by several orders of magnitude from those obtained by image analysis of the same rocks (KLEINBERG, 1996). Measurements differ primarily due to the presence of clay, which has a huge surface area that is included in BET gas adsorption measurements but missed by pore image analysis. A further problem is that pore sizes in natural rocks range over several orders of magnitude. Figure 6.25 shows the specific surface area results obtained from 3D X-ray CT analyses measured in the pore networks by Avizo (Figure 6.8 and Figure 6.9) and C3DE (Figure 6.17) programs.

The BET method generated the largest total surface area for both rocks (A-11V = 0.76 m^2/g, A-17V = 1.00 m^2/g). Specific surface area estimated with X-ray CT images was calculated as the measured total surface area with (Avizo or C3DE) divided by the sample mass, which was in turn calculated as the volume times the bulk density (A-11V = 2.66 g/cm^3 and A-17V = 2.65 g/cm^3) measured by MICP experiments. There may be certain scale effects on bulk density which will result in different specific surface area. However, the values estimated from the high- and low-resolutions X-ray CT images are at least one order-magnitude smaller than the BET measured. This indicates the significance of small pores in the pore surface area for analyzed TGS.

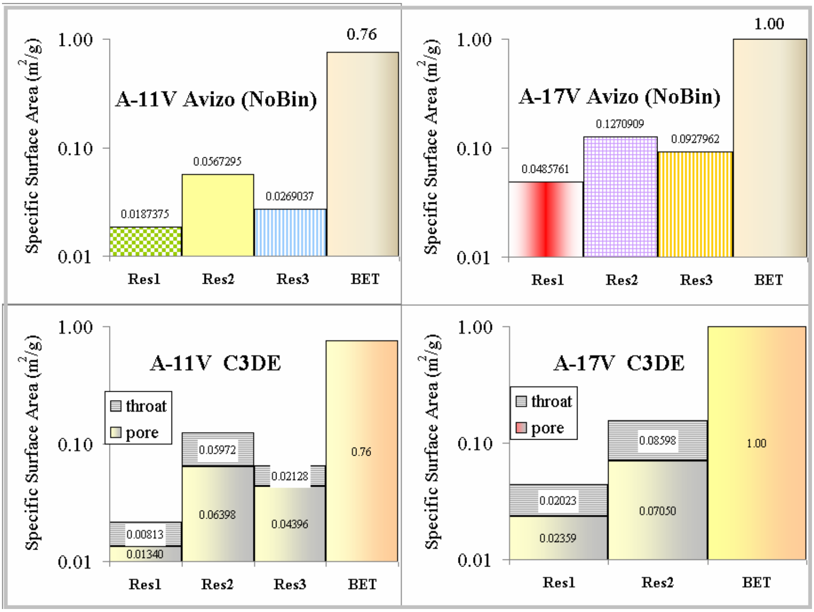

Figure 6.25: Specific surface area results from X-ray CT using Avizo and C3DE programs.

6.2.4.4. Aspect ratio distribution, phi and theta orientations

The pore aspect ratio spectrum may be simplified into round pores and cracks. The latter refers to the pores with aspect ratio equal to or less than 0.1 while 1 would be a perfect sphere. The amount of cracks and round pores are related to lithologic factors; clay contents effect on the elastic moduli of rocks may be ascribed to its role in changing the pore aspect ratio spectrum (ZHANG and BENTLEY, 2003). XU and WHITE (1995) set the pore aspect ratio to be 0.15 for sand-related pores and 0.04 for clay-related pores, attributing velocity reduction in clay-bearing rocks chiefly to flatter pores in clay. The results of the distribution of the pore aspect ratio spectra, one important pore structure property, was already employed to interpret the elastic properties in sandstones, e.g. (ZHANG and BENTLEY, 2003). Figure 6.26 shows obtained results for the pore aspect ratios distributions obtained in the connected pore network (NoBin) and after pore separation (Bin1 more separations than Bin10) in samples A-11V and A-17V. As one can see the results indicate that rock A-11V is comprised by more compacted (narrow) pores than A-17V is.

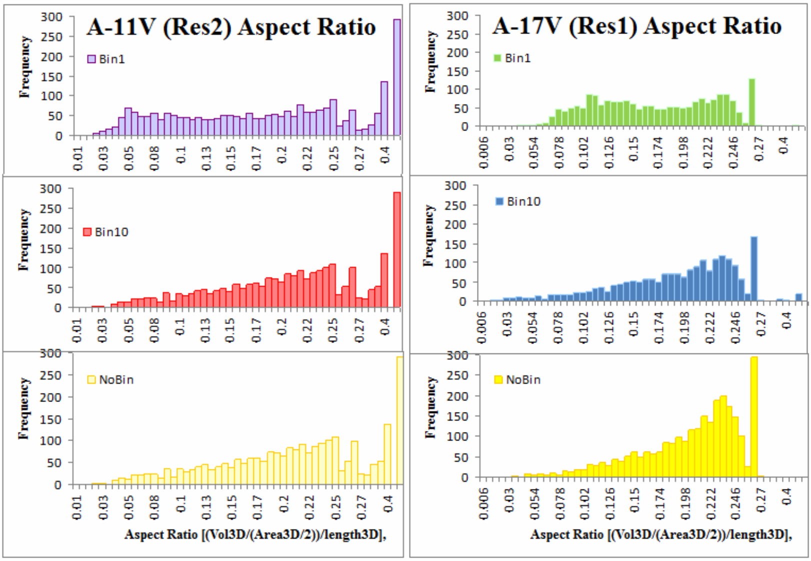

Figure 6.26: Results of aspect ratio for samples A-11V and A-17V.

To evaluate Phi and Theta Orientation of pores, the interconnected pore structure needs to be separated. Having all particles (pores) separated as individual “bins” (where Bin1 contains smaller pores sizes then Bin10), the characteristic orientation of each pore can be measured. This evaluation of preferential pore orientation can give an indicative into which direction in the analyzed field the hydrocarbons prospection should be easier, therefore optimal. As the name already defines, investigated samples A-11V and A-17V were plugs extracted vertically to the bedding field direction, so all experimental permeability PDP measurements were performed in the Z-axis direction. Thereby, we also respect the vertical direction being Z-axis in all mini-cylinders manufactured for X-ray CT scan and analysis. The command “orientation phi” and “orientation theta” from *Avizo Fire* Software where applied being the orientation phi the angle between orientation of the particle and the Z-axis in degrees between [0,+90] and orientation theta the angle between the projection of the orientation of the particle on the XY plane and X-axis in degrees between [-180,+180]. Figure 6.27 shows the obtained results for the pore preferential orientations found in both A-11V Res2 and A-17V Res3, while Figure 6.28 illustrates the spatial position for the main orientations phi (90^{o}) and theta (0^{o} and 110^{o}) obtained. As one can see, any considerable effect on the orientation was observed within pore size decreasing (Bin10 to Bin1). On the other hand, the results indicate that in both samples the pores tend to be organized more to the X- or Y-axis directions, tough in sample A-11V this characteristic is even more representative (observe the counts of frequency in Figure 6.27). If these results would be transposed to the macro-scale of the reservoir one could affirm that the horizontal hydrocarbons prospection would be favorable in the horizontal bedding direction.

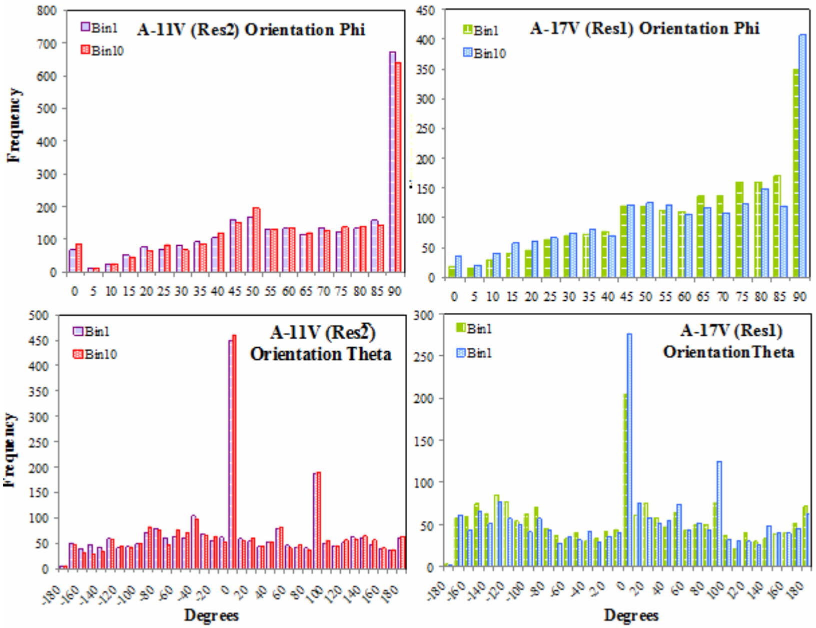

Figure 6.27: Phi and Theta pores orientation of samples A-11V and A-17V after pore separation using Bin1 and Bin10.

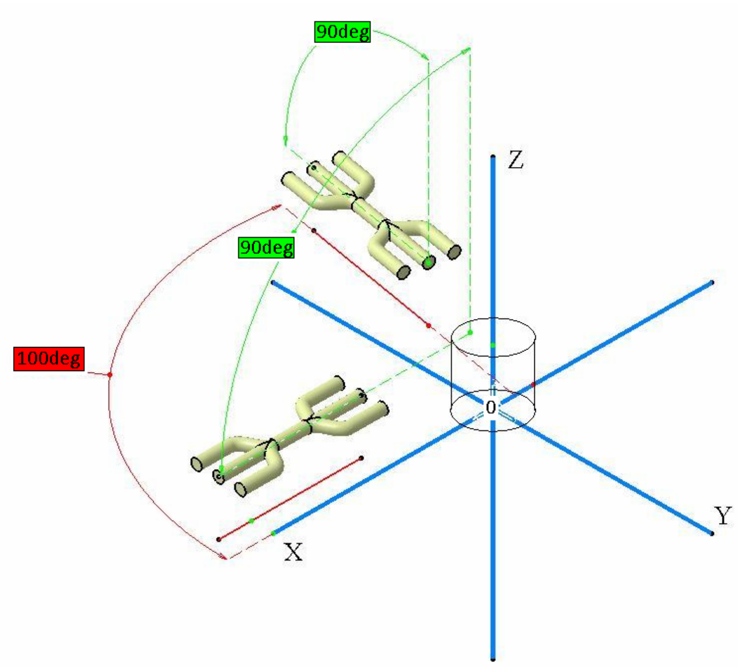

Figure 6.28: Spatial position of particles having the same “orientation phi” (90°) and “orientation theta” equal 0° and 110°.

6.3. Mineralogical characterization, textural and structural aspects for TGS field A

As structural phases and compositional analysis can be used for interpretation of the N_2GA, MICP, LFNMR, nano- and microCT measurements, both XRD and scanning electron microscopy analysis were performed on samples of field A. These analyses were also used to help define mineralogical controls on permeability variations within depth in field A. The TGS samples were collected in location within 4944 to 5040 meters depth along field A. Considering the SEM, FESEM and XRD analyses performed in these samples we observed that the Brazilian field studied is well defined by a significant change in lithologies. As stated before, the samples shown considerable change in porosity and permeability, the most obvious change is the presence of calcite in the sample located in the upper part of the field. For all samples we observed that framework grains are mainly plagioclase feldspar with sub-dominat components of quartz, alkali feldspar and clay minerals. The main clays found were biotite, chlorite and muscovite. The textural, mineralogical and structural results are exposed as follows.

6.3.1. XRD analysis

Figure 6.29 shows the recorded XRD patterns corresponding to the tight gas sandstones originating from field A, as described in Table 4.1. The phase identification and quantitative analysis were performed based on reference intensity ratios values from database ICDD (International Center for Diffraction Data) using the *Diffract.Suite EVA* software. In Figure 6.30 it is possible to visualize the results of the quantitative analysis for TGS of field A, also described in Table 6.3.

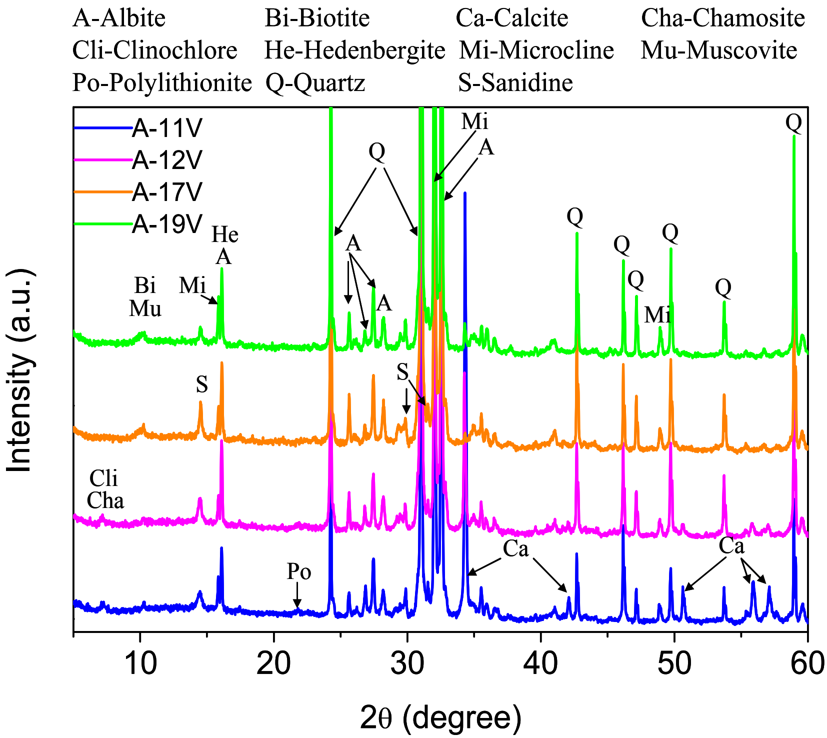

Figure 6.29: Recorded X-ray diffraction patters for the tight gas sandstones from well A. The main peaks from the identified phases using Diffract.Suite EVA software are also depicted.

Table 6.3: Quantitative analysis of the mineralogic components identified from from the X-ray diffraction patters of TGS of field A, using Diffract.Suite EVA software.

SAMPLE			A-11V	A-12H	A-17V	A-19V
	Name	Chemical composition	S-Q (%)			
Mineralogical Phases (Components)	Albite	Al Na O8 Si3	19.41	25.61	23.91	21.72
	Quartz low	O2 Si	16.25	20.17	21.99	23.55
	Microcline	Al K0.95 Na0.05 O8 Si3	13.24	12.38	19.08	14.8
	Polylithionite	Al F Fe H K Li Mg O Si2	8.74	1.8	2.05	1.92
	Muscovite-2M1	KAl2(Si3Al)O10(OH,F)2	6.43	4.33	2.99	6.52
	Calcite	Ca C O3	10.17	7.61	0.89	1.56
	Hedenbergite	CaFeSi2O6	4.66	6.7	3.77	4.02
	Wollastonite-1A	Ca5.81 Mn0.19 O18 Si6	3.83	1.66	1.49	2.19
	Mica	Al3.68 Be0.58 Ca H2 Li0.5 O12 Si1.74	3.43	4.95	3.08	3.06
	Sanidine-high	Al K O8 Si3	2.30	2.67	3.36	2.26
	Pigeonite	(Mg,Fe,Ca)(Mg,Fe)Si2O6	1.94	1.84	1.2	1.65
	Chayesite	Fe2 K2 Mg3 O30 Si12	1.59	1.66	1.98	1.95
	Clinochlore	Al1.67 Cr0.28 H8 Mg5 O18 Si3.04	1.55	1.83	1.43	1.43
	Biotite	K(Mg,Fe)3[AlSi3O10(OH,F)2	1.65	1.69	2.2	2.63
	Goosecreekite	Al2 Ca H5 O16 Si6	1.42	1.58	1.44	1.06
	Chlorite	Al1.2 Cr0.7 Fe0.1 H7.9 Mg5 O18 Si3	1.34	1.4	1.25	1.24
	Kaolinite	Al2 H4 O9 Si2	1.13	1.07	1.43	1.75
	Chamosite	Al1.2 Fe2.482 H10 Mg2.518 O18 Si3.8	0.97	1.04	1.07	0.79
	Illite	Al2 H2 K O12 Si4			4.89	5.07
	Siderophyllite	Al2.54 Fe2.38 H2 K O12 Si2.28			0.51	0.83
Total			100.00	100.00	100.00	100.00

By comparing the patterns it is possible to see that they have mainly the same peaks associated with the albite, quartz and microcline phases but they are well different from the extreme samples located in the upper (A-11V) and bottom (A-19V) areas in the well. From the differences between the analyzed samples in Figure 6.29, the intensities of XRD patterns show that A-11V and A-12V (from the upper regions) have nucleated phases of calcite and clinochlore which get much smaller in the samples A-17V and A-19V. On the other hand for A-12V and A-17V it is possible to see nucleated phase of sanidine and A-17V and A-19V nucleated phases of biotite (black mica), siderophyllite (rare type of mica) and muscovite (white mica) besides an increase of intensity in the peak of quartz. One can see that the analyzed samples exhibit a succession of particular mineral phases of stable elements, being more similar as closer located to each other through the depths in the analyzed well. For sample A-11V the high intensity of calcite peak in the mainly difference observed between the samples. From the XRD patterns one can assume that the calcite phase from the samples in deeper regions practically disappears because it was already either dissolved or precipitated by groundwater (telodiagenesis). When conditions are right for precipitation, calcite forms mineral coatings that cement the existing rock grains together or it can fill fractures. When conditions are right for dissolution, the removal of calcite can dramatically increase the porosity and permeability of the rock. A better understanding will be discussed further in the work by the SEM and FESEM analysis.

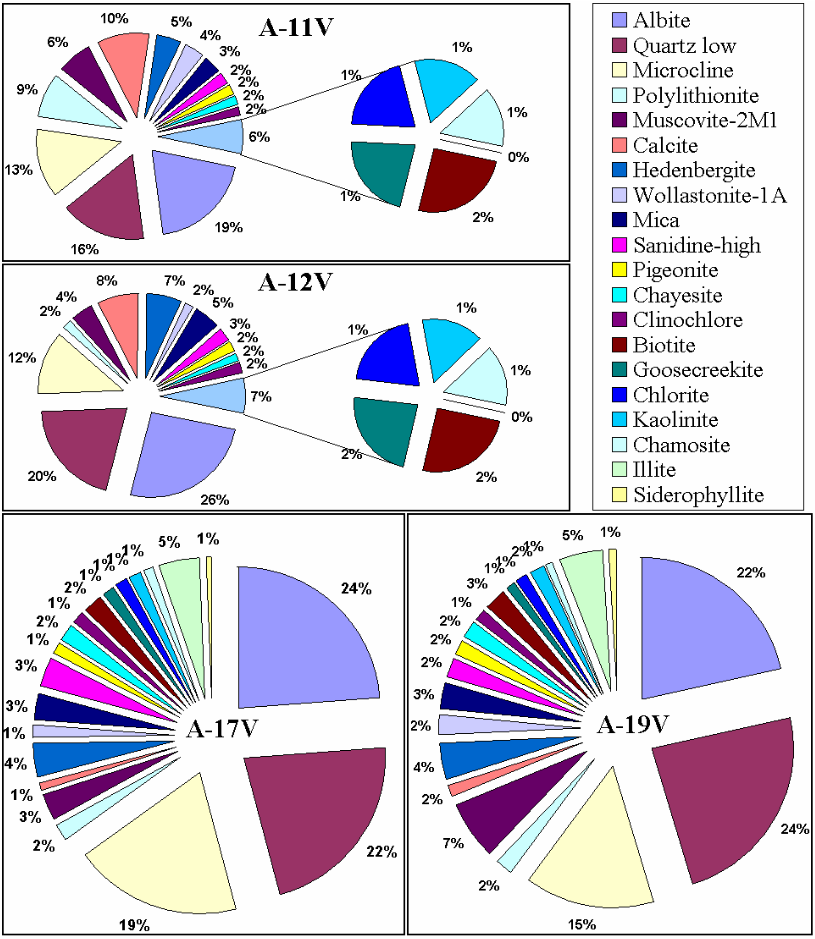

Figure 6.30: Quantitative analysis from the XRD patterns of TGS field A. Legend is displayed in increasing amount order.

6.3.2. SEM and FESEM analyses

Stable backscattered electron (BSE) signals from scanning electron microscope (SEM) were used to generate X-ray mapping images of the studied TGS samples from field A. The average BSE gray value of every region is directly related to a mineral of unique average atomic number. Therefore from this analysis most important minerals present in the analyzed samples and its organization could be differentiated. Although the BSE mode was used in all five samples from field A to create chemical maps, only samples A-11V and A-17V located in the top and bottom of field, are shown here. Figure 6.31 shows the obtained results with right column exhibiting each mineral grain delineated from BSE image and left column displaying the elements discriminated using simple X-ray mapping.

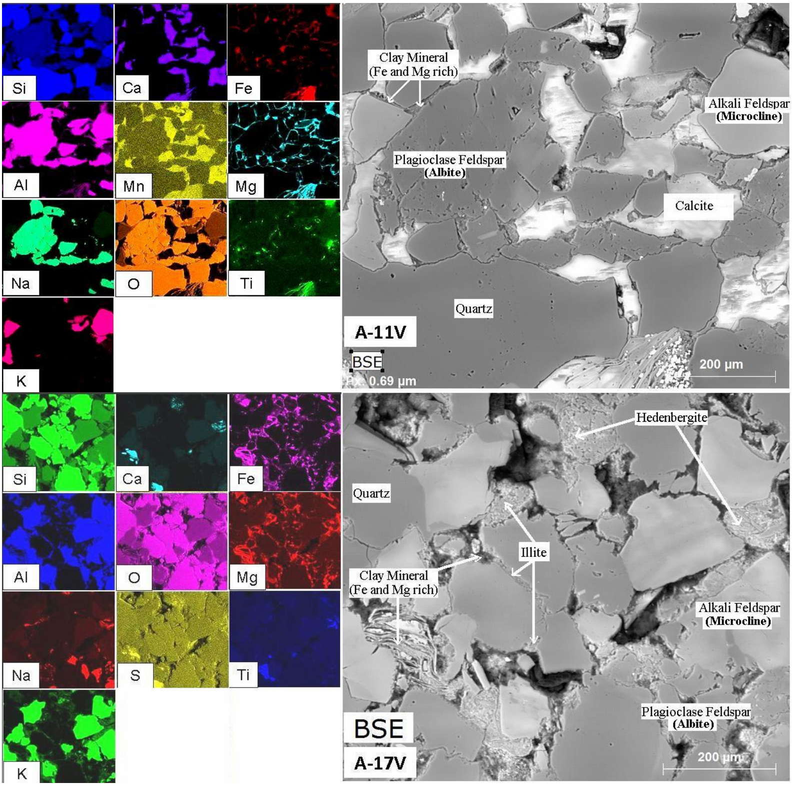

Figure 6.31: Backscattered electron signal and X-ray mapping from the FESEM analyses in TGS from field A (A-11V top, A-17V bottom).

As one can see for the analyzed samples BSE images provide details of mineral intergrowth and very fine pore-structures. Each scanned BSE image area (~ 800 μm^2) returned relative abundance maps of Si, Al, Na, K, Ca, O, Fe and Mg for both samples. The textural relationships between various grains and pores, amount of Ca, Fe, Mg and Mn and organization of minerals, though, is considerable distinct between A-11V and A-17V samples with two of the most striking and distinct features observed being:

- Sample A-11 - presence of phases constituted by Ca and Mg elements, mainly calcite and wollastonite identified by XDR measurements, suggesting that the pores once present in this sample are now filled by calcite overgrowth;
- Sample A-17V - even being comprised by considerable amount of pores (and less compressed then in A-11V) this sample shows Fe and Mg rich clay minerals (illite, chlorite, and illite/chlorite mixed layers) lining/filling/bridging pore.

According to Soeder and Chowdiah (1990), tight gas sandstones are divided into three types based on their pore geometry. This classification emphasizes the effects of the original deposition environment and the invasive influence of diagenesis in the development of the reservoir. Type I sandstones have open intergranular pores whose pore throats are blocked by authigenic[5] clay minerals; Type II have intergranular pores that have largely been occluded by authigenic cements (mainly quartz and calcite) and reduced to narrow slots that connect large secondary pores formed by grain dissolution. Type III sandstones have their intergranular volume filled by dentrital clay matrix and have mainly microporosity. It is known in the literature that Type II reservoirs are by far the most common in commercial tight gas fields (LERCHE and NOETH, 2004). For rocks of field A we can assume that sample A-11V tends to follow the classification as Type II, Samples A-12H and A-12V Type III, while samples A-17V and A-19V showed more microstruture similarities to be of Type I.

---

[5] Authigenic clay minerals form mainly during diagenesis, catagenesis, and metagenesis (SARKISYAN, 1970). Authigenic clays can occur as pore-fillings, pore-bridges or pore-linings and as complex combinations of these three forms. The various clay morphologies produce pore-systems with large surface areas and numerous micropores, and the overall effect is to reduce reservoir quality (BROWN, 1985).

According to Rushing *et al*. (2008) important forms of diagenesis (in order of frequency of occurrence and severity) are: mechanical compaction, cementation from quartz overgrowths, calcite cementation, grain-coating/pore lining clay development, grain dissolution, and ankerite cementation. Only the last form was not observed in the TGS of field A. The enhanced level of compaction is most easily identified by the ductile grain deformation and elongate grain contacts. Grain deformation is recognized by argillaceous rock fragments that are squeezed into the adjacent primary pore space and effectively eliminating those pores. The occurrence of this phenomenon appears to be stronger for sample A-17V then in A-11V. This fact would be expected since massive calcite cementation (as one can see occurring in sample A-11V, Figure 6.33 and Figure 6.34) ceases the effect of mechanical compaction (UMAR *et al*., 2011). Calcite cementation with significant pore volume losses appear to be restricted more to the upper regions in field A. In these regions it appears that quartz cementation, in the form of overgrowths, is extensive in the sandstones with limited intergranular clay (A-11V and A-12V). The overgrowth crystals developing on adjacent grains tend to coalesce and eventually link, thereby occluding the intergranular pores destroying the primary pore system (RUSHING *et al*., 2008).

Figure 6.32 and Figure 6.33 illustrate the field emission scanning electron photomicrographs for rocks A-11V, A-12V, A-17V and A-19V, fractured and polished samples, respectively. In these figures it can be seen that for samples A-17V and A-19V considerable amounts of diagenetic chlorite, chayesite and illite are present filling quartz-cemented walls, occurring primarily as thin coatings on portions of the grain surfaces. We could judge that a portion of the matrix clay has been recrystallized changing its morphology for these two higher porosity rocks, while for samples A-11V and A-12V (lower porosity samples) the matrix clay appears to have less recrystallization. For the rocks A-11V and A-12V it is also observed that the intergranular pore structure is more occluded (lacking even small open apertures) and secondary pore space is calcite filled (A-11V) or not representative visible (A-12V). Figure 6.34 elucidates in 3D the interaction of pore and calcite phases plus its quantification for two chosen distinct ROIs in sample A-11V. In both ROIs the amount of calcite is much higher than porosity. For ROI x=y=z = 450 pixels, a big amount of porosity was intentionally taken to better visualize the pore-calcite interaction in sample A-11V.

Overall, one can see that the analyzed samples displayed important information about structural, mineralogical and textural organization in field A which appear to be highly heterogenic within depth. Additionally the mainly observed features (calcite cementation and diagenetic chlorite and illite) contribute to the decreasing of permeability and porosity values in varied regions in the studied reservoir. Calcite cement frequently seals (degrades) porosity and it is usually found in sediments near the surface where meteoric water may displace original marine pore water, resulting in distinct types of cements. Most calcite present in upper part of the field A has been disappeared through the increasing of depth. It was observed that the decrease of calcite content reflected in this field higher porosity and permeability values as obtained from the petrophysical analysis.

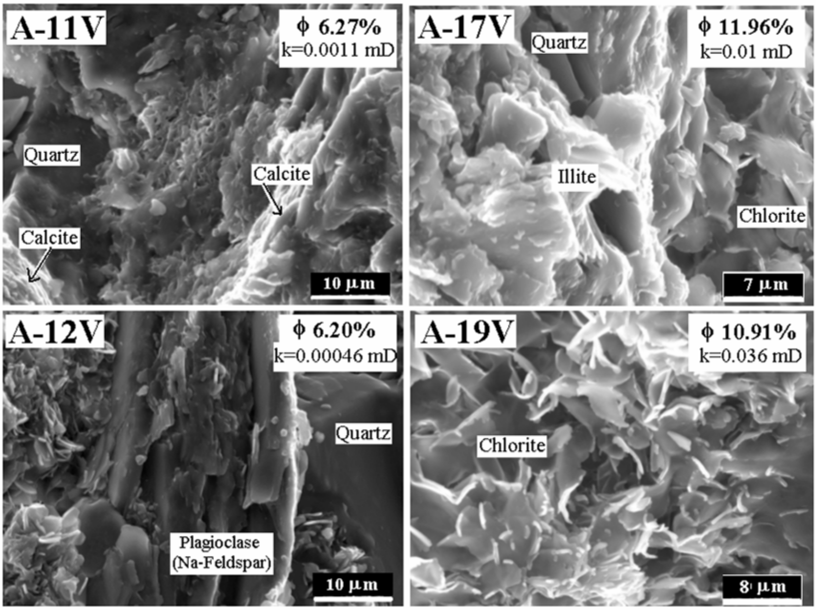

Figure 6.32: Photomicrographs from SE signal obtained from FESEM analysis in fractured samples of the TGS from field A.

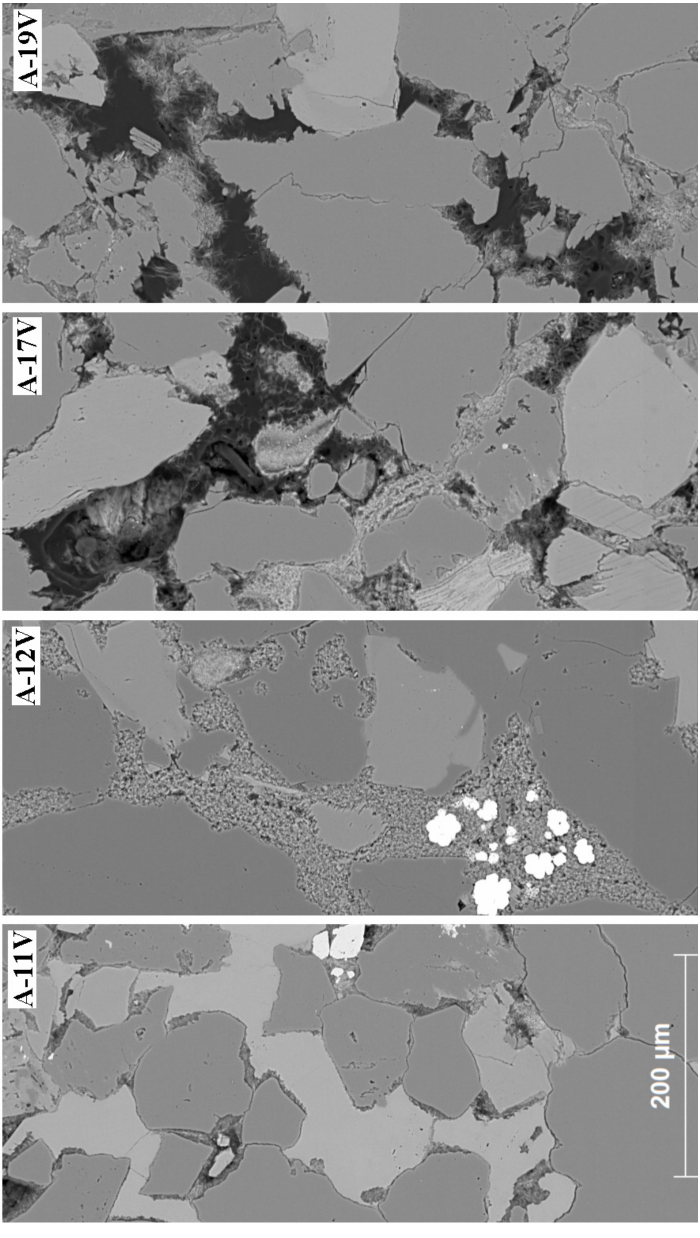

Figure 6.33: Photomicrographs from BSE signal obtained from FESEM analysis in polished samples of the TGS from field A.

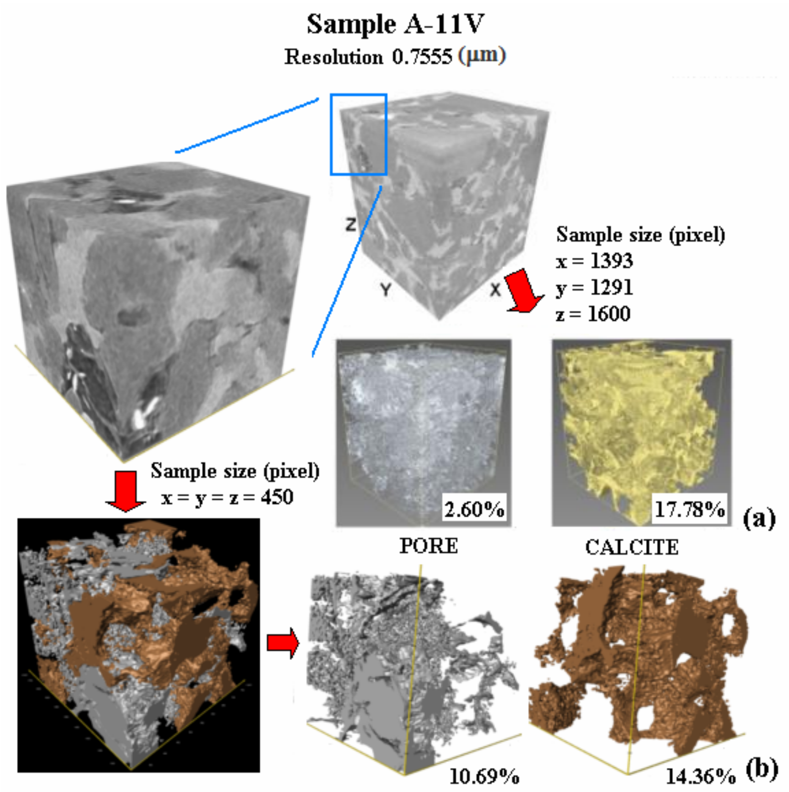

Figure 6.34: Percentage and interaction pore-calcite in sample A-11V.

6.4. Empirical permeability results

To describe the transport mechanism in ultra-tight porous media more accurately, a combination of the processes Knudsen diffusion, slip flow and adsorption/desorption is required (DARABI *et al.*, 2012). In addition, the effect of pore-surface roughness is one example of local heterogeneity on the pore surface and it can account in the permeability results (COPPENS 1999; COPPENS and DAMMERS, 2006). Increasing surface roughness leads to an increase in residence time of molecules in porous media and a decrease in Knudsen diffusivity. Pore dimension fractal (Df) is a quantitative measure of surface roughness that varies between 2 and 3, representing a smooth surface and a space-filling surface, respectively (COPPENS and DAMMERS, 2006). Considering the characteristic radius found in TGS samples of field A and the N_2 molecular mean free path (2.15 nm), the Knudsen number was found to be $0.0215 < Kn < 0.1075$, a range located in the slip flow regime, therefore, Klinkenberg' corrections were applied in the measured PDP permeability. Also, the pore-surface roughness and local heterogeneities were observed in the analyzed TGS rocks allowing a better understanding on the permeability results.

A number of permeability prediction tools were used in this chapter to estimate absolute permeability in the five samples of well A. Each applied correlation was already discussed in section 2.5, whilst a brief explanation upon permeability simulations in 3D nano- and microCT reconstructions is exposed in 3.6.5. To evaluate the predicted and simulated permeabilities, PDP results were set as a basis. Figure 6.35 shows the permeability-porosity relation of investigated TGS, with permeability and porosity measured by PDP technique (after Klinkenberg' correction) and N_2GA+MICP combination.

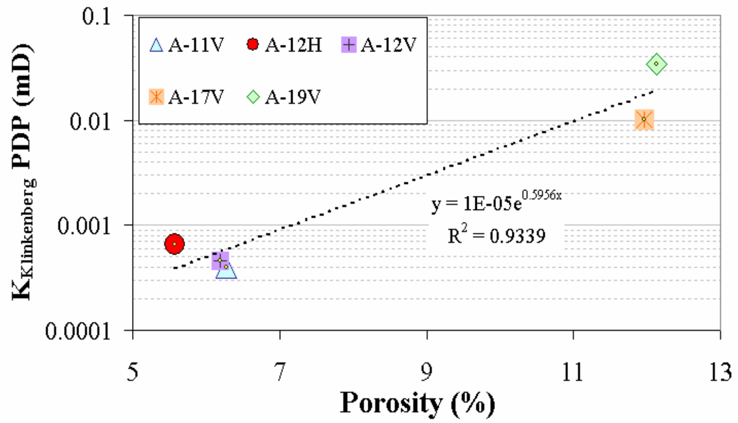

Figure 6.35: Log plot of permeability *versus* porosity of samples from well A. Correlation is given by $R^2 = 0.9339$

In the graphic above, a direct tendency of more porous samples having higher permeability values is shown. Exclusively sample A-12H does not really follow this trend; despite being the less porous sample it displayed a higher permeability value than A-12V, originating exactly from the same field region but plugged in a distinct well bedding direction. This behavior can be understood by the horizontal direction to the well bedding taken for the plug sample A-12H used in the PDP experiments. This horizontal direction corresponds to our 3D coordinate system where X- and Y-axis are oriented. As already discussed in

6.2.4.4 and displayed in Figure 6.27, the pore bodies present on samples of field A (A-11V and A-17V) have a preferential orientation to the X- and Y-axis. As a consequence, one can expect a favored fluid flow in the horizontal bedding direction and so the increase of permeability values.

If a sandstone has only moderate amount of cementing material, permeability can be correlated directly with grain size. On the other hand, if a formation has about the same grain size but varying amount of cements (our case), then a direct relation between porosity and permeability has been claimed. In general, however, just a simple measure of either grain size or porosity will not prove to be a reliable guide to the permeability of sandstones (DULLIEN, 1992). For tight gas sandstones the rule is not different, as we observed for the samples originating from the same well studied in the present work, the experimental PDP values of permeability varied from 0.0004 to 0.034 mD. Porosities of studied tight gas sandstones are almost entirely a function of the kind of cementing material between the sand grains, clay bordering pore walls and the extent to larger grains. From the standpoint of geological processes, two main reasons account for loss of porosity and consequently permeability. The first is cementation by calcite, silica and other minerals introduced into the rock by circulating ground water. The second is compaction that squeezes fine-grained matrix material into inter-connected larger grains by grain-boundary solutions (ink-bottle pore type) at points of higher stress. As reported by Dullien (1992), the porosity of sandstones tends to diminish systematically with depth and the amount of fluids in storage, though it was the complete opposite for the five analyzed samples of field A. Within a depth of about 100 meters (see Table 4.1) indeed significant differences were observed in the microstructure of the sample resulting in differences of permeability of at least three decimal orders.

In this part of the thesis we investigate the prediction of intrinsic permeability using models stated in the literature for low-permeability (or conventional reservoir) rocks and making use of the pore structure parameters measured for the TGS rocks. Also the simulated permeability from 3D reconstructed medium was performed using Lattice-Boltzmann method and the Darcy' law flow through the generated equivalent resistor obtained by the C3DE program. The simulated permeability was executed only in the Z-axis direction of the manufactured nano- and microCT mini-plugs as being the vertical direction to the well bedding of plugs used in the PDP experiments (A-

11V and A-17V). Distinct pore structure parameters were applied and investigated for the calculations of permeability correlations exploited in this chapter. Table 6.4 summarizes the best results obtained from each model by handling distinct pore microstructure parameter applied to our samples. The results are discussed as follows.

Table 6.4: Predicted and simulated permeability results.

	Predicted permeability (mD)													Simulated Z-axis SV1 (mD)		Experimental PDP (mD)
Models	**Based on the *Pc* curves**						**For fine-grained rocks**					**From NMR curves**				
Samples	Winland (KOLODZIE 1980)	AGUILERA 2002	Katz & Thomp. 1986	r_{70}, μm	$l_{cinf.}$, μm	*F*	K-C	Pape, 1999	S-P	*Fo*	τ	Coates, C=21.6; 38	Mean-T_2, *b=20.2; 0.79*	ER	L-B	
A-11V	**0.0022**	**0.00113**	**0.00945**	*0.055*	*0.114*	*70.8*	**0.00057**	**0.00012**	**0.00026**	*6.11*	*4.45*	**0.00132**	**0.00118**	**84.86**	**5.52**	**0.0004**
A-12H	**0.0007**	**0.0003**	**0.00169**	*0.032*	*0.048*	*81.6*	**0.00034**	**9.1E-05**	**0.00015**	*6.11*	*4.45*	**0.00018**	**0.00034**			**0.00066**
A-12V	**0.0005**	**0.00019**	**0.00155**	*0.025*	*0.046*	*72.7*	**0.00059**	**0.00012**	**0.00019**	*6.11*	*4.45*	**0.00034**	**0.00065**			**0.00046**
A-17V	**0.0121**	**0.00592**	**0.08449**	*0.087*	*0.211*	*23.1*	**0.0162**	**0.00646**	**0.00185**	*2.34*	*2.76*	**0.01488**	**0.01096**	**28.57**	**9.77**	**0.0101**
A-19V	**0.0228**	**0.01334**	**0.17823**	*0.124*	*0.305*	*25.3*	**0.00742**	**0.00739**	**0.00119**	*2.34*	*2.76*	**0.02316**	**0.03309**			**0.0344**

P_c = Capillary pressure curves

r_{70} is the pore radius corresponding to 70% mercury saturation

l_{cinf} = the por throat size estimated from the inflection point of the Hg injection curve

F is the formation factor (ϕ/τ). τ is the tortusity and Fo the shape factor calculated by Nano and MicroCT

K-C and S-P stays for Kozeny-Carman and Series-Parallel models

ER = Equivalent resitor network obtained by C3DE program; L-B = Lattice-Boltzmann simulation

6.4.1. Permeability from the empirical correlations

The figure above depicts comparisons between the permeability results obtained in the experimental PDP tests and the models from capillary pressure curves, fine-grained rocks and low-field NMR curves for the samples A-11V, A-12H, A-12V, A-17V and A-19V. If the agreement is perfect the data points will fall exactly on the diagonal line plotted in the graph. As can be seen, the values obtained with the models based in the capillary pressure curves and from NMR measurements in closed symbols tend to be higher then the measured PDP permeability. These results were calculated using mainly the parameters values suggested in the literature for sandstones. Calculations performed using calibration through measured PDP permeability are presented by the open symbols.

6.4.1.1. Results based on the capillary pressure curves

For the three permeability correlations already discussed in section 2.5.1, Winland-Pittman, Aguilera and Katz-Thompson models, the data resulting from the PSD curves obtained by the N_2GA+MICP combination was applied. Table 6.5 displays this data while the formation factor *(F)* was already displayed in Table 6.4 and is a result from the 3D X-ray CT measurements of tortuosity and total porosity obtained by the N_2GA+MICP combination. Only for samples A-11V and A-17V tortusoity was measured. For samples A-12H and A-12V these values were considered to be the same as for A-11V and for A-19V the same for A-17V.

Table 6.5: Pore structure parameters used for the models based in P_c.

From the P_c curves of N_2GA+MICP combination				
Samples	**Porosity (%)**	**r_{35} (μm)**	**r_{70} (μm)**	**$l_{c\ inflection}$ (μm)**
A-11V	6.28	0.2549	0.0551	0.1135
A-12H	5.45	0.0793	0.032	0.048
A-12V	6.12	0.0724	0.0248	0.046
A-17V	11.96	0.3655	0.0867	0.21
A-19V	10.91	0.5261	0.1242	0.305

As one can see in

Figure 6.36 (a), the values of estimated permeability assuming a corresponding pore throat radius with 35% fluid saturation, r_{35}, (Winland-Pittman and Aguilera models) were higher than the measured results obtained using the PDP technique. A better agreement for the Winland-Pittman and Aguilera models in the analyzed TGS of field A was found when the pore radius corresponding to the 70% fluid saturation, r_{70}, is applied. For the Katz-Thompson equation, the smallest throat at the percolation threshold, l_c, equal the inflection point from the PSD saturation curve also gived reasonable results when compared with the PDP results. This agreement was better especially for samples A-11V and A-17V which had the tortuosity value to calculate formation factor, as exposed in Eq. (2.26), measured from the 3D X-ray CT.

6.4.1.2. Kozeny-Carman, Pape et al (1999) and Series-Parallel models

Figure 6.36(b) depicts the results for the permeability models in fine-grained rocks as described in section 2.5.2. The dataset for the calculations were defined based on the values of porosity, PSD and specific surface area, S_o, calculated by the N_2GA+MICP combination (S_o only by N_2GA technique, BET theory), shown in Table 5.2, and the values of tortuosity and shape factor calculated by 3D X-ray CT, exposed in Table 6.4. As can be seen from the comparison between the experimental and estimated permeability values, the Kozeny-Carman equation shows the best results whereas the values predicted by Pape *et al.* and Series-Parallel models tend to be slightly lower than the measured results obtained using the PDP-200. Nonetheless, the results of the fully empirical models analyzed in this section were all within the same magnitude as the PDP experimental results. We consider that these results for the TGS rocks of field A provide reasonable evidence of the validity of the K-C, Pape *et al.* (1999) and S-P approaches in these rocks. The best estimation reached by the K-C model could be attributed to the fact that this model considers effects besides the porosity, like the tortuosity, shape factor and S_o, which were properly measured for the analyzed rocks in this work. By the FESEM and PSD curves we could subdivide the TGS rocks of field A in two main regions having similar microstructure/petrophysical properties: the upper region (samples A-11V, A-12H and A-12V) and the lower region (A-17V and A-19V). Therefore, in the K-C model we used the so called K-C constant ($F_o\tau^2$) calculated by the X-ray CT analysis for samples A-11V and A-17V, equal to 121 and 17.8 for samples located in the upper and lower regions of field A, respectively. The same procedure of establishing two distinct regions from the analyzed samples of field A was also applied to calculate the pore geometry parameters related to the NMR models, balancing the ability to meaningfully estimate the properties involved in the distinct rocks regions found in this field.

6.4.1.3. Coates 1999 and Mean-T_2 models from low-field NMR results

The theoretical basis about the Coates 1999 and the Mean-T_2 models for permeability estimation using NMR measurements was given in sub-chapter 2.5.3. Figure 6.36 (c) shows the comparison between the estimated and measured permeability results. The calculations concerning the $T_{2cutoff}$ and T_{2gm} values were already performed and discussed in 6.1.3; Table 6.6 shows the porosity and the calibrated pore geometric constants, C and b, from low-field NMR measurements. Both models used in this chapter can only be as accurate and precise as the constant is chosen. In the case of the Coates model the literature suggests a value of 10 for the constant C. With this value and using $T_{2cutoff}$ = 33 ms (from the literature in sandstones) or our measured values (right column in Table 6.1) the prediction for permeability leads to higher values than the ones measured by PDP-200, see orange and green full circles in Figure 6.36 (c). If the experimental PDP values are in turn used to first calculate a more refined value for C for the two field regions in the analyzed TGS rocks, which would be $C = 21.57$ for the upper regions and $C = 37.93$ for the lower regions, we can obtain much more accurate predictions (see open circles in Figure 6.36 (c)). The refined constant is based on the average of the individual values of C when inserting the experimental permeability values into the Coates equation. Note though, that in order to performe it you first need to characterize well the rock you want to analyze and you need up front a refined value for C from previous studies for that same type of rock, as the analyses performed here by PDP technique. The same proceeding was applied to the Mean-T_2 model. With the literature suggestion for b equal 4 we receive mixed results for the permeability prediction but all in a reasonable range to the measured permeability. The calculation of a refined constant based on the experimental PDP results lead us to the value of $b = 20.26$ for rocks located in the upper regions and $b = 0.79$ for rocks from the lower regions. As can be seen in Table 6.6 the individual values of constant b differed considerably between the samples analyzed while the individual C values were not far from the average of 28. This is explained since b is a parameter depending from the porosity and the permeability formation while C is a parameter of pore geometry.

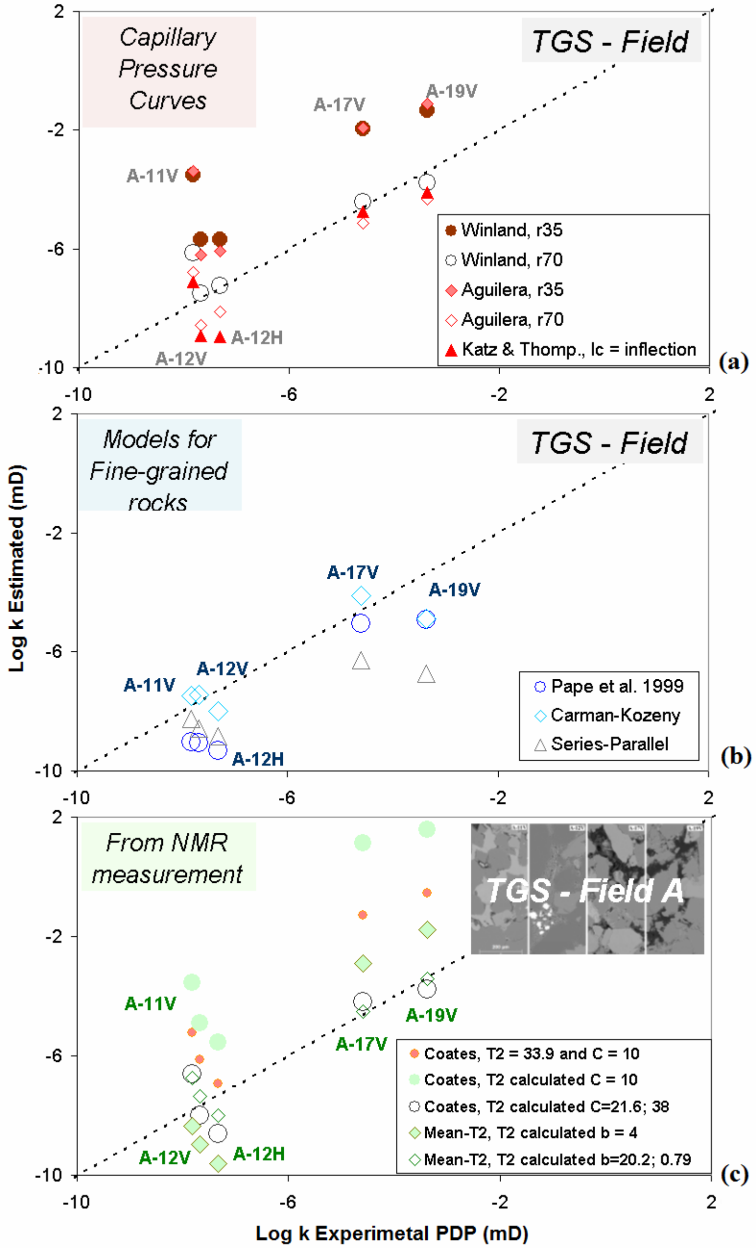

Figure 6.36: Results of permeability prediction from empirical correlations.

Table 6.6: Pore structure parameters permeability estimation from NMR.

Low-field NMR measurements		Coates et al. (1999) model			Mean T_2 model		Experimental PDP (mD)
		from $T_{2cutoff}$ in our TGS		Calibrated C	T_{2gm}	Calibrated b	
Sample	Porosity (%)	FFI	BVI				
A-11V	6.83	48829.49	134714.49	29.10	1.63	6.89	0.0004
A-12H	5.69	24973.36	129104.26	15.63	1.26	39.48	0.0007
A-12V	6.20	29753.40	133387.76	19.98	1.47	14.42	0.0005
A-17V	10.93	109074.62	74256.05	41.89	9.88	0.72	0.0101
A-19V	10.05	152237.38	70208.83	33.97	20.31	0.86	0.0360
	Average	Upper region field A		21.57		20.26	
		Lower region field A		37.93		0.79	

6.4.2. Results for simulation of single-phase flow

A microstructure defined by a digital image is already discretized and lends itself immediately to numerical computation of many properties (KNACKSTEDT *et al.*, 2006). In this subsection we show the results obtained of the single-phase permeability on samples, A-11V and A-17V, based on the numerical Lattice-Boltzmann method (LBM) (MARTYS and CHEN, 1996; DOS SANTOS *et al.*, 2005; BAKER *et al.*, 2012) and applying Darcy's law in the pore equivalent resistor network (skeleton) extracted using the C3DE program (CUNHA, 2012) as shown in Figure 6.17. Simulations using the LBM were performed in a subset of 600^3 pixels for sample A-11V Res2 (Figure 6.37(a)) and in two subsets from distinct regions of sample A-17V Res1 with 1000^3 pixels each (Figure 6.37(b)). The results of simulated permeability are shown in Table 6.7.

From the results with gas nitrogen passing through a network of pore equivalent resistor (C3DE), one can see that permeability simulation varies from distinct sample axis, being bigger especially in the X-axis direction. These results are in perfect agreement to the pore preferential orientation found and discussed in Figure 6.27. Another interesting result is observed by the comparison of Res1 and Res2 in rock A-17V. One can see that Res1 shows a much defined axis direction (X) where the permeability is bigger, while in Res2 the values tend to be close. These results suggest that simulated permeability is being highly influenced by the volume of sample analyzed (i.e. Res1 was about 10 times bigger than Res2, so more representative although with low resolution).

However in the investigated TGS, from both pore equivalent resistor (C3DE) and LB methods, simulation of permeability on the resolvable connected porosity did not provide reliable results compared to the experimental PDP values. Recently, working with LB method, BAI *et al.* (2010) demonstrated by systematically varying sample size and resolution, that calculated permeabilities for samples with porosity lower than 30% decreased by about two orders of magnitude with a five times increased sample size at full tomographic resolution (4.76 µm per voxel/lattice node). Low-porosity samples were especially sensitive to simulation resolution, with the permeability increasing by at least one order of magnitude for every halving of the grid resolution. Furthermore an important factor to be considered when comparing experimental PDP results and simulated permeability is the pressure condition applied on the sample to be analyzed. When the sample is scanned and X-ray CT data are collected, there is only the effect of atmospheric pressure acting while in a PDP experiments a net stress pressure is applied. To see the influence on the permeability results with the confining pressure in the studied TGS, compare Figure 5.1.

Giving the importance of microporosity to the overall properties in the analyzed tight gas sandstones (compare N_2GA+MICP curves, Figure 5.9, also FESEM micrographics, Figure 6.32) there is a need to undertake a study considering the permeability in the 3D medium incorporating both the resolvable porosity (Figure 6.37) and the microporosity out of investigated resolution, as suggested already by Knacksted *et al.* (2006), studying carbonates. However for unconventional reservoir rocks such as TGS this task is still unsolved in 3D pore network simulations once that even for the resolution of utilized nanoCT (0.064 µm) the complete range of smaller pore found in such rocks (down to 0.01 µm) is not reached. Besides, the presence of clay minerals (i.e. chlorite/ biotite/ chamosite/ illite), K-mineral alterations and grains/pore compaction observed by the SEM/FESEM analyses, play a significant role of micro-barriers inhibiting the fluid circulation. These textures could not be completely observed in our 3D images.

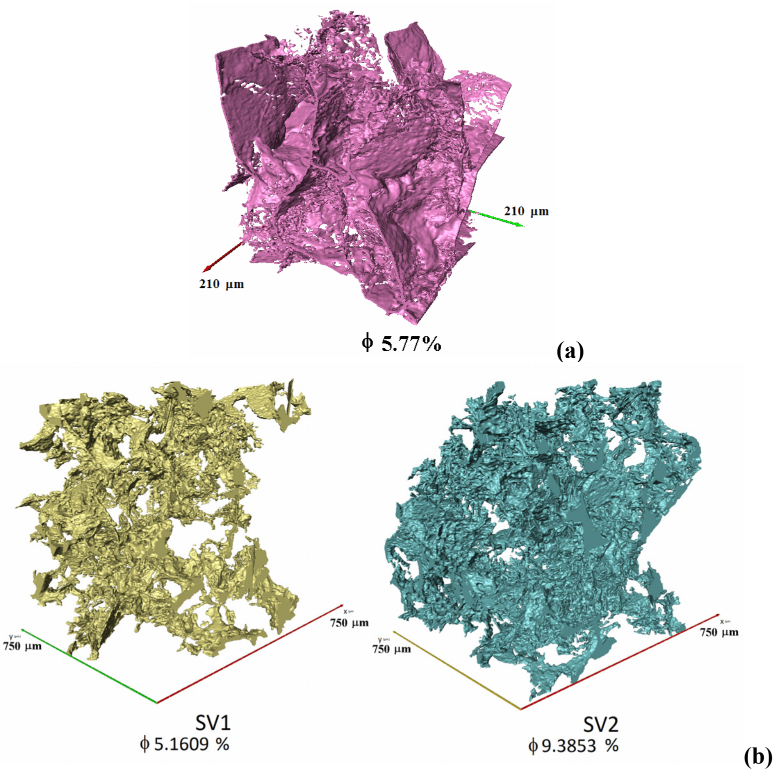

Figure 6.37: 3D connected network pores: (a) 600^3 pixel size 0.35µm volume of sample A-11V Res2 and (b) two sub-volumes (1000^3, pixel size 0.75µm) of Sample A-17V Res1.

Table 6.7: Results for simulated permeability.

Sample		**Simulation from 3D CT images**								**Experimenatl**	
		Pore equivalent resistor (C3DE)				Lattice-Boltzmann				N_2GA+MICP	PDP
		Porosity, %	Permeability (axis direction), mD			Porosity, %		Permeability (Z-axis), mD		Porosity, %	Permeability, mD
			X	Y	Z	SV1	SV2	SV1	SV2		
A-11V	Res1	3.22	**0**	**0**	**0**					6.28	**0.0004**
	Res2	5.77	**146.83**	**127.05**	**84.86**	5.77		**5.52**			
	Res3	5.4	**0**	**0**	**0**						
A-17V	Res1	9.62	**137.66**	**18.83**	**12.16**	5.16	9.39	**9.76**	**30.26**	11.96	**0.01**
	Res2	9.38	**81.92**	**71.4**	**44.99**						
	Res3										

7. USAGE OF PHOTOACOUSTIC TECHNIQUE TO CHARACTERIZE THERMAL DIFFUSIVITY AND POROSITY IN SEAL ROCKS

Measurement of thermal diffusivity of rocks is important to understand the thermal properties and the characteristics of heat flow into the formation of oil or gas. The sealing capacity is controlled either by the rock microstructure or by chemical interactions between minerals and the permeating fluid (DESBOIS and URAI, 2009). In this chapter we describe the results obtained from the PAS method applied in three seal rocks originated from distinct oil and gas wells in Brazil. Each of the rock samples were prepared for the PAS analysis as a disc sample sliced in the vertical direction of well bedding and as a manufactured disc sample after rock grinding and compaction. Both samples (disc and powder compressed) were taken from cleanned core rock samples. The inetention of preparing a powder compressed sample is to verify the values of termal diffusivity only of the matrix rock without the influene of porosity. Our main task was to verify how thermal properties of seal rocks are related to the porosity since it is known that cap rocks can act as excellent insulators over oil and gas reservoirs, aiding the formation and thermal maturation of petroleum (FENG *et al.,* 2013). We also propose a model to correlate measured thermal diffusivity (TD) to porosity values. The results show that thermal diffusivity decline as apparent porosity of the samples decreases.

7.1. PAS results for signal phase and amplitude

As previously discussed, the characteristic frequency $f_c = \left(\alpha / \pi l^2\right)$ characterizes the transition from the thermally thin regime $(f < f_c)$ to the thermally thick regime $(f > f_c)$. In this work, for the analyzed seal rocks, which are a type of shale having heterogeneous pore structure and mixtures of muscovite, illite, quartz and clays in its matrix, we considered an average value of thermal diffusivity of 0.019 cm^2/s (GUIMARÃES *et al.,* 2013) and by considering that the largest thickness of the samples was 510 μm, the smallest characteristic frequency of $f_c \approx 2{,}33$ Hz was calculated. Therefore, in order to achieve the thermally thick regime, for the analyzed seal rocks the PAS data was measured in the 10-250 Hz modulation frequency range.

Figure 7.1(a) shows the PAS signal amplitudes of samples SR-42, SR-47 and SR-57 while their corresponding phases are shown in Figure 7.1(b). The legends show (v) for sliced samples in the vertical direction to the bedding depostion and (p) for powder samples compressed to 6 tf/in^2 (about 92 MPa).

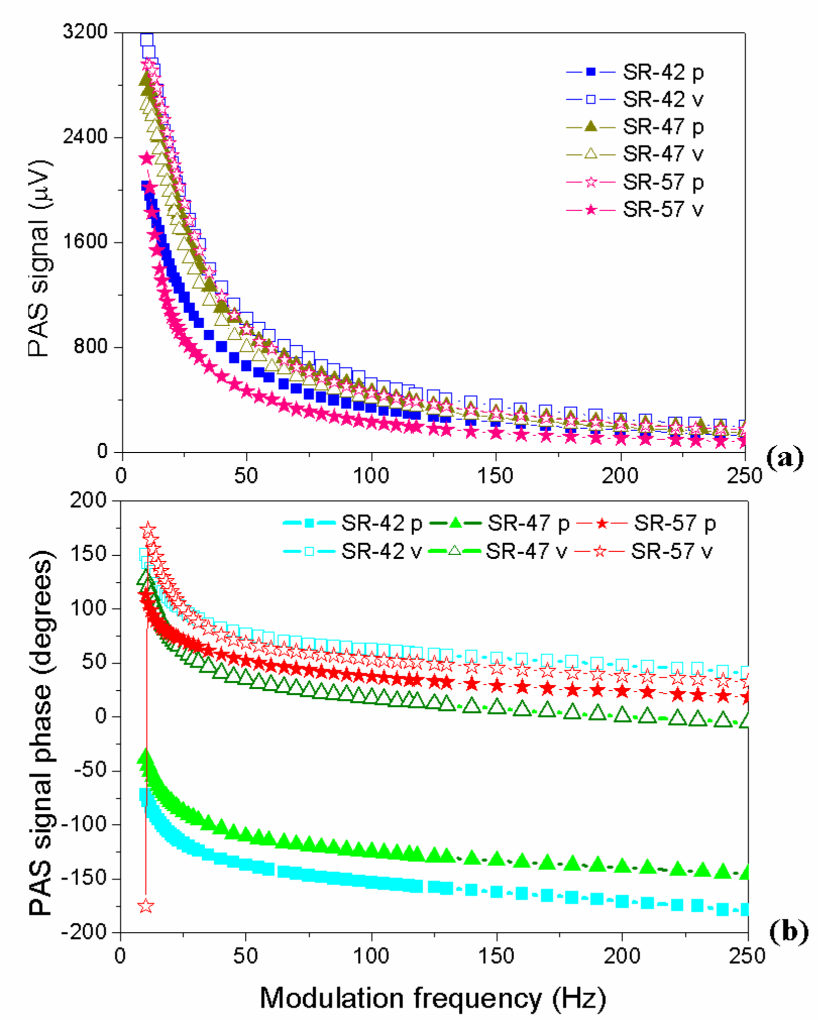

Figure 7.1: PAS signal amplitude (a) PAS signal phase (b) versus modulation frequency, for the three analyzed seal rocks of powder compressed to 6 tf/in^2 (p) and vertical sliced (v) samples.

According to Figure 7.1(a), the signal amplitudes of all samples are similar regardless of being vertical or powder samples, while for Figure 7.1(b), only the phases of vertical sliced samples are similar but a discontinuity at 10 Hz is seen in the phase of SR-57. The phase behavior of powder compresses samples SR-42 and SR-47 is similar. The procedure described in the section 3.8 for obtaining the thermal diffusivity of each process to the PAS signal amplitude was used as discussed following.

7.2. PAS mechanisms and thermal diffusivity results

Figure 7.2 shows PAS signal and PAS signal phase versus the square root modulation frequency of the intraband nonradiative thermalization (thermal diffusion) mechanism contribution observed for the analyzed seal rocks. As one can see only SR-42 and SR-57 presented this main contribution to the PAS signal and phase. For the SR-42 vertical sample, the slope of the dash lines fitted between 10 and 17 Hz were a = 0.30308 (from the signal amplitude data) and a = 0.30472 (from phase data), whereas for the SR-42 powder compressed sample, the slope of the straight lines fitted between 8 and 15 Hz were a = 0.32457 (from the signal amplitude data) and a = 0.31684 (from phase data). For the SR-57 powder compressed sample, the slope of the straight lines fitted between 1 and 6 Hz were a = 0.65639 (from the signal amplitude data) and a = 0.64758 (from phase data). Using the expression $a = l_s\sqrt{\pi/\alpha_s}$ and considering the average value of a from signal and phase data, the calculated thermal diffusivity values were α_s=0.08848 cm^2/s and α_s=0.07636 cm^2/s for SR-42 vertical and powder compressed, respectively, and α_s=0.01667 cm^2/s for SR-57 powder compressed. Due to the phase inversion observed in Figure 7.1 equations (3.29) and (3.30) were applied to obtain the thermal diffusivity of the SR-57 vertical sample from the thermal diffusion mechanism contribution. The signal phase shows a discontinuity at 10 Hz, which is a fingerprint of the contribution of thermal diffusion to the PAS signal and refers to the signal phase inversion of 180^o. The integer number n is related to the discontinuity points due to the *tan(x)* dependence of the phase. Use of the value 10 Hz in expression (3.30) and $n=0$ (first discontinuity) leads to the value of f_c=4.053 Hz and α_s=0.01937 cm^2/s.

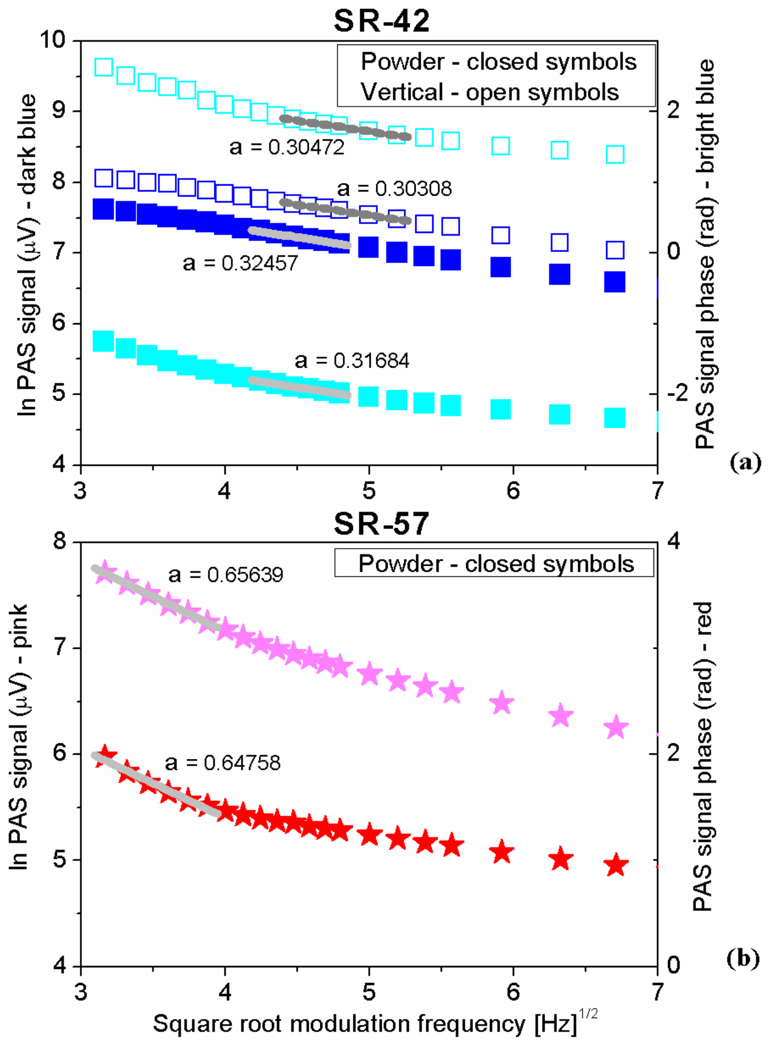

Figure 7.2: (Gray online) on PAS signal (pink symbol) and PAS signal phase (red symbol) versus modulation frequency for samples SR-42 (a) and SR-57 (b) showing the thermal diffusion mechanism.

As shown in Figure 7.3(a), between 16 and 31 Hz, the PAS signal amplitude for SR-42 in both vertical and powder compressed samples change with modulation frequency as $f^{-0.9314}$ and $f^{-0.8633}$, respectively. For SR-47 vertical and powder compressed samples the

PAS signal amplitude change with modulation as $f^{-0.9816}$ and $f^{-0.9952}$ between 19-33 Hz and 21-29 Hz, respectively. These changes are close to $f^{-1.0}$, indicating the presence of thermoelastic bending (TB) mechanism. Therefore the procedure already described in section 3.8 was applied, and an excellent fit was obtained considering thermoelastic bending process, Eq. ((3.31), for SR-42 vertical and powder compressed samples α_s=0.08289 cm^2/s and α_s=0.06570 cm^2/s, respectively, for SR-47 vertical and powder compressed samples α_s=0.09298 cm^2/s and α_s=0.08158. The fits are shown in Figure 7.4 for both seal rock vertical sliced and powder compressed samples.

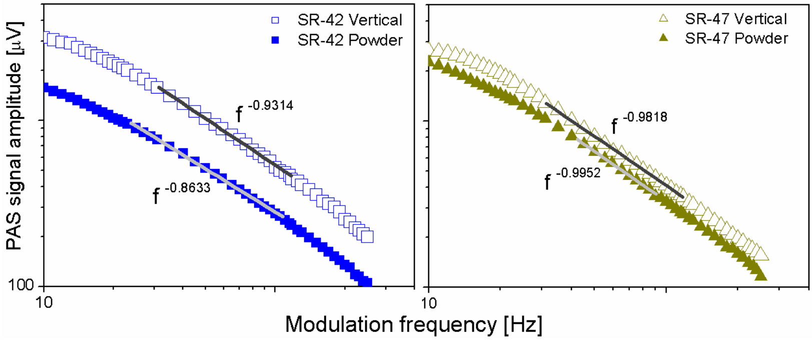

Figure 7.3: (Gray online) PAS signal amplitude versus modulation frequency for SR-42 (a) and SR-47 (b) samples showing TB mechanism.

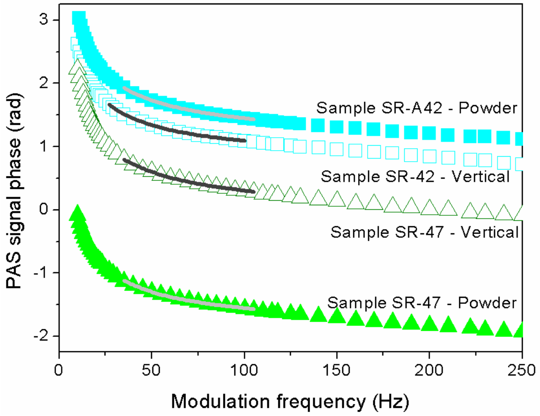

Figure 7.4: PAS signal phase versus modulation frequency for SR-42 and SR-47 samples showing the TB mechanism with gray solid lines corresponding to the best fit of experimental data to Eq. ((3.31).

All results obtained from the thermal diffusion (TD) or thermoelastic bending (TB) mechanisms in PAS measurements and the porosity and density of the analyzed seal rocks can be seen in Table 7.1.

7.3. Results of thermal diffusivity and predicted porosity

The results show that independently of the well of origin for all seal rocks grinded and compressed to 6 tf/in^2 samples there was a small reduction in the thermal diffusivity when compared to the values obtained from the original rocks (vertical sliced pellets). On the other hand, compared to each other the three samples present different thermal diffusivity values increasing from the sample SR-57 to SR-47 (similar to SR-42). These results suggest that these samples originating from distinct wells are constituted of specific microstructure organizations and crystalline and amorphous mineralogical phases which lead to rather different thermal properties, especially in sample SR-57 from which very low diffusivity values were obtained (in the order of 0.02 cm^2/s).

Firstly, to discuss the reduction of the thermal diffusivity values of the powder compressed samples compared to the vertical sliced pellets we will base our argumentation towards a macroscopic property description of a disordered media having two main volume phases: pores and solid matrix. By considering the vertical sliced sample (an original piece of clean and dry seal rock) as a two-phase network in which pores are randomly embedded in a solid matrix, the thermal diffusivity of the specimen can be given as:

$$\alpha_{m+p} - \alpha_m = x_p \alpha_p \tag{7.1}$$

where α_{m+p} and α_m are the thermal diffusivity of the vertical sample comprised by solid matrix and pores and the powder compressed samples containing only the solid matrix. α_p is the thermal diffusivity of the pores network in this case considered to be filled by air and equal to 0.19 cm^2/s; x_p finally is the amount of pores embedded in the solid matrix of vertical sliced sample, i.e. the porosity value. Using Eq. (7.1), one can obtain the porosity of SR-42 equal 6.38% from the thermal diffusion results and 9.05% from the thermal bending; for sample SR-47 a value of 6.00% was found from the thermal bending and for sample SR-57 a value of 1.42% was calculated. These values of porosity were compared with the results obtained in the same rock samples using the combination of nitrogen gas adsorption and mercury injection capillary porosimetry techniques in a previous work (SCHMITT, 2009) as can be seen in Figure 7.5. In this previous work it was concluded that much of the observed variations in permeability of analyzed seal rocks could be attributed to variations in porosity. However shale (as seal rocks) also exhibit wide ranges in fabric and clay content. Anisotropy in transport properties may be pronounced in clay-bearing and soils which revel grain shape alignments (KWON *et al.*, 2004). The mineralogy, texture and grains orientation are discussed in the next paragraph. Table 7.1 shows the comparison of porosity results presenting a good agreement between the techniques. Therefore it can be concluded that the PAS technique proves to be an alternative method for the calculation of porosity in seal rocks.

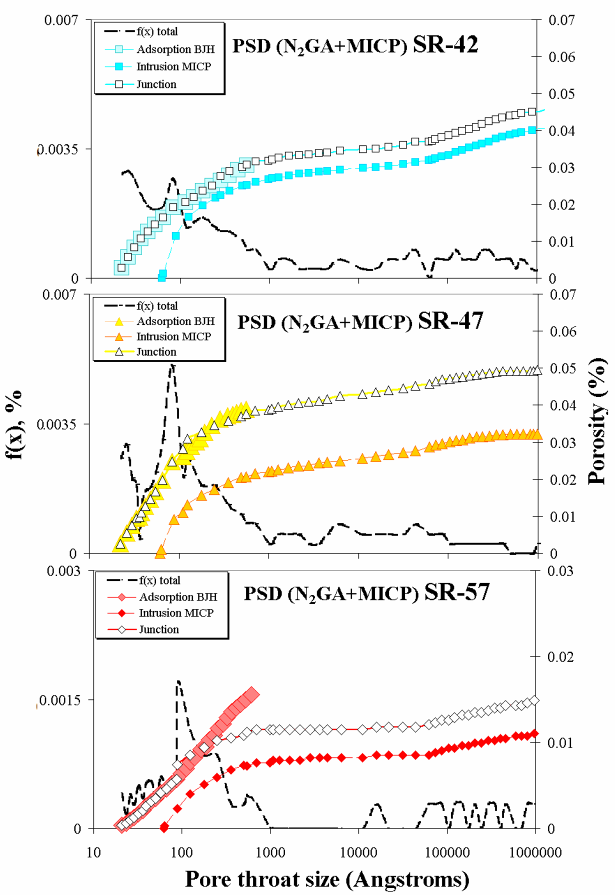

Figure 7.5: PSD and porosity obtained for the analyzed seal rocks using the combination of N_2GA and MICP techniques (SCHMITT, 2009).

Table 7.1: Results obtained from PAS measurements; porosity and density values obtained by N_2GA and MICP techniques and; values of thermal diffusivity for common materials and elements.

PAS Technique										**N_2GA+MICP**			**Literature**	
Samples			Thermal Diffusion (TD)			Thermoelastic Bending (TB)			Porosity (%)	Porosity (%)	ρ_{real} (g/cm^3)	ρ_{bulk} (g/cm^3)	(GUIMARÃES, 2013) (BROWN and MARCO, 1958) (WANG and MANDELLS, 1999)	
Name	State	l (µm)	Range (Hz)	Coef. $a_{average}$	α_s (cm^2/s)	Range (Hz)	Coef. f	α_s (cm^2/s)					α_s (cm^2/s)	
SR-42	vertical	510	10-17	0.3039	0.08848	16-31	$f^{-0.931}$	0.08289	6.38 (TD) 9.05 (TB)	4.60	2.55	2.66	Shale	0.019
	powder	500	8-15	0.3207	0.07636	16-31	$f^{-0.863}$	0.0657					Sandstone	0.012
SR-47	vertical	470				19-33	$f^{-0.982}$	0.09298	6.00	4.95	2.62	2.71	Quartz	0.072
	powder	510				21-29	$f^{-0.995}$	0.08158					Fe	0.23
SR-57	vertical	390	f_c=4.053		0.01937				1.42	1.48	2.83	2.87	Al	0.84
	powder	475	1-6	0.6520	0.01667								Air	0.19

7.4. Mineralogical characterization, textural and structural aspects for analyzed SR

7.4.1. Results of X-ray diffraction and FESEM analyses

In order to understand the differences of the thermal diffusivity values in the three seal rocks wells the microstructure of SR-42, SR-47 and SR-57 samples was analyzed. Figure 7.6 shows the recorded XRD patterns for the analyzed seal rocks; Figure 7.7 and Table 7.2 present the quantification of phases measured in the XRD patterns, and Figure 7.8 shows the clay-bearing content, the microstructure of grains and pores and the rock aspect of the analyzed seal rocks.

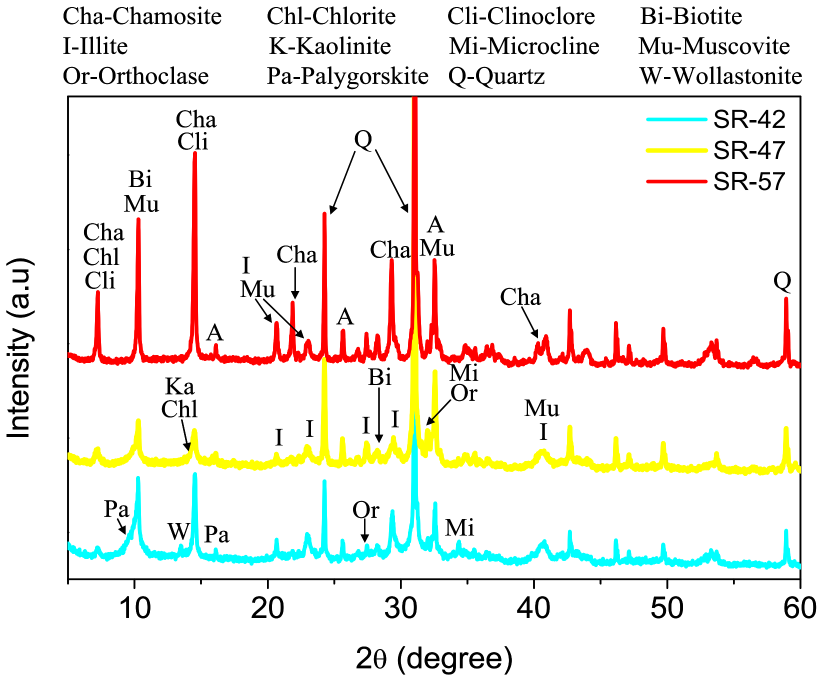

Figure 7.6: Recorded X-ray diffraction patters for the seal rocks from three distinct wells. The main peaks from the identified phases using Diffract.Suite EVA software are also depicted.

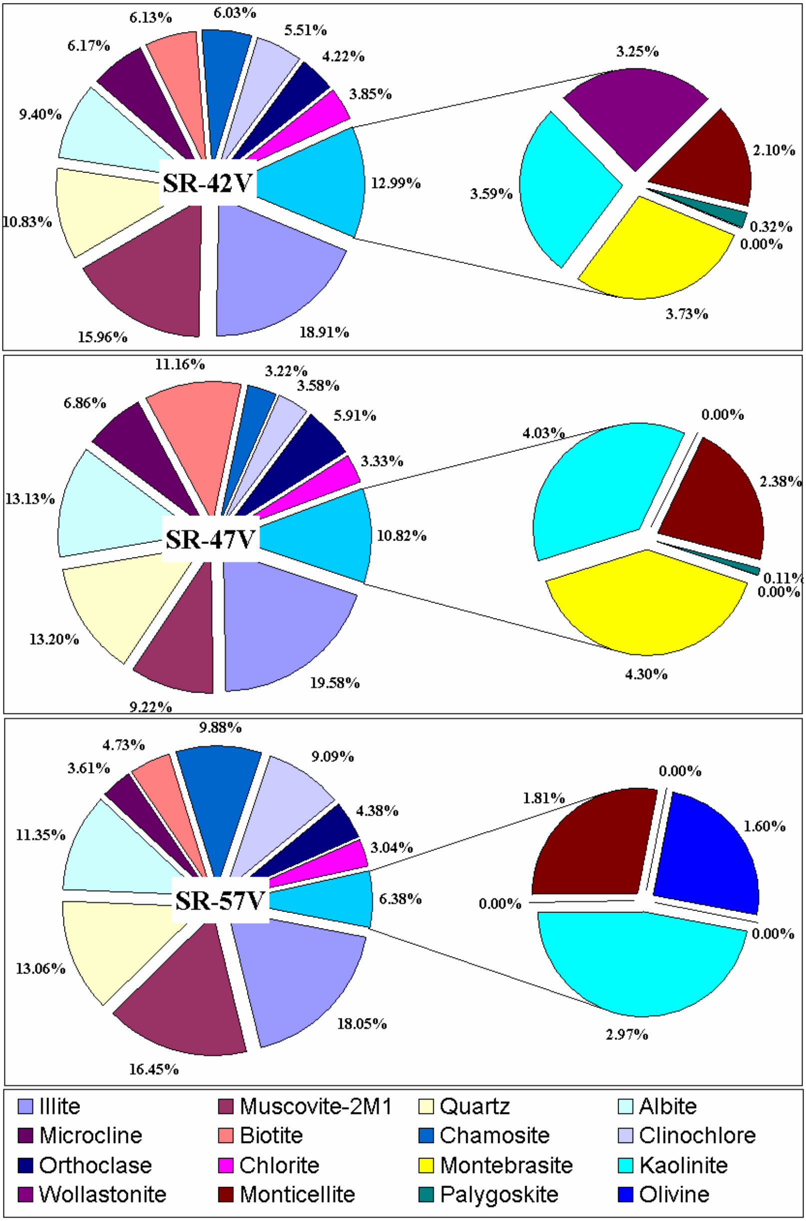

Figure 7.7: Quantitative analysis performed using Diffract.Suite EVA software from the X-ray diffraction patters of analyzed seal rocks.

Table 7.2: Quantitative analysis of the mineralogic components identified from from the X-ray diffraction patters for the analyzed seal rocks, using Diffract.Suite EVA software.

SAMPLE			SR-42V	SR-47V	SR-57V
	Name	Chemical composition	S-Q (%)		
Mineralogical Phases (Components)	Illite	Al4 K O12 Si2	18.91	19.58	18.05
	Muscovite-2M1	Al0 F H KO Si	15.96	9.22	16.45
	Quartz	O2 Si	10.83	13.2	13.06
	Albite	Al Ca0.02 Na O8 Si3	9.40	13.13	11.35
	Microcline	Al K0.95 Na0.05 O8 Si3	6.17	6.86	3.61
	Biotite	Al Ca Cr Fe K Mg Mn Na O12 Si2 Ti	6.13	11.16	4.73
	Chamosite	Al Fe2 H10 Mg3 O18 Si4	6.03	3.22	9.88
	Clinochlore	Al2 H8 Mg5 O18 Si3	5.51	3.58	9.09
	Orthoclase	Al K O8 Si3	4.22	5.91	4.38
	Chlorite	Al Cr0.7 Fe0.1 H8 Mg5 O18 Si3	3.85	3.33	3.04
	Montebrasite	Al F Li O4 P	3.73	4.3	
	Kaolinite	Al2 H4 O9 Si2	3.59	4.03	2.97
	Wollastonite	Ca3 O9 Si3	3.25		
	Monticellite	Ca Mg O4 Si	2.10	2.38	1.79
	Palygoskite	H9 Mg2 O15 Si4	0.32	0.11	
	Olivine	Mg1.6 Ni0.4 O4 Si			1.6
Total			100.00	100.00	100.00

As one can see from Figure 7.6, Figure 7.7 and Table 7.2, the microstructure of each of the three seal rocks is comprised by numerous mineralogical phase structures. By comparing the identification and the quantification of the phase structures one can see that mostly, each of them is present in all the three wells although the amounts differ slightly. However, by comparing the recorded XRD diffraction patterns in Figure 7.6 important characteristics can be observed: all the peaks associated with the phases in SR-57 are sharper then in SR-42 and SR-47 indicating a better crystallinity in this sample; The XRD patterns of the SR-42 and SR-47 samples are very similar and show peaks with an enlarged base, suggesting that these samples present a bigger amount of disorder such as amorphous phases like pores or clays (FARRAND and SINGER, 1990) then sample SR-57.

There are numerous theoretical and experimental studies in the literature showing that the thermal conductivity is proportional to thermal diffusivity, see Eq. (3.25), and lessens with decreasing grain size (ZHONG and WANG, 2006; BODAPATI *et al.*, 2006). In the present study this fact was observed for sample SR-57 having a smaller thermal diffusivity then SR-42 and SR-47. The microstructure of seal rock samples is constituted by the crystalline and amorphous mineralogical phases. We believe that the amorphous phase (like pores and hardly crystalline clays) located among the grain matrix particles, has a considerable influence in the thermal diffusivity value. Some materials, including rocks, exhibit macroscopic thermal anisotropy; for example, different numerical values for thermal conductivity result from measurements across different pairs of opposing faces on a sample of the material (pellets with micro thickness in the micrometer order in our case). The simplest type of thermal anisotropy, common in rocks, arises when the material has a layered structure at fine scales. The thermal conductivity in the direction perpendicular to the layering is generally lower than the conductivity in any direction parallel to the layering (CHEKHONIN, *et al.*, 2012). This layered structure is strongly present in sample SR-57 as can be seen in the FESEM analysis on fractured Figure 7.8(a) and polished samples Figure 7.8(b). For samples SR-42 and SR-47 this characteristic of layered structures is much smaller and the matrix grains are much bigger compared to SR-57. Besides that, samples SR-42 and SR-47 show some sort of fractures/pores that are not aligned to the bedding direction (see column b). Due to a chemical and microstructural disorder present in the amorphous SR-42 and SR-47 phases the pores and clays appeared among the rock matrix particles might create temperature gradients inside the sample. These temperature gradients are responsible for the predominance of the thermoelastic bending process in the PAS signal amplitude and phase signals observed for samples SR42 and SR-47. The small difference between the thermal diffusivity values for these two samples even originating from distinct wells suggests that the amorphous phases and lattice mismatch (a result of the coexistence of the numerous crystalline phases from the rock matrix) have similar effects on the propagation of thermal waves in the samples SR-42 and SR-47. On the other hand, the lesser amount of amorphous phase component present in the sample SR-57 and the smaller grain sizes with preferential direction (vertical to bedding) are the mainly responsible for the reduction of the thermal diffusivity of this well formation.

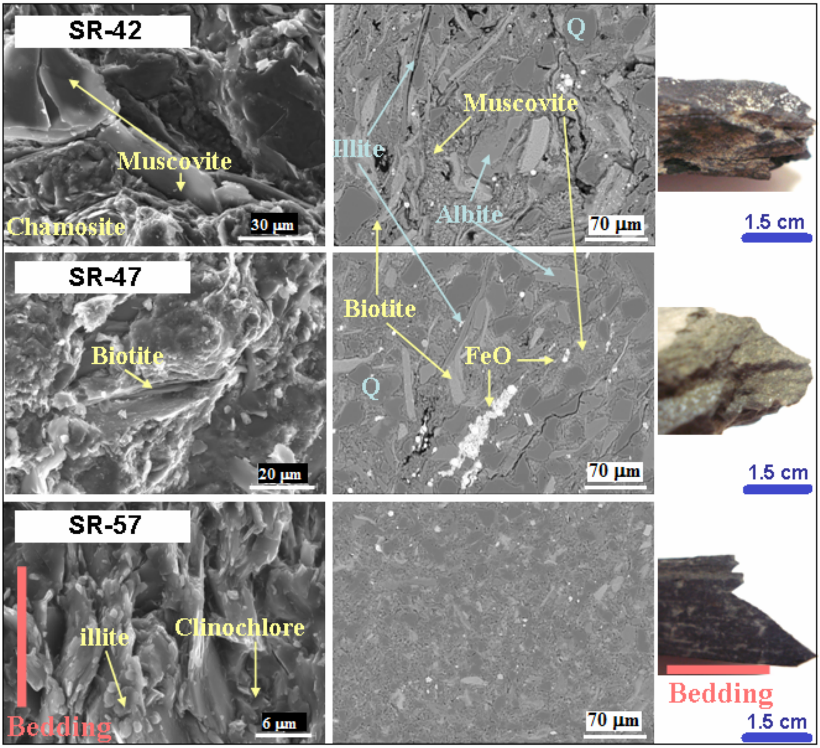

(a) (b) (c)

Figure 7.8: Mineral content, pore microstructure and rock aspects of the three analyzed seal rocks: Field Emission SEM analysis on fractured (a) and polished surface (b) samples; macrography of analyzed rocks.

8. CONCLUSIONS AND OUTLOOK

The distribution of pores and its morphologies in sedimentary rocks such as tight gas sandstones and seal rocks play essential roles in characterizing gas and oil reservoirs to predict the flux transport inside these underground deposits. This work focused on the pore-structure characterization of low-permeability TGS and seal rocks, providing an overview of techniques and methodologies which can be applied to investigate the geological evolution and properties of the reservoirs systems reflected mainly by their pore organization.

Understanding that considerable volumes of hydrocarbons are trapped in tight gas reservoirs onshore/offshore basins, some attempts have been made to find an explanation of the stress-dependence porosity and permeability behavior of these rocks. TGS represent one type of gas accumulations generally referred to as unconventional reservoirs due to their significantly lower permeability and the attendant operational challenges for achieving viable production rates and recovery volumes. In order to relate the overall flow behavior to the average geometrical characteristics of the rocks, we must consider carefully certain statistical aspects of the microscopic flow through individual pores or regions of inhomogeneity. In the first two chapters of this thesis we obtained by a compendium of techniques results for the pore structure characterization and the analysis of the petrophysical properties on tight gas sandstones. By the usage of distinct techniques it was possible to evaluate the benefits and limitations of each method and consequently obtain specific properties in these rocks which allowed us to estimate and simulate permeability.

TGS originating from distinct gas fields were investigated by PDP, N_2GA and MICP techniques to measure experimentally permeability and pore structure information. The device used for the measurements of permeability by the transient method was a CoreLab PDP-200 inserting nitrogen gas through the bedding plane (in the horizontal or vertical directions) into samples of TGS plugs. Thus the dependence of transverse flow permeability could be investigated and also the Klinkenberg' corrections could be obtained. For such low-permeability rocks the slip flow regime was present and Klinkenberg' corrections lead us to reach the absolute permeability values of analyzed samples. Also the PDP equipment had its accuracy validated by comparing results of steady-state versus pulse-decay permeability. By evaluating the permeability values of these rocks under compression and decreasing porosity level by increasing the confining pressure in the core holder, we found it to be smaller, regarding the absolute values of permeability, as higher the value of the applied net stress (dependence on porosity and clay content). The two analyzed samples of field D showed a dependence of $k = 0.2341P^{-0.8033}$ and $k = 0.0854P^{-0.7251}$. Samples of field A having considerable amount of calcite were fitted by the equations $k = -0.0018Ln(P) + 0.0073$ and $k = 0.0032P^{-0.4233}$, while sample A-17V having the pores filled by clay content showed a dependence of $k = 0.0347P^{-0.3591}$. For all samples the net stress is given in MPa. The application of PDP technique demonstrated the potential of utilizing the transient method for solving fluid flow in unconventional reservoirs and allowed us to have measured permeability values which were the basis for validating the distinct permeability correlations applied in this work. The N_2GA method, performed in an ASAP-2020 Analyzer-Micrometrics, showed primary experimental curves identified as adsorption/desorption isotherms of type II for all the TGS analyzed, though the hysteresis loops were dissimilar between distinct reservoirs investigated. The main textural parameters (surface area, pore volume and pore size distribution) in the micro and mesoporous range were assessed using five calculation methods from N_2GA technique: Langmuir and BET models for surface area calculation; BJH, Dollimore-Heal and DFT theory for pore volume calculations. The calculated values of the specific surface area using the Langmuir method were higher than those of BET due to its monolayer approach as explained in section 5.2.5. In this case more accurate BET values were between: 0.75 and 1.56 m^2/g for TGS of field A; 1.61 and 2.21 m^2/g for field B; 4.93 and 11.65 m^2/g for field C. Although the PSD derived from BJH and Dollimore-Heal adsorption models were very similar, we choose only the BJH model to be used for the combination of N_2GA and MICP techniques. The highest amounts of pore volumes measured by N_2GA technique were found in the samples of field C, an outcrop which is made up by a considerably higher amount of microposity. The experiments for the mercury capillary pressure curves were performed in an Autopore IV 9500 Micromeritics and in combination with the N_2GA results provided the main information about porosity and pore size distributions used for the investigation of permeability predictions and comparison of results obtained by the application of the compendium of techniques in TGS. The values of density obtained for each rock sample and used for the porosity conversion were measured by MICP.

Low-field NMR measurements showed to be an import tool for the porosity and PSD quantification as well as permeability predictions for the investigated low-permeability TGS rocks of field A. After keeping the sample to be 100% brine saturated for about 1 week, the experiments were obtained rapidly, in about a half hour on cleaned state mini-core samples. NMR measurements using low magnetic fields in TGS of field A have given accurate porosity values and reasonable agreements with T_2 distributions and correspond to pore size distributions from mercury porosimetry. Differently than the values of $T_{2cutoff}$ found in the literature for sandstones (33 ms) and carbonates (92 ms) the analyzed TGS rocks displayed values between 2 and 5 ms. The $T_{2cutoff}$ value is the boundary between the Bulk Volume Irreducible (BVI), comprised by clay- and capillary-bound water, and the Free Fluid Index (FFI). In our work we considered the value of BVI to be the much defined first peak in the lower region of transverse relaxation time curve. As we observed in the analyzed samples from field A, the choice of a fixed $T_{2cutoff}$ may not represent this boundary once that it is higly depend on lithology and changes considerable from distinct depths in a reservoir. Also the T_{2gm} values (the geometric mean of the relaxation spectra) was calculated to predict permeability using the Mean-T2 model and were between 1.26 and 20.3 ms. The parameter b and C from the Mean-T2 and Coates 1999 models were refined based on the experimental PDP results. The values adjusted for b were between 0.72 and 39.48 increasing with decreasing of porosity, while the values fitted for C tended to increase with porosity and were between 15.63 and 41.89.

By analyzing the 3D volumes reconstructed from integrated slices and view processes, researchers made quantitative estimations of pore bodies and characteristic connected lengths in samples. From the results of X-ray nano- and microCT measurements performed in the TGS of well A we were able to quantify porosity and PSD in distinct scales. Two methods were applied for the extraction of a 3D pore-network, mathematical morphology and equivalent resistor (skeleton). Using both methods we integrated the scales to obtain total porosity and PSD in 3D multi-scale. We observed that when the frequency number of pore sizes is used to integrate the scales, more reliable results were obtained. The curves of incremental and cumulative pore volumes from the N_2GA+MICP combination and from the low-field NMR measurements were used to compare the results of the 3D X-ray multi-scale. Additionally, important pore structure parameters for permeability estimation were measured and discussed on samples A-11V and A-17V. From the results of porosity and PSD curves (measured by N_2GA+MICP and low-field NMR) and from the textural analyses (performed by XRD and SEM/FEM) we considered that TGS of field A could be divided in an upper and a lower region with distinct microstructures, respectively represented by samples A-11V and A-17V. These measured parameters were: connectivity, tortuosity and shape factors, specific surface area *(S_o)*, aspect ratio, phi and theta orientations. We observed that the tortuosity and shape factor values increased with decreasing porosity and depth location. The results of S_o from the 3D image analysis (IA) were at least by one decimal order smaller than those of the BET results. This fact is expected because in the N_2GA analysis using BET method, the molecules of nitrogen reach even the sub-micron pores adding surface area to the final result, while in IA the results are limited to the image resolution. For both analyzed samples (A-11V and A-17V) the S_o determined by X-ray CT in the Res2 was higher than Res1 (poorest resolution). The phi and theta orientations analysis provided the information for both samples A-11V and A-17V that there is a preferred orientation of pores to the X- and Y-axis. Transposing these results to the macro-scale of the reservoir one could affirm that the horizontal hydrocarbons prospection would be favorable in the horizontal bedding direction in the regions of the reservoirs from where A-11V and A-17V were extracted. This evidence was confirmed by the experimental permeability measurements and also by simulated permeability values obtained in each the X-, Y- and Z-axis directions from the generated equivalent resistor. The simulations of single-phase flow across the generated 3D pore structure, though, were in an unreasonable level of agreement to the PDP permeability results. Nevertheless, the effort expended towards relating the calculated values of tortuosity and shape factors, geometrical and topological attribute of pore space, lead to the prediction of more accurate permeability values using the Kozeny-Carman model. We observed that from the SEM/FESEM to the nano- and microCT analyses, considerable microstructural information (pore morphology and especially clay content) was lost. We attribute this loss mainly to the low spatial resolution of microCT and to the sample size limitation when a high resolution of 0.064 µm is achieved in the nanoCT. In the nanoCT acquisition only a very small sample (volume and mass around 5.66E+04 μm^3 and 4.E-07 g, respectively) subjected to a randomly cutting place is manufactured. So for very heterogeneous samples such as the analyzed TGS A-11V and A-17V (see e.g Figure 6.31 and Figure 6.32) the usage of nanoCT proceeding would need to be carried in a statistical level, i.e. acquisition of many volume regions, meticulous work to be conceded. In fact, the dimensions of the pores and their connectivity are so small that they change the physics of gas behavior needed for reservoir simulators. Another factor which accounts for the distinction between measured and simulated permeability is the net stress pressure applied to the sample under PDP analysis; this condition is needed to perform the same pressure conditions from the original field. However, while performing a nano- and microCT acquisition only the atmospheric pressure is applied on the analyzed sample. In brief, the presence of high content of clay filling pores and also the existence of very small pores below the range of the analyzed image resolutions, create an obstacle to the segmentation process due to the unsolved grey-level distribution. As a result, the segmented pore vessels tend to be wider then they truly are. Obtaining such detailed properties of the pore morphologies information on TGS reservoir rocks would be very difficult by usage of direct experiments or conventional techniques and even in the nowadays 3D high resolution techniques. Nano- and microCT imaging technology is a new technique that provides valuable information about the 3D microstructure of TGS. The ability to characterize the pore structure of TGS in distinct scales, a very new topic, enables improved estimations of porosity and a better understanding of the pore network and structural pore parameters in the reservoir rock. Also the insights gleaned from this study using nano- and microCT images to simulate permeability in very low-permeability rocks such as TGS, have made the need to modify and develop new models for these rocks obvious. Ultimately, 3D X-ray CT technology is a gateway to investigate quantitatively the pore network and the pore morphologies in tight gas sandstones, as we observed for our rocks.

In the last part of this work we have shown a new method to measure the thermal diffusivity coefficient and porosity through muscovite-, biotite-, chamosite- and clinochlore-rich seal rocks. In this study, the measurements were performed at room temperature and atmospheric pressure, looking on the photoacoustic spectroscopy technique (PAS) applied in an open photoacoustic cell (OPC). This new methodology has the advantage of being simple and of low costs, besides it needs only a small piece (1 x 1 cm) of the sample to be analyzed. In principle, the technique is applicable to all materials and in our knowledge was never applied in seal rocks from petroleum industry before. We found from the PAS analysis that only the thermal diffusion and the thermoelastic bending mechanisms were present in the analyzed seal rocks. Measuring the thermal diffusivity of seal rocks from distinct wells we can determine the influence of each rock on the generation and preservation of oil and gas. By the support of the FESEM and XRD analyses, the PAS results allowed us to draw three main conclusions. Firstly, the thermal diffusivity of seal rocks from the distinct Brazilian fields ranges from 0.01667 to 0.09298 cm^2/s. Secondly, a strong correlation of thermal diffusivity with chemical composition and crystal orientation was observed. For sample SR-57 values of the thermal diffusivity were found to be in almost one order smaller then for samples SR-42 and SR-47. This fact was attributed to a better crystallization, preferential crystal orientation (vertical to bedding) and smaller grain sizes in sample SR-57. This rock is considered, therefore, a better thermal insulator compared to the other two samples. Nevertheless, in addition to being nonporous and non-permeable cap rocks, combined with the stable nature of each analyzed seal rock we can assume that these samples make good trapping to oil and gas reservoirs and are conductive to petroleum generation as well as preservation. Lastly, it was possible to predict very low porosity from seal rocks (between 1.42 to 9.05%) by usage of the PAS technique. This approach was reached by the proposed correlation of the measured thermal diffusivity on cleaned vertical-cutted samples (having the influence of porosity) and powder-compressed samples (with only the rock matrix influence). The results show that thermal diffusivity declines as apparent porosity of samples decreases. The PAS method, although simple, is useful in estimating the thermal diffusivity and porosity of seal rocks with accuracy and has the advantage that it avoids the use of complicated experimental setups.

SUGGESTIONS FOR FUTURE RESEARCH

- Evaluation of pore properties using N_2 gas adsorption applied in distinct samples state (size and amount of mass) of a same material;
- 3D quantification of mineralogical phases in TGS using X-ray CT technique;
- Application of the Series-Parallel model using PSD results obtained by the multi-scale 3D X-ray CT images to compare with the results obtained by the N_2GA+MICP combination.

BIBLIOGRAPHY

ADAMSON, A. W. (1990). Physical Chemistry of Surfaces, fifth ed. John Wiley & Sons, New York, 777p.

ADLER, P. M., Jacquin, C. G., and Quiblier, J. A. (1990). Flow in simulated porous media. International Journal of Multiphase Flow, vol. 16, pp. 691-712.

AGARWAL, R.K., Keon-Young, Y., Balakrishnan, R. (2001). Beyond Navier–Stokes: Burnett equations for flows in the continuum–transition regime. Physics of Fluids, vol. 13, pp. 3061-3085.

AGUILERA, R. (2002). Incorporating capillary pressure, pore throat aperture radii, height above free water table, and Winland r35 values on Pickett plots. AAPG Bulletin, vol. 86, pp. 605-624.

AHR, W. M., Allen, D., Boyd, A., Bachman, N. H., Smithson, T., Clerke, E. A., Gzara, K. B. M., Hassall, J. K., Murty, C. R. K., Zubari, H. and Ramamoorthy, R. (2005). Confronting the carbonate conundrum: Schlumberger Oilfield Review, Spring, pp. 18-29.

AL-KHARUSI, A. S. and BLUNT, M. J (2007). Network extraction from sandstone and carbonate pore space images. Journal of Petroleum Science and Engineering, vol. 56, pp. 219-231.

ALMOND, D. P. and PATEL, P. M. (1996). Photothermal Science and Techniques. Springer Netherlands, 241p.

ANDREW, T. C. (1986). Applications of photoacoustic sensing techniques. Reviews of Modern Physics, vol. 58, No. 2, pp. 381-431

ARRIAGA, M. C. S. (1993). Rock thermal conductivity at the cap rock and initial conditions in two-phase volcanic hydrothermal systems. SGP-TR-145, pp. 147-152.

ASAP 2020 (2007). Version 3.03. Copyright © Micromeritics Instrument Corporation 1994-2007.

ASHKAR, A., Fisher, Q. J. and Grattoni, C. A. (2010). Determination of Surface Relaxivity from NMR T2 Measurements. AAPG GEO 2010 Middle East Geoscience Conference & Exhibition, Manama, Bahrain.

AVIZO® 7 (2012), Avizo user's guide. © 1995-2012 Konrad-Zuse-Zentrum für Informationstechnik Berlin (ZIB), Germany; © 1999-2012 Visualization Science Group (VSG), 908p.

AWCOCK, G. J. and AWCOCK, T. (1995). Applied Image Procesing. McGraw-Hill Companies, NY, 300p.

BAI, L., Baker, D. R., Hill, R. J. (2010). Permeability of vesicular Stromboli basaltic glass: lattice Boltzmann simulations and laboratory measurements. Journal of Geophysical Research Solid Earth 115, B07201. http://dx.doi.org/10.1029/2009JB007047.

BAKER, D.R., Mancini, L., Polacci, M., Higgins, M. D., Gualda, G. A. R., Hill, R. J and Rivers, M. L. (2012). An introduction to the application of X-ray microtomography to the three-dimensional study of igneous rocks. Lithps, vol. 148, pp. 262-276.

BALDERAS-LÓPEZ, J. A. (2006). Photoacoustic signal normalization method and its application to the measurement of the thermal diffusivity for optically opaque materials. Review of Scientific Instruments, vol. 77, 064902, 4p.

BALDERAS-LÓPEZ, J. A., Moreno-Márquez, M. M., Martínez, J. L. and Sánchez-Sinencio, F. (1999). Thermal characterization of some dental resins using the photoacoustic phase lag discontinuites. Superficies y Vacío, vol. 8, pp. 42-45.

BARNETT, A. J., Wright, V. P. and Khanna, M. (2010). Porosity Evolution in the Bassein Limestone of Panna and Mukta Fields, Offshore Western India: Burial Corrosion and Microporosity Development. Search and Discovery Article #50326, 4p.

BARRET, E.P., Joyner, L.G., Halenda, P.P. (1951). The determination of pore volume and area distribution in porous substances. I. Computations from nitrogen isotherms. Journal of the American Chemical Society, vol. 73, pp. 373-380.

BARRETT, L. K., and YUST, C S. (1970). Some fundamental ideas in topology and their application to problems in metallurgy. Metallurgy, vol. 3, pp. 1-33.

BEAR, J. and BACHMAT, Y. (1966). Hydrodynamic dispersion in non-uniform flow through porous media taking into account density and viscosity differences, Technion Institute of Technology, Hydraulics Lab. P.N. 4/66, 308p.

BEAR, J. (1972). Dynamics of fluids in porous media. Dover Publications, Inc., Mineola. 764p.

BENZAGOUTA, M. S. (2012). Reservoir characterization: evaluation for the channel deposits sequence – upper part using scanning electron microscope (SEM) ad mercury injection (MICP): case of tight reservoirs (North Sea). Journal of King Saud University – Engineering Science. http://dx.doi.org/10.1016/j.jksues.2012.10.001

BERA, B., Mitra, S. K. and Vick, D. (2011). Understanding the micro structure of Berea Sandstone by the simultaneous use of micro-computed tomography (micro-CT) and focused ion beam-scanning electron microscopy (FIB-SEM). Micron, vol. 42, pp. 412-418.

BERG, R. R. (1975). Capillary pressures in stratigraphic traps. American Association of Petroleum, Geologists Bulletin, vol. 59, pp. 939-956.

BISWAS, A., Telschow, K. L., Ahmed, T. and Johnson, K. W. (1983). Photoacoustic microscopic analysis of a heterogeneous material– coal. Ultrasonics Symposium, pp. 704-707.

BJØRLYKKE, K. (2010). Petroleum Geoscience: From Sedimentary Environments to Rock Physics. Springer Heidelberg Dordrecht London New York e-ISBN 978-3-642-02332-3, 508p.

BLASINGAME, T. A. (2008). The Characteristic Flow Behavior of Low-Permeability Reservoir Systems. Society of Petroleum Engineers, SPE Unconventional Reservoirs Conference, 978-1-55563-171-0, 31p.

BLUNT, M. J., Jackson, M. D., Piri, M. and Valvatne, O. H. (2002). Detailed physics, predictive capabilities and macroscopic consequences for pore-network models of multiphase flow. Advances in Water Resources, vol. 25, pp. 1069-1089.

BLUNT, M. J., Bijeljic, B., Dong, H., Gharbi, O., Iglauer, S., Mostaghimi, P., Paluszny, A. and Pentland, C. (2013). Pore-scale imaging and modeling. Advances in Water Resources, vol. 51, pp. 197-216.

BODAPATI, A., Schelling, P.K., Phillipot, S.R. and Keblinski, P. (2006). Vibrations and thermal transport in nanocrystalline silicon. Physical Review B, vol. 74, 245207, 11p.

BROWN and MARCO (1958). Introduction to Heat Transfer, 3rd Ed, McGraw-Hill, 1958 and Eckert & Drake, Heat and Mass Transfer, McGraw-Hill, 1959. Retrieve on October 29th, 2013 from: http://en.wikipedia.org/wiki/Thermal_diffusivity.

BROWN, P. R. (1985). Clays and the petroleum industry, an overview. Applied ClayScience Elsevier Science Publishers B.V., Amsterdam -- Printed in The Netherlands, vol. 1, pp. 219-223.

BRUNAUER, S., Emmett, P.H., Teller, E. (1938). Adsorption of gases in multimolecular layers. Journal of the American Chemical Society, vol. 60, pp. 309-319.

BRUNAUER, S., Deming, L. S., Deming, W. S. and Teller, E. J. (1940). On a theory of the Van der Waals adsorption of gases. Journal of the American Chemical Society. Vol. 62:7, pp. 1723-1732.

BUHRKE, V. E., Jenkins, R. and Smith, D. K. (1998). A practical guide for the preparation of specimens for X-ray fluorescence and X-ray diffraction analysis. Wiley-VCH, 333p.

BUTCHER, A. R. and LEMMENS, H. J. (2011). Advanced SEM technology clarifies nanoscale properties of gas accumulations in shales. The American Oil & Gas Reporter, vol. 54:7, pp. 118-124.

CAI, Q., Buts, A., Biggs, M. J. and Seaton, N. A. (2007). Evaluation of methods for determining the pore size distribution and pore-network connectivity of porous carbons. Langmuir, vol. 23, No. 16, pp. 8430-40.

CAI, Y., Liu, D., Pan, Z., Yao, Y., Li, J., Qiu, Y. (2013). Petrophysical characterization of Chinese coal cores with heat treatment by nuclear magnetic resonance. Fuel, vol. 108, pp. 292-302.

CAPP- Canadian Association of Petroleum Producers. Available at http://www.capp.ca/canadaIndustry/naturalGas/Conventional-Unconventional/Pages/default.aspx#Z8roKEkBHchn, Access in 21/01/2011

CARLES, P., Egermann, P., Lenormand, R. and Lombard, JM. (2007) Low permeability measurements using steady-state and transient methods. SCA2007-07, 12p.

CALLISTER, W. D. (2002). Ciência e engenharia de materiais: uma introdução. 5ed. LTC, São Paulo, 408p.

CANTRELL, D. L and HAGERTY, R. M. (1999). Microporosity in Arab Formation Carbonates, Saudi Arabia. GeoArabia, vol. 4:2, pp. 129-154.

CARMAN, P. C. (1937). Fluid flow through granular beds. Transactions of the Institution of Chemical Engineers, vol. 15, pp. 150-166.

CHEKHONIN, E. et al., (2012). When rocks get hot: thermal properties of reservoir rocks. Oilfield Review Autumn, vol. 24, No. 3, pp 20-37.

CHEN, Q., Kinzelbach, W., Ye, C. and Yue, Y. (2002). Variations of Permeability and Pore Size Distribution of Porous Media with Pressure. Journal of Environmental Quality, vol. 31, pp. 500-505.

CHILDS, E. C. and COLLIS-GEORGE, N. (1950). The permeability of porous materials. Proceedings of the Royal Society of London A A201, pp. 392-405.

CHOQUETTE, P.W. and PRAY, L.C. (1970). Geologic nomenclature and classification of porosity in sedimentary carbonates: AAPG Bulletin, vol. 54:2, pp. 207-244.

CIVAN, F. (2010). Effective correlation of apparent gas permeability in tight porous media. Transport in Porous Medium, vol. 82, pp. 375-384.

CLARKSON, C. R. Freeman, M., He. L., Agamalian, M., Melnichenko, Y. B., Mastalerz, M., Bustin, M., Radlinski, A. P. and Blach, T. P. (2011). Characterization of tight gas reservoirs pore structure using USANS/SANS and gas adsorption analysis. Fuel, vol. 95, pp. 371-385.

CLENNELL, M. B. (1997). Tortuosity: a guide through the maze. Geological Society London Special Publications, vol. 122, pp. 299-344.

CLERKE, E. A., Mueller, H. W., Phillips, E. C., Eyvazzadeh, R. Y., Jones, D. H., Ramamoorthy, R. and Srivastava, A. (2008). Application of Thomeer Hyperbolas to decode the pore systems, facies and reservoir properties of the Upper Jurassic Arab D Limestone, Ghawar field, Saudi Arabia: A “Rosetta Stone” approach. GeoArabia, vol. 13:4, pp. 113-160.

COASNE, B., Gubbins, K. E., Pellenq, R. J. M. (2004). A grand canonical Monte Carlo study of adsorption and capillary phenomena in nanopores of various morphologies and topologies: testing the BET and BJH characterization methods. Particle & Particle Systems Characterization, vol. 21, pp. 149-160.

COATES, G. R., Xiao, L. and Prammer, M. G. (1999). NMR Logging: principles & applications. Halliburton Energy Services, Houston, H02308, 234p.

COMISKY, J. T., Santiago, M., Mccollom, B., Buddhala, A. and Newsham, K. E. (2011). Sample size effects on the application of mercury injection capillary pressure for determining the storage of tight gas and oil shales. CSUG/SPE 149432, 23p.

COPPENS, M.-O. (1999). The effect of fractal surface roughness on diffusion and reaction in porous catalysts from fundamentals to practical applications. Catalysis Today, vol. 53:2, pp. 225-243.

COPPENS, M.-O. and DAMMERS, A. J. (2006). Effects of heterogeneity on diffusion in nanopores from inorganic materials to protein crystals and ion channels. Fluid Phase Equilibria.. vol. 246:1-2, pp. 308-316.

COSSÉ, R. (1993). Basics of reservoir engineering. Oil and gas field development techniques. Gulf Publishing Company, ISBN 0884151840, Houston, USA. 342p.

CRISP, P. T., Ellis, J., Hutton, A. C., Korth, J., Martin, F. A., Saxby, J. (1987). Australian oil shales: a compendium of geological and chemical data. ISBN 0 86418 057 8, 109p.

CSIRO – Project proposal (SHARPP) Shale Rock Physics and Petrophysics. http://www.google.com.br/url?sa=t&rct=j&q=&esrc=s&source=web&cd=1&cad=rja&ved=0CCsQFjAA&url=http%3A%2F%2Fwww.researchgate.net%2Fpublication%2F257298885_SHARPP_Consortium_-_Rock_Physics__Petrophysics_in_Shales%2Ffile%2F60b7d524cda4125fe1.pdf&ei=ME3hUuzBKtKkkQfDy4CgDw&usg=AFQjCNHTTQe_0oBMuq5qg7nabbk7G1IZEQ&bvm=bv.59568121,d.eW0, Access in 23/01/2014.

CUNHA, A. R. (2012). Caracterização de sistemas porosos de rochas reservatório de petróleo a partir da extração de redes poro-ligação. Dissertação de mestrado, Programa de Pós-Graduação em Ciência e Engenharia de Materiais da Universidade Federal de Santa Catarina. Florianópolis, SC, Brasil.

CUSSLER, E. L. (1997). Diffusion Mass Transfer in Fluid Systems. 2nd edition, Cambridge University Press, 580p.

DAKE, L. P. (1978). Developments in petroleum science 8, fundamentals of reservoir engineering. Elsevier Science B.V., Amsterdam, The Netherlands. 443p.

DANDEKAR, O. (2008). High-performance 3D image processing architectures for image-guided interventions. Ph.D. Thesis, University of Maryland, College Park, Department of Electrical and Computer Engineering, 220p.

DARABI, H., Ettehad, A., Javadpour, F., and Sepehrmoori, K. (2012). Gas flow in ultratight shale strata. Journal of Fluid Mechanics, vol. 710, pp. 641-658.

DARCY, H. (1856). Les Fontaines Publiques de la Ville de Dijon, Dalmont, Paris, 647p.

DA SILVA JÚNIOR, G. (2013). Estudo de rochas reservatório de petróleo que contêm argilominerais expansíveis por relaxometria. Monografia em Química com atribuição tecnológica, Universidade Federal do Rio de Janeiro, Instituto de Química, 59p.

DE LIMA, J. C., Cella, N., Miranda, L. C. M., Anchying, C., Franzan, A. H. and Leite, N. F. (1992). Photoacoustic characterization of chalcogenide glasses: Thermal diffusivity of Ge_xTe_{1-x}. Physical Review B, vol. 46, pp. 14186-14189.

DE LIMA, J. C., Schmitt, M., Souza, S. M., Almeida, T. O., Jeronimo, A. R., Trichês, D. M., Grandi, T. A. and Campos, C. E. M. (2007). Structural and thermal study of nanostructured GaSb alloy prepared by mechanical alloying. Journal of Alloys and Compounds, vol. 436, pp. 13-18.

DESBOIS, G. and URAI, J. (2009). The benefit of BIB/FIB-cryo-SEM techniques for characterization of elusive microstructures in clay-rich geomaterials. Physical Properties of Earth Materials Newsletter, pp. 13-18.

DESBOIS, G., Urai, J. L., Kukla, P. A., Konstanty, J. and Baerle (2011). High-resolution 3D fabric and porosity model in a tight gas sandstone reservoir: A new approach to investigate microstructures from mm- to nm-scale combining argon beam cross-sectioning and SEM imaging. Journal of Petroleum Science and Engineering, vol. 78, pp. 243-257.

DICKER, A. I. and SMITS, R. M. (1988). A practical Approach for Determining Permeability from Laboratory Pressure-Pulse Decay Measurements, SPE 17578 International Meeting on Petroleum Engineering, Tianjin, China, 1-4 November.

DO CARMO, M. (1976). Differential Geometry of Curves and Surfaces, Prentice-Hall, 503p.

DO, D. D. and DO, H. D. (2003). Characterization of carbonaceous materials by DFT and GCMC simulations: A review. Adsorption Science and Technology, vol. 21:5, pp. 389-423.

DOLLIMORE, D. and HEAL, G. R. (1964). An improved method for the calculation of pore size distribution from adsorption data. Journal of Applied Chemistry, vol. 14, pp. 109-114.

DOLLIMORE, D. and HEAL, G. R. (1970). Pore-size distribution in typical adsorbent systems Journal of Colloid Interface Science. Vol. 33, pp. 508-519.

DONG, H. and BLUNT, M. J. (2009). Pore-networking extraction from micro-computerized-tomography images. Physical Review E, vol. 80, pp. 036307-1 to 11.

DOS SANTOS, L. O. E.; Ortiz, C. E. P.; de Gaspari, H. C.; Haverroth, G. E.; Philippi, P. C. (2005). Prediction of intrinsic permeabilities with lattice boltzmann method. Proceedings of the COBEM, 2005.

DULLIEN, F. A. L. (1992). Porous Media: Fluid Transport and Pore Structure, 2nd ed. Academic Press Inc. San Diego 574p.

ECHEVERRÍA, J. C., Morera, M. T., Mazkiarán, C. and Garrido, J., (1999). Characterization of the porous structure of soils: adsorption of nitrogen (77K) and carbon dioxide (273K), and mercury porosimetry. European Journal of Soil Science, vol. 50, pp. 497-503

EDWARDS, J. C. (2010). *Principles of NMR.* Process NMR Associates LLC, 87A Sand Pit Rd, Danbury CT 06810. Available at : http://www.process-nmr.com/pdfs/NMR%20Overview.pdf, Access in 04/12/2013.

ELGMATI, M. (2011). Shale gas rock characterization and 3d submicron pore network reconstruction. Master Thesis, Presented to the Faculty of the Graduate School of the Missouri University of Science and Technology, 78p.

ESEME, E., Krooss, B.M. and Little, R. (2012). Evolution of petrophysical properties of oil shales during high-temperature compaction tests: implication for petroleum expulsion. Marine and Petroleum Geology, vol. 31, pp. 110-124.

FARRAND, W. H. and SINGER, R. B. (1990). Analysis of poorly crystalline clay mineralogy: near infrared spectrometry versus X-ray diffraction. Lunar and Planetary Institute, pp. 347-348.

FATT, I. and DAVIS, D. H. (1952). Reduction in permeability with overburden pressure. Trans. AIME, Tech. Note 147, 194, 329.

FAVVAS, E. P., Sapalidis, A. A., Stefanopoulos, K. L., Romanos, G. E., Kanellopoulos, N. K., Kargiotis, E. K. and Mitropoulos, A. (2009). Characterization of carbonate rocks by combination of scattering, porosimetry and permeability techniques. Micropores and Mesopores Materials, vol.. 120, pp. 109-114.

FELDKAMP, L. A., Davis, L. C. and Kress, J. W. (1984). Practical cone beam algorithm. Journal of the Optical Society of America A, v. 1:6, pp. 612-619.

FENG, J., Gao, Z., Zhu, R., Luo, Z. and Zhang, L. (2013). The application of thermal conductivity measurements to the Kuqa River profile, China, and implications for petrochemical generation. SpringerPlus, vol. 2, 6p.

FERNANDES, C. P. (1990). Estudo dos processos de condensação e migração de umidade em meios porosos consolidados: análise experimental de uma argamassa de cal e cimento, Dissertação de mestrado. Programa de Pós-Graduação em Engenharia Mecânica, Florianópolis.

FERNANDES, C. P. (1994). Caracterização morfológica de espaços porosos: reconstrução multiescala e simulação de processos de invasão de fluidos não-molhantes. Tese de Doutorado. Programa de Pós-Graduação em Engenharia Mecânica da Universidade Federal de Santa Catarina. Florianópolis, SC, Brasil.

FERNANDES, C. P., Philippi, P. C., Gaspari, H. C. (2003). Permeability determination from pore size distributions. In: Second Brazilian P&D Congress in Petroleum and Natural Gas, Brazil.

FORMOSO, M. L. L. (1984). Técnicas Analíticas Instrumentais Aplicadas à Geologia: Difratometria de Raios X. Ed. Edgar Blücher, 218p.

GAO, S., Chapman, W. G and House W. (2009). Application of low field NMR T2 measurements to clathrate hydrates. Journal of Magnetic Resonance, vol. 197, pp. 208-212.

GODEFROY, S. and CALLAGHAN, P. T. (2003). 2D relaxation/diffusion correlations in porous media. Magnetic Resonance Imaging, vol. 21, pp. 381-383.

GOLAB, A. N.; Knackstedt, M. A.; Averdunk, H.; Senden, T.; Butcher, A. R. and Jaime, P. (2010). 3D porosity and mineralogy characterization in tight gas sandstones. The Leading Edge, pp. 1476-1483.

GOLDSTEIN, J. I., Newbury, D.E., Joy, D.C., Lyman, C.E., Echlin, P., Lifshin, E., Sawyer, L. and Michael, J.R. (2003). Scanning electron microscopy and X-ray microanalysis. Third Edition. Springer Science=Business Media, LLC, USA, 690p.

GREGG, S. J. and SING, K. S. (1982). Adsorption, Surface Area and Porosity. Academic Press, New York, 313p.

GRIFFIN, D. D., Kleinberg, R. L., and Fukuhara, M. (1993). Low-frequency NMR spectrometer. Measurement Science and Technology, vol. 4 (9), pp. 968-975.

GROEN, J. C., Peffer, L. A. A. and Pérez-Ramírez, J. (2003). Pore size determination in modified micro- and mesoporous materials. Pitfalls and limitations in gas adsorption data analysis. Microporous and Mesoporous Materials, vol. 60, pp. 1-17.

GUIMARÃES, A. O., Viana, D. A., Cordeiro, T. C., Sampaio, J. A., Da Silva, E. C., Toledo, R., Ribeiro, H. J. P. S., Carrasquilla, A. A. G. and Vargas, H. (2013). On the use of photothermal methods for thermal charcaterization of sedimentary rocks from the Paraná Basin in Brazil. Marine and Petroleum Geology, vol. 43, pp. 121-126.

HAI, G., Wan-Chi, S. and Chao-Huan, H.. (2001). Improved Techniques for Automatic Image Segmentation. IEEE Transactions on Circuits and Systems for Video Technology, vol 11:12, pp. 1273-1280.

HALSEY, G. (1948). Physical adsorption on non-uniform surfaces. Journal of Chemical Physics, vol. 16, pp. 931-937.

HAMADA, G. M., Al-Blehed, M. S., Al-Award, M. N. and Al-Saddique, M. A. (2001). Petrophysical evaluation of low-resistivity sandstone reservoirs with nuclear magnetic resonance log. Journal of Petroleum Science and Engineering, vol. 29, pp 129-138.

HAO, S., Huang, Z., Liu, G., Zheng, Y. (2000). Geophysical properties of cap rocks in Qiongdongnan Basin, South China Sea. Marine and Petroleum Geology, vol. 17, pp 547-555.

HILDENBRAND, A., Krooss, B. M., and Urai, J. L. (2005). Relationship between pore structure and fluid transport in argillaceous rocks, Solid Mechanics and Its Applications, IUTAM Symposium on Physicochemical and Electromechanical Interactions in Porous Media, vol. 125, pp. 231-237.

HIRASAKI, G. J., Lo, S. W., Zhang, Y. (2003). NMR properties of petroleum reservoir fluids, Magnetic Resonance Imaging, vol. 21, pp. 269-277.

HODGKINS, M. A. and HOWARD, J. J. (1999). Application of NMR logging to reservoir characterization of low-resistivity sands in the Gulf of Mexico. AAPG Bull, vol.83:1, pp. 114-27.

HOLDITH, S. A. (2006). Tight Gas Sands, SPE, Texas A&M U. jpt Distinguished Author Series, pp. 86-94.

HOLMES, D. (2012). Basic Practical NMR Concepts: A Guide for the Modern Laboratory. 42p.

HOSSAIN, Z., Grattoni, C. A., Solymar, M., Fabricius, I. L. (2011). Petrophysical properties of greensand as predicted from NMR measurements. Petroleum Geoscience, Vol. 17:2, pp. 111-125.

HOU, Y. (2012). Experimental characterization and modeling of the permeability of fibrous preforms using gas for direct processes application. THÈSE Docteur de l'École Nationale Supérieure des Mines de Saint-Étienne, NNT 2012 EMSE 0667, 178 pp.

HUGGETT, J. M, and SHAW, H. F. (1997). Field scanning electron microscopy – a high-resolution technique for the study of clay minerals in sediments. Clay Minerals, vol. 32, pp. 197-203.

IEO-2011(EIA) – International Energy Outlook 2011, from U.S. Energy Information Administration. Washington (2011), 292 pp.

IMAGO – Image Analysis System from ESSS - Engineering Simulation and Scientific Software, Florianópolis, SC, Brasil April 19, 2005. http://www.imagosystem.com.br.

INCROPERA, F. P., David, P. D., Theodore, L. B. and Adrienne, S. L. (2006). Fundamentals of heat and mass transfer, 6th Edition, John Wiley & Sons. Inc., New York, 997 pp.

IQBAL, M., Chen, J., Yang, W., Wang, P. and Sun, B. (2013). SAR image despeckling by selective 3D filtering of multiple compressive reconstructed images. Progress In Electromagnetics Research, vol. 134, pp. 209-226.

IONNIDIS, M. A. and CHATZIS, I. (2000). On the geometry and topology of 3D stochastic porous media. Journal of Colloid and Interface Science, vol. 229, No. 2, pp. 323-334.

IVANOV, S. N., Kozorezov, A. G., Taranov, A. V. and Khazanov, E. N. (1992). Propagation of nonequilibrium phonons in ceramic materials. Journal of Experimental and Theoretical Physics, vol. 75 (2), pp. 319-328.

JACKSON, S., Chang, M. M. and Tham, M. (1993). Data requirements and acquisition for reservoir characterization. NIPER-615 (DE93000121) 35p.

JANSSEN, C., Wirth, R., Reinicke, A., Rybacki, E., Naumann, R., Wenk, H.-R. and Dresen, G. (2011). Nanoscale porosity in SAFOD core samples (San Andreas Fault). Earth Planetary Science Letter, vol. 201, pp. 179-189.

JAVADPOUR, F., Fisher, D. and Unsworth, M. (2007). Nanoscale Gas Flow in Shale Gas Sediments. Journal of Canadian Petroleum Technology, pp. 55-61.

JAVADPOUR, F. (2009). Nanopores and apparent permeability of gas flow in mudrocks (shales and siltstone). Journal of Canadian Petroleum Technology, vol. 48 (8), pp. 16-21

JAYA, I., Sudaryanto, A. and Widarsono, B. (2005). Permeability Prediction Using Pore Throat and Rock Fabric: a Model from Indonesian Reservoirs. SPE 93363.

JONES, S. C. (1972). A rapid accurate unsteady-state Klinkenberg permeameter. SPE 3535, pp. 383-397.

JONES, S. C. (1997). A technique for faster pulse-decay permeability measurements in tight rocks. SPE 28450, pp. 19-25.

KAK, A. C. and SLANEY, M. (1999). Principles of computed tomography imaging. IEEE Press, New York.

KATE, J. M. and GOKHALE, C. S. (2006). A simple method to estimate complete pore size distribution of rocks. Engineering Geology, vol. 84, pp. 48-69.

KATZ, A. J. and THOMPSON, A. H. (1986). Quantitative Prediction of Permeability in Porous Rock, Physical Review B, vol. 34, pp. 8179-8181.

KAUFMANN, J., Loser, R. and Leemann, A. (2009). Analysis of cement-bonded materials by multi-cycle mercury intrusion and nitrogen sorption. Journal of Colloid Interface Science, vol 336, pp. 730-737.

KENYON, W. E. (1992). Nuclear magnetic resonance as a petrophysical measurement. Nuclear Geophysics, vol. 6, No. 2, pp. 153-171.

KETCHAM, R. A., and CARLSON, W. D. (2001). Acquisition, optimization and interpretation of X-ray computed tomographic imagery: applications to the geosciences. Computers & Geoscience, vol. 27, pp. 381-400.

KLEINBERG, R. L., Farooqui, S. and Horsfield, M. A. (1993). T_1/T_2 ratio and frequency dependence of NMR relaxation in porous sedimentary rocks. Journal of Colloid and Interface Science, vol. 158, pp. 195-198.

KLEINBERG, R (1996). Utility of NMR T_2 distributions, connection with capillary pressure, clay effect, and determination of the surface relaxivity parameter ρ_2. Magnetic Resonance Imaging, vol. 14, pp. 761-767.

KLINKENBERG, L.J. (1941). The permeability of porous media to liquids and gases. API: Drilling and Production Practice, pp.200-213.

KNACKSTED, C. H., Arns, C. H., Ghous, A., Sakellarious, A., Senden, T. J., Sheppard, A. P., Sok, R. M.., Nguyen, V. and Pinczewski, W. V. (2006). 3D imaging and characterization of the pore space of carbonate core implications of single and two phase flow properties. SPWLA 47th Annual Logging Symposium, 15p.

KNUDSEN, M.. (1909). Die Gesetze der molecular Stromung und die inneren Reibungstromung der Gase durch Rohren. Annalen der Physik, vol. 28, pp. 75-130.

KNUDSEN, M. (1950). Kinetic Theory of Gases: Some Modern Aspects. Third ed., London: Methuen & Co. Ltd.

KOLODZIE, S. (1980). Analysis of pore throat size and use of Waxman-Smits equation to determine OOIP in Spindle Field, Colorado. SPE9382, presented at 1980 SPE Annual Technical Conference and Exhibition, Dallas.

KOVSCEK, A. R., Zhou, D., Jia, L. and Kamath, J. (2001). Scalling of counter-current imbibition processes in low-permeability porous media. DOE/BC/15311-2 (OSTI ID: 773294), 31p.

KUMAR, J., Abulrub, A-H. G., Attride, A., and Williams, M. A. (2011). Effect of X-ray computed tomography scanning parameters on the estimated porosity of foams specimens. 2nd International onference on Mechanical, Industrial, and Manufacturing Technologies, MIMT, V1, pp. 99-103.

KWON, O., Kronenbeg, A. K., Gangi, A. F., Johnson, B. and Herbert, B. E. (2004). Permeability of illite-bearing shale: 1. Anisotropy and effects of clay content and loading. Journal of Geophysical Research, vol. 109, B10205, 19p.

LACHAINE, A. and POULET, P. (1984). Photoacoustic measurement of thermal properties of a thin polyester film. Applied Physics Letter, vol. 45 (9), pp. 953-954.

LANDERS, J., Gor, G. Y. and Neimark, A. V. (2013). Density functional theory methods for characterization of porous materials. Colloids and

Surfaces A: Physicochemical and Engineering Aspects, vol. 437, pp. 3-32.

LATIEF, F. D. and FAUZI, U. (2012). Kozeny–Carman and empirical formula for the permeability of computer rock models. International Journal of Rock Mechanics & Mining Sciences, vol. 50, pp. 117-123.

LATORRACA, G. A., Dunn, K. J. and Brown, R. J. S (1993). Predicting permeability from nuclear magnetic resonance and electrical properties measurements. In Proceedings: SPE Annual Technical Conference. Society of Petroleum Engineers, Paper 18272.

LAW, B. E., and CURTIS, J. B. (2002). Introduction to unconventional petroleum systems: AAPG Bulletin, v. 86, pp. 1851-1852.

LERCHE, I and NOETH, S. (2004). Economics of petroleum production a compendium. v. 2, Value and worth, Brentwood, Essex : Multi-Science Pub., 284p.

LI, S., Dong, M., Li, Z., Huang, S., Qing, H. and Nickel, E. (2005). Gas breakthrough pressure for hydrocarbon reservoir seal rocks: implications for the security of long-term CO_2 storage in the Weyburn field. Geofluids vol. 5, pp. 326-334.

LIANG, Z., Ionnidis, M. A. and Chatzis, I. (2000). Permeability and electrical conductivity of porous media from 3D stochastic replicas of the microstructure. Chemical Engineering Science, vol. 55, pp. 5247-62

LIANG, X., Chang-chun, Z., Zhi-qiang, M., Yu-jiang, S., Xiao-peng, L., Yan, J., Hao-peng, G and Xiao-xin, H. (2013). Estimation of water saturation from nuclear rmagnetic resonance (NMR) and conventional logs in low permeability sandstone reservoirs. Journal or Petroleum and Engineering, vol. 108, pp. 40-51.

LIMA, W. M., Biondo, V., Weinand, W. R., Nogueira, E. S., Medina, A. N., Baesso, M. L. and Bento, A. C. (2005). The effect of porosity on thermal properties: towards a threshold of particle contact in sintered stainless steel. Journal of Physics: Condensed Matter, vol. 17, pp. 1239-1249.

LIN, C., and COHEN, M.H. (1982). Quantitative methods for micro-geometric modeling. Journal of Applied Physics, vol. 53, pp. 4152-4165.

LIU, J. and REGENAUER-LIEB, K. (2011). Application of percolation theory to microtomography of structured media: percolation threshold, critical exponents, and upscaling. Physical Review E, vol. 83, 016106.

LOIZOU, C. P. and PATTICHIS, C. S. (2008). Despeckle Filtering Algorithms and Software for Ultrasound Imaging Synthesis Lectures on Algorithms and Software in Engineering, 166 pp.

LOUCKS, R. G., Reed, R. M., Ruppel, S. C. and Hammes, U. (2012). Spectrum of pore types and networks in mudrocks and a descriptive classification for matrix-related mudrock pores. AAPG Bulletin, v. 96:6, pp. 1071-1098.

MAGOON, L.B., and BEAUMONT, E. A. (1999). Petroleum system, in Beaumont, E.A. and Foster, N.H., eds., Exploring for oil and gas traps: American Association of Petroleum Geologists Treatise of Petroleum Geology, Chap. 3, pp. 3.1-3.34.

MANTOVANI, I. F. (2013). Microtomografia e nanotomografia de raios X aplicada à caracterização multiescalar de sistemas porosos carbonáticos, Tese de Doutorado. Programa de Pós-Graduação em Ciência e Engenharia de Materiais da Universidade Federal de Santa Catarina. Florianópolis, SC, Brasil.

MARTYS, N. S. and CHEN, H. (1996). Simulation of multi-component fluids in complex three-dimensional geometries by the lattice Boltzmann method, Physical Review E, vol. 53, pp. 743-750.

MARQUES FILHO, O. and VIEIRA NETO, H. (1999). Processamento Digital de Imagens. Edição. Rio de Janeiro: Brasport.

MARSCHALL, D., Gardner, J. S., Mardon, D. and Coates, G. R. (1995). Method for correlating NMR relaxometry and mercury injection data. SCA Conference Paper Number 9511, 12p.

MASTERS, J. A. (1979). Deep Basin Gas Trap, Western Canada. AAPG Bulletin, vol. 63, No. 2, pp. 152-181.

MAXWELL, J. C. (1867). On stresses in rarefied gases arising from inequalities of temperature. Philosophical Transactions of the Royal Society London, vol. 170, pp. 231-256.

MENGER, S. and PRAMMER, M. (1998). Can NMR porosity replace conventional porosity in formation evaluation. SPWLA 39th Annual Logging Symposium, Keystone, Paper RR, 4p.

MOREIRA, A. C. (2013). Análise da influência da morfologia porosa de implantes de titânio no processo de crescimento ósseo. Tese de Doutorado. Programa de Pós-Graduação em Ciência e Engenharia de Materiais da Universidade Federal de Santa Catarina. Florianópolis, SC, Brasil.

MORRISS, C., Rossini, D., Straley, C., Tutunjian, P., and Vinegar, H. (1997). Core analysis by low-field MNR. Society of Petrophysicists and Well-Log Analysts, The Log Analyst, vol. 38, No. 2, 12p.

NAIK, G. C. (2004). Tight gas reservoir – an unconventional natural energy source for the future 32p. http://www.sublettewyo.com/DocumentCenter/Home/View/358, Access in 20/01/2014.

NATIONAL RESEARCH COUNCIL (1989). Materials Science and Engineering for the 1990s: Maintaining Competitiveness in the Age of Materials. Washington, DC: The National Academies Press, 296p.

NELSON, P. H. (2009). Pore-throat sizes in sandstones, tight sandstones, and shales. AAPG Bulletin, v. 93, no. 3, pp. 329-340.

NGUYEN, H-Y. (2011). Computed tomography for the non-destructive imaging of cultural heritage: X-ray, Gamma and Neutron sources. Master Degree Thesis of Art Conservation, Queen's University, Ontario, Canada 188p.

NOZIK, A. J. (2001). Spectroscopy and hot electron relaxation dynamics in semiconductor quantum wells and quantum dots. The Annual Review of Physical Chemistry, vol. 53, pp. 193-231.

OILFIELD GLOSSARY – Schlumberger. http://www.glossary.oilfield.slb.com/en.aspx, Access in 22/01/2014.

PAPE, H., Clauser, C. and Iffland, J. (1999). Permeability prediction based on fractal pore-space geometry. Geophysics, vol. 64:5, pp. 1447-1460.

PAPE, H., Tillich, J. E. and Holz, M. (2006). Pore geometry of sandstone derived from pulse field gradient NMR. Journal of Applied Geophysics, vol. 58, pp. 323-252.

PENG, S., Hu, Q., Dultz, S. and Zhang, M. (2012). Using X-ray computed tomography in pore structure characterization for a Berea sandstone: Resolution effect. Journal of Hydrology, vol. 472:473, pp. 254-261.

PERONI, L. F. and MIRANDA, L. C. M. (1987). Minimal volume photoacoustic cell measurement of thermal diffusivity: Effect of the thermoelastic sample bending. Journal of Applied Physics, vol. 62 (7), pp. 2955-2959.

PERRY, K. and LEE, J. Unconventional gas reservoirs – tight gas, coal seams, and shales (2007). Working Document of the NPC Global Oil and Gas Study, 52p.

PHILIPPE & PARTNES, (2011). Final report on unconventional gas in Europe. Framework contact: TREN/R1/350-2008lot1. 104p.

POFFO, C. M., De Lima, J. C., Souza, S. M., Trichês, D. M., Grandi, T. A. and Biasi, R. S. (2011). Photoacoustic study of nanocrystalline silicon produced by mechanical grinding. Physica B, vol. 406, pp. 1627-1632.

RAVIKOVITCH, P.I. and NEIMARK, A.V. (2002). Experimental confirmation of different mechanisms of evaporation from ink-bottle type pores: equilibrium, pore blocking, and cavitation. Langmuir, vol. 18, pp. 9830-9837.

REED, J. S. (1995). Principles of Ceramics Processing, second ed. John Wiley & Sons, New York, 126p.

REZAEE, R., Saeedi, A. and Clennell, B. (2012). Tight gas sands permeability estimation from mercury injection capillary pressure and nuclear magnetic resonance data. Journal of Petroleum Science and Engineering, vol. 88-89, pp. 92-99.

REZNIK, A. A. (1971). Permeability and Porosity Predictions from a Cut-and-rejoining Model and Pore-size Distribution, PhD thesis., University of Pittsburgh.

RITMAN, E. (2004). Micro-computed tomography: current status and developments. Annual Review of Biomedical Enggineering, vol. 6, pp. 185-208.

ROOTARE, H. M. and PRENZLOW, C.F. (1967). Surface area from mercury porosimetry measurements. Journal of Physical Chemistry, vol. 71, pp. 2733-2735.

ROSENCWAIG, A. and GERSHO, A. (1976). Theory of the photoacoustic effect with solids. Journal of Applied Physics, vol. 47 (1), pp. 64-69.

ROUQUEROL, J., Avnir, D., Fairbridge, C. W., Everett, D. H., Haynes, J. M., Pernicone, N., Ramsay, J. D. F, Sing, K. S. W and Unger, K. K (1994). Recommendations for the characterization of porous solids (Technical Report). Pure Applied Chemistry, vol. 66:8, pp. 1739-1758

ROUSSET, G., Lepoure, F. and Bertrand, L. (1983). Influence of thermoelastic bending on photoacoustic experiments related to measurements of thermal diffusivity of metals. Journal of Applied Physics, vol. 54, pp. 2383-2391.

RUBIO, C. M. (2013). A laboratory procedure to determine the thermal properties of silt loam soils beased on ASTM D 5334. Applied Ecology and Environmental Sciences, vol. 1:4, pp. 45-48.

RUSHING, J. A., Newsham, K. E., Lasswell, P. M., and Blasingame, T. A. (2004). Klinkenberg-Corrected Permeability Measurements in Tight Gas Sands: Steady-State Versus Unsteady-State Techniques. SPE 89867.

RUSHING, J. A., Newsham, K. E. and Blasingame, T. A. (2008). Rock typing - keys to understanding productivity in tight gas sands. SPE 114164, 3p.

RUSS, J. C. (2007). The image processing handbook, 5th ed. ISBN: 0849372542, CRC Press, Taylor & Francis Group, Boca Raton, USA, 817p.

RUTHVEN, D. M. (1984). Principles of Adsorption and Adsorption Processes. Wiley, New York, 464p.

SALH, R. (2011). Silicon nanocluster in silicon dioxide: Cathodoluminescence, energy dispersive X-ray analysis and infrared spectroscopy studies, Crystalline Silicon - Properties and Uses, Prof. Sukumar Basu (Ed.), InTech, DOI: 10.5772/35404, 39p.

SAKHAEE-POUR, A. and BRYANT, S. L. (2012). Gas permeability of shale. Society of Petroleum Engineers ISSN 1094-6470, vol. 15, number 4, pp. 401-409.

SARKISYAN, S.G. (1970) Sarkisyan Origin of authigenic clay minerals and their significance in petroleum geology. Sedimentary Geology, vol. 7:1, pp. 1-22.

SCHEIDEGGER, A. E. (1974). The physics of flow through porous media. University of Toronto Press, 3th edition.

SCHLÖMER, S. and KROOSS, B. M. (1997). Experimental characterization of the hydrocarbon sealing efficiency of cap rocks. Marine and Petroleum Geology, vol. 14, pp. 565-580.

SCHMITT, M (2009). Caracterização do sistema poroso de rochas selantes combinando-se adsorção de nitrogênio e intrusão de mercúrio. Dissertação de Mestrado, Programa de Pós-Graduação em Ciência e Engenharia de Materiais da Universidade Federal de Santa Catarina. Florianópolis, SC, Brasil.

SCHMITT, M., Fernandes, C. P., Da Cunha Neto, J. A. B., Wolf, F. G., Dos Santos, V. S. S. (2013). Characterization of pore systems in seal rocks using Nitrogen Gas adsorption combined with Mercury Injection capillary pressure techniques. Marine and Petroleum Geology, vol. 39, pp. 138-149.

SEZGIN, M. and SANKUR, B. (2004). Survey over image thresholding techniques and quantitative performance evaluation. Journal of Electronic Imaging, vol. 13, pp. 146-165.

SING, K. S. W., Everett, D. H., Haul, R. A. W., Moscou, L., Pierotti, R. A., Rouquerol, J. and Siemieniewska, T. (1985). Reporting physisorption data for gas/solid systems with special reference to the determination of surface area and porosity (Recommendations 1984), Pure & Applied Chemistry, vol. 57, pp. 603-619, IUPAC.

SMITH, C. (2001). Environmental Physics, Routledge, London 320p.

SOEDER, D. J. and CHOWDIAH, P. (1990). Pore geometry in high- and low-permeability sandstones, Travis Peak Formation, east Texas: Society of Petroleum Engineers Formation Evaluation, v. 5: 4, pp 421-430.

SOMERTON, W. H. (1992). Thermal properties and temperature-related behavior of rock-fluid systems. Elsevier, Developments in Petroleum Science, vol. 37, 257p.

SONDERGELD, C. H, Newsham, K.E., Comisky, J. T. and Rice, M. C. (2010). Petrophysical considerations in evaluating and producing shale gas resources. SPE 131768, 34p.

SORLAND, G.H., Djurhuus, K., Widerøe, H. C., Lien, J. R. and Skauge, A. (2007). Absolute pore size distributions from NMR. Diffusion Fundamentals, vol. 5, pp. 4.1-4.15.

STRALEY, C., Rossini, D., Vinegar, H., Tutunjian, P. and Morriss, C. (1997). Core analysis by low-field NMR. The core analyst, pp. 84-95.

SUN, C.-K., Sun, S.-Z., Lin, K.-H., Zhang, K. Y.-J., Liu, H.-L., Liu, S.-C. and Wu, J.-J. (2005). Ultrafast carrier dynamics in ZnO nanorods. Applied Physics Letters, vol. 87, 023106, 3p.

TIAB, D. and DONALDSON, E. (2004). Petrophysics: Theory and Practice of Measuring Reservoir Rock and Fluid Transport Properties. Gulf Professional, Amsterdam, Oxford.

TISSOT, B. P. and WELTE, D. (1984). Petroleum formation and occurrence. Springer-Velarg, Berlin, GE, 699p.

TIWARI, P., Deo, M., LIN, C.L. and Miller, D. J. (2013). Characterization of oil shale pore structure before and after pyrolysis by using X-ray micro CT. Fuel, vol. 107, pp. 547-554.

TORQUATO, S. (2000). Modeling of physical properties of composite materials. International Journal of Solids and Structures, vol. 37, pp. 411-422.

UMAR, M., Friis, H., Khan, A. S., Kassi, A. M., and Kasi, A. K. (2011). The effects of diagenesis on the reservoir characters in sandstones of the Late Cretaceous Pab Formation, Kirthar Fold Belt, southern Pakistan. Journal of Asian Earth Sciences, vol. 40, pp. 622-635.

VAIRIGS, J., Hearn, C. L., Dareing, D. W. and Rhoades, V. W. (1971). Effect of rock stress on gas production from low permeability rocks. Journal of Petroleum Technology. pp. 1161-1167.

VOSTEEN, H.-D. and SCHELLSCHMIDT (2003). Influence of temperature on thermal conductivity, thermal capacity and thermal diffusivity for different types of rock. Physics and Chemistry of the Earth, vol. 28 pp. 499-509.

XU, S. and WHITE, R. E. (1995). A new velocity model for clay-sand mixtures, Geophysical Prospecting, vol. 43, pp. 91-118.

WANG, C. and MANDELLS, A. (1999). Measurement of thermal diffusivity of air using photopyroelectric interferometry. Review of Scientific Instruments, vol. 70, No. 5, pp. 2372-2378.

WANG, Z., Lv, K., Wang, G., Deng, K. and Tang, D. (2010). Study on the shape control and photocatalytic activity of high-energy anatase titania. Applied Catalysis B: Environmtal, vol. 100, pp. 378-385.

WEBB, P. A. (1993). Micromeritics PoreSizer 9320 and AutoPore II 9220 – Data collection, reduction and presentation, 17p.

WEBB, P. A. (2001). An introduction to the physical characterization of materials by mercury intrusion porosimetry with emphasis on reduction and presentations of experimental data. Micromeritics Corp. Internal Publications, Norcross, GA.

WEO-2011, World Energy Outlook (2011). Are we entering a gold age of gas? Special report of international Energy Agency (IEA), 131p.

WEO-2012, World Energy Outlook (2012). Presentation available at http://www.worldenergyoutlook.org/pressmedia/recentpresentations/PresentationWEO2012launch.pdf, access in 11/12/2013.

WILDENSCHILD, D. and SHEPPARD, A. P. (2013). X-ray imaging and analysis techniques for quantifying pore-scale structure and processes in subsurface porous medium systems. Advances in Water Resources, vol. 51, pp. 217-246.

WIKIPEDIA – Characterization (materials science). Available at http://en.wikipedia.org/wiki/Characterization_%28materials_science%29 Access in 20/02/2014.

WIKIPETRO– NMR Petrophysics. Available at http://petrowiki.org/NMR_petrophysics. Access in 02/12/2013.

WIKIPETRO– Tight Gas Reservoirs. Available at http://petrowiki.org/Tight_gas_reservoirs, access in 20/01/2014.

WOJNAR, L. (1998). Image analysis applications in materials engineering. ISBN 0-8493-8226-2, CRC Press LLC, Boca Raton, 245p.

WOLF, F. G. (2006). Modelagem de interação fluido-sólido para simulação de molhabilidade e capilaridade usando o modelo Lattice-Boltzmann.

Tese de Doutorado. Programa de Pós-Graduação em Engenharia Mecânica da Universidade Federal de Santa Catarina, Florianópolis-SC.

WU, Y.S., Pruess, K. and Persoff, P. (1998). Gas flow in porous media with Klinkenberg effects. Transport in Porous Media, vol. 32 (1), pp. 117-137.

WYLLIE, M. R. J and SPANGLER, M. B. (1952). Application of electrical resistivity measurements to problem of fluid flow in porous media. Bulletin of the American Association of Petroleum Geologists, vol. 36:2, pp. 359-403.

YANG, Y. and APLIN, A. C. (2007). Permeability and petrophysical properties of 30 natural mudstones. Journal of Geophysics Research, vol. 112, B03206.

YANG, Y. S., Liu, K. Y., Mayo, S., Clennell, M. B. and Xiao, T. Q. (2013). A data-constrained modelling approach to sandstone microstructure characterization. Journal of Petroleum Science and Engineering, vol. 105, pp. 76-83.

YAO, Y., Liu, D., Che, Y., Tang, D., Tang, S. and Huang, W. (2010). Petrophysical characterization of coals by low-field nuclear magnetic resonance (NMR). Fuel, vol. 89, pp. 1371-1380.

YEO, L. (2006). Wetting and Spreading, pp. 2186-2196. Available at http://users.monash.edu/~lyeo/Dr_Leslie_Yeo/Publications_files/Wetting&Spreading_Encyclopedia%20of%20Microfluidics%20and%20Nanofluidics.pdf, accessed in 17/04/2014.

YOUNG, T. (1805). An Essay on the Cohesion of Fluids, Philosophical Transactions of the Royal Society of London, vol. 95, pp. 65-87.

YOUSSEF, S., Maire, E., Gaertner, R. (2005). Finite element modelling of the actual structure of cellular materials determined by X-ray tomography. Acta Materialia, vol. 53, pp. 719-730.

YU, J., Yu, J. C., Leung, M. K.-P., Ho, W., Cheng, B., Zhao, X., Zhao, J. (2003). Effects of acidic and basic hydrolysis catalysts on the photocatalytic activity and microstructures of bimodal mesoporous titania. Journal of Catalysis, vol. 217, pp. 69-78.

YUSGIANTORO, P. (2004). Petroleum will still be the major energy resource in the 21st century. Speeches of the Organization of the

Petroleum Exporting countries (OPEC), Available at http://www.opec.org/opec_web/en/902.htm. Access in 02/12/2013.

ZHANG, J. J. and BENTLEY, L. R. (2003). Pore geometry and elastic moduli in sandstones. CREWES Research Report, vol. 15, 20p.

ZHANG, X. (2011). Modeling of Diagenetic Controls on Reservoir Characteristics. SPE148270.

ZHANG, X., Ding, M., Hou, W. and Yin, Z. (2013). Decision-based non-local means filter for removing impulse noise from digital images. Signal Processing, vol. 93, pp. 517-524.

ZHONG, Z. and WANG, X. (2006). Thermal transport in nanocrystalline materials. Journal of Applied Physics, vol. 100, 044310.

ZIARANI, A. S. and AGUILERA, R. (2012). Pore-throat radius and tortuosity estimation from formation resistivity data for tight-gas sandstone reservoirs. Journal of Applied Geophysics, vol. 83, pp. 65-73.

ZIEGLER, G. and HASSELMAN, D. P. H. (1981). Effect of phase composition and microstructure on the thrmal diffusivity of silicon nitride. Journal of Materials Science, vol. 16, pp. 495-503.

ZIMMERMAN, R. W. (1988). Thermal conductivity of fluid-saturated rocks. Journal of Petroleum Science and Engineering, vol. 3, pp. 219-227.

Appendix A – Data from generated skeleton using C3DE algorithm.

Classes of Radius	A-11V Res1 (0.75 um)								A-11V Res2 (0.35 um)								A-11V Res3 (0.064 um)							
	Pore Body				Throat				Pore Body				Throat				Pore Body				Throat			
	Frequency		Volume		Frequency		Volume		Frequency		Volume		Frequency		Volume		Frequency		Volume		Frequency		Volume	
	(n)	(%)	Incremental (%)	Cumulative (%)	(n)	(%)	Incremental (%)	Cumulative (%)	(n)	(%)	Incremental (%)	Cumulative (%)	(n)	(%)	Incremental (%)	Cumulative (%)	(n)	(%)	Incremental (%)	Cumulative (%)	(n)	(%)	Incremental (%)	Cumulative (%)
0	0	0.00	0	0	0	0.00	0	0	0	0.00	0	0	0	0.00	0	0	0	0.00	0	0	0	0.00	0	0
0.02	0	0.00	0	0	0	0.00	0	0	0	0.00	0	0	0	0.00	0	0	0	0.00	0	0	0	0.00	0	0
0.04	0	0.00	0	0	0	0.00	0	0	0	0.00	0	0	0	0.00	0	0	0	0.00	0	0	1	0.20	4.6296E-07	4.6296E-07
0.06	0	0.00	0	0	0	0.00	0	0	0	0.00	0	0	0	0.00	0	0	3	0.60	3.7037E-06	3.7037E-06	5	1.02	6.0185E-06	6.4815E-06
0.08	0	0.00	0	0	0	0.00	0	0	0	0.00	0	0	0	0.00	0	0	6	1.20	1.8519E-05	2.2222E-05	39	7.96	0.00011296	0.00011944
0.1	0	0.00	0	0	0	0.00	0	0	0	0.00	0	0	0	0.00	0	0	17	3.39	0.00010139	0.00012361	55	11.22	0.00031852	0.00043796
0.2	0	0.00	0	0	0	0.00	0	0	0	0.00	0	0	0	0.00	0	0	184	36.65	0.00523426	0.00535787	278	56.73	0.00574398	0.00618194
0.3	0	0.00	0	0	0	0.00	0	0	149	0.83	9.2519E-05	9.2519E-05	338	1.02	0.00021896	0.00021896	111	22.11	0.01300555	0.01836343	56	11.43	0.00574583	0.01192778
0.4	0	0.00	0	0	0	0.00	0	0	243	1.35	0.00049123	0.00058375	1169	3.53	0.00243236	0.00265132	48	9.56	0.01522176	0.03358518	27	5.51	0.00765972	0.0195875
0.5	65	0.67	3.0093E-05	3.0093E-05	14	0.13	6.7106E-06	6.7106E-06	468	2.60	0.00195479	0.00253854	2539	7.67	0.0106912	0.01334253	31	6.18	0.02130138	0.05488657	19	3.88	0.01251342	0.03210092
0.6	33	0.34	3.0556E-05	6.0648E-05	22	0.20	2.1091E-05	2.7801E-05	851	4.72	0.00638159	0.00892013	3329	10.05	0.02468136	0.03802389	24	4.78	0.02791157	0.08279814	5	1.02	0.00605648	0.0381574
0.7	27	0.28	3.75E-05	9.8148E-05	24	0.22	3.4512E-05	6.2313E-05	975	5.41	0.01172608	0.02064621	3431	10.36	0.04109371	0.07911759	21	4.18	0.04199537	0.12479352	1	0.20	0.00175278	0.03991018
0.8	52	0.53	9.6296E-05	0.00019444	54	0.50	0.00010354	0.00016585	1128	6.26	0.02070482	0.04135103	3213	9.70	0.05866042	0.13777801	15	2.99	0.04619771	0.17099123	0	0.00	0	0.03991018
0.9	109	1.12	0.00029537	0.00048981	425	3.92	0.00129084	0.00145669	1056	5.86	0.02811425	0.06946527	2882	8.70	0.07680246	0.21458047	4	0.80	0.01949397	0.1904852	0	0.00	0	0.03991018
1	91	0.93	0.00035787	0.00084769	497	4.58	0.00202039	0.00347708	997	5.53	0.03697446	0.10643974	2874	8.68	0.10632653	0.320907	6	1.20	0.03857408	0.22905928	0	0.00	0	0.03991018
2	2541	26.10	0.04978287	0.05063056	6836	63.01	0.10078155	0.10425862	8829	48.97	1.31950916	1.42594889	12873	38.86	1.39009262	1.71099962	25	4.98	0.44500522	0.6740645	3	0.61	0.09451808	0.13442826
3	3586	36.84	0.2584852	0.30911575	1997	18.41	0.13186864	0.23612726	2957	16.40	1.72561584	3.15156473	475	1.43	0.22867377	1.93967339	4	0.80	0.42539826	1.09946276	0	0.00	0	0.13442826
4	1943	19.96	0.35748332	0.66659907	576	5.31	0.10766857	0.34379584	341	1.89	0.54559318	3.69715792	1	0.00	0.00127191	1.9409453	0	0.00	0	1.09946276	1	0.20	0.40038074	0.534809
5	679	6.97	0.26576619	0.93236527	226	2.08	0.09309592	0.43689176	30	0.17	0.10583312	3.80299104	0	0.00	0	1.9409453	1	0.20	0.68996924	1.789432	0	0.00	0	0.534809
6	284	2.92	0.20736157	1.13972684	84	0.77	0.06172315	0.49861491	4	0.02	0.02550478	3.82849582	0	0.00	0	1.9409453	1	0.20	0.94461971	2.73405171	0	0.00	0	0.534809
7	134	1.38	0.16118422	1.30091105	49	0.45	0.0603307	0.55894561	0	0.00	0	3.82849582	0	0.00	0	1.9409453	1	0.20	2.13114421	4.86519591	0	0.00	0	0.534809
8	83	0.85	0.15463848	1.45554953	20	0.18	0.03751399	0.59645959	0	0.00	0	3.82849582	0	0.00	0	1.9409453	0	0.00	0	4.86519591	0	0.00	0	0.534809
9	39	0.40	0.10559031	1.56113984	15	0.14	0.0443339	0.6407935	0	0.00	0	3.82849582	0	0.00	0	1.9409453	0	0.00	0	4.86519591	0	0.00	0	0.534809
10	22	0.23	0.08646388	1.64760372	3	0.03	0.01031859	0.65111208	0	0.00	0	3.82849582	0	0.00	0	1.9409453	0	0.00	0	4.86519591	0	0.00	0	0.534809
20	44	0.45	0.51140161	2.15900533	7	0.06	0.0458927	0.69700478	0	0.00	0	3.82849582	0	0.00	0	1.9409453	0	0.00	0	4.86519591	0	0.00	0	0.534809
30	2	0.02	0.12905423	2.28805956	0	0.00	0	0.69700478	0	0.00	0	3.82849582	0	0.00	0	1.9409453	0	0.00	0	4.86519591	0	0.00	0	0.534809
40	1	0.01	0.15387921	2.44193877	0	0.00	0	0.69700478	0	0.00	0	3.82849582	0	0.00	0	1.9409453	0	0.00	0	4.86519591	0	0.00	0	0.534809
50	0	0.00	0	2.44193877	0	0.00	0	0.69700478	0	0.00	0	3.82849582	0	0.00	0	1.9409453	0	0.00	0	4.86519591	0	0.00	0	0.534809
60	0	0.00	0	2.44193877	0	0.00	0	0.69700478	0	0.00	0	3.82849582	0	0.00	0	1.9409453	0	0.00	0	4.86519591	0	0.00	0	0.534809
Sum	**9735**				**10849**				**18028**				**33124**				**502**				**490**			
									Accumulation of all resolutions ->Total porosity (%)															**14.308**

Classes of Radius	A-17V Res1 (0.74 um)								A-17V Res2 (0.31 um)							
	Pore Body				Throat				Pore Body				Throat			
	Frequency		Volume		Frequency		Volume		Frequency		Volume		Frequency		Volume	
	(n)	(%)	Incremental (%)	Cumulative (%)	(n)	(%)	Incremental (%)	Cumulative (%)	(n)	(%)	Incremental (%)	Cumulative (%)	(n)	(%)	Incremental (%)	Cumulative (%)
0	0	0.00	0	0	0	0.00	0	0	0	0.00	0	0	0	0.00	0	0
0.02	0	0.00	0	0	0	0.00	0	0	0	0.00	0	0	0	0.00	0	0
0.04	0	0.00	0	0	0	0.00	0	0	0	0.00	0	0	0	0.00	0	0
0.06	0	0.00	0	0	0	0.00	0	0	0	0.00	0	0	0	0.00	0	0
0.08	0	0.00	0	0	0	0.00	0	0	0	0.00	0	0	0	0.00	0	0
0.1	0	0.00	0	0	0	0.00	0	0	0	0.00	0	0	0	0.00	0	0
0.2	0	0.00	0	0	0	0.00	0	0	23	0.30	1.06481E-05	1.06481E-05	33	0.33	1.52778E-05	1.52778E-05
0.3	0	0.00	0	0	0	0.00	0	0	34	0.44	3.88889E-05	4.9537E-05	60	0.60	7.12963E-05	8.65741E-05
0.4	0	0.00	0	0	0	0.00	0	0	82	1.07	0.000228704	0.000278241	294	2.93	0.000849074	0.000935648
0.5	0	0.00	0	0	12	0.31	5.55556E-06	5.55556E-06	317	4.13	0.002032407	0.002310648	666	6.64	0.003980093	0.004915741
0.6	11	0.44	1.01852E-05	1.01852E-05	8	0.20	7.40741E-06	1.2963E-05	597	7.78	0.006477778	0.008788426	805	8.03	0.008816204	0.013731944
0.7	6	0.24	8.33331E-06	1.85185E-05	12	0.31	1.66666E-05	2.96296E-05	623	8.12	0.011198152	0.019986578	705	7.03	0.012784726	0.02651667
0.8	8	0.32	1.75926E-05	3.61111E-05	16	0.41	3.37963E-05	6.34259E-05	539	7.03	0.01482407	0.034810648	661	6.59	0.018312034	0.044828704
0.9	4	0.16	1.11111E-05	4.72222E-05	23	0.59	6.71297E-05	0.000130556	498	6.49	0.019883794	0.054694442	707	7.05	0.028374998	0.073203702
1	3	0.12	1.25E-05	5.97222E-05	28	0.71	0.000119444	0.00025	419	5.46	0.023185184	0.077879626	687	6.85	0.038375923	0.111579625
2	88	3.48	0.001963427	0.002023149	479	12.22	0.010564351	0.010814351	2845	37.09	0.619642124	0.69752175	3608	35.99	0.727890268	0.839469893
3	353	13.97	0.030121753	0.032144902	1080	27.56	0.082059247	0.092873599	1039	13.55	0.992275903	1.689797653	1295	12.92	1.252451488	2.091921381
4	513	20.30	0.105654615	0.137799516	897	22.89	0.176770334	0.269643932	387	5.05	1.057686481	2.747484135	370	3.69	0.971106424	3.063027805
5	471	18.64	0.195891204	0.333690721	577	14.72	0.238771778	0.508415711	160	2.09	0.903552838	3.651036972	100	1.00	0.54501159	3.608039395
6	300	11.87	0.231371288	0.565062009	293	7.48	0.221953232	0.730368942	66	0.86	0.683100477	4.334137449	23	0.23	0.232723592	3.840762986
7	223	8.82	0.282774162	0.847836171	179	4.57	0.227451876	0.957820819	24	0.31	0.415380158	4.749517607	8	0.08	0.141446335	3.982209322
8	157	6.21	0.304529657	1.152365829	105	2.68	0.204792563	1.162613382	11	0.14	0.291971102	5.041488709	2	0.02	0.059750055	4.041959377
9	97	3.84	0.286995793	1.439361622	69	1.76	0.196625935	1.359239317	4	0.05	0.148837829	5.190326538	0	0.00	0	4.041959377
10	77	3.05	0.306511137	1.745872759	32	0.82	0.126043976	1.485283293	2	0.03	0.107124542	5.29745108	0	0.00	0	4.041959377
20	171	6.77	2.271161849	4.017034608	109	2.78	1.07951827	2.564801563	0	0.00	0	5.29745108	0	0.00	0	4.041959377
30	44	1.74	2.876713555	6.893748163	0	0.00	0	2.564801563	0	0.00	0	5.29745108	0	0.00	0	4.041959377
40	1	0.04	0.158946561	7.052694724	0	0.00	0	2.564801563	0	0.00	0	5.29745108	0	0.00	0	4.041959377
50	0	0.00	0	7.052694724	0	0.00	0	2.564801563	0	0.00	0	5.29745108	0	0.00	0	4.041959377
60	0	0.00	0	7.052694724	0	0.00	0	2.564801563	0	0.00	0	5.29745108	0	0.00	0	4.041959377
Sum	**2527**				**3919**				**7670**				**10024**			
							Accumulation of all resolutions ->Total porosity (%)									18.95690674

Appendix B – Incremental pore and throat volumes, obtained for each scale after the combination of frequencies generated by C3DE.

Classes of Radius	A-11V - Pore Size Distribution (Combination of all resolutions)									
	Pore Body (Volume)					Throat (Volume)				
	Res3 (0.064 um)	Res2 (0.35 um)	Res1 (0.75 um)	**Combined**		Res3 (0.064 um)	Res2 (0.35 um)	Res1 (0.75 um)	**Combined**	
	Incremental (%)	Incremental (%)	Incremental (%)	Incremental (%)	Cumulative (%)	Incremental (%)	Incremental (%)	Incremental (%)	Incremental (%)	Cumulative (%)
0	0	0	0	0	0	0	0	0	0	0
0.02	0	0	0	0	0	0	0	0	0	0
0.04	0	0	0	0	0	4.62963E-07	0	0	4.62963E-07	4.62963E-07
0.06	3.7037E-06	0	0	3.7037E-06	3.7037E-06	6.01852E-06	0	0	6.01852E-06	6.48148E-06
0.08	1.85185E-05	0	0	1.85185E-05	2.22222E-05	0.000112963	0	0	0.000112963	0.000119444
0.1	0.000101389	0	0	0.000101389	0.000123611	0.000318519	0	0	0.000318519	0.000437963
0.2	0.00523426	0	0	0.00523426	0.005357871	0.005743981	0	0	0.005743981	0.006181944
0.3	0.013005554	0	0	0.013005554	0.018363425	0.005745833	0	0	0.005745833	0.011927777
0.4	0.015221758	0	0	0.015221758	0.033585184	0.007659723	0	0	0.007659723	0.0195875
0.5	0.021301384	0	0	0.021301384	0.054886568	0	0.010691203	0	0.010691203	0.030278704
0.6	0.027911575	0	0	0.027911575	0.082798143	0	0.024681361	0	0.024681361	0.054960065
0.7	0	0.011726081	0	0.011726081	0.094524223	0	0.041093707	0	0.041093707	0.096053772
0.8	0	0.020704817	0	0.020704817	0.11522904	0	0.058660418	0	0.058660418	0.15471419
0.9	0	0.028114246	0	0.028114246	0.143343286	0	0.076802458	0	0.076802458	0.231516648
1	0	0.036974463	0	0.036974463	0.180317749	0	0.106326529	0	0.106326529	0.337843177
2	0	1.319509155	0	1.319509155	1.499826905	0	1.390092618	0	1.390092618	1.727935795
3	0	0	0.258485198	0.258485198	1.758312103	0	0	0.13186864	0.13186864	1.859804435
4	0	0	0.35748332	0.35748332	2.115795423	0	0	0.107668573	0.107668573	1.967473009
5	0	0	0.265766193	0.265766193	2.381561615	0	0	0.093095923	0.093095923	2.060568931
6	0	0	0.207361571	0.207361571	2.588923186	0	0	0.061723148	0.061723148	2.122292079
7	0	0	0.161184215	0.161184215	2.750107401	0	0	0.060330702	0.060330702	2.182622781
8	0	0	0.15463848	0.15463848	2.904745881	0	0	0.037513985	0.037513985	2.220136766
9	0	0	0.105590307	0.105590307	3.010336188	0	0	0.044333901	0.044333901	2.264470667
10	0	0	0.086463882	0.086463882	3.09680007	0	0	0.010318588	0.010318588	2.274789255
20	0	0	0.511401612	0.511401612	3.608201682	0	0	0.045892699	0.045892699	2.320681954
30	0	0	0.129054229	0.129054229	3.737255911	0	0	0	0	2.320681954
40	0	0	0.153879208	0.153879208	3.89113512	0	0	0	0	2.320681954
50	0	0	0	0	3.89113512	0	0	0	0	2.320681954
60	0	0	0	0	3.89113512	0	0	0	0	2.320681954
						Combination of all resolutions -> Total porosity (%)		**->**	**3.89+2.32 =**	**6.2118**

A-17V - Pore Size Distribution (Combination of all resolutions)

Classes of Radius	Pore Body (Volume)					Throat (Volume)				
	Res3 (0.064 um)	Res2 (0.31 um)	Res1 (0.74 um)	Combined		Res3 (0.064 um)	Res2 (0.31 um)	Res1 (0.74 um)	Combined	
	Incremental (%)	Incremental (%)	Incremental (%)	Incremental (%)	Cumulative (%)	Incremental (%)	Incremental (%)	Incremental (%)	Incremental (%)	Cumulative (%)
0	0	0	0	0	0	0	0	0	0	0
0.02	0	0	0	0	0	0	0	0	0	0
0.04	0	0	0	0	0	0	0	0	0	0
0.06	0	0	0	0	0	0	0	0	0	0
0.08	0	0	0	0	0	0	0	0	0	0
0.1	0	0	0	0	0	0	0	0	0	0
0.2	0	1.06481E-05	0	1.06481E-05	1.06481E-05	0	1.52778E-05	0	1.52778E-05	1.52778E-05
0.3	0	3.88889E-05	0	3.88889E-05	4.9537E-05	0	7.12963E-05	0	7.12963E-05	8.65741E-05
0.4	0	0.000228704	0	0.000228704	0.000278241	0	0.000849074	0	0.000849074	0.000935648
0.5	0	0.002032407	0	0.002032407	0.002310648	0	0.003980093	0	0.003980093	0.004915741
0.6	0	0.006477778	0	0.006477778	0.008788426	0	0.008816204	0	0.008816204	0.013731944
0.7	0	0.011198152	0	0.011198152	0.019986578	0	0.012784726	0	0.012784726	0.02651667
0.8	0	0.01482407	0	0.01482407	0.034810648	0	0.018312034	0	0.018312034	0.044828704
0.9	0	0.019883794	0	0.019883794	0.054694442	0	0.028374998	0	0.028374998	0.073203702
1	0	0.023185184	0	0.023185184	0.077879626	0	0.038375923	0	0.038375923	0.111579625
2	0	0.619642124	0	0.619642124	0.69752175	0	0.727890268	0	0.727890268	0.839469893
3	0	0	0.030121753	0.030121753	0.727643503	0	0	0.082059247	0.082059247	0.92152914
4	0	0	0.105654615	0.105654615	0.833298118	0	0	0.176770334	0.176770334	1.098299474
5	0	0	0.195891204	0.195891204	1.029189322	0	0	0.238771778	0.238771778	1.337071252
6	0	0	0.231371288	0.231371288	1.260560611	0	0	0.221953232	0.221953232	1.559024484
7	0	0	0.282774162	0.282774162	1.543334773	0	0	0.227451876	0.227451876	1.78647636
8	0	0	0.304529657	0.304529657	1.84786443	0	0	0.204792563	0.204792563	1.991268924
9	0	0	0.286995793	0.286995793	2.134860223	0	0	0.196625935	0.196625935	2.187894859
10	0	0	0.306511137	0.306511137	2.44137136	0	0	0.126043976	0.126043976	2.313938835
20	0	0	2.271161849	2.271161849	4.712533209	0	0	1.07951827	1.07951827	3.393457105
30	0	0	2.876713555	2.876713555	7.589246764	0	0	0	0	3.393457105
40	0	0	0.158946561	0.158946561	7.748193325	0	0	0	0	3.393457105
50	0	0	0	0	7.748193325	0	0	0	0	3.393457105
60	0	0	0	0	7.748193325	0	0	0	0	3.393457105
						Combination of all resolutions -> Total porosity (%)			**-> 7.74+3.39 =**	**11.14165043**